SYNTHESIS AND APPLICATIONS OF RUTHENIUM(II)QUATERPYRIDINIUM COMPLEXES AND POLY-N-ISOPROPYLACRYLAMIDE/ ACRYLIC ACID COPOLYMERS

by

PUBUDU HASANKA SIYAMBALAGODA GAMAGE

B.Sc. (Hons), University of Peradeniya, Sri Lanka, 2004

AN ABSTRACT OF A DISSERTATION

submitted in partial fulfillment of the requirements for the degree

DOCTOR OF PHILOSOPHY

Department of Chemistry
College of Arts and Science

KANSAS STATE UNIVERSITY
Manhattan, Kansas

2009

Abstract

Tris-homoleptic ruthenium(II)-quaterpyridyl and quaterpyridinium complexes, with +8 and +14 charge were synthesized by utilizing high pressure reaction pathway. These complexes have diameters ranging from 1.82 to 4.55 nm according to the molecular modeling calculations. These ruthenium complexes are highly luminescent and contain long excited state life times. The novel ruthenium(II)-quaterpyridinium complexes exhibit superior reactivity as sensitizer-relay-assemblies (SRA's) in sacrificial systems for water and carbon dioxide reductions, while harvesting the ultraviolet- and most of the visible fraction of the incident solar spectrum. Ru(II)-quaterpyridinium complexes and Pd/TiO_2 catalysts were successfully used as the catalytic system for the photo catalytic reduction of water and carbon dioxide to hydrogen and methane respectively. Phosphonate-tethered Ru(II)-quaterpyridinium complexes were synthesized from Ru(II)-tris-quaterpyridyl complexes. These complexes form stable adhesive layers on indium tin oxide (ITO) electrodes. A series of differential pulse voltammetry experiments were carried out to measure the ground state and excited state redox potentials of all the Ru(II)quaterpyridinium complexes. The reductive potentials obtained were compared with the reductive potentials of CO_2 to CH_4 and H_2O to H_2 reductions. The measurements obtained from the experiments confirmed that it is possible to thermodynamically oxidize water and reduce CO_2 by using phosphonate-tethered Ru(II)-quaterpyridinium complexes.

These complexes are successfully utilized as prototypes for mycobacterial channel blockers. The Ru(II) complexes show distinct changes in their luminescence spectra when bound to the porin MspA from *M. smegmatis*, which is a non-pathogenic relative of *M. tuberculosis*. By using HPLC, we have determined binding constants of the Ru(II)-complexes to MspA in phosphate buffer (0.05 M, pH = 6.8) ranging from 5.2×10^9 M^{-1} (Ru-C2) to 1.8×10^9 M^{-1} (Ru-C4). Our findings indicate that channel blocking is a promising treatment strategy for mycobacterial infections.

Poly-N-isopropyl-acrylamide/acetic acid copolymers were synthesized and characterized by elemental analysis and gel permeation chromatography. The average composition of the copolymers determined from CHN analysis is in excellent correlation with the feed composition indicating that the radical polymerization process is indeed statistical. Crosslinking of individual polymer chains permitted the generation of ultraflat layers on Mica surfaces by a simple spin-casting procedure, which are able to host the mycobacterial channel protein MspA, while retaining its channel function.

SYNTHESIS AND APPLICATIONS OF RUTHENIUM(II)QUATERPYRIDINIUM COMPLEXES AND POLY-N-ISOPROPYLACRYLAMIDE/ ACRYLIC ACID COPOLYMERS

by

PUBUDU HASANKA SIYAMBALAGODA GAMAGE

B.Sc. (Hons), University of Peradeniya, Sri Lanka, 2004

A DISSERTATION

submitted in partial fulfillment of the requirements for the degree

DOCTOR OF PHILOSOPHY

Department of Chemistry
College of Arts and Science

KANSAS STATE UNIVERSITY
Manhattan, Kansas

2009

Approved by:

Major Professor
Dr. Stefan H. Bossmann

Copyright

Abstract

Tris-homoleptic ruthenium(II)-quaterpyridyl and quaterpyridinium complexes, with +8 and +14 charge were synthesized by utilizing high pressure reaction pathway. These complexes have diameters ranging from 1.82 to 4.55 nm according to the molecular modeling calculations. These ruthenium complexes are highly luminescent and contain long excited state life times. The novel ruthenium(II)-quaterpyridinium complexes exhibit superior reactivity as sensitizer-relay-assemblies (SRA's) in sacrificial systems for water and carbon dioxide reductions, while harvesting the ultraviolet- and most of the visible fraction of the incident solar spectrum. Ru(II)-quaterpyridinium complexes and Pd/TiO_2 catalysts were successfully used as the catalytic system for the photo catalytic reduction of water and carbon dioxide to hydrogen and methane respectively. Phosphonate-tethered Ru(II)-quaterpyridinium complexes were synthesized from Ru(II)-tris-quaterpyridyl complexes. These complexes form stable adhesive layers on indium tin oxide (ITO) electrodes. A series of differential pulse voltammetry experiments were carried out to measure the ground state and excited state redox potentials of all the Ru(II)quaterpyridinium complexes. The reductive potentials obtained were compared with the reductive potentials of CO_2 to CH_4 and H_2O to H_2 reductions. The measurements obtained from the experiments confirmed that it is possible to thermodynamically oxidize water and reduce CO_2 by using phosphonate-tethered Ru(II)-quaterpyridinium complexes.

These complexes are successfully utilized as prototypes for mycobacterial channel blockers. The Ru(II) complexes show distinct changes in their luminescence spectra when bound to the porin MspA from *M. smegmatis*, which is a non-pathogenic relative of *M. tuberculosis*. By using HPLC, we have determined binding constants of the Ru(II)-complexes to MspA in phosphate buffer (0.05 M, pH = 6.8) ranging from $5.2 \times 10^9\ M^{-1}$ (Ru-C2) to $1.8 \times 10^9\ M^{-1}$ (Ru-C4). Our findings indicate that channel blocking is a promising treatment strategy for mycobacterial infections.

Poly-N-isopropyl-acrylamide/acetic acid copolymers were synthesized and characterized by elemental analysis and gel permeation chromatography. The average composition of the copolymers determined from CHN analysis is in excellent correlation with the feed composition indicating that the radical polymerization process is indeed statistical. Crosslinking of individual polymer chains permitted the generation of ultraflat layers on Mica surfaces by a simple spin-casting procedure, which are able to host the mycobacterial channel protein MspA, while retaining its channel function.

Table of Contents

List of Figures

List of Tables

Acknowledgements

First, I would like to thank my advisor Dr. Stefan H. Bossmann for his kindness, encouragement, guidance, suggestions and continuous support throughout my Ph.D. program. In particular, I would like to thank him for giving me the independence to carry out my ideas in my research and standing beside me to help out whenever I needed help. He has played a huge role in molding me to be a good chemist.

Special appreciation goes to all the committee members Dr. Kenneth Klabunde, Dr. Om Prakash, Dr. Eric Maatta Dr. Duy Hua and Dr. James Edgar for their excellent support.

I would like to express my gratitude to Kathrin Bossmann for helping me in all the possible ways during the past few years. I would like to thank my group members for their continuous support, especially to Thilani Samarakoon for the all the assistance she has given me throughout the Ph.D program.

I would like to thank Dr. Kenneth Klabunde and Dr. Daniel Higgins for allowing me to use the equipment in their research labs. I also want to extend my gratitude to our department technicians James Hodgson, Richard Bachamp, Tobe Eggers and Ronn Jackson for all the help they have given me to repair the equipment that I used in my research. I would like to thank all of my friends, co-workers and staff members in the Kansas State University who have helped me to have a pleasurable time here in Manhattan during my stay.

Most importantly, I would like to thank my dear wife for her understanding, love and all the help she has given me during my Ph.D. It would have been impossible to achieve all this without her help, love, and encouragement during the last few years. I also want to thank my parents, brother and two sisters for helping me in various ways and for the love and caring they have shown me throughout the years.

DEDICATION

Dedicated to my wife and parents for their continues support

CHAPTER 1 - SYNTHESIS OF HIGHLY CHARGED RUTHENIUM (II)QUATERPYRIDINE COMPLEXES

1.1 Introduction

Ruthenium(II)polypyridine complexes (Figure 1.1) are a class of compounds, which has been widely studied during the last three decades.[1,2] These compounds possess an exclusive combination of photo-physical properties, which make them a very important class of complexes in pure and applied chemistry. Ruthenium-polypyridine complexes have fascinated many researchers due to their chemical stability in the redox states (+1, +2, and +3), excited state reactivity, long excited state life times, redox properties, and luminescence efficiencies.[2] Therefore, these ruthenium complexes play a vital role in photochemistry, photocatalysis, electro-chemistry, photoelectrochemistry, chemiluminescence, energy transfer, and electron transfer.[2]

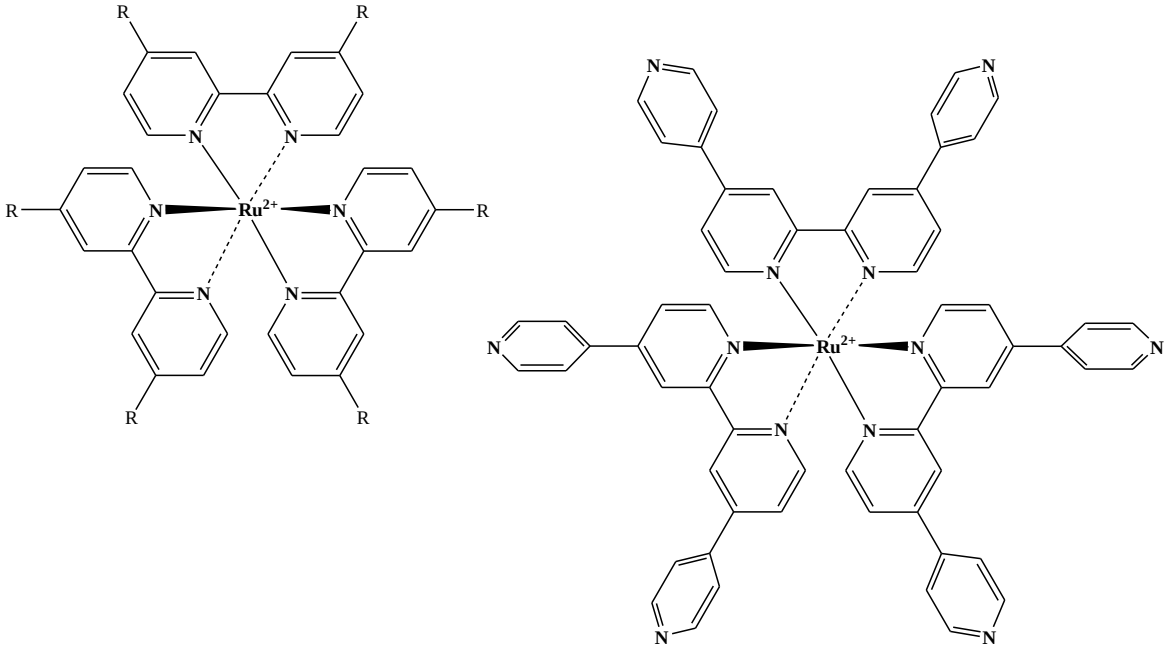

Figure 1.1: Ruthenium(II)-polypyridine complexes

Ruthenium(II)polypyridine complexes has the ability to absorb one or several photons (Figure 1.2)[2] in any photochemical or photophysical process. Upon absorption of one photon (at least), an electronically excited state is reached. If this absorption occurs in the visible range of the electromagnetic spectrum, a singlet MLCT (metal to ligand charge transfer) state is populated, which undergoes rapid intersystem crossing to a second MLCT state, which is mostly a triplet. The excited triplet MLCT state has a lifetime of up to several hundred nanoseconds. This can be achieved via thermal deactivation, luminescence, energy- or electron transfer or a diabatic or adiabatic photochemical reaction.[2] Figure 1.2 illustrates the deactivation pathways of excited ruthenium(II)polypyridinine complexes.[2] 1. The excited species can undergo a photochemical reaction to produce a new chemical species. This can be achieved during the lifetime of the excited MLCT state or in a "hot" ground state after deactivation 2. Excited complexes can release energy as luminescence. This process has to compete with the thermal deactivation 3. Energy can be released as heat, which is known as radiationless or thermal deactivation. 4. Excited complexes can undergo energy- and/or electron-transfer quenching to external acceptors.[2] This process is diffusion controlled, unless the ruthenium(II)complex and the acceptor are chemically linked or form a supramolecule.

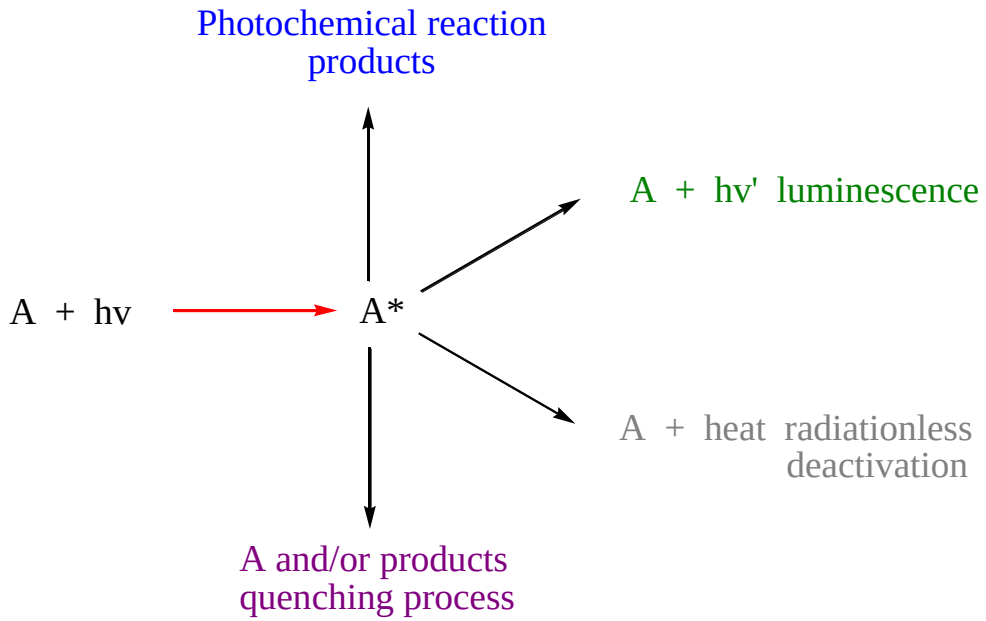

Figure 1.2: Schematic illustration of deactivation procedures of an excited ruthenium(II)poly-pyridine complex [2]

In most of the transition metal complexes, the ground state is a singlet state and the lowest excited state is a triplet state, or has mostly triplet character.[3] However, transitions from ground state to the excited state with a different spin are spin-forbidden.[3] Therefore, the lowest excited state (triplet) cannot be filled efficiently by absorbing energy in a photochemical process. First, electrons excite to the lowest singlet state, which is spin-allowed (Figure 1.3) or to higher singlet state and deactivate to the lowest excited singlet state, from which all photochemistry occurs ("rule of Kasha").[3,4] Excited complexes can release their energy via different pathways as depicted in the Jablonski diagram in Figure 1.3.

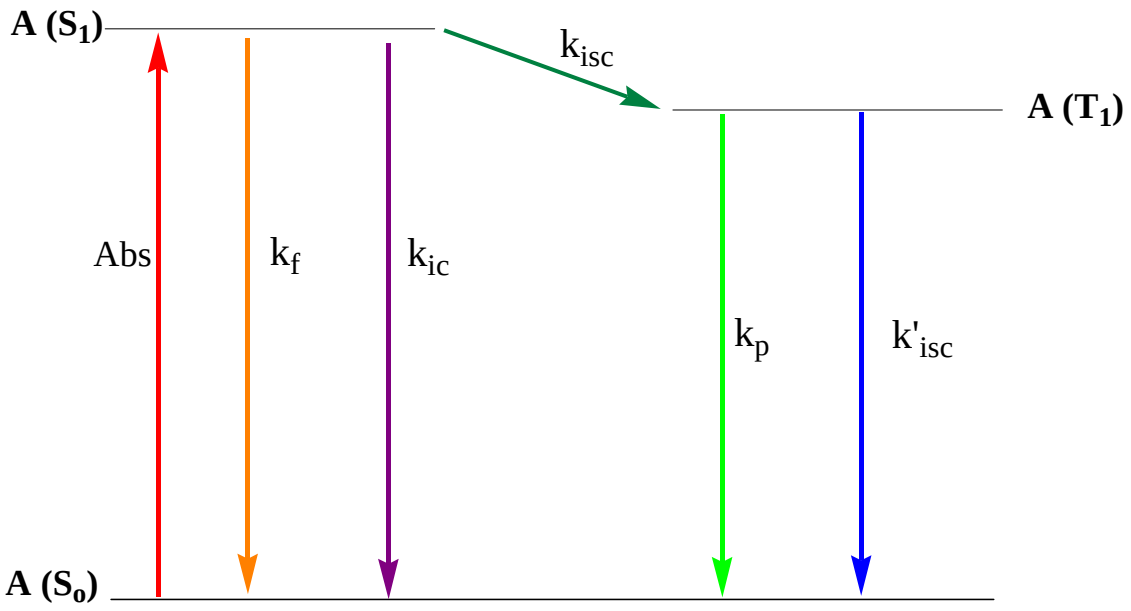

Figure 1.3: Jablonski energy diagram of different deactivation processes [2]
(k_f: fluorescence; k_{ic}: internal conversion; k_{isc}: intersystem crossing; k_p: phosphorescence; K'_{isc}: T_1 to S_o intersystem crossing)

The deactivation can take place via fluorescence (k_f), in which excited singlet state is relaxed back to the singlet ground state by releasing energy in the form of light. There is another type of relaxation which is known as radiation-less deactivation. When the radiation-less deactivation occurs between states with the same spin (singlet-singlet or triplet-triplet), it is called internal conversion.[2] When it occurs between states with different spins, it is called intersystem crossing.[2] Intersystem crossing can occupy the lowest excited triplet state. The triplet

state can be deactivated via two pathways, phosphorescence and intersystem crossing (T_1 to S_o). Each of these deactivating pathways is characterized by its own rate constant, which results in different lifetimes. The life times of each state can be calculated by the equation (Equation 1) given below.[5]

$$\tau = 1/\Sigma_i\, k_i \qquad (1)$$

Where k_i is the first order rate constant of each unimolecular deactivating pathway and τ is the life time of the excited state.[6] When the intramolecular deactivation process is considerably slow, the excited state can have a longer lifetime. The longer lifetime can facilitate the interaction of excited molecules with another species in the solution as depicted in Figure 1.4.[2] Only the excited states which live longer than 10^{-9}s have the ability to encounter with the solute molecules, because the diffusion in solution does not occur faster.[7] In the case of transition metal complexes, only the lowest spin forbidden transition excited state life time is longer than 10^{-9} s.[8]

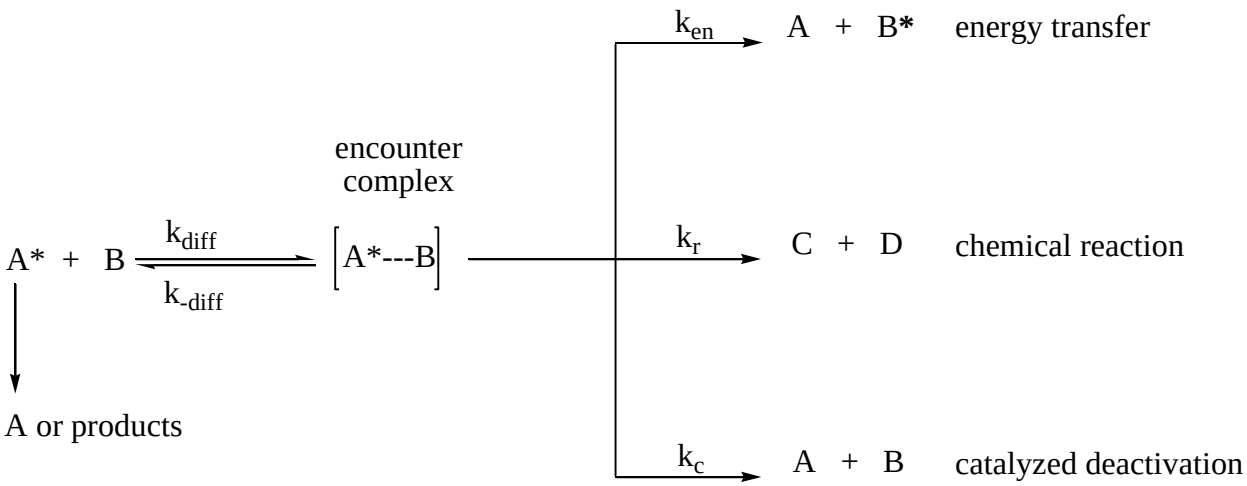

Figure 1.4 : Schematic diagram of bimolecular deactivation process[2]

If the complexes have longer half lives in their excited states, they can form encounter complexes with another chemical species and deactivate via three different pathways as shown in

Figure 1.4. These types of reactions are called bimolecular reactions.[9] Encounter complexes can transfer their energy to other molecules and excite them while deactivating the initially excited transition metal complexes. The encounter complexes can undergo a chemical reaction to produce different products. These encounter complexes can catalyze the deactivation process and produce the initial compounds. Ruthenium(II)polypyridine complexes are widely used in energy and electron transfer processes due to their longer excited state life times, which often exceed 500ns.[10]

Ruthenium(II)polypyridine complexes consist of a d^6 electron configuration of Ru^{+2}, which posses a donor orbital on the nitrogen atom of the aromatic heterocyclic ring system, as well as π donor and π^* acceptor orbitals.[11] $[Ru(bpy)_3]^{2+}$ (bpy=bipyridine) has been used extensively as an excellent photosensitizer in electron transfer processes during last three decades.[12] These $[Ru(bpy)_3]^{2+}$ and other tris-homoleptic $[Ru(L)_3]^{2+}$ complexes (L= bidentate polypyridine ligand) exhibit D_3 symmetry (Figure 1.5).[13]

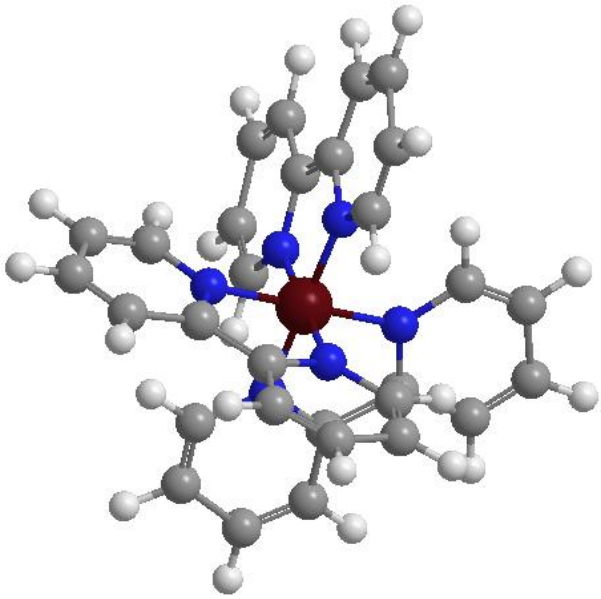

Figure 1.5: 3D structure of $Ru(bpy)_3^{+2}$ generated by chem. 3D

Among the ruthenium(II)polypyridine complexes, the $Ru(bpy)_3^{+2}$ complex was studied the most due to a combination of factors such as its chemical stability, excited state life time, excited state reactivity, suitable redox properties and the simplicity of the structure.[2,12]

$Ru(bpy)_3^{+2}$ is thermodynamically stable and kinetically inert, and it shows a broad absorption band in the visible region of electromagnetic spectrum featuring a maximum in the vicinity of 450 nm (Figure 1.6), which has attributed to a MLCT-state (Metal to Ligand Charge Transfer).[2] The excited ^{1}MLCT can relax (intersystem crossing) to the more stable ^{3}MLCT, which is the much longer lived excited state (approx 450ns vs. 10ps). The ^{3}MLCT excited state can be considered a good reductant as well as a good oxidant, which is depicted in Figure 1.6. ^{3}MLCT can easily be oxidized to $Ru(bpy)_3^{+3}$ (thermodynamically favorable) and it can be reduced back to $Ru(bpy)_3^{+1}$ state.[12] Due to the stored photonic energy, the ^{3}MLCT excited state can act as a good reducing and a good oxidizing agent,[12] depending on the reaction conditions. Also, the thermal (electrochemical) reduction of $Ru(bpy)_3^{+2}$ to $Ru(bpy)_3^{+}$ as well as its thermal oxidation to $Ru(bpy)_3^{+3}$ is easily achievable, therefore, it can act as an electron shuttle.

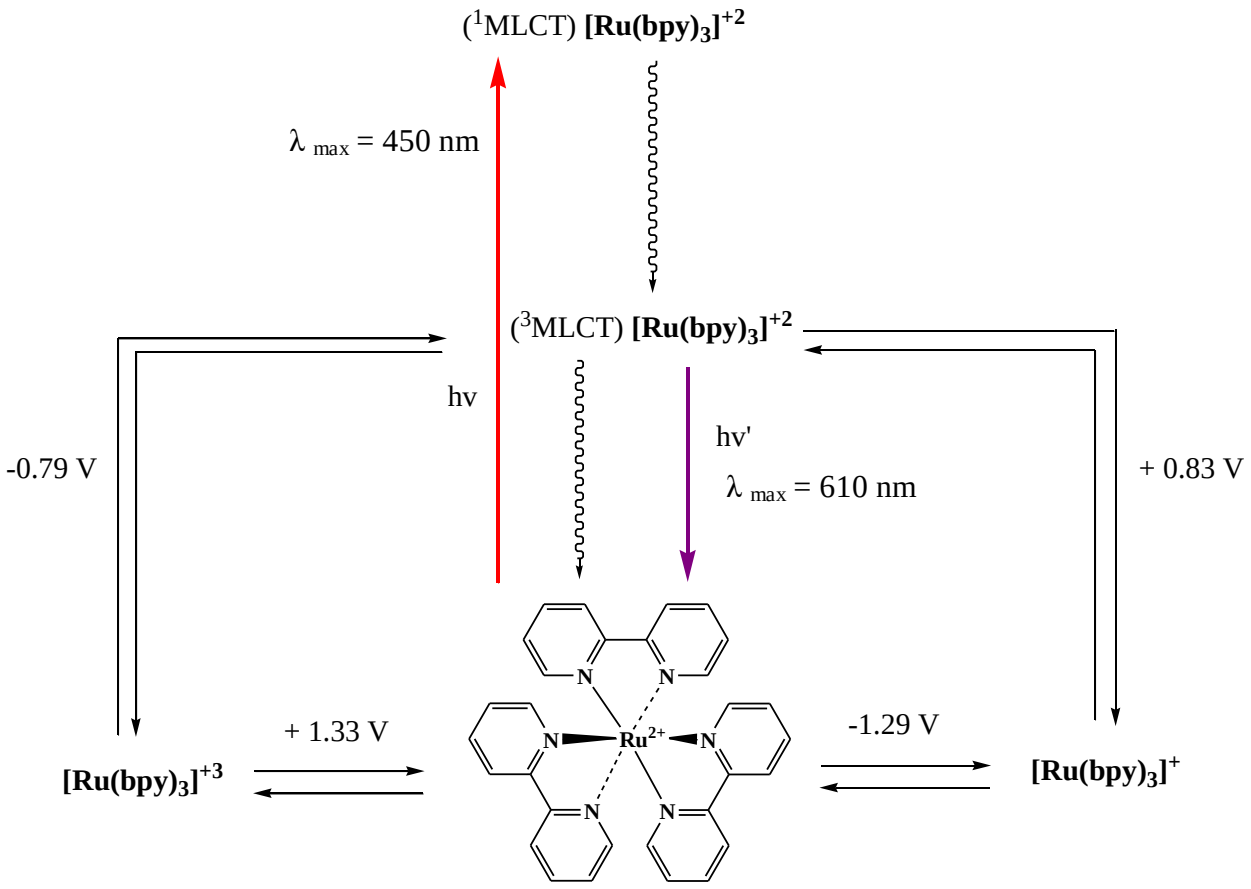

Figure 1.6: Schematic demonstration of photochemical properties of $Ru(bpy)_3^{+2}$ [12]

However, $Ru(bpy)_3^{+2}$ and related complexes have a major drawback due to the light induced ligand photodissociation.[14] $Ru(bpy)_3^{+2}$ complexes can photodissociate via a thermally activated radiationless transition from its excited metal to ligand charge transfer (^{3}MLCT) to a metal centered (^{3}MC) state, which results in the cleavage of the Ru-N bond and, consequently, ligand loss.[15] There are two strategies, which have been developed to overcome the ligand photodissociation (photoanation).[16] One approach has aimed to increase the energy gap between the ^{3}MLCT and the ^{3}MC, which in return decreases the probability of radiationless energy transfer from the ^{3}MLCT to the ^{3}MC.[17] The other approach is to link the ligand by using covalent bonding in a cage-like structure creating Ru-cryptands, -podands and -coronands.[18] These approaches were used to synthesize new ruthenium(II)polypyridinium complexes with higher photostability as well as higher excited state life time.

The photophysical properties of $Ru(bpy)_3^{+2}$ can be altered by changing the bipyridine ligand by adding more heteroatoms to the ring (especially nitrogens) or by attaching substituents to the ligand. Figure 1.7 shows the synthetic strategies for the synthesis of tris-homoleptic and bis-heteroleptic Ru(II) complexes.[19] The complexes, which are formed by coordination of the same ligand with ruthenium(II) are called tris-homoleptic Ru(II) complexes. When the ruthenium cation coordinates with two different ligands, the complexes are called bis-heteroleptic Ru(II) complexes. Tris-homoleptic Ru(II) complexes can be synthesized by refluxing $RuCl_3$ with DMSO (dimethyl sulfoxide), which will then form a coordination complex with DMSO as depicted in Figure 1.7. At the next step, DMSO can be substituted with bidentate ligands to form trishomoleptic Ru(II) complexes with D^3 symmetry. Bisheteroleptic Ru(II) complexes can be synthesized by attaching two bidentate ligands to the $RuCl_3$ first, followed by the addition of the second ligand.

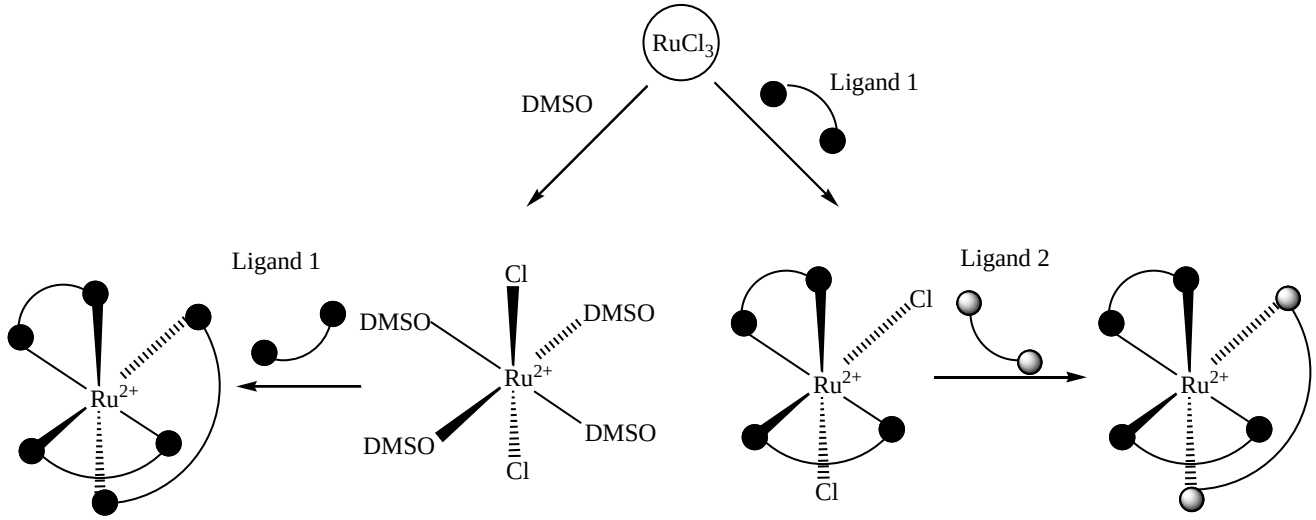

Figure 1.7: Schematic representation of the synthesis of ruthenium polypyridine complexes [19]

Electron transfer process of ruthenium(II)polypyridine complexes were compared by Dürr *et. al.*[19] using three different types of supramolecular assemblies. The authors have considered three major interactions of complexes with acceptors in formation of supramolecular assemblies, namely, 1. Supramolecular noncovalently or coordinatively linked 2. Supramolecular mechanically or catenane linked 3. Covalently linked assemblies.

Noncovalently linked assemblies used π-π stacking and H bonding to link the host guest complexes.[20] Figure 1.8 shows two examples for noncovalently linked supramolecular assemblies. Both of the assemblies have bisheteroleptic Ru(II) complexes, which are mainly held by the π-π stacking interactions between the aromatic groups of the ligand and violegens. These non-covalently linked supramolecular assemblies have two electron transfer pathways upon the irradiation (Figure 1.9).

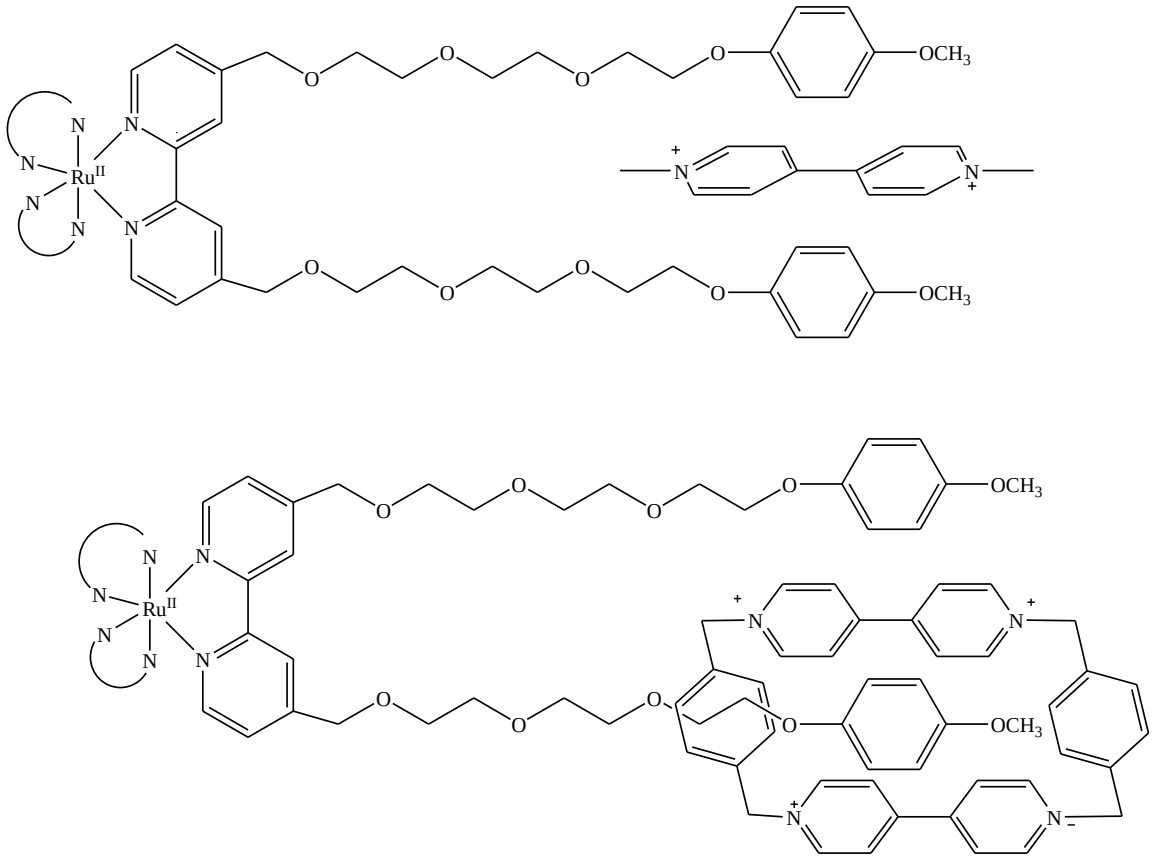

Figure 1.8: Non-covalently linked ruthenium(II)polypyridyl supramolecular assemblies [20]

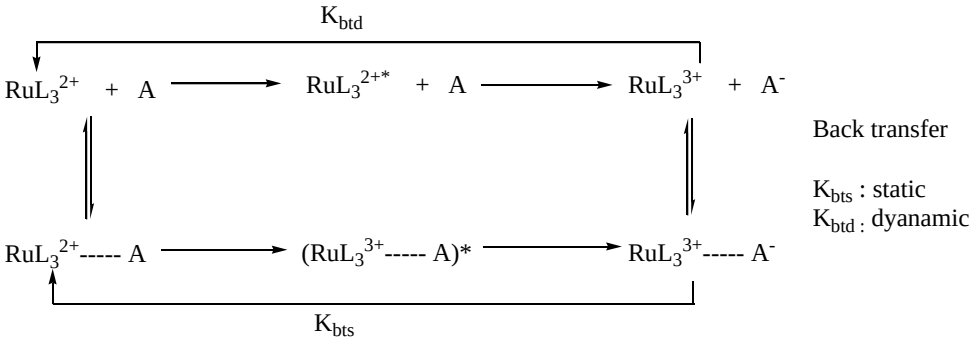

Figure 1.9: Electron transfer pathways of the non-covalently linked supramolecular assemblies[19]

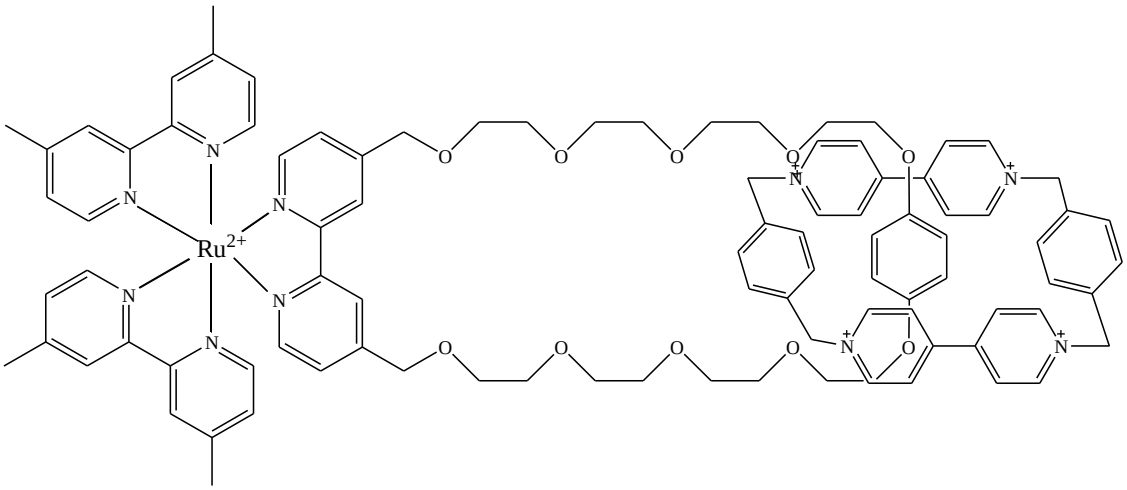

Figure 1.10: Mechanically linked ruthenium(II)polypyridyl supramolecular assemblies[19]

An example for a mechanically linked supramolecular assembly is depicted in Figure 1.10, which is a [2]catenane incorporated with a cyclobis(paraquat-p-phenylene).[19] Cyclic bisviologen (cyclobis(paraquat-p-phenylene)) is mechanically locked while surrounding the aromatic fraction of the [2]catenane. Cyclic bisviologen remains in the same place of the [2]catenane due to the π-π stacking interactions. Figure 1.11 shows the electron transfer process of the [2]catenane complexes upon irradiation. The electron transfer process in the mechanically linked supramolecular assemblies can happen via two intermediates as depicted in the figure (Figure 1.11) below. After the irradiation, ruthenium(II)polypyridine complexes form an excited supramolecular assembly. Afterwards, the violegens are reduced by the ruthenium polypyridine complex which results in two charge separated intermediates. These intermediates differ from each other due to the distance between the host and the guest. Finally, the excited intermediates relaxed back to the initial [2]catenane complexes.

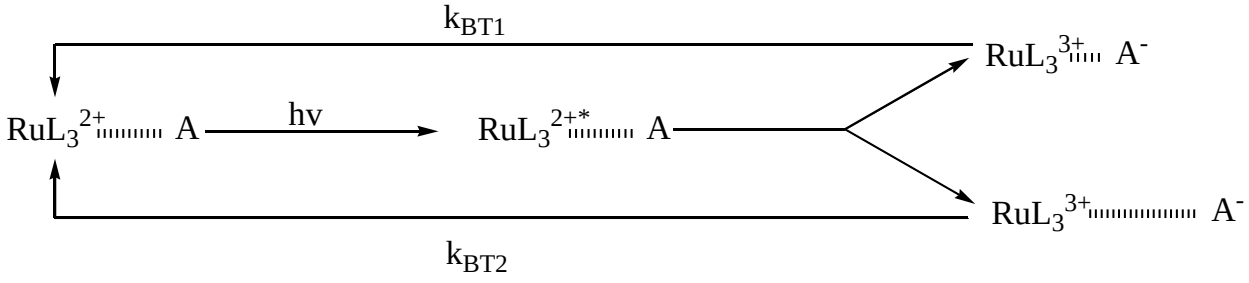

Figure 1.11: Electron transfer process in the [2]catenane complex [19]

Couple of examples for covalently linked supramolecualr assemblies which were studied by Durr *et. al* are given in Figure 1.12.[19] Both of these complexes are bisheteroleptic Ru(II) complexes with additional +4 charges, which resulted from the attached violegen. The violegen groups are attached covalently to the bidentate ligands.

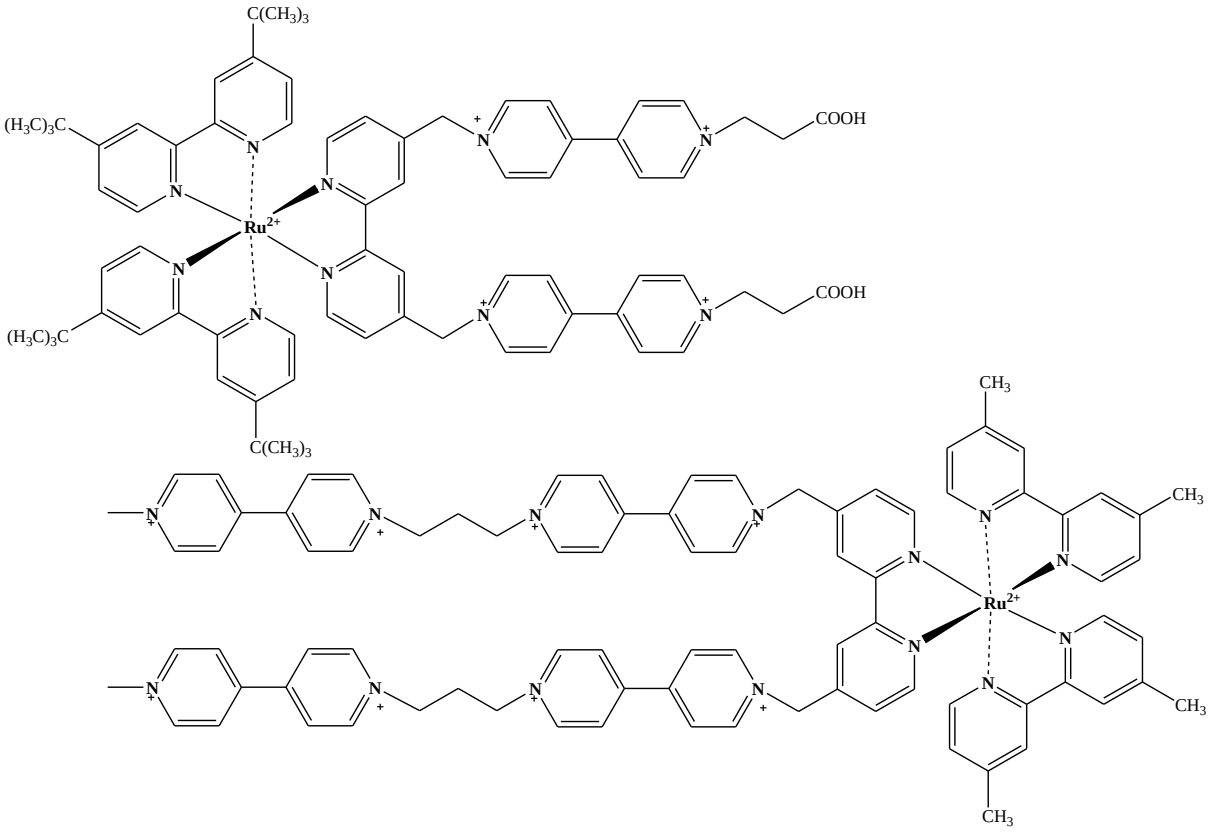

Figure 1.12: Covalently linked ruthenium(II)polypyridyl supramolecular assemblies [19]

Finally Dürr *et. al*. have compared the efficiency of electron transfer reactions to produce charge separated states.[19] They discovered that the efficiency of the electron transfer processes increase in the order of non-covalently linked, mechanically linked and covalently linked supramolecular assemblies. These studies confirm that the covalently linked ruthenium(II)polypyridine complexes can be occupied as a more efficient agent in the photochemical electron transfer reactions.

Many research groups have studied the photochemical properties of different ruthenium(II)polypyridinium complexes and the synthesis of novel trishomoleptic and bisheteroleptic Ru(II) complexes. The ruthenium(II)polypyridine complexes with higher charges

are more efficient in the photochemical electron transfer reactions and they have longer excited state life times.[21] However, lower synthetic yield was a major problem associated with these highly charged ruthenium complexes . The Bossmann research group has overcome this problem by utilizing high pressure reactor in the synthesis of highly charged ruthenium complexes.[22]

Synthesis of +8 and +14 charged tris-homoleptic ruthenium(II)quaterpyridinium complexes are described in this chapter. Since all the tris-homoleptic ruthenium(II) complexes exhibit D^3 symmetry, these highly charged ruthenium complexes are expected to have the same symmetry with slight distortion due to viologens used in the formation of covalently linked supramolecular assemblies.

Ruthenium(II)polypyridine complexes have been widely used as effective sensitizers in photolysis of water to generate hydrogen. Specially ruthenium(II)bypyridines were studied the most as sensitizers in photolysis of water. But the ruthenium(II)bypyridinium complexes have some limitations due to the photodissociation and lack of electron transfer reaction. Due to the higher photo stability and the efficient electron transfer reactions, these novel complexes would be utilized in the artificial photosynthesis as more efficient sensitizer-relay assemblies. That is discuss in detail in chapter two. In addition, the highly charged ruthenium complexes are expected to bind well into porin protein MspA,[23] which is extracted from *Mycobacterium smegmatis*. Strong binding of the charged ruthenium complexes to MspA can close the porin channel, which can then shut down the nutrition supply pathway via porin channels.

1.2 Synthesis of Ruthenium(II)quaterpyridinium Complexes

There are two basic strategies for the synthesis of Ruthenium(II)quaterpyridinium complexes.[24] Both strategies were carefully approached before optimizing the procedure for the synthesis of these ruthenium complexes. The first strategy consist of the synthesis of ruthenium(II)-tris-quaterpyridinium complexes, which contain six non-bonded tertiary sp^2 nitrogen moieties. Those six pyridine groups can be quaternized in the next step to obtain charged ruthenium(II)quaterpyridinium complexes. This strategy is depicted in Figure 1.13.

The second strategy involves the selective quaternization of the sterically least hindered pyridine moieties of 4, 4':2',2":4",4"'-quaterpyridine. Then, the quaternized ligands react with $RuCl_3$ to form Ruthenium(II)quaterpyridinium (Figure 2.14). Quaternization of external

pyridines was achieved easily using methyl iodide, but the selectivity decreased dramatically if larger alky groups were used for the quaternization of 4,4':2',2":4",4"'-quaterpyridine. Therefore, strategy one was used primarily for the synthesis of ruthenium(II) quaterpyridinium complexes.

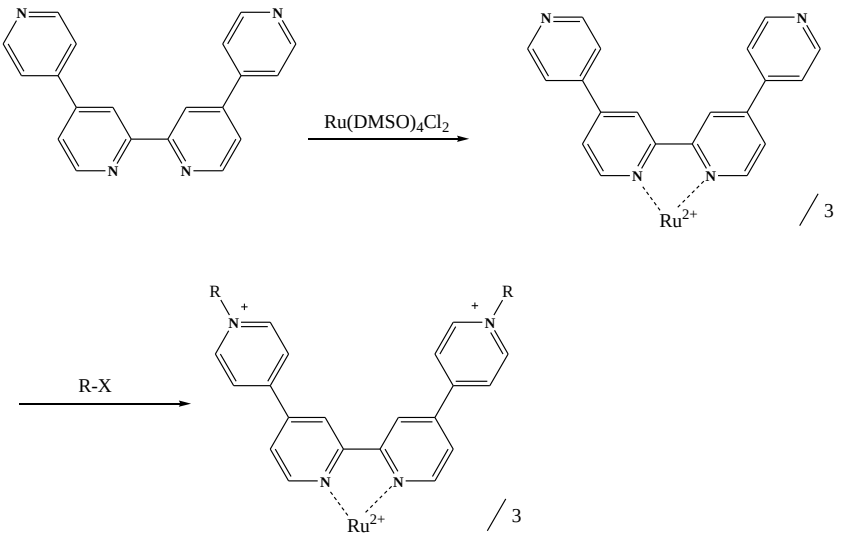

Figure 1.13: - Synthesis of ruthenium(II)quaterpyridinium and quarternization of six pyridine moieties (Strategy 1)

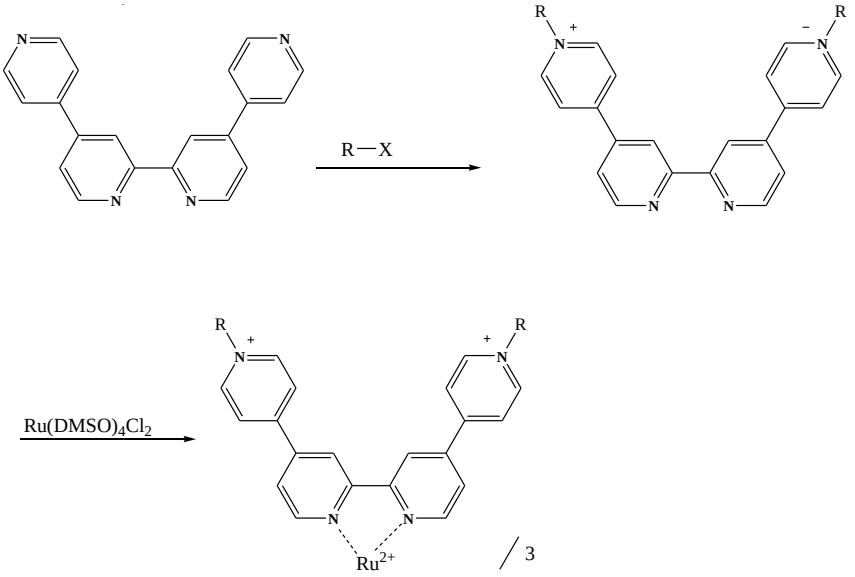

Figure 1.14: Quaternization of 4,4':2',2":4",4"'-quaterpyridine followed by the synthesis of ruthenium complexes (Strategy 2)

The previously reported synthesis method of 4, 4':2',2":4",4"'-quaterpyridine from 4,4'-bipyridine was used in the synthesis of the tetrapyridine ligands. Subsequently 4,4':2',2":4",4"'-quaterpyridine and $RuCl_3$ has been used to synthesize the ruthenium(II)quaterpyridinium complexes, which are used as the basic complex to synthesize the +8 and +14 charged ruthenium complexes.

Thermal activation has proven to be inadequate for the synthesis of tris-homoleptic ruthenium(II)quaterpyridine complexes with larger alkyl groups. A more effective high pressure synthetic procedure has been developed in our group for the synthesis of ruthenium(II) quaterpyridine complexes.[22] Higher yields were obtained by using moderate temperatures and higher pressures. High-pressure conditions decrease the activation energy for quaternization, which facilitates the S_N2 reactions.[25] The decrease in activation energy is caused by the diminished entropic effect at high pressure conditions.

My synthesis of the complexes started with the synthesis of 4,4':2',2":4",4"'-quaterpyridine from 4,4'-bipyridine. Three synthetic routes were found in literature for the synthesis of 4,4':2',2":4",4"'-quaterpyridine. All three pathways were thoroughly tested and optimized to determine the best scheme for synthesis, which also agrees with previously published results of Dr. Bossmann's group.[22]

Path one (Figure 1.15) involves the reductive coupling of 4-(2-chloropyridin-4-yl)pyridine, which requires three stages in the synthesis of 4,4':2',2":4",4"'-quaterpyridine.[26] These stages in this reaction can be identified as the formation of pyridinium-N-oxide, formation of 4-(2-chloropyridin-4-yl)pyridine and the synthesis of the target compound. This pathway resulted in lower yields; 20% is the maximum yield obtained by reductive coupling using tetrakis(triphenylphosphine)- nickel(0) as the coupling agent.

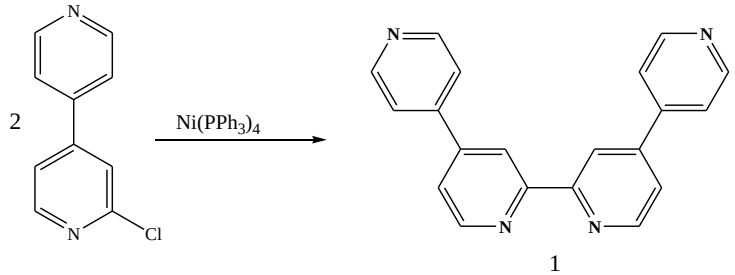

Figure 1.15: Synthesis of 4,4':2',2":4",4"'-quaterpyridine by using tetrakis(triphenylphosphine)-nickel(0) as coupling agent

Pathway two (Figure 1.16) utilizes the coupling of 4,4'-bipyridine using butyl-lithium and diisopropyl-amide as the coupling agent. This pathway gives lower yields than pathway one (10%), which is lower than the reaction yield recorded in literature.[27]

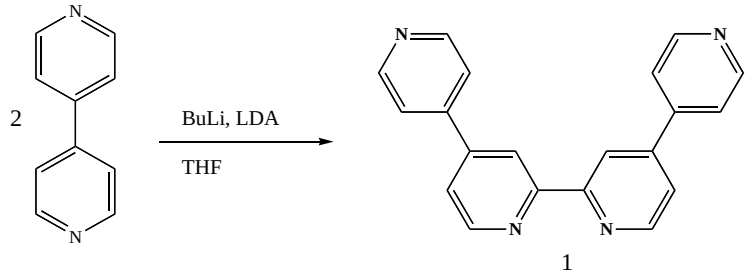

Figure 1.16: Synthesis of 4,4':2',2":4",4"'-quaterpyridine from 4,4'-bipyridine using LDA as the coupling reagent

Pathway three (Figure 1.17) comprises the oxidative coupling of 4,4'-bipyridine by using Pd on activated carbon as the coupling reagent. A dipolar aprotic solvent was used as the solvent, which is different from the originally reported synthesis, which does not use a solvent for the reaction.[28] A mixture of 4,4'-bipyridine and Pd/C (10 weight percent of Pd) was refluxed for 48 hours and the catalyst was removed by filtration using nylon 66 membrane filters (150 microns). The use of these membrane filters decreased the loss of product upon purification which increases the yield up to 45 - 48 %. According to the present yields, pathway three turned out to be the best path to synthesize 4,4':2',2":4",4"'-quaterpyridine and therefore, oxidative coupling using Pd/ C has been primarily used for the synthesis of ruthenium complexes.

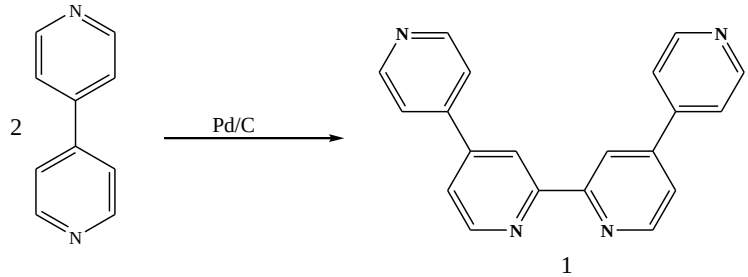

Figure 1.17: Synthesis of 4,4':2',2":4",4"'-quaterpyridine from 4,4'-bipyridine using Pd on activated carbon as the coupling agent

The synthesis of tris(4,4':2',2":4",4"'-quarterpyridine-N',N")ruthenium(II) dichloride has been optimized in the next step (Figure 1.18). This procedure was slightly altered from the procedure which has been published by Shi *et. al*.[22] Ruthenium(III)chloride and 4,4':2',2":4",4"'-quaterpyridine (in excess) was refluxed for 15 hours. The solvent was evaporated by vacuum distillation. After the purification using solvent extraction and recrystallization, pure tris(4,4':2',2":4",4"'-quarterpyridine-N',N")ruthenium(II) dichloride was obtained. Formation of bis-ruthenium(II) complex was avoided by using excess 4,4':2',2":4",4"'-quaterpyridine for the synthesis.

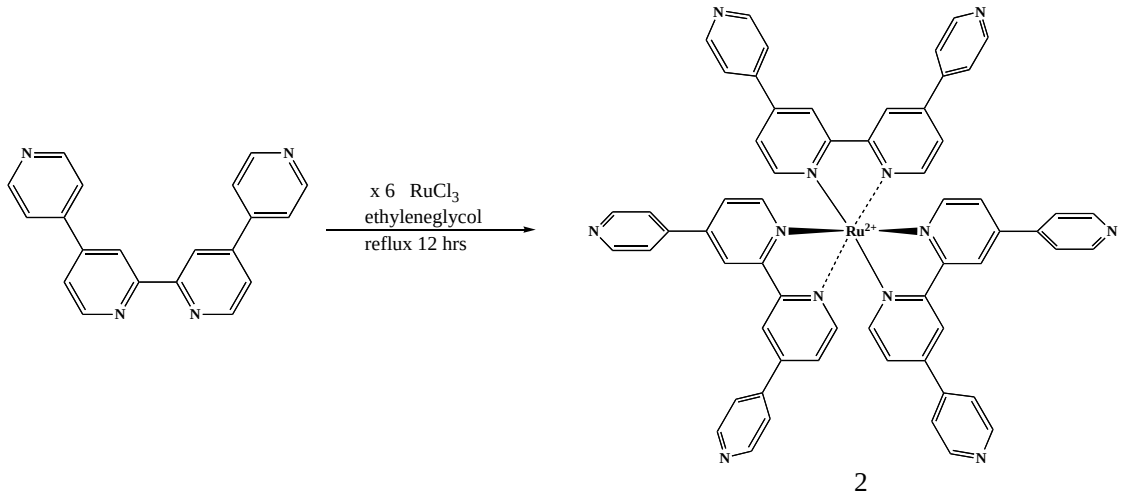

2

Figure 1.18: Synthesis of tris(4,4':2',2":4",4"'-quarterpyridine-N',N")ruthenium(II) dichloride

High pressure and moderate temperature conditions were used to increase the yield of compound 2, but it does not affect the reaction yield in a favorable manner. According to the results, it has been concluded that heat is a more important factor for the synthesis of tris-homoleptic ruthenium(II) complexes than pressure. We explain this finding with the existence of alternative binding sites in the 4,4':2',2":4",4"'-quarterpyridine ligands, which leads to oligo-ruthrnium(II)complexes under high pressure reaction conditions.[22]

Subsequently, the sizes of targeted +8 and +14 charged ruthenium(II) complexes were computer-modeled by modified MM2 force field calculations. Diameters of the complexes found by the MM2 calculations are summarized in Table 1.

Table 1.1: Estimated diameters of ruthenium complexes

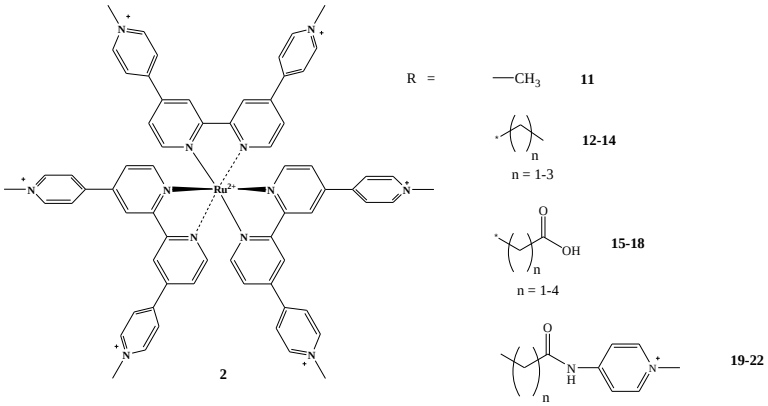

Compound	*Complex, Molecular Formula*	*N*	*R*	*Diameter (nm)*
2	$Ru(qpy)_3^{2+}$ $C_{60}H_{42}Cl_2N_{12}Ru$	-	-	1.82
11	$Ru(QP\text{-}Me)_3^{8+}$ $C_{66}H_{60}Cl_8N_{12}Ru$	-	CH_3	2.11
12	$Ru(QP\text{-}C_1)_3^{8+}$ $C_{72}H_{82}Cl_8N_{12}Ru^{8+}$	1	CH_3CH_2	2.46
13	$Ru(QP\text{-}C_2)_3^{8+}$ $C_{78}H_{94}Cl_8N_{12}Ru^{8+}$	2	$CH_3(CH_2)_2$	2.64
14	$Ru(QP\text{-}C_3)_3^{8+}$ $C_{84}H_{106}Cl_8N_{12}Ru^{8+}$	3	$CH_3(CH_2)_3$	2.86
15	$Ru(QP\text{-}C1)_3^{8+}$ $C_{72}H_{60}Cl_8N_{12}O_{12}Ru$	1	CH_2CO_2H	2.43
16	$Ru(QP\text{-}C2)_3^{8+}$ $C_{78}H_{72}Cl_8N_{12}O_{12}Ru$	2	$(CH_2)_2CO_2H$	2.92
17	$Ru(QP\text{-}C3)_3^{8+}$ $C_{84}H_{84}Cl_8N_{12}O_{12}Ru$	3	$(CH_2)_3CO_2H$	2.99
18	$Ru(QP\text{-}C4)_3^{8+}$ $C_{90}H_{96}Cl_8N_{12}O_{12}Ru$	4	$(CH_2)_4CO_2H$	3.18
19	$Ru(QP\text{-}C_1\text{-}py)_3^{14+}$ $C_{108}H_{102}Cl_{14}N_{24}O_6Ru$	1	CH_2CO(4-Py*Me)	3.76
20	$Ru(QP\text{-}C_2\text{-}py)_3^{14+}$ $C_{114}H_{114}Cl_{14}N_{24}O_6Ru$	2	$(CH_2)_2CO$(4-Py*Me)	3.89
21	$Ru(QP\text{-}C_3\text{-}py)_3^{14+}$ $C_{120}H_{126}Cl_{14}N_{24}O_6Ru$	3	$(CH_2)_3CO$(4-Py*Me)	4.09
22	$Ru(QP\text{-}C_4\text{-}py)_3^{14+}$ $C_{126}H_{138}Cl_{14}N_{24}O_6Ru$	4	$(CH_2)_4CO$(4-Py*Me)	4.55

There are several requirements for highly charged ruthenium complexes, which have to be satisfied for the use as channel blockers of mycobacterial porins or sensitizer components on titanium dioxide surface. These charged complexes synthesized from tris(4,4':2',2":4",4"'-quarterpyridine-N',N")ruthenium(II) dichloride should contain flexible bonds, which allow a considerable amount of motion for the substituents. The diameter of the complexes should range from 2-5 nm, and these tris homoleptic structures should allowed to have +8 and +14 charges per molecule, because the mycobacterial porins known so far have many negative charges in their inner pores (MspA, which has up to 72 available negative charges).

Substituents used to synthesize +14 complexes have been synthesized by a straight-forward method, which is depicted in Figure 1.19. Briefly, ω-bromoalkanoic acid was with 4-aminopyridine by dissolving the reactants in toluene and stirring the mixture at 70^0C for 48 hours. The resulting amides (3-6) were reacted with excess (2.5 fold) of methyl iodide to form a series of ω-bromo-N-(1-methylpyridinium-4-yl)alkanamide iodides (7-10).

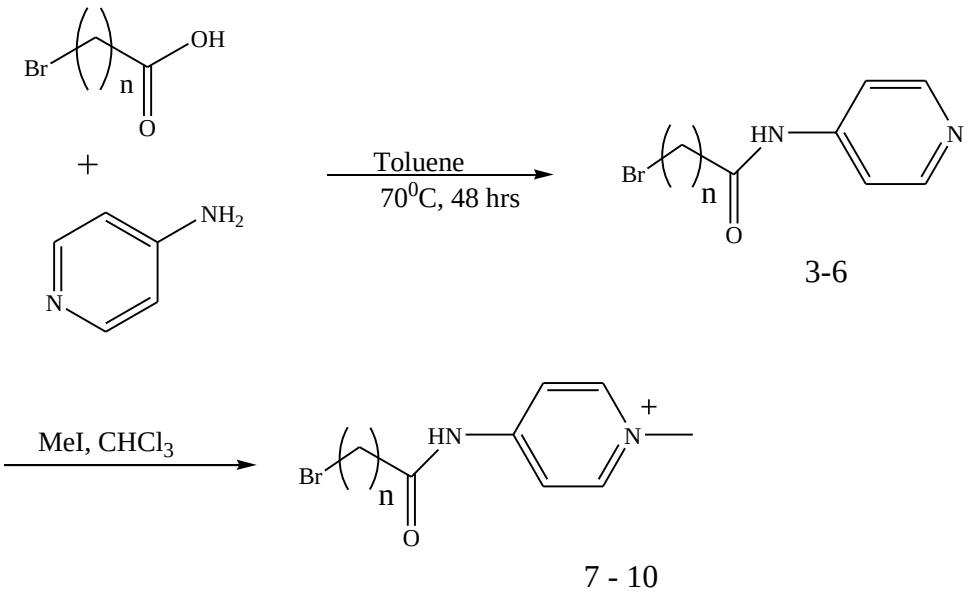

Figure 1.19: Synthesis of ω-bromo-N-(1-methylpyridinium-4-yl)alkanamide iodides

Highly charged (+8 and +14) ruthenium(II)quaterpyridinium complexes were synthesized by using a high pressure reactor. First series of complexes have been synthesized (Figure 1.20) by reacting tris(4,4':2',2":4",4"'-quarterpyridine-N',N")ruthenium(II) dichloride with a set of ω-bromoalkanes (C_1-C_3). Reactants were reacted at 50 ^{0}C and 1250 psi for 24 hours. NMR and MS

data provide the evidence for the quaternization of sp^2 nitrogen of quaterpyridine. This high pressure reaction pathway results in yields between 75 - 80% for the synthesis of +8 charged ruthenium complexes with non polar alkyl substituents.

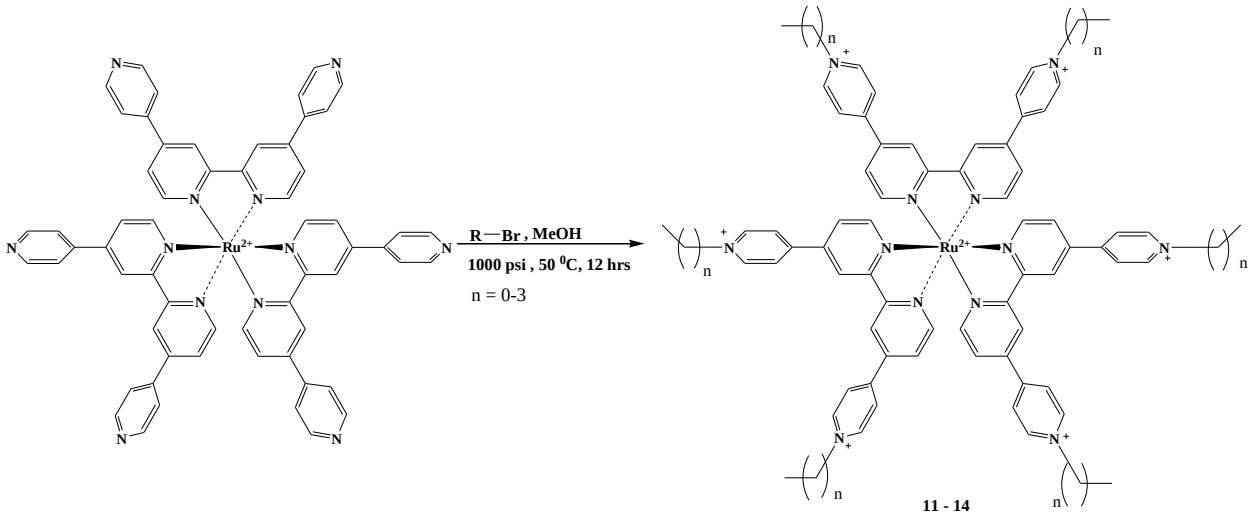

Figure 1.20: Synthesis of +8 charged ruthenium(II)quaterpyridinium complexes from ω-bromo-alkanes

Another four complexes (+8 charged) were synthesized by using ω-bromoalkanoic acids (C1-C4) as depicted in Figure 1.21. Tris(4,4':2',2":4",4"'-quarterpyridine-N',N")ruthenium (II)dichloride was reacted with a set of ω-bromoalkanes (C_1-C_3) in high pressure reactor. These reactions were carried out at 80 ^{0}C temperature and 1000 psi pressure for 14 hours.[22] Complexes 15-18 were formed with more than 90% yields. Once again, quaternization was confirmed by NMR and MS data.

Highly charged (+14) ruthenium(II)quaterpyridinium complexes were synthesized from the same high pressure reaction pathway (Figure 1.22) used in the synthesis of +8 charged complexes by changing the temperature to 50 ^{0}C instead of 80 ^{0}C and using the same pressure (1000 psi). Again, more than 90 % yields were obtained for the synthesis of the complexes and the resulted compounds were analyzed by NMR and MS data.

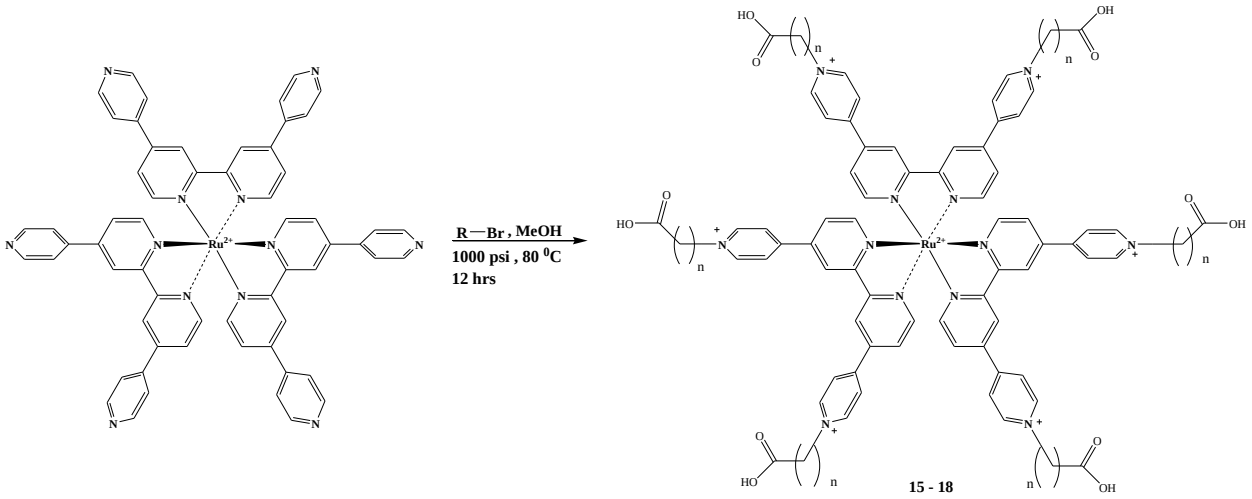

Figure 1.21: Synthesis of +8 charged ruthenium(II)quaterpyridinium complexes from ω-bromo-alkanoic acids (C1-C4)

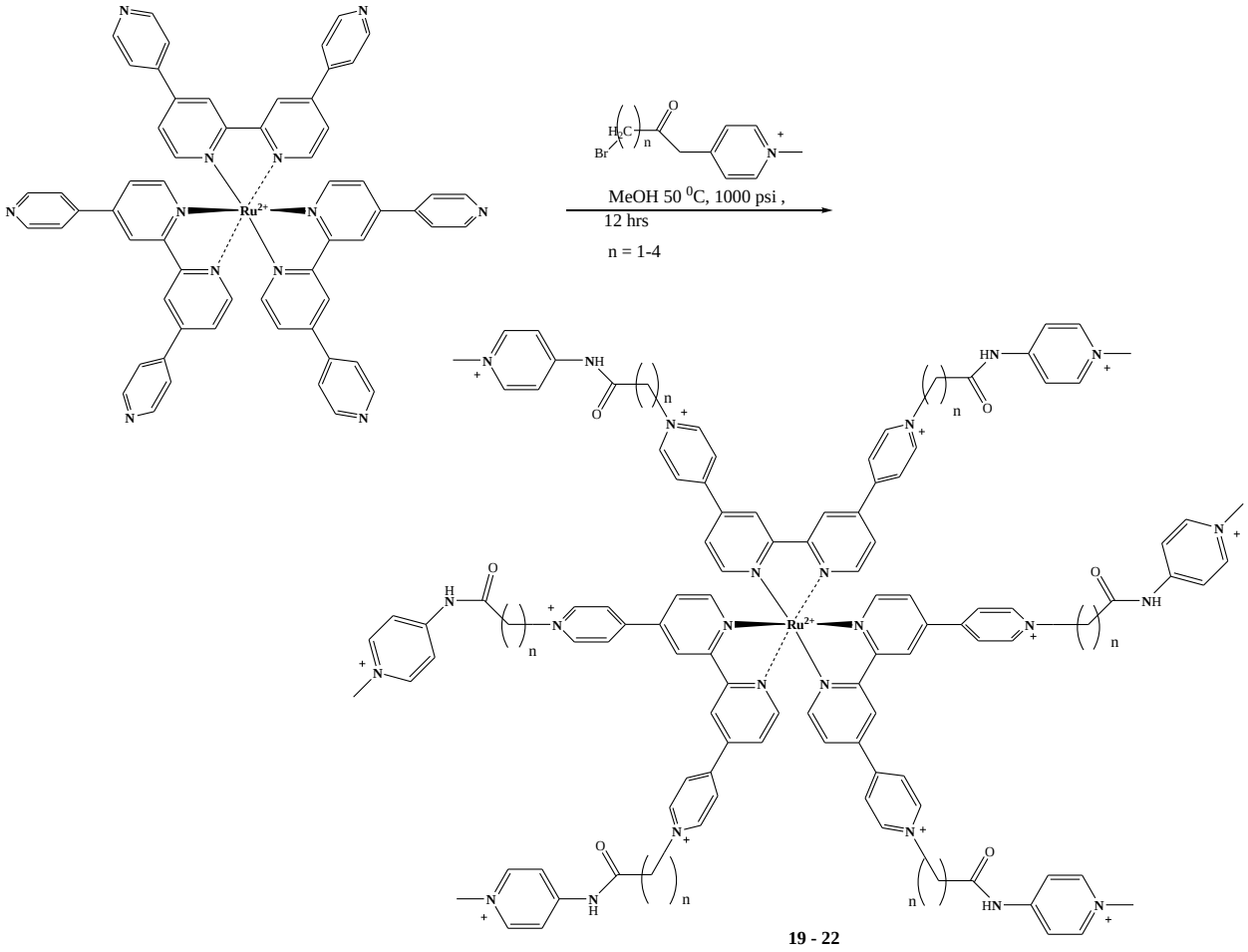

Figure 1.22: Synthesis of +14 charged ruthenium(II)quaterpyridinium complexes

All the ruthenium(II)quaterpyridinium complexes were analyzed by Bruker Esquire 3000 electrospray quadrupole ion trap instrument to study their molecular masses. These data have been summarized in Table 1.2 given below.

Table 1.2: Molecular weights of ruthenium(II)quaterpyridinium complexes

Compound	*Complex Formula*	*Estimated MS*	*MS Found*
2	$Ru(qpy)_3^{2+}$ $C_{60}H_{42}Cl_2N_{12}Ru$	1032.3 $[C_{60}H_{42}N_{12}Ru]^+$	1032.3
11	$Ru(QP\text{-}Me)_3^{8+}$ $C_{66}H_{60}Cl_8N_{12}Ru$	1192.4 $[C_{60}H_{42}Cl_2N_{12}Ru]^+$	1192.4
12	$Ru(QP\text{-}Et)_3^{8+}$ $C_{72}H_{72}Cl_8N_{12}Ru^{8+}$	1206.5 $[C_{72}H_{72}N_{12}Ru]^+$	1206.5
13	$Ru(QP\text{-}Pr)_3^{8+}$ $C_{78}H_{84}Cl_8N_{12}Ru^{8+}$	1290.6 $[C_{78}H_{84}N_{12}Ru]^+$	1291.6
14	$Ru(QP\text{-}Bu)_3^{8+}$ $C_{84}H_{106}Cl_8N_{12}Ru^{8+}$	1374.7 $[C_{84}H_{96}N_{12}Ru]^+$	1375.7
15	$Ru(QP\text{-}C1)_3^{8+}$ $C_{72}H_{60}Cl_8N_{12}O_{12}Ru$	1379.3 $[C_{72}H_{60}ClN_{12}O_{12}Ru]^+$	1379.3
16	$Ru(QP\text{-}C2)_3^{8+}$ $C_{78}H_{72}Cl_8N_{12}O_{12}Ru$	1540.4 $[C_{78}H_{72}Cl_2N_{12}O_{12}Ru]^+$	1540.4
17	$Ru(QP\text{-}C3)_3^{8+}$ $C_{84}H_{84}Cl_8N_{12}O_{12}Ru$	1589.5 $[C_{84}H_{84}ClN_{12}O_{12}Ru]^+$	1589.5
18	$Ru(QP\text{-}C4)_3^{8+}$ $C_{90}H_{96}Cl_8N_{12}O_{12}Ru$	1673.6 $[C_{90}H_{96}Cl_8N_{12}O_{12}Ru]^+$	1673.6
19	$Ru(QP\text{-}C_1\text{-}py)_3^{14+}$ $C_{108}H_{102}Cl_{14}N_{24}O_6Ru$	1392.4 $[C_{72}H_{68}Cl_2N_{16}O_4Ru]^+$	1392.4, 1032.3
20	$Ru(QP\text{-}C_2\text{-}py)_3^{14+}$ $C_{114}H_{114}Cl_{14}N_{24}O_6Ru$	1448.5 $[C_{80}H_{84}Cl_2N_{16}O_4Ru]^+$	1448.5, 1032.3
21	$Ru(QP\text{-}C_3\text{-}py)_3^{14+}$ $C_{120}H_{126}Cl_{14}N_{24}O_6Ru$	1505.6 $[C_{80}H_{84}Cl_2N_{16}O_4Ru]^+$	1505.6, 1032.3
22	$Ru(QP\text{-}C_4\text{-}py)_3^{14+}$ $C_{126}H_{138}Cl_{14}N_{24}O_6Ru$	1560.6 $[C_{84}H_{92}Cl_2N_{16}O_4Ru]^+$	1560.6, 1032.3

Destructionless ionization detections were observed for the tris-homoleptic complexes with +8 charged (11-18), but in the case of +14 charged complexes, mass peaks corresponding to the tris-homoleptic were not obtained. For the +14 charged complexes, two characteristic peaks were observed instead of the base mass signal. Those two peaks suggested two possible

pathways of fragmentations during the experiments. For these +14 complexes, masses corresponding to bis-heteroleptic were obtained, which can be explained by the loss of one ligand and substitution of the coordination site with two chlorides. Fragmentation corresponding to the *m/z* 1032.3 can be explained by loss of all the alkyl substituents from the external pyridine moieties of quaterpyridine in the complex and regenerating of the tris-(4,4':2',2":4",4"'-quarterpyridine-N',N")ruthenium(II) dichloride.

Important photophysical parameters of the synthesized Ru(II)complexes are summarized in Table 1.3.

Table 1.3: Photophysical properties of highly charged ruthenium complexes

Compound	***Absorption λ_{max} (nm) [log ε ($M^{-1}cm^{-1}$)]***			***Luminescence $\lambda_{max,em}$ (nm)***
	π –π*	***d –π****	***^{3}MLCT***	***^{3}MLCT***
2	247 [5.12]	307 [4.98]	474 [4.53]	638
11	254 [4.77]	319 [4.08]	487 [4.20]	668
12	252 [4.75]	324 [4.02]	490 [4.05]	665
13	255 [4.80]	318 [4.04]	493 [4.12]	664
14	259 [4.72]	320 [3.98]	498 [4.02]	667
15	257 [4.84]	323 [4.41]	491 [4.23]	662
16	258 [5.04]	316 [4.48]	490 [4.27]	669
17	248 [4.85]	309 [4.59]	479 [4.21]	663
18	257 [5.03]	306 [4.55]	481 [4.19]	659
19	248 [5.01]	317 [4.61]	490 [4.14]	664
20	253 [5.03]	311 [4.63]	492 [4.04]	667
21	250 [5.00]	315 [4.48]	490 [4.22]	661
22	252 [4.98]	314 [4.58]	491 [4.60]	671

Distinct ^{3}MLCT absorption bands can be observed in the UV/Vis-spectra of all synthesized complexes, which can be considered as evidence for the existence of ligand fields around the center transition metal ion. This transition is typical for the class of tris-homoleptic

ruthenium(II) complexes featuring D_3 symmetry.[2] Moreover, there is a bathochromic shift of the luminescence of ^{3}MLCT's of the quaterpyridinium complexes in comparison to the luminescence of tris-homoleptic ruthenium(II) bipyridine quaterpyridine complexes. According to Balzani *et. al.*[2], the ^{3}MLCT bands of ruthenium(II)complexes are the more red-shifted the more extended their aromatic ligand systems are. This is exactly the case here: a progressive red-shift can be discerned in the sequence Ru(II)-tris-bipyridine (λ_{MLCT} = 452nm), Ru(II)-tris-quaterpyridine (λ_{MLCT} = 474nm), Ru(II)-tris-quaterpyridinium (λ_{MLCT} >490nm).

1.2.1 Luminescence Experiments:

Laser Flash Photolysis and Laser Picosecond Absorption Spectroscopy experiments were performed for all the charged ruthenium(II)quaterpyridinium complexes. These experiments were used to calculate the excited state life times of different ruthenium(II)quaterpyridinium complexes. Both experiments were carried out in 4.0 mL quartz-cuvettes (Helma) using a spectrofluoro-meter (Fluoromax2) with dual monochromators and a diode array UV-vis absorption spectrometer (HP 8453). 0.05M Phosphate buffer (pH=6.8) was used as solvent.

1.2.1.1 Laser Flash Photolysis:

The times-resolved (ns) measurements of the luminescence and Vis-absorption lifetimes were performed in the research laboratories of Dr. Claudia Turró, Department of Chemistry, Ohio State University, Columbus Ohio.

The transient absorption spectra and lifetimes were measured by using a previously published procedure.[29,30] Briefly, instrument was pumped by a triplet (355nm) Spectra Physics GCR-150 Nd:YAG laser. The lamp (150 W Xe arc lamp) was focused onto sample at 90^0 angle with respect to the laser beam. The transmitted white light from the sample was focused to entrance slit of a Pex HR-20 single monochromator (1200 gr/mm). Hamamatsu R928 photomultiplier tube was used as the detector and the data were processed by Tektronics 400 MHz oscilloscope (TDS 380)

The excitation wavelength used was 532nm (second harmonic of the exciting YAG laser). Luminescence was recorded at 680nm, excited state absorbance at 480nm. Excited state

absorption spectra of all the ruthenium complexes were recorded. Nanosecond excited state absorption spectrum of RuC1COOH complex is depicted in Figure 1.23.

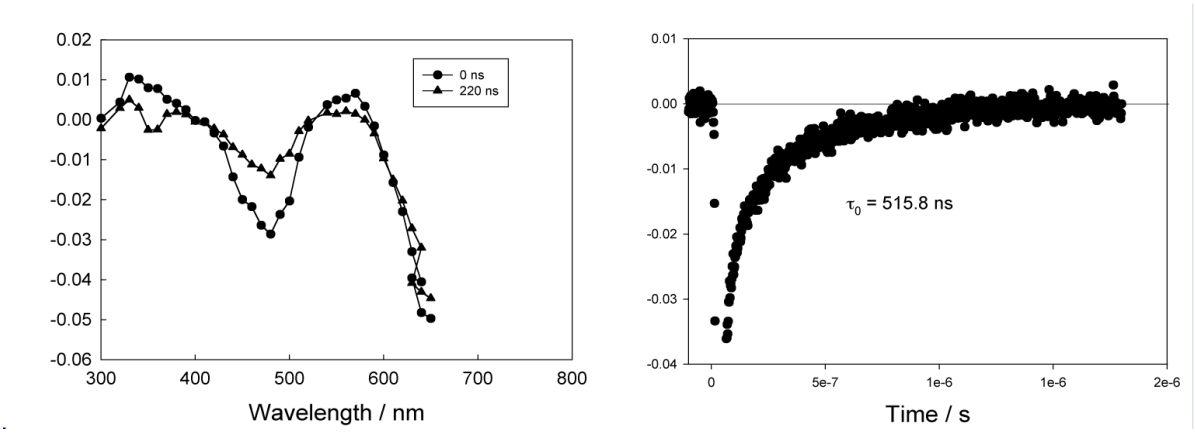

Figure 1.23: Nanosecond excited state absorption spectrum
(recorded point by point, λ_{exc}=532 nm and mono-exponential decay at λ=480nm of RuC1COOH (2.0×10^{-5}M) in phosphate buffer (pH=6.8))

It shows the typical bleach of the electronically excited ^{3}MLCT-state around 490nm and the development of two absorption-bands in the region of 350nm and 580-600nm, which are indicative of the absorption of one reduced viologen ligand.[31] This excited state returns in a single-exponential decay (τ_0=515.8nm) to the electronic ground state. The luminescence and time-resolved absorption data are summarized in Table 1.4.

Note that there are differences in the observed lifetimes of luminescence and absorption decay. The Bossmann group has reported in an earlier paper that the ability of the ruthenium complexes to undergo electron transfer reactions with each other (from an excited complex to a ground state complex) greatly influences the decay efficiency of ^{3}MLCT-states.[32] All of the measurements summarized in Table 1.4 are performed at a concentration of 2.0×10^{-5}M. However, when the electron transfer rate constants between the individual ruthenium quaterpyridinium complexes differ, it is likely that there are different effects on the observed lifetimes of the excited ^{3}MLCT states.

Table 1.4: Results from the steady-state and time resolved emission studies, as well as the time resolved absorption studies in the nanosecond time domain

Complex	^{3}MLCT-emission λ_{max} (nm)	^{3}MLCT-emission τ (ns)	^{3}MLCT-absorption τ (ns)
RuC1^{2+} (pH=6.8)	677	445	421
RuC2^{2+} (pH=6.8)	662	422	407
RuC3^{2+} (pH=6.8)	659	394	388
RuC4^{2+} (pH=6.8)	661	247	252
RuC1COO^{2+} (pH=6.8)	662	601	516
RuC2COO^{2+} (pH=6.8)	666	263	166
RuC3COO $^{8+}$ (pH=6.8)	638	133	49
RuC4COO^{8+} (pH=6.8)	640	140	107
RuC1py^{8+} (pH=6.8)	668	224	-
RuC2py^{8+} (pH=6.8)	642	197	-
RuC3py^{8+} (pH=6.8)	635	193	-
RuC4py^{8+} (pH=6.8)	623	115	-

1.2.1.2 Laser Picosecond Absorption Spectroscopy

The laser picosecond absorption spectroscopy studies were also performed in the research laboratories of Dr. Claudia Turró, Department of Chemistry, Ohio State University, Columbus Ohio. Picosecond measurements permit the observation of the very first events, which take place after the absorption of a photon, which requires approximately 1 x 10^{-15} s to complete.

These picosecond absorption spectra were recorded by home-built instrument which was made by Dr. Claudia Turró's research group according to a previously described method. [33,34] Briefly, Xe arc lamp (150 W) in a PTI housing (MIlliarc Compact Lamp Housing) was used for the steady state photolysis experiments. Long-pass colored glass filters were placed 10 cm water cell in the light path for the selection of irradiation wavelength. Absorption spectra were collected by HP diode array spectrometer with HP8453 Win system software.

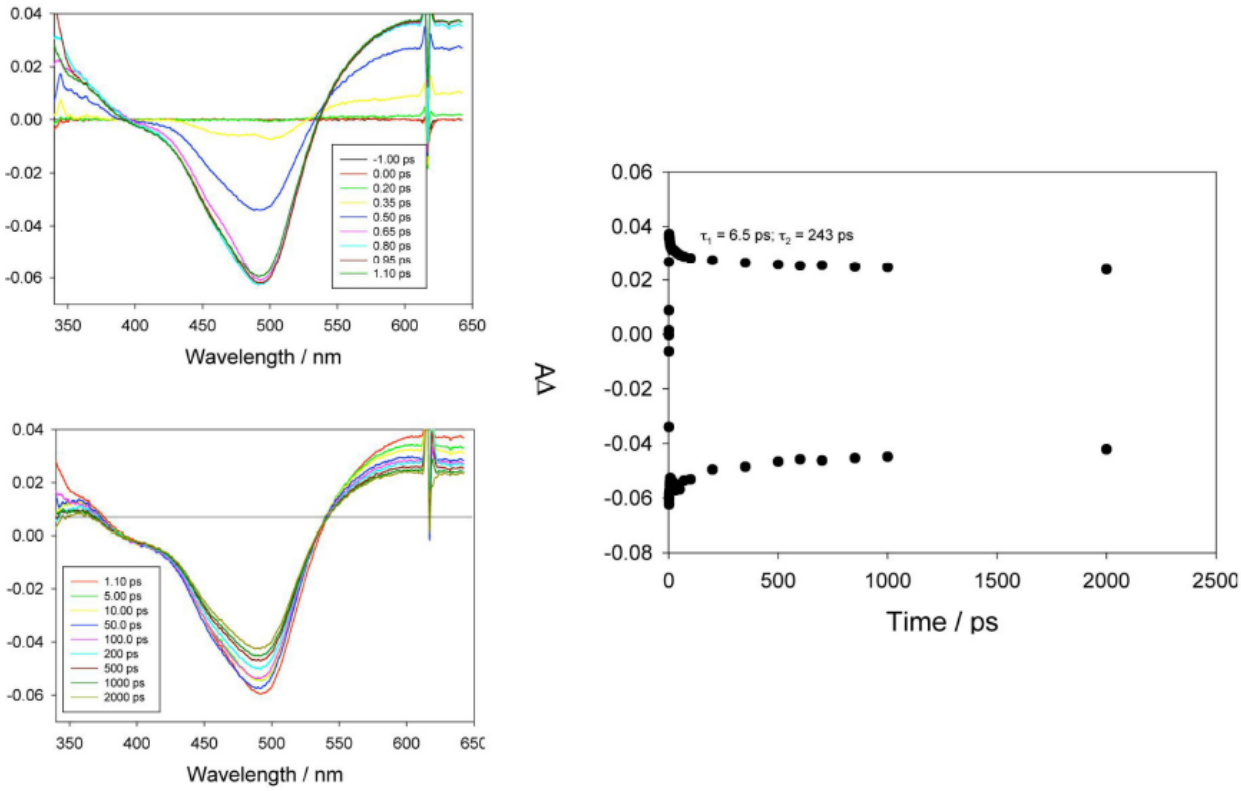

Figure 1.24: Picosecond absorption measurements of the photoexcited (λ_{ex}=310nm) ^{3}MLCT state of RuC1COOH in aqueous solution
(0.050M of phosphate buffer, pH=6.8, The observation wavelength for the determination of the kinetics of this process were λ = 490 and 600nm)

As it can be seen from Figure 1.24, the picosecond absorption spectra are not that different from the nanosecond absorption spectra. The ^{3}MLCT-state becomes quickly depleted, resulting in a bleach around 490nm, which is in the maximum of the ^{3}MLCT-absorption band. Two new positive absorption bands are discernible (around 350nm and 600nm), which are indicative of the presence of the one-electron-reduced viologen structure (Figure 1.25). The bleach at 490nm and the rise at 600 nm have a lifetime of τ_1 =6.5 ps. The simultaneous rise and bleach, which occurs according to the same kinetics, is indicative of a coupled process: the electron moves from the central metal (Ru(II)) to the quaterpyridinium ligand, as one would expect this for a MLCT-transition. The observed decay of the photochemically generated Ru(+3)-Ligand(-1) is bi-exponential: A fast decay τ_2 =243 ps is observed, as well as a very slow

decay, which cannot be resolved during the time window of observation. The slowest decay has been already determined by using nanosecond absorption spectroscopy (τ_3 =421ns).

According to a paradigm by Balzani and coworkers[2], the initial photon absorption and the intersystem crossing ^{1}MLCT -> ^{3}MLCT occurs within one Ru-bonded ligand. τ_1 =6.5 ps can be identified with this process, τ_2 =243 ps can be identified with the subsequent delocalization of the ^{3}MLCT. That is illustrated in Figure 1.25.

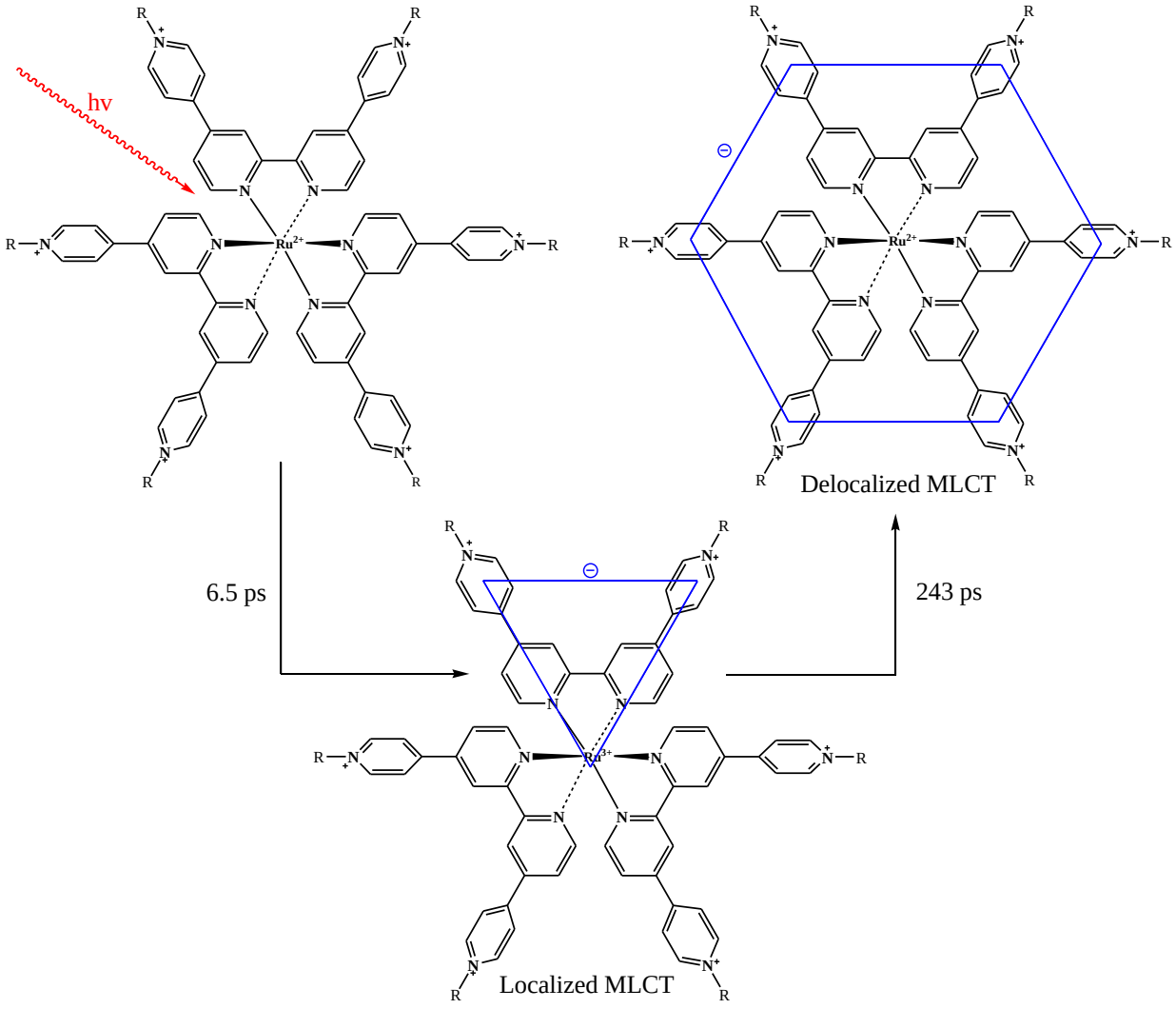

Figure 1.25: Transformation of the localized to the delocalized ^{3}MLCT

1.2.1 Experimental section

Synthesis of 4,4':2,2'':4'',4'''-Quaterpyridine (1): Pathway 3

4,4'-Bipyridine (5 g) was dissolved in 70 ml of DMF. Pd/ C (10 % w/w, 0.8 g) were added to the solution. The mixture was refluxed for 48 hours while stirring. The solvent was removed by a rotary evaporator at 120 ^{0}C. The dark grey residue was dissolved in $CHCl_3$ (50 ml) and the catalyst was filtered off by gravity filtration and nylon 66 membrane filters. A clear yellow solution was obtained. Solvent was evaporated using a rotary evaporator; a dark yellow residue was obtained. The residue was washed using cold acetone (10 ml x 2), to remove the unreacted 4,4'-bipyridine. The residue was then recrystallized from ethanol and pale white crystals were obtained. Yield 2.4 g (48%), mp 336 ^{0}C.

^{1}H NMR (400 MHz, $CDCl_3$) δ 8.88 (dd, *J*=1, 2H), 8.77 (m, *J*=1, 4H), 8.73 (dd, *J*=1.4, 2H), 7.92 (dd, *J*=2.8, 4H), 7.83 (dd, *J*=2.4, 2H). ^{13}C NMR (400 MHz, $CDCl_3$) δ 150.74, 150.64, 122.11, 121.50, 121.38, 118.11.

Synthesis of 4,4':2,2'':4'',4'''-Quaterpyridine (1): Pathway 1

$NiCl_2.6H_2O$ (0.35 g) and Ph_3P (1.5 g) were dissolved in 15 ml of anhydrous DMF. The mixture was stirred for 20 minutes at 50 ^{0}C under nitrogen atmosphere. Zinc powder (0.1g) was added to the mixture, which was stirred for 30 minutes. The color of the solution changed to dark green. Another solution was prepared by dissolving 4-(2-chloropyridin-4-yl)pyridine (0.55 g) in 5 ml of anhydrous DMF. The second solution was added dropwise to the first solution under nitrogen. The resulting mixture was stirred for 3 hours at 60 ^{0}C. The appearance of a dark brown color indicates the end of the coupling reaction. The solution was cooled to room temperature and 50 ml of 40 % NH_3 was added to the mixture. All organic compounds were extracted with CH_2Cl_2 (10 ml x 5), the solvent was then evaporated. The crude product was purified by descending column chromatography (silica gel, CH_2Cl_2 to CH_2Cl_2:MeOH 95:5). Pale white crystals were obtained. Yield 89 mg (20%).

Synthesis of 4,4':2,2'':4'',4'''-Quaterpyridine (1): Pathway 2

4,4'-Bipyridine (1.07 g) was dissolved in 300 ml of anhydrous THF and cooled to -50 ^{0}C (solid CO_2 / EtOH bath). Next, a mixture of freshly prepared LDA solution (1.5 g), anhydrous Et_2O and

1.6 M BuLi in hexane was added dropwise. The mixture was kept at -50 ^{0}C during the addition and then allowed to warm up. The mixture was stirred for 30 minutes at room temperature. The mixture was refluxed for 3 hours, the color of the solution turned to dark purple. The solution was allowed to cool down to room temperature again and 20 ml of water was added to the solution. The organic layer was separated; the aqueous solution was extracted with CH_2Cl_2 (20ml x 4). The organic layers were combined and the solvent was evaporated. A dark brown oil was obtained. The crude product was purified by descending column chromatography (neutral alumina, CH_2Cl_2:MeOH 95:5). The pale white crystals were obtained. Yield 106 mg (10%).

Synthesis of tris(4,4':2,2'':4'',4'''-Quaterpyridine-N'N'')ruthenium(II) dichloride (2)

$RuCl_3$ (0.40 g) was dissolved in DMSO (15 ml) and refluxed till the color changes from dark red to bright yellow. The solution was cooled to room temperature, ethylene glycol (45ml) and 4,4':2,2'':4'',4'''-quaterpyridine (2.5 g) were added to the solution. Mixture was refluxed under argon for 15 hours. A dark red solution was obtained; the solution was removed by vacuum distillation. This residue was dissolved in 60 ml of hot water: methanol (90: 10) mixture. The dark red solution was cooled to room temperature. Unreacted quaterpyridine was extracted with CH_2Cl_2 (40 ml x 4). Aqueous layers were collected and the solvent was removed. The residue was refluxed with acetone (30 ml) for 30 minutes. Acetone was removed in a rotary evaporator. A dark red product was obtained after drying the residue in high vacuum for 24 hours. Yield 1.95 g (85%).

^{1}H (400 MHz, DMSO-d6) δ 8.08 (12 H, *J*=6, m), 8.18 (12 H, *J*=7, dd), 8.67 (6H, *J*=5, dd), 8.89 (6 H, *J*=6, m), 9.56 (6H, s). ^{13}C NMR (400 MHz, DMSO-d6) δ 157.65, 150.63, 146.48, 146.39, 142.12, 129.62, 124.92, 121.45.

Synthesis of Tris(N,N'''-dimethyl-4,4':2,2'':4'',4'''-Quaterpyridine-N'N'')ruthenium(II) octachloride (11)

$Ru(qpy)_3Cl_2$ (0.11 g, 0.1 mmol) was dissolved in MeOH (30 ml), 0.50 ml of MeI was added to the mixture. The mixture was stirred under N_2 (1000 psi) for 15 hours at 80 ^{0}C in a high pressure reactor (PARR 5500 series compact reactor). Solvent was removed and a dark red residue was obtained. This residue was washed with acetone (15 ml x 3) to remove any unreacted MeI. The residue was dissolved in warm 1 M HCl (20 ml) and stirred for two hours. The solvent was

evaporated and the residue was refluxed with acetone for 30 minutes. The solvent was evaporated and the product was dried under vacuum for 48 hours; dark red crystals were obtained. Yield 0.10 g (68%).

^{1}H (400MHZ, DMSO-d6) δ (400MHZ, DMSO) δ 4.41(18H,s), 8.18 (d, *J*=8, 12H), 8.67 (d, *J*=7, 6H), 8.95 (s, 6H), 9.51 (d, *J*=7,6H), 9.97 (d, *J*=8, 12H). ^{13}C (200MHZ, DMSO-d6) δ 64.20, 121.36, 123.28, 125.28, 142.72, 144.81 , 148.08 , 151.28 ,160.12.

Synthesis of tris(N,N'''-diethyl-4,4':2,2'':4'',4'''-Quaterpyridine-N'N''-dium-N',N''') ruthenium(II) octachloride (12): Typical Procedure 1

A mixture of tris(4,4':2,2'':4'',4'''-quaterpyridine-N'N'')ruthenium(II) dichloride (110 mg) and bromoethane (150 mg) was dissolved in MeOH (30 ml). The mixture was stirred under N_2 (1250 psi) for 24 hours at 50 ^{0}C in high pressure reactor (PARR 5500 series compact reactor). The solvent was removed by rotary evaporator. The dark red residue was washed with acetone (15 ml) three times to remove any unreacted organic materials. Solvent was evaporated and the residue was dissolved in warm 1 M HCl (20 ml) and stirred for two hours. The solvent was evaporated and the residue was refluxed with acetone for 30 minutes. Acetone was evaporated and the product was dried under high vacuum for 24 hours. Dark red crystals were obtained. Yield 110 mg (65%).

^{1}H (400MHZ, DMSO-d6) δ 2.04(t, *J* =4, 18H), 4.19 (m, *J* =4, 12H), 8.20 (d, *J*=8,12H), 8.87 (d, *J*=7, 6H), 8.97 (s, 6H), 9.56 (d, *J*=7,6H), 9.95 (d, *J*= 8, 12H). ^{13}C (400MHZ, DMSO-d6) δ 20.16, 60.88, 122.38, 124.38, 125.55, 142.81, 143.98, 147.16, 150.08, 160.41.

Synthesis of tris(N,N'''-dipropyl-4,4':2,2'':4'',4'''-Quaterpyridine-N'N''-dium-N',N''') ruthenium(II) octachloride (13)

1-bromopropane (172 mg) was reacted with compound 2 (110 mg) by following the typical procedure 1. Dark red crystals were obtained. Yield 120 mg (67.8%).

^{1}H (400MHZ, DMSO-d6) δ 1.24 (t, *J* =4, 18H), 2.22 (12H,m), 4.25 (t, *J* =4, 12H), 8.29 (d, *J*=8,12 H), 8.93 (d, *J*=7, 6 H), 9.05(6 H, s), 9.58 (d, *J*=7,6H), 10.03 (d, *J*=8, 12 H). ^{13}C (200MHZ, DMSO-d6) δ 13.44, 26.36, 58.62, 121.23, 123.36, 125.76, 142.16, 144.48, 148.48, 151.76, 160.41.

Synthesis of tris(N,N'''-dibutyl-4,4':2,2'':4'',4'''-Quaterpyridine-N'N''-dium-N',N''') ruthenium(II) octachloride (14)

1-bromobutane (193 mg,) was reacted with compound 2 (110 mg) by following the typical procedure 1. Dark red crystals were obtained. Yield 130 mg (70%).

^{1}H (400MHZ, DMSO-d6) δ 0.88 (t, *J* =4, 18H), 1.39 (12H, m), 1.85 (12 H, m), 4.19 (t, *J* =3, 12H), 8.17 (d, *J*=8, 12H), 8.84 (d, *J*=7, 6H), 8.95 (6H, s), 9.51 (d, *J*=7, 6H), 9.91 (d, *J*=8, 12H) . ^{13}C (200MHZ, DMSO-d6) δ 15.76, 23.36, 34.32, 59.52, 121.44, 124.48, 125.84, 142.24, 144.56, 150.12, 159.96.

Synthesis of tris[N,N'''-bis(carboxymethyl)-4,4':2,2'':4'',4'''-Quaterpyridine-N'N''-dium-N',N''') ruthenium(II) octachloride (15): Typical Procedure 2

Compound 2 (0.11 g) and bromoacetic acid (770 mg) were dissolved in MeOH (30 ml). The mixture was stirred under N_2 (1000 psi) for 15 hours at 80 ^{0}C in high pressure reactor (PARR 5500 series compact reactor). The solvent was removed by rotary evaporator. The dark red residue was washed with acetone (15 ml) three times to remove unreacted organic materials. Residue was dissolved in warm 1 M HCl (20 ml) and stirred for two hours. The solvent was evaporated and the residue was refluxed with acetone for 30 minutes. Solvent was evaporated and the product was dried under high vacuum for 24 hours. Dark red crystals were obtained. Yield 152 mg (85%).

^{1}H (400MHZ, DMSO-d6) δ 4.43 (12H, s), 8.23 (d, *J*=8, 12H), 8.97 (d, *J*=7,6H), 9.04(s, 6H), 9.52(d, *J*=7, 6H), 10.07 (d, *J*=8, 12H). ^{13}C (200MHZ, DMSO-d6) 63.62, 121.84, 124.08, 125.36, 141.92, 144.56, 148.55, 151.94, 160.08, 174.78.

Synthesis of tris[N,N'''-bis(2-carboxyethyl)-4,4':2,2'':4'',4'''-Quaterpyridine-N'N''-dium-N',N''') ruthenium(II) octachloride (16)

3-bromopropanoic acid (844 mg) was reacted with compound 2 (110 mg) by following the typical procedure 2. Dark red crystals were obtained. Yield 130 mg (67%).

^{1}H NMR (400 MHz, DMSO) δ 3.08 (t, *J*=4, 12H), 4.34 (t, *J*=4, 12 H), 8.28 (d, *J*=8, 12 H), 8.96 (d, *J*=7, 6H), 9.02 (s, 6H), 9.48 (d, *J*=7, 6H), 10.03 (d, *J*=8, 12 H). ^{13}C (DMSO, 200MHz) δ 33.84, 61.76, 121.68, 123.92, 125.22, 142.08, 144.42, 151.84, 160.24, 174.96.

Synthesis of tris[N,N'''-bis(3-carboxypropyl)-4,4':2,2'':4'',4'''-Quaterpyridine-N'N''-dium-N',N''') ruthenium(II) octachloride (17)

4-bromobutanoic acid (920 mg) was reacted with compound 2 (110 mg) by following the typical procedure 2. Dark red crystals were obtained. Yield 140 mg (69.6%).

^{1}H NMR (400 MHz, DMSO-d6) δ 2.02 (t, *J*=7, 12H), 2.28 (m, 12H), 4.12 (t, *J*=5, 12H), 8.14 (d, *J*=8, 12H), 8.86 (d, *J*=7, 6H), 8.93 (6H, s), 9.42 (d, *J*=7, 6H), 9.98 (d, *J*=8, 12H). ^{13}C NMR (200 MHz, DMSO-d6) δ 27.36, 32.08, 60.72, 121.12, 124.24, 125.44, 141.84, 144.24, 147.92, 151.28, 160.32, 177.12.

Synthesis of tris[N,N'''-bis(4-carboxybutyl)-4,4':2,2'':4'',4'''-Quaterpyridine-N'N''-dium-N',N''') ruthenium(II) octachloride (18)

5-bromopentanoic acid (1 g) was reacted with compound 3 (110 mg) by following the typical procedure 2. Dark red crystals were obtained. Yield 167 mg (80%).

^{1}H NMR (400 MHz, DMSO-d6) δ 1.85 (t, *J*=7, 12H), 2.05 (12H, m), 2.34 (12H, m), 4.04 (t, *J*=4, 12H), 8.16 (d, *J*=8, 12H), 8.33 (d, *J*=7, 6H), 8.89 (s, 6H), 9.47(d, *J*=7, 6H), 10.03 (d, *J*=8, 12H). ^{13}C (400MHZ, DMSO-d6) 20.32, 31.12, 32.79, 59.68, 122.32 ,124.88, 126.05, 141.76, 144.72, 148.72,151.21, 159.12, 173.82.

Synthesis of 2-bromo-*N*-(1-methyl-pyridinium-4-yl)acetamide bromide (7): Typical procedure 3

Bromoacetic acid (200 mg) and 4-aminopyridine (94 mg) were dissolved in 10 ml of toluene (partially dissolved). The mixture was stirred at 70 ^{0}C for 48 hours. A white precipitate was formed. The solvent was evaporated in a rotary evaporator, and the 2-bromo-*N*-(pyridin-4-yl)acetamide (3) was dried in the oven (150 ^{0}F) for 24 h. Yield 310 mg (95%).

^{1}H (200 MHz, DMSO) δ 3.89 (s, 2H), 6.83 (dd, *J*=4, 2H), 7.91 (s, 1H), 8.16 (dd, *J*=4, 2H).

Compound 3 (300 mg) and methyl iodide (139 mg) were dissolved in 15 ml of $CHCl_3$ and refluxed for 24 hours. The solvent turned to yellow in color. The solvent was evaporated, and then a pale white solvent was obtained. The solid was dried in the oven for 24 hours. The product was recrystallized from MeOH. Yield 230 mg (72%).

^{1}H NMR (200 MHz, DMSO-d6) δ 3.81 (s, 2H), 4.19 (s, 3H), 6.94 (s, 1H), 7.21 (d, *J*=4, 2H), 9.44 (d, *J*=4, 2H). ^{13}C NMR (200 MHz, CDCl3) δ 44.08, 60.76, 110.16 ,143.28, 159.04, 170.24.

Synthesis of 3-bromo-*N*-(1-methylpyridinium-4-yl) propanamide bromide (8)

3-Bromopropanoic acid (300 mg) and 4-aminopyridine (141 mg) were reacted by following typical procedure 3 to synthesize 3-bromo-*N*-(pyridin-4-yl)propanamide. Yield 465 mg (95%).

^{1}H (200 MHz, DMSO) δ 2.86(t, *J*=3, 2H), 3.65 (t, *J*=3, 2H), 6.81(dd, *J*=4, 2H),7.84 (s, H), 8.19 (dd, *J*=4, 2H)

3-bromo-*N*-(pyridin-4-yl)propanamide (300 mg) and CH_3I (185 mg) were reacted by the following typical procedure 3. Product was recrystallized from MeOH: EtOH (1:1). Yield 220 mg (69%).

^{1}H (400 MHz, DMSO-d6) δ 2.85 (t, *J*=3, 2H), 3.67 (t, *J*=3, 2H, t), 4.24 (s, 3H), 7.22 (d, *J*=4, 2H), 8.21 (s, 1H), 9.41 (d, *J*=4, 2H, d). ^{13}C NMR (400 MHz, DMSO-d6) δ 29.12, 38.16, 60.64, 109.84, 144.41, 158.96, 172.32.

Synthesis of 4-bromo-*N*-(1-methylpyridinium-4-yl) butanamide bromide (9)

4-Bromobutanoic acid (300 mg) and 4-aminopyridine (169 mg) were reacted by following the typical procedure 3 to synthesize 4-bromo-*N*-(pyridin-4-yl)butanamide. Yield 410 mg (93%).

^{1}H (200 MHz, DMSO) δ 1.89 (2H, m), 2.21 (t, *J*=3, 2H), 3.58 (t, *J*=3, 2H), 6.84 (d, *J*=4, 2H) ,7.89(1H, s), 8.18(d, *J*=4, 2H)

4-bromo-*N*-(pyridin-4-yl)butanamide (300 mg) and CH_3I (174 mg) were reacted by following typical procedure 3. Product was recrystallized from EtOH. Yield 235 mg (74%).

^{1}H δ (400 MHz, DMSO-d6) δ 1.91 (m, 2H), 2.23 (t, *J*=3, 2H), 3.61 (t, *J*=3, 2H), 4.21 (s, 3H), 7.24 (d, *J*=4, 2H), 7.96 (s, 1H), 9.44 (d, *J*=4, 2H). ^{13}C (200 MHz, DMSO-d6) δ 24.08, 29.76, 36.16, 61.52, 109.36, 144.32, 160.56, 176.16.

Synthesis of 5-bromo-*N*-(1-methylpyridinium-4-yl)pentanamide iodide (10)

5-Bromopentanoic acid (300 mg) and 4-aminopyridine (156 mg) were reacted by the following typical procedure 3 to synthesize 4-bromo-*N*-(pyridin-4-yl)butanamide. Yield 412 mg (97%).

^{1}H (200 MHz, DMSO-d6) δ 1.61 (m, 2H), 1.81 (m, 2H), 2.24 (t, *J*=3, 2H), 3.53 (t, *J*=3, 2H), 6.86 (d, *J*=4, 2H), 6.99 (1H, s), 8.19 (d, *J*=4, 2H).

5-bromo-*N*-(pyridin-4-yl)pentanamide (300 mg) and CH_3I (165 mg) were reacted by following typical procedure 3. Product was recrystallized from EtOH. Yield 210 mg (66%).

^{1}H (400 MHz, DMSO-d6) δ 1.76 (m, 2H), 2.27 (t, *J*=3, 2H), 2.44 (m, 2H), 3.62 (t, *J*=3, 2H), 4.19 (s, 3H), 7.24 (d, *J*=4, 2H), 7.78 (s, 1H), 9.41 (d, *J*=4, 2H). ^{13}C (200 MHz, DMSO-d6) δ 22.40, 31.36, 32.24, 34.48, 60.64, 108.08, 108.56, 143.12, 159.20, 173.52.

Synthesis of Ruthenium(II)-tris-[4-(1-(N-(pyridin-4-yl)acetamide) py-ridinium-4-yl)-2-(4-1-(N-(pyridin-4-yl)acetamide) pyri-dinium-4-yl)pyridin-2-yl)pyridine] tetradecachloride (19): Typical procedure 4

Compound 2 (0.11 g) and compound 7 (400 mg) were dissolved in MeOH (30 ml). The mixture was stirred under N_2 (1000 psi) for 15 hours at 50 ^{0}C in a high-pressure reactor (PARR 5500 series compact reactor). Solvent was removed in a rotary evaporator. The dark red residue was washed with acetone (15 ml) three times to remove unreacted organic materials. Residue was dissolved in warm 1 M HCl (20 ml) and stirred for two hours. The solvent was evaporated and the residue was refluxed with acetone for 30 minutes. Solvent was evaporated and the product was dried under high vacuum for 24 hours. Yield 152 mg (85%).

^{1}H NMR (400 MHz, DMSO-d6) δ 4.17 (18H, s), 4.41 (12H, s), 7.32 (d, *J*=4, 12H), 8.31 (d, *J*=8, 12H, d), 8.97 (d, *J*=7, 6H), 9.04 (s, 6H), 9.46 (d, *J*=4, 12H), 9.52 (d, *J*=7, 6H), 10.03 (d, *J*=8, 12H,d). ^{13}C NMR (200 MHz, DMSO-d6) δ 58.24, 60.56, 111.21, 120.96, 124.24, 124.64, 141.92, 143.28, 145.36, 150.03, 158.96, 160.02, 168.96.

Synthesis of Ruthenium(II)-tris-[4-(1-(N-(pyridin-4-yl)propanamide) pyridinium-4-yl)-2-(4-(1-(N-(pyridin-4-yl) propanamide) pyridinium-4-yl)pyridin-2-yl)pyridine]tetradecachloride (20)

Compound 8 (420 mg) was reacted with compound 2 (110 mg) by following the typical procedure 4. Dark red crystals were obtained. Yield 167 mg (80%).

^{1}H NMR (400 MHz, DMSO-d6) δ 3.09 (t, *J*=3, 12H), 4.14 (18H, s), 4.35 (t, *J*=3, 12H), 7.18 (d, *J*=4, 12H), 8.24 (d, *J*=8, 12H), 8.92(d, *J*=7, 6H), 8.99 (s, 6H), 9.31 (d, *J*=4, 12H), 9.36 (d, *J*=7, 6H), 9.93(d, *J*=8, 12H).^{13}C NMR (400 MHz, DMSO-d6) δ 29.68, 59.84, 61.52, 111.12, 123.52, 125.84, 126.48, 141.44, 141.92, 144.32, 147.44, 150.16, 158.24, 161.36, 171.84.

Synthesis of Ruthenium(II)-tris-[4-(1-(N-(pyridin-4-yl)butanamide) pyridinium-4-yl)-2-(4-(1-(N-(pyridin-4-yl)butanamide) pyridinium-4-yl)pyridin-2-yl)pyridine]tetradecachloride (21)

Compound 9 (430 mg) was reacted with compound 2 (110 mg) by following the typical procedure 4. Dark red crystals were obtained. Yield 182 mg (78%)

^{1}H NMR (400 MHz, DMSO-d6) δ 2.12 (m, 12H), 2.41 (t, *J*=3, 12H), 4.09 (t, *J*=3, 12H), 4.22 (s, 18H), 7.27 (d, *J*=4, 12H), 8.31(d, *J*=8, 12H), 8.95(d, *J*=7, 6H), 9.01(s, 6H), 9.43(d, *J*=4, 12H), 9.52 (d, *J*=7, 6H), 10.02 (d, *J*=8, 12H). ^{13}C NMR (200 MHz, DMSO-d6) δ 26.40, 31.68, 59.52, 61.36, 111.68, 122.48, 124.48, 125.52, 141.92, 145.36, 147.84, 149.04, 158.64, 160.16, 172.32.

Synthesis of Ruthenium(II)-tris-[4-(1-(N-(pyridin-4-yl)pentanamide) pyridinium-4-yl)-2-(4-(1-(N-(pyridin-4-yl)pentanamide) pyridinium-4-yl)pyridin-2-yl)pyridine]tetradecachloride (22)

Compound 10 (440 mg) was reacted with compound 2 (110 mg) by following the typical procedure 4. Dark red crystals were obtained. Yield 212 mg (83%).

^{1}H NMR (400 MHz, DMSO-d6) δ 1.82 (12H, m), 2.11(12H, m), 2.45 (t, *J*=3, 12H), 3.97(t, *J*=3, 12H), 4.31 (s, 18H), 7.32 (d, *J*=4, 12H), 8.37 (d, *J*=8, 12H), 9.02 (d, *J*=7, 6H), 9.14(s, 6H), 9.51 (d, *J*=4, 12H), 9.58 (d, *J*=7, 6H), 10.09 (d, *J*=8, 12H). ^{13}C NMR (200 MHz, DMSO-d6) δ 23.36, 32.96, 34.72, 59.28, 60.96, 109.12, 122.64, 125.04, 125.44, 141.12, 144.64, 145.04, 148.08, 150.07, 159.52, 161.04, 173.92.

1.3 Synthesis of Mechanically Linked Acceptor in [2]Catenane

The synthesis of this [2]catenane was started from 4-methyl-2-(4-methylpyridin-2-yl)pyridine and tetraethylene glycol. First, the methyl groups of 4-methyl-2-(4-methylpyridin-2-yl)pyridine have to be converted to 4,4'-bis(hydroxymethyl)-2,2'-bipyridine (Figure 1.23).[35] This synthetic pathway started with the oxidation of both methyl groups in compound 23 by using $H_2SO_4/K_2Cr_2O_7$. This oxidation gives a virtually 100 % yield with high purity of 2-(4-carboxypyridin-2-yl)pyridine-4-carboxylic acid. Carboxylic acid 24 was attempted to be reduced to an alcohol by using $LiAlH_4$ as a reducing agent, but that reaction did not succeed. Therefore, another path was chosen for the reduction of carboxylic acid, where carboxylic acid was esterified, and then the ester was reduced to an alcohol.[30]

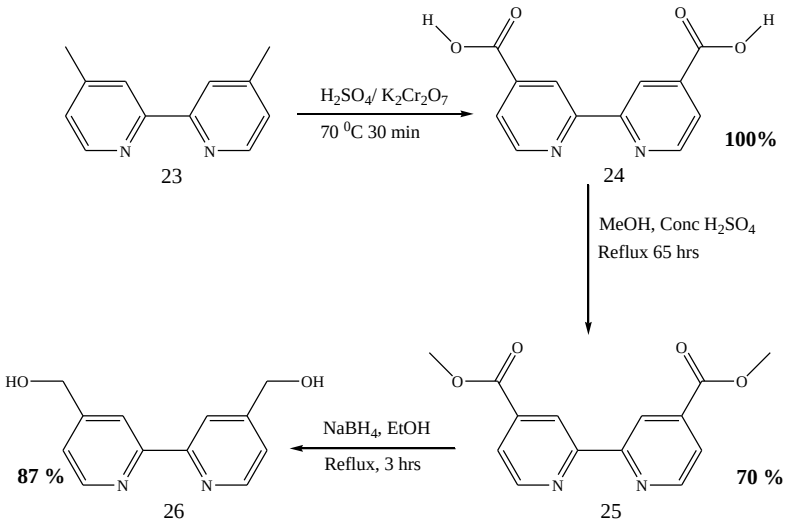

Figure 1.26: Synthesis of 4,4'-bis (hydroxymethyl)-2,2'-bipyridine

2-(4-carboxypyridin-2-yl)pyridine-4-carboxylic acid was esterified by refluxing in methanol for 65 hours in the presence of an acid catalyst (sulfuric acid). The targeted ester, methyl 2-(4-(methoxycarbonyl)pyridin-2-yl)pyridine-4-carboxylate was formed with 70 % yield. Finally, the ester groups of methyl 2-(4-(methoxycarbonyl)pyridin-2-yl)pyridine-4-carboxylate were reduced to an alcohol by refluxing the ester with $NaBH_4$ for 3 hours. The crude product was recrystallized from toluene to obtain pure crystals of the desired compound.

The synthesis of 1,4-Bis{2-(2-(2-(-2-hydroxyethoxy)ethoxy)ethoxy)ethoxy}benzene was started with tetraethylene glycol (Figure 1.12). First, the alcohol groups of tetraethylene glycol

were protected with tosyl protecting groups. A solvent free reaction was used for the protection of alcohol groups. Tetraethylene glycol, TsCl and K_2CO_3 were grinded in a mortar for ten minutes and the preferred compound 28 was formed with more than 80 % yield.[36]

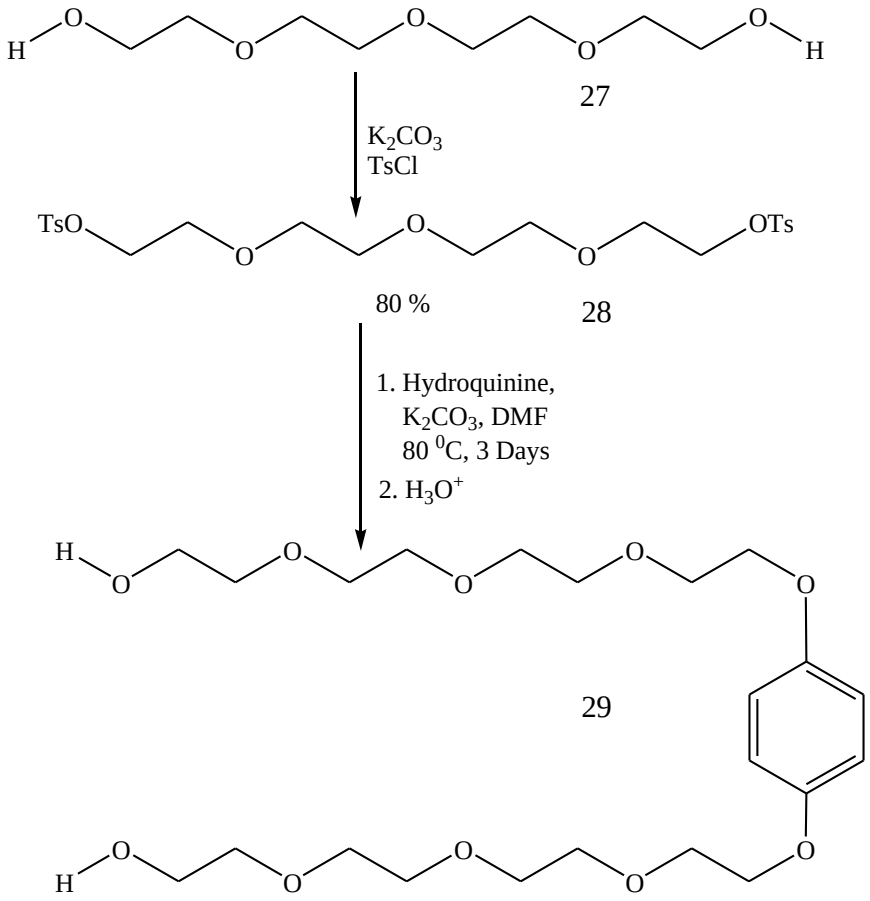

Figure 1.27: Synthesis of 1,4-Bis{2-(2-(2-(-2-hydroxyethoxy)ethoxy)ethoxy)ethoxy}benzene (path one)

Next, two molecules of compound 28 were attempted to react with hydroquinone to form compound 29. That reaction failed due to the polymerization reaction of tosylated tetraethylene glycol with the hydroquinone. The results confirmed that it is hard to react only one tosylated group with the hydroquinone. In most attempts, hydroquinone reacts with both tosylated ends of tetraethylene glycol, which results in a polymerization. These results confirm that it is necessary to have only one good leaving group in tetraethylene glycol to avoid the polymerization reaction.

Figure 1.28 shows another pathway used to synthesize 1,4-Bis{2-(2-(2-(2-(p-tolylsulfonyl) ethoxy)ethoxy) ethoxy)ethoxy}-benzene, which started with mono chlorination of tetraethylene glycol.[37]

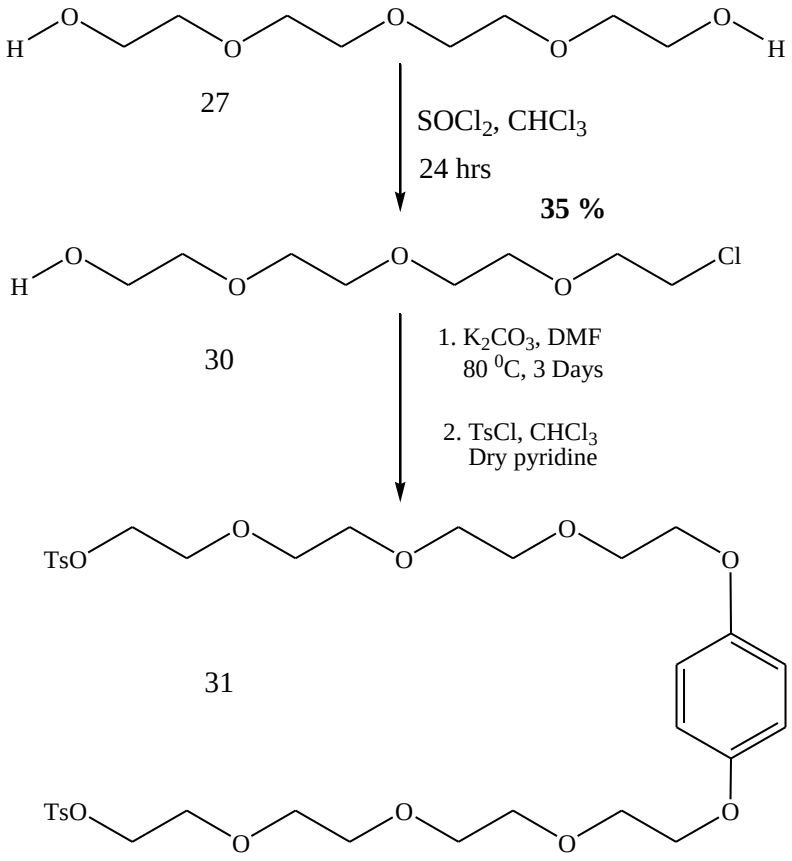

Figure 1.28: Synthesis of 1,4-Bis{2-(2-(2-(2-(p-tolylsulfonyl)ethoxy)ethoxy)ethoxy)ethoxy}-benzene

First, tetraethylyne glycol was reacted with $SOCl_2$ by using $CHCl_3$ as the solvent, which forms 2-(2-(2-(2-chloroethoxy)ethoxy)ethoxy)ethanol with a 35% yield. Compound 30 has a good leaving group (Cl) on one side, which can be reacted with a hydroquinone to synthesize 1,4-Bis{2-(2-(2-(-2-hydroxyethoxy)ethoxy)ethoxy)ethoxy}benzene. This reaction was attempted by the procedure developed by Amabilino *et. al.*,[31] but the desired product was not obtained. The same reaction was carried out by changing the solvents used in the solvent extraction step to separate the product. The desired product was formed in 25% yield. In this reaction procedure, first, hydroquinone was reacted with K_2CO_3 in an inert atmosphere (N_2) to convert hydroquinone

into a good nucleophile. Then 2-(2-(2-(2-chloroethoxy)ethoxy)ethoxy)-ethanol was added dropwise to the reaction mixture. It is important to keep the reaction solvents dry and inert to avoid the oxidation of hydroquinone to quinine.[38] At the next step, alcohol groups of the 1,4-Bis{2-(2-(2-(-2-hydroxyethoxy)ethoxy)ethoxy) ethoxy}benzene was protected with tosyl groups to convert those terminal alcohol groups to good leaving groups. Finally, p-phenylene-4,4'-dimethylene-2,2'-bipyridyl[38]crown-10 was synthesized by reacting compound 31 and 26 as depicted in Figure 1.29.[39]

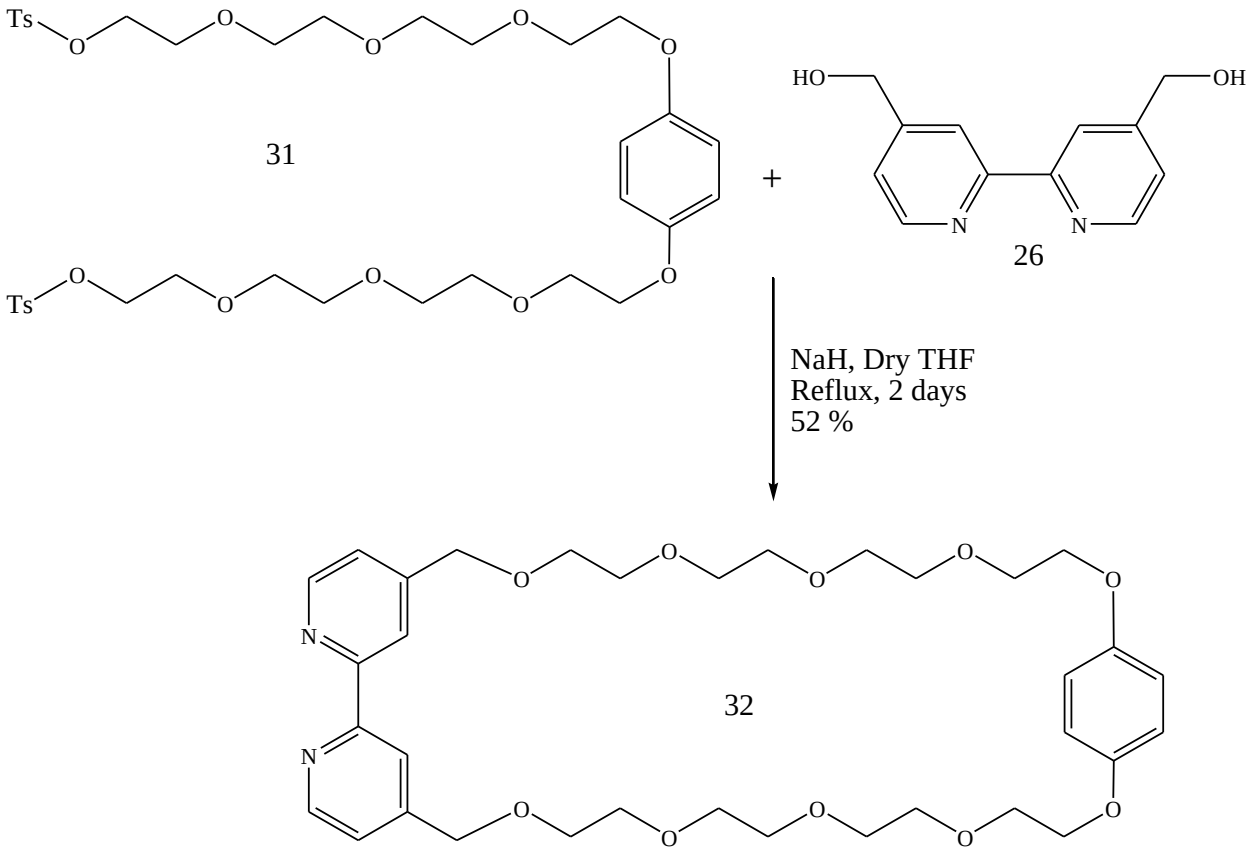

Figure 1.29**:** Synthesis of p-phenylene 4,4'-dimethylene-2,2'-bipyridyl[38]crown-10

First, 4,4'-bis(hydroxymethyl)-2,2'-bipyridine was reacted with NaH to form the nucleophile. Then 1,4-Bis{2-(2-(2-(2-(p-tolylsulfonyl)ethoxy)ethoxy)ethoxy)ethoxy}-benzene was dissolved in THF and added to the reaction mixture drop wise. It is essential to maintain a very low concentration for this reaction to facilitate the two nucleophilic attacks from the 4,4'-bis

(hydroxymethyl)-2,2'-bipyridine onto the same 1,4-Bis{2-(2-(2-(2-(p-tolylsulfonyl)ethoxy) ethoxy)ethoxy)ethoxy}-benzene molecule to synthesize p-phenylene-4,4'-dimethylene-2,2'-bipyridyl[38] crown-10.

1.3.1 Future Work on Synthesis of Mechanically Linked Acceptor in a [2]Catenane

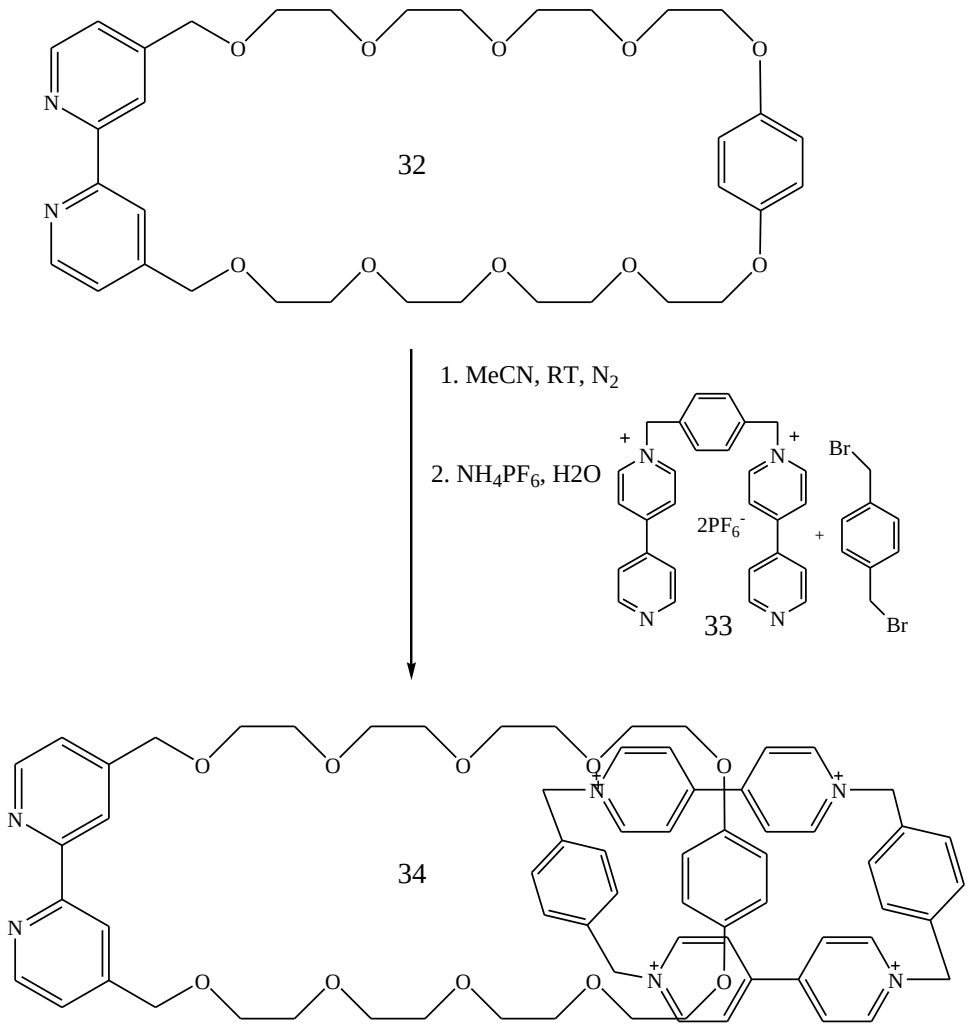

Figure 1.30: Synthesis of [2]-[p-phenylene-4,4'-dimethylene-2,2'-bipyridyl[38]crown-10] cyclobis(paraquat-p-phenylene)catenane hexafluorophosphate

By using the synthetic improvements from my thesis work, we will be able to synthesize a mechanically linked acceptor in a [2]catenane as given in Figure 1.30,[40] in much higher overall-yields than previously described. We aim at 10-20 overall percent, instead of less than 1 percent.

In compound 36, the +4 charged cyclic viologen remains stationary inside the [2]catenane due to the π-π stacking interactions of the hydroquinone group with the viologen. This has been proven by Dürr *et. al* by using an X-ray analysis, NMR-measurements and molecular modeling.[34]

Finally, the mechanically linked acceptor in [2]catenane (compound 34) can be reacted with bis-heteroleptic Ru(II) complex to synthesize bis(4,4'-dimethyl-2,2'-bipyridine)(p-phenylene-4,4'-dimethylene-2,2'-bipyridyl[38]crown-10)ruthenium(II) dichloride (Figure 1.31).[19] This ruthenium(II) polypyridine complex has a non-covalently linked sensitizer and an acceptor, and therefore, it could be utilized as a model compound for mechanically linked electron transfer couples in systems for artificial photosynthesis.[19]

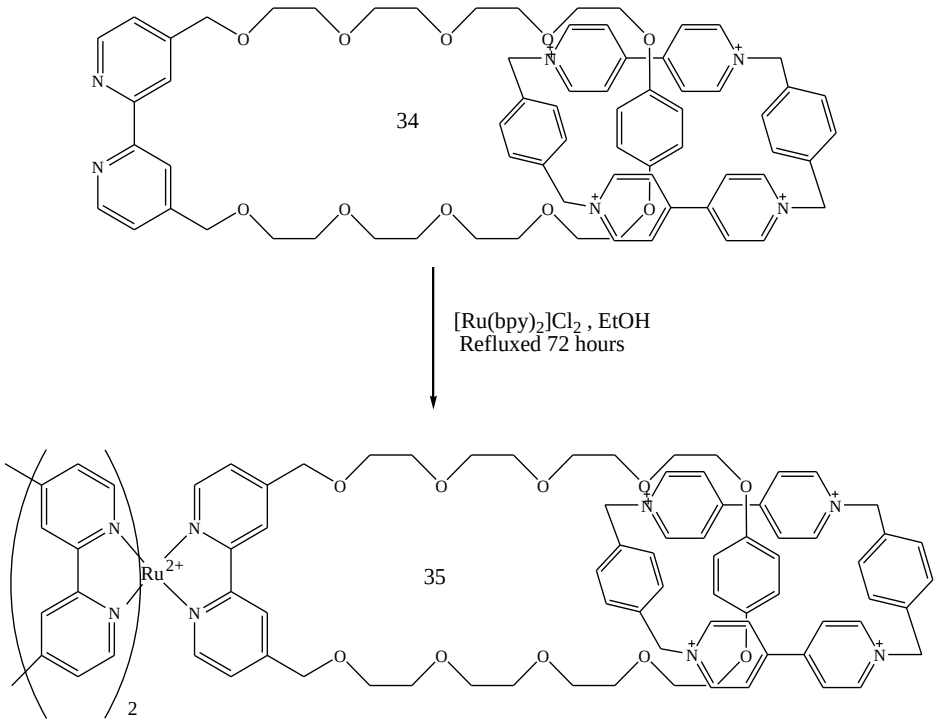

Figure 1.31: Synthesis of bis(4,4'-dimethyl-2,2'-bipyridine)(p-phenylene-4,4'-dimethylene-2,2' -bipyridyl[38]crown-10)ruthenium(II) dichloride

1.3.2 Experimental Section

Synthesis of 2-(4-carboxypyridin-2-yl)pyridine-4-carboxylic acid (24)

4-methyl-2-(4-methylpyridin-2-yl)pyridine (5.0 g) was dissolved in 100 ml of concentrated sulfuric acid. $K_2Cr_2O_7$ (16 g) was added to the mixture (an ice bath was used to control the sudden increase in temperature). The mixture was stirred for 30 minutes at 70 ^{0}C. The mixture was poured into ice (600 ml); a white precipitate was formed. The precipitate obtained was filtered and dissolved in saturated NaOH solution (30 ml). Solution was stirred for 2 hours, 10% HCl was added to the mixture and the pH was adjusted to 2. A white precipitate was formed. Yield 6.66 g (100%).

^{1}H (DMSO-d6, 200 MHz) δ 8.92 (d, *J*=3, 2H), 8.84 (2H, s), 7.91 (2H, dd). ^{13}C(DMSO-d6, 200 MHz) δ 118.86, 122.81, 138.98, 149.97, 154.81, 165.36

Synthesis of methyl 2-(4-(methoxycarbonyl)pyridin-2-yl)pyridine-4-carboxylate (25)

2-(4-carboxypyridin-2-yl)pyridine-4-carboxylic acid (5.5 g) , CH_3OH (100 ml) and concentrated sulfuric acid (13 ml) was refluxed for 65 hours (mixture turned into pink). The mixture was poured into water and the pH was adjusted to 8 using saturated NaOH. Organic component was extracted with CH_2Cl_2 (50 ml X 6). The solvent was evaporated; white crystals were obtained. Yield 4.36 g (71%).

^{1}H ($CDCl_3$, 400) δ 8.95 (d, *J*=3, 2H), 8.85 (2H, dd), 7.89 (2H, dd), 3.98 (6H, s). ^{13}C ($CDCl_3$, 200) δ 53.00, 120.62, 123.33, 138.57, 150.38, 156.77, 166.11.

Synthesis of 4,4'-bis(hydroxymethyl)-2,2'-bipyridine (26)

Methyl 2-(4-(methoxycarbonyl)pyridine-2-yl)pyridine-4-carboxylate (4.0 g) was suspended in 150 ml of absolute alcohol. $NaBH_4$ (2.72 g) was added to the solution and refluxed for three hours. The solvent was evaporated and the residue was collected. The residue was dissolved in 150 ml of saturated NH_4Cl. Organic components were extracted using ethyl acetate (50 ml x 6). The solvent was evaporated; a pale white residue was obtained. The product was recrystallized from toluene; white crystals were obtained (2.7 g, 87%).

^{1}H (DMSO-d6, 200 MHz) δ 8.60 (2H,d), 8.39 (2H,s) 7.37 (2H, dd), 5.51 (t, 2H), 4.63 (d, 4H).

^{13}C (DMSO-d6, 200 MHz) δ 60.90, 116.93, 120.63, 148.28, 152.23, 154.45.

Synthesis of 2-(2-(2-(2-chloroethoxy)ethoxy)ethoxy)ethanol (30)

A mixture of tetraethyleneglycole (50 g), pyridine (20 ml) and dry CH_3Cl (70 ml) was cooled to 0 ^{0}C. $SOCl_2$ (31 g) was added dropwise to the solution while keeping the reaction temperature under 10 ^{0}C. The temperature was raised to 60 ^{0}C and the mixture was stirred for 24 hours under N_2 atmosphere. $CHCl_3$ was evaporated and the residue was extracted with water (25 ml X 3). Aqueous layer was washed with hexane and the crude product was extracted into toluene (30ml x 4). The toluene extracts were dried using $MgSO_4$ and toluene was evaporated to get the final crude product, which is a yellow colored oil. The crude product was vacuum-distilled (110-115 ^{0}C, 2 mmHg) to obtain a colorless oil. Yield 16.42 g (30%).

^{1}H ($CDCl_3$, 400 MHz) δ 3.57-3.74 (16H, m), 2.53 (1H, s).^{13}C NMR ($CDC1_3$, 200MHz) 42.7,61.7,70.4,70.5,70.7, 70.7, 71.4, 72.5.

Synthesis of 1,4-Bis{2-(2-(2-(-2-hydroxyethoxy)ethoxy)ethoxy)ethoxy}benzene (31-a)

Hydroquinone (0.55 g) was dissolved in 10 ml of DMF and added dropwise to a mixture of K_2CO_3 (3.45 g) in dry DMF (10 ml). The mixture was stirred for 10 minutes in a N_2 atmosphere; color of the mixture changed to dark yellow. 2-(2-(2-(2-chloroethoxy) ethoxy)ethoxy)ethanol (2.5 ml) was dissolved in 10 ml of dry DMF and added to the reaction mixture. The mixture was stirred at 80 ^{0}C for 3 days. The residue was filtered and washed with 15 ml of DMF, and a dark brown solution was obtained. The solvent was removed and the viscous liquid was partitioned between CH_2Cl_2 (15 ml) and H_2O (25 ml). The aqueous phase was washed with CH_2Cl_2 (15 ml x 2) and combined with the organic fractions. Solvent was evaporated; a light brown oil was obtained. Yield 1.13 g (49%).

^{1}H ($CDCl_3$, 400 MHz) δ 3.52-3.75(28 H ,m), 3.80 (4H,t), 4.06(4H, t), 6.81 (4H,s). ^{13}C ($CDCl_3$, 200 MHz) δ 61.85, 68.14, 70.41, 70.65, 70.70,70.78, 70.88, 71.51, 72.70, 72.77, 115.70, 153.15

Synthesis of 1,4-Bis{2-(2-(2-(2-(p-tolylsulfonyl)ethoxy) ethoxy)ethoxy)ethoxy}benzene (31-b)

1,4-Bis{2-(2-(2-(-2-hydroxyethoxy)ethoxy)ethoxy)ethoxy}benzene (2.0 g) and triethyl amine (1.5 ml) were dissolved in CH_2Cl_2 (10 ml). The temperature of the mixture was maintained at 0 ^{0}C. Powdered p-toluenesulfonyl chloride (1.82 g) was added to the reaction mixture while stirring the mixture. The temperature of the mixture was kept below 5 ^{0}C during the addition of

p-toluenesulfonyl chloride. The mixture was stirred for another 6 hours at room temperature. Water (2.5 ml) was added to the mixture and stirred for another 10 hours. The organic layer was separated and washed with water (10 ml X 3). The solvent was evaporated; a light brown viscous liquid was obtained. Yield 2.61 g (78%)

^{1}H ($CDCl_3$, 400 MHz) 2.38 (6H, s), 3.47-3.68 (20H, m), 3.74-3.78 (4H, m), 6.78 (4H,s), 7.28(4H, m), 7.72 (4H, m). ^{13}C δ ($CDCl_3$, 200 MHz) 22, 68.16, 68.84, 69.53, 70.06, 70.36, 70.69, 70.79,70.88, 72.74, 115.74, 127.84, 130.39, 132.87, 144.98, 144.8, 153.37.

4,4'-dimethylene-2,2'-bipyridyl[38]crown-10 (32)

4,4'-Bis (hydroxymethyl)-2,2'-bipyridine (30 mg) and NaH (35 mg, 10 fold excess) was mixed with 15 ml of THF; a slurry was formed. The slurry was stirred for 15 minutes at room temperature. 1,4-Bis{2-(2-(2-(2-(p-tolylsulfonyl)ethoxy)ethoxy)ethoxy)ethoxy}benzene(60mg) was dissolved in 10 ml of THF and added to the reaction mixture drop wise. Reaction mixture was refluxed for 2 days. Reaction was quenched by adding 10 ml of water. The solvent was evaporated and the residue was dissolved in CH_2Cl_2. The organic layer was washed with 0.5M HCl (5 ml x 2). The organic layer was dried with $MgSO_4$ and the solvent was evaporated. A dark orange oil was obtained as the crude product. The crude product was purified by descending column chromatography (Silica column, CH_2Cl_2: MeOH, 90:10); an orange oil was obtained. Yield 15 mg (52%).

^{1}H (400 MHz, acetone-d6) δ 3.49-3.74 (m, 32 H), 4.76 (s, 4H), 6.84 (d, 4H), 7.49(d,2H), 8.47(s, 2H), 8.57(d, 2H). ^{13}C ($CDCl_3$, 200 MHz) δ 68.08, 69.88, 69.95, 70.40, 70.80, 70.86, 70.90, 70.93, 71.80, 115.53, 119.61, 122.17, 149.11, 149.42, 153.05, 156.00.

1.4 Conclusions

Highly charged tris-homoleptic ruthenium(II)-quarterpyridinium complexes were synthesized by using high pressure reaction conditions in the synthetic pathway. This high pressure reaction methodology has opened an more effective passageway to synthesize ruthenium(II) polypyridinium complexes with higher excited state life times.

These complexes were tested in different applications during last three years due to their higher charge, longer excited state life time, size and luminescent properties. The tris-homoleptic ruthenium(II)-quarterpyridinium complexes with +8 charged are successfully utilized as

effective sensitizers in the photocatalytic generation of hydrogen by the reduction of water (Chapter 2). Due to the higher positive charge and the size, these complexes are effectively tested as mycobacterial channel blockers in the protein-binding experiments (Chapter 3). Currently these ruthenium tetrapyridinium complexes are investigated as photodynamic therapy agents to inhibit cell growth of B16F10 cancer cell lines.

1.5 References

[1] Chao, Hui; Ji, Liang-Nian, DNA interactions with ruthenium (II) polypyridine complexes

[2] Juris, A.; Balzani, V.; Barigelletti, F.; Campagna, S.; Belser, P.; Von Zelewsky, A., Ruthenium(II)-polypyridine complexes : photophysics, photochemistry, electrochemistry, and chemiluminescence, *Coordination Chemistry Reviews* (1988), 84, 85-277.

[3] H.H. Jaffe; M. Orchin, Theory and Applications of Ultraviolet Spectroscopy, Wiley, New York, (1962).

[4] V. BaIzani; and V. Carassiti, Photochemistry of Coordination Compounds, Academic Press, London, (1970).

[5] (a)J.B. Birks, Photophysics of Aromatic Molecules, Wiley-Interseience, London, 1970.
(b) N.J. Turro, Modem Molecular Photochemistry, Benjamin, Menlo Park, California, 1978.

[6] (a) A.B.P. Lever, Inorganic Electronic Spectroscopy, 2nd edn., Elsevier, Amsterdam, (1984). (b). Balzani, V.; Moggi, L.; Manfrin, M. F.; Bolletta, F.; Laurence, G. S., Quenching and sensitization processes of coordination compounds, *Coordination Chemistry Reviews* (1975), 15(4), 321-433.

[7] Kavarnos, George J.; Turro, Nicholas J.,Photosensitization by reversible electron transfer: theories, experimental evidence, and examples, *Chemical Reviews* (Washington, DC, United States), (1986), 86(2), 401-49.

[8] Balzani, Vincenzo; Bolletta, Fabrizio; Gandolfi, Maria, Teresa; Maestri, Mauro., Bimolecular electron transfer reactions of the excited states of transition metal complexes, *Topics in Current Chemistry* (1978), 75, 1-64.

[9] Porter, Gerald B.; Balzani, Vincenzo; Moggi, Luca, Primary processes and energy transfer: consistent terms and definitions, *Advances in Photochemistry*, (1974), 9, 147-96.

[10] Sutin, Norman; Creutz, Carol, Electron-transfer reactions of excited states, *Journal of Chemical Education*, (1983), 60(10), 809-14.

[11] K. Mandal; T.D.L. Pearson; W.P. Krug; J.N. Demas, *J. Am. Chem. Sot.*, (1983), 105, 701.

[12] Balzani, Vincenzo; Bergamini, Giacomo; Marchioni, Filippo; Ceroni, Paola, Ru (II)-bipyridine complexes in supramolecular systems , devices and machines, *Coordination Chemistry Reviews*, (2006), 250(11+12), 1254-1266.

[13] D.P. RiIlema; D.S. Jones; H.A. Levy, *J. Chem. Sot, Chem. Commun.*, (1979), 849.

[14] Crutchley, R. J.; Lever, A. B.P., Comparative chemistry of bipyrazyl and bipyridyl metal complexes: spectroscopy, electrochemistry and photoanation, *Inorganic Chemistry*, (1982), 21(6), 2276-82.

[15] Orellana, Guillermo; Braun, Andre M., Quantum yields of ^{3}MLCT excited state formation and triplet-triplet absorption spectra of ruthenium(II) tris-chelate complexes containing five- and six-membered heterocyclic moieties, *Journal of Photochemistry and Photobiology*, A: Chemistry (1989), 48(2-3), 277-89.

[16] Duerr, Heinz; Schwarz, Ralph; Andreis, Christine; Willner, Itamar, Highly photostable sensitizers for artificial photosynthesis. Ruthenium(II)-3,3'-bis(diazine)-6,6'-oligo(ethylene glycol) complexes and a new class of podates, *Journal of the American Chemical Society* (1993), 115(26), 12362-5.

[17] Wacholtz, William F.; Auerbach, Roy A.; Schmehl, Russell H., Independent control of charge-transfer and metal-centered excited states in mixed-ligand polypyridine ruthenium(II) complexes via specific ligand design, *Inorganic Chemistry*, (1986), 25(2), 227-34.

[18] Sargeson, A. M., Caged metal ions, *Chemistry in Britain*, (1979), 15(1), 23-7.

[19] Duerr, Heinz; Bossmann, Stefan, Ruthenium Polypyridine Complexes. On the Route to Biomimetic Assemblies as Models for the Photosynthetic Reaction Center, *Accounts of Chemical Research*, (2001), 34(11), 905-917.

[20] Seiler, M.; Duerr, H.; Willner, I.; Joselevich, E.; Doron, A.; Stoddart, J. F., Photoinduced Electron Transfer in Supramolecular Assemblies Composed of Dialkoxybenzene -Tethered Ruthenium(II) Trisbipyridine and Bipyridinium Salts, *Journal of the American Chemical Society*, (1994), 116(8), 3399-404.

[21] Duerr, Heinz; Thiery, Urs; Infelta, P. P.; Braun, A. M., A sensitizer-relay assembly with improved properties in electron transfer processes, *New Journal of Chemistry*, (1989), 13(8-9), 575-7.

[22] Shi, Aibin; Pokhrel, Megh Raj; Bossmann, Stefan H., Synthesis of highly charged ruthenium(II)-quaterpyridinium complexes: a bottom-up approach to monodisperse nanostructures, *Synthesis*, (2007), (4), 505-514.

[23] Faller, Michael; Niederweis, Michael; Schulz, Georg E., The Structure of a Mycobacterial Outer-Membrane Channel, *Science* (Washington, DC, United States), (2004), 303(5661), 1189-1192.

[24] Morgan, Robert J.; Baker, A. David., 2,2':4,4":4',4"'-quaterpyridyl: a building block for the preparation of novel redox reagents. 1. Preparation and quaternization, *Journal of Organic Chemistry*, (1990), 55(7), 1986-93.

[25] Shorter, J., Nucleophilic aliphatic substitution., Organic Reaction Mechanisms, (1987), 299-328.

[26] Bossmann, Stefan H.; Duerr, Heinz; Pokhrel, Megh Raj, Synthesis of crown-ester-bipyridines and crown-ester-viologens, *Synthesis*, (2005), (6), 907-914.

[27] Thiery, U. *Thesis*; University of Saarland: 1988.

[28] Coe, Benjamin J.; Harris, James A.; Brunschwig, Bruce S.; Asselberghs, Inge; Clays, Koen; Garin, Javier; Orduna, Jesus, Three-Dimensional Nonlinear Optical Chromophores Based on Metal-to-Ligand Charge-Transfer from Ruthenium(II) or Iron(II) Centers, *Journal of the American Chemical Society*, (2005), 127(38), 13399-13410.

[29] Bradley, Patricia M.; Bursten, Bruce E.; Turro, Claudia, Excited-State Properties of Rh2(O2CCH3)4(L)2 (L = CH3OH, THF, PPh3, py), *Inorganic Chemistry*, (2001), 40(6), 1376-1379.

[30] Warren, Jeremy T.; Chen, Wei; Johnston, Dean H.; Turro, Claudia, Ground-State Properties and Excited-State Reactivity of 8-Quinolate Complexes of Ruthenium(II), *Inorganic Chemistry*, (1999), 38(26), 6187-6192.

[31] Hu, Yi-Zhen; Bossmann, Stefan H.; Van Loyen, Dietmar; Schwarz, Oliver; Durr, Heinz, A novel 2,2'-bipyridine[2]catenane and its ruthenium complex: synthesis, structure, and intramolecular electron transfer - a model for the photosynthetic reaction center. *Chemistry A European Journa l*, (1999), 5(4), 1267-1277.

[32] Schild, Volker; Van Loyen, Dietmar; Duerr, Heinz; Bouas-Laurent, Henri; Turro, Claudia; Woerner, Michael; Pokhrel, Megh Raj; Bossmann, Stefan H., Tuning the Charge-Separated Lifetimes of Ruthenium(II) polypyridyl-Viologen Dyads and Ruthenium(II) polypyridyl-Viologen Triads by the Formation of Supramolecular Assemblies with Crown Ethers, *Journal of Physical Chemistry A*, (2002), 106(40), 9149-9158.

[33] Burdzinski, Gotard; Hackett, John C.; Wang, Jin; Gustafson, Terry L.; Hadad, Christopher M.; Platz, Matthew S., Early Events in the Photochemistry of Aryl Azides from Femtosecond UV/Vis Spectroscopy and Quantum Chemical Calculations, *Journal of the American Chemical Society*, (2006), 128(41), 13402-13411.

[34] Nakayama, Toshihiro; Amijima, Yutaka; Ibuki, Kazuyasu; Hamanoue, Kumao, Construction of a subpicosecond double-beam laser photolysis system utilizing a femtosecond Ti:sapphire oscillator and three Ti:sapphire amplifiers (a regenerative amplifier and two double passed linear amplifiers), and measurements of the transient absorption spectra by a pump-probe method, *Review of Scientific Instruments*, (1997), 68(12), 4364-4371.

[35] (a) Haddour, Naoufel; Cosnier, Serge; Gondran, Chantal, Electrogeneration of a biotinylated poly (pyrrole - ruthenium (ii)) film for the construction of photoelectron chemical immunosensor, *Chemical Communications* (Cambridge, United Kingdom), (2004), (21), 2472-2473.
(b) Miyoshi, Daisuke; Karimata, Hisae; Wang, Zhong-Ming; Koumoto, Kazuya; Sugimoto, Naoki, Artificial G - wire switch with 2,2'-bipyridine units responsive to divalent metal ions, *Journal of the American Chemical Society*, (2007), 129(18), 5919-5925.

[36] Kazemi, Foad; Massah, Ahmad R.; Javaherian, Mohammad, Chemoselective and scalable preparation of alkyl tosylates under solvent-free conditions, *Tetrahedron*, (2007), 63(23), 5083-5087.

[37] Amabilino, David B.; Ashton, Peter R.; Brown, Christopher L.; Cordova, Emilio; Godinez, Luis A.; Goodnow, Timothy T.; Kaifer, Angel E.; Newton, Simon P.; Pietraszkiewicz, Marek; *et al.* Molecular Meccano. 2. Self - Assembly of [n] Catenanes, Journal of the American Chemical Society, (1995), 117(4), 1271-93.

[38] Doskocil, J., The oxidation of hydroquinone with tyrosinase and air oxygen, *Collection of Czechoslovak Chemical Communications* , (1950), 15 614-29.

[39] Hu, Yi-Zhen; Bossmann, Stefan H.; Van Loyen, Dietmar; Schwarz, Oliver; Durr, Heinz, A novel 2 , 2 '- bipyridine [2] catenane and its ruthenium complex : synthesis, structure, and intramolecular electron transfer - a model for the photosynthetic reaction center, Chemistry--A *European Journal*, (1999), 5(4), 1267-1277.

[40] Hu, Yi-Zhen; van Loyen, Dietmar; Schwarz, Oliver; Bossmann, Stefan; Duerr, Heinz; Huch, Volker; Veith, Michael, Intramolecular Electron Transfer between Noncovalently Linked Donor and Acceptor in a [2]Catenane, *Journal of the American Chemical Society*, (1998), 120(23), 5822-5823.

CHAPTER 2 - BIOINSPIRED HYBRID SYSTEMS FOR THE PHOTOCATALYTIC GENERATION OF HYDROGEN AND METHANE

2.1 Introduction

Finding an affordable, reliable and environmentally sustainable energy source is one of the major challenges in the next fifty years and beyond. The global population is going to increase by 36% by the year 2050.[1,2] In other words, the global population is going to reach 8.9 billion by 2050. With the increase of the population, global energy consumption is projected to increase by 77%.[1,2] During the last century, fossil fuel has been the world's primary energy source. The use of fossil fuels release CO_2 to the atmosphere, which increases the CO_2 % in the atmosphere. This is a one of the major reasons for the global warming and leads to changes in the global weather and the climate.[3] Therefore, it is important to consider the environmental effect during the development of new energy sources .

There are several renewable energy sources which have the potential to supply the energy demand of the future generations. Wind, solar, geothermal and tides can be considered as some of the potential energy sources. Nevertheless, these energy sources have certain problems associated with them as continuous sources of energy. Hydrogen is considered as an excellent energy storage media and has the potential to solve both daily and seasonal energy requirements. There are several car manufactures who have already started the production of cars with advanced vehicle propulsion system fuel cell engines using hydrogen as the energy source.[4] Another important feature of this hydrogen powered fuel cell vehicles, is that it does not emit any harmful products in the generation of power. One kilogram of hydrogen is adequate to drive a fuel cell vehicle up to about 60 miles.[5] There are several methods which are currently available to produce hydrogen and, have the potential to produce hydrogen commercially.

Currently, the main method used to produce hydrogen is the electrolysis of water. However, in this method the required electricity for this process is primarily generated by burning fossil fuels. This method has some disadvantages due to the high cost to produce 1 kg of hydrogen as well as the emission of green house gases by burning fossil fuels in the generation

of electricity. The US Department of Energy (U.S. DOE) and the National Renewable Energy laboratory have identified solar energy as the most efficient, cost effectively and environment friendly way to generate hydrogen.[5] The U.S. DOE has set the target for the cost of hydrogen to be $2.00 to $3.00 per kg of hydrogen produced, including the production and transportation cost to be able to compete with the fossil fuels.[6]

Methods, which have a high potential to generate hydrogen by using solar energy are specified in Figure 2.1. The U.S. DOE has identified electrolysis, thermolysis, biomass and photolysis as the most efficient ways to generate hydrogen gas commercially. These methods have been experimented, and their advantages and weaknesses are identified.

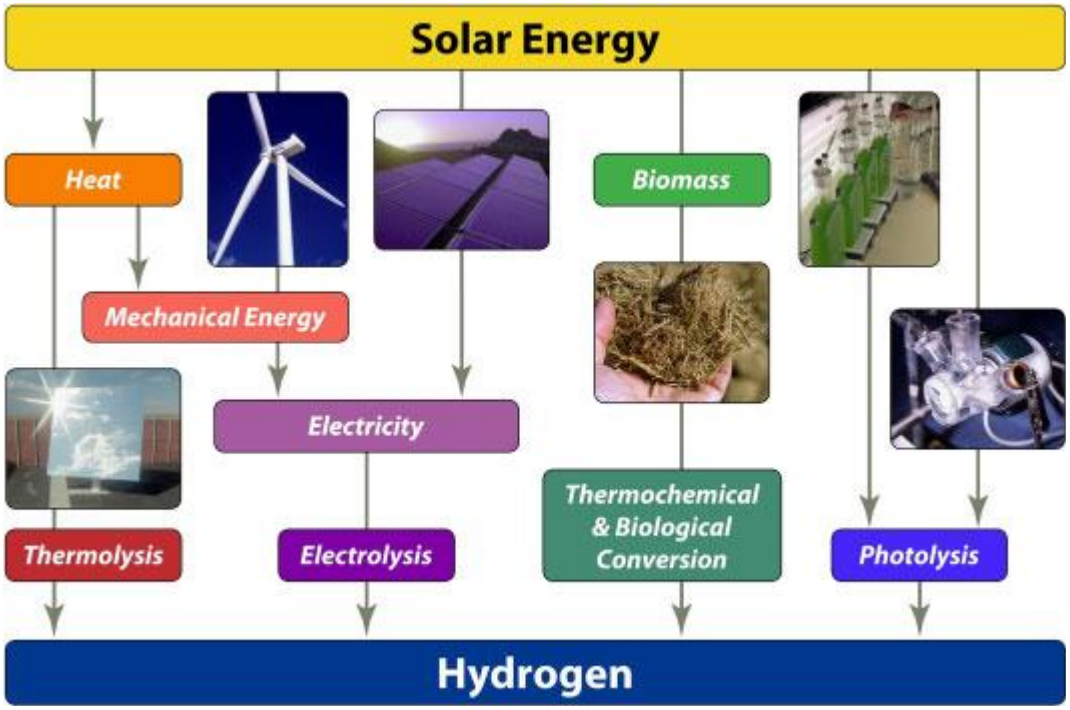

Figure 2.1: Available renewal pathways for hydrogen production[5]

Electrolysis is considered as the simplest method to generate hydrogen by splitting water using an electric potential. To produce 1 kg of hydrogen at atmospheric pressure requires about 39 kW (at 100% efficiency) electricity and 8.9 liters of water by using the electrolysis method.[7] However, the current commercial electrolyzer systems have maximum efficiencies around 53 %, which corresponds to 70.1 kW of energy to generate a 1 kg of hydrogen.[7]

The alkaline electrolyzer is the most common type used to generate hydrogen by electrolysis, which uses water and 25-30 wt% KOH as the electrolyte.[5] The other commonly used electrolytes are NaOH and NaCl. The anode and cathode reactions are shown in equation 1 and 2 respectively. In this method, hydrogen is produced in the cathode while oxygen is released from the anode. This method has a major drawback due to the necessity of electrolyte in large quantities.

$$4OH^- \longrightarrow O_2(g) + 2H_2O(l) \qquad (1)$$

$$2H_2O(l) + 2e^- \longrightarrow H_2(g) + 2OH^-(aq) \qquad (2)$$

The other common electrolytic method is called polymer electrolyte or proton exchange membrane which is commonly referred to as PEM. In the PEM, deionized water is used as the electrolyte.[5] Deionized water is introduced to the anode and it is dissociated as given in equation 3 upon the application of an electrical potential. The H^+ produced in the anode migrates to the cathode via a membrane. The membrane in the PEM has two functions: 1. It acts as an ion conductor, and 2. The membrane acts as a gas separation device to avoid the reaction of H_2 and O_2 to produce water. Protons are reduced in the cathode as given in equation 4.

$$2H_2O(l) \longrightarrow 4H^+(aq) + 4e^- + O_2(g) \qquad (3)$$

$$4H^+(aq) + 4e^- \longrightarrow 2H_2(g) \qquad (4)$$

Both of these electrolysis methods have some drawbacks due to the high cost of electricity. Still the electricity is generated mainly by burning fossil fuels, which releases harmful byproducts such as CO_2 and CO to the atmosphere. Therefore, the electricity to be used in the electrolysis process should be generated mainly from wind or solar energy to make hydrogen as a completely renewable fuel. To satisfy the U.S. DOE stated prices for the production of hydrogen cost, electricity cost should be lower than $ 0.045 per kW.[5] However, current electricity costs are much higher than that value, making hydrogen generation by electrolysis not cost effective until now.

Conversion of biomass to hydrogen is another path which has a high potential to generate hydrogen economically according to the U.S. DOE.[5] There are two particular methods used to

convert biomass into hydrogen (Figure 2.2); one is a chemical method which involves the conversion of bio-mass into syn gas. This method has major problems due to the difficulties in the downstream processing, and lack of efficient stable catalysts.[8]The other method is the biological pathway which is the fermentation of biomass.

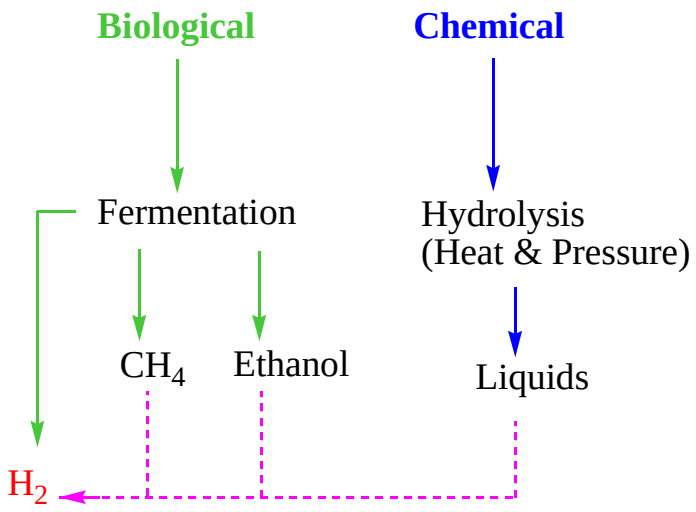

Figure 2.2: Conversion of biomass into hydrogen [5]

Many anaerobic microorganisms such as bacteria can perform dark fermentation reactions during their metabolism of glucose and other carbohydrates. They can produce hydrogen, methane, carbon dioxide and other small hydrocarbons as by products from their metabolism. Figure 2.3 shows the glucose metabolism of anaerobic bacteria which produce hydrogen as the final product. According to Figure 2.3, two hydrogen molecules can be formed by consuming one glucose molecule.[9,10]

Fermentation has distinct advantages such as: 1. These types of reactors can be operated even at night; 2. These microorganisms are readily available in the anaerobic composites, soil and sewage[11] 3. Inexpensive waste materials can be use as the feeding stocks for the bacteria.[12,13] Nevertheless, this process has certain disadvantages as well, such as production of CO_2 by microorganisms during their metabolism. Glucose has to be use as feeding stocks for the bacteria to get higher yield from the process, which is more expensive than the price of hydrogen. This method could be more effective if the glucose feed stocks can be replaced with waste, which are rich in carbohydrates.

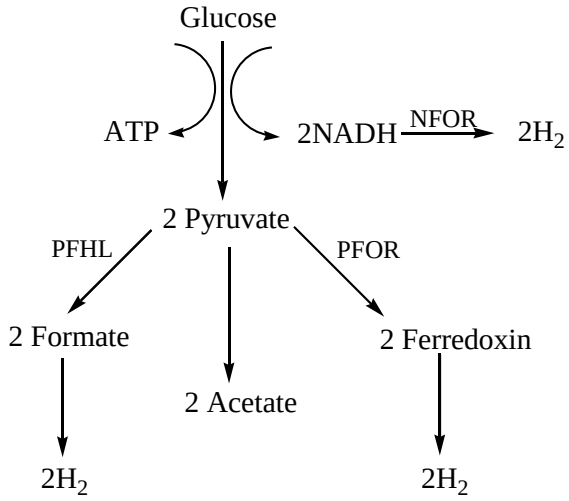

Figure 2.3: Fermentation of glucose by anaerobic bacteria to produce hydrogen gas[9,10]

Solar driven thermo chemical reactions are considered as another method which has high potential to produce hydrogen without using fossil fuels.[5] Water is the most abundant source of hydrogen, but it requires huge amounts of energy to dissociate water into its elements to get hydrogen and oxygen. Water does not dissociate into its elements at temperatures lower than 2500 K.[14] This dissociation temperature can be lowered by using different catalysts, which help the water dissociation by a series of chemical transformations. If the catalyst can lower the dissociation temperature to about 800 K, thermo chemical water splitting can be achieved more efficiently by the solar collectors[15] (Figure 2.4).

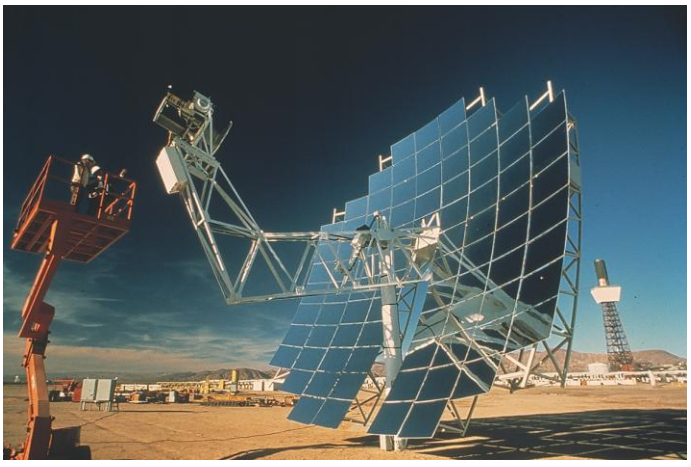

Figure 2.4: Picture of a parabolic solar collector system[16]

However, this method also has some major drawbacks due to the high manufacturing cost of solar collectors and the environmental impacts caused by the catalyst which is use to lower the dissociation temperature of the water.[5] The use of high temperatures also provides the need for higher concerns regarding safety requirements.

The other most promising way to generate hydrogen is the photolysis, in which water splits into hydrogen and oxygen photochemically. Water needs a 1.23 V potential at 25 ^{0}C to split into hydrogen and oxygen.[5] The most important factor in the photolysis is to find the correct material to harvest the light and use that energy to split water more efficiently.

2.1.1 Photolysis of Water

Water can be split into hydrogen and oxygen without applying an electric field if it can fulfill one of two major conditions.[17] 1. Oxygen should evolve at a much more negative potential than the potential at which hydrogen evolves at normal conditions. 2. Hydrogen should evolve at a potential which is more positive than the oxygen evolution potential in the normal conditions.[17] Photolysis of water into hydrogen and oxygen was first achieved by Fujishima and Honda in 1972.[17] Fugishima *et. al* used a TiO_2 anode and a Pt cathode for photolysis of water as given in the equations below. First, the TiO_2 electrode was irradiated with the 500 W xenon lamp which oxidizes water to oxygen gas and H^+ (equation 6). Protons migrate to the Pt cathode and reduce to hydrogen gas (equation 7).

$$TiO_2 + 2\,hv \longrightarrow 2\,e^- + 2p^+ \qquad 5$$

(excitation of TiO2 by light)

$$2\,p^+ + H_2O \longrightarrow 1/2\ O_2 + 2\,H^+ \qquad 6$$

(at the anode)

$$2e^- + 2\,H^+ \longrightarrow H_2 \qquad 7$$

(at the Pt cathode)

After the first discovery of photolysis of water, many people attempted to find more efficient systems to split water to hydrogen and oxygen by using visible and UV light. Fine TiO_2 nanoparticles have been widely used as the photocatalyst due to their chemical stability, high photocatalytic activity and non-toxicity.[18] UV light has enough energy to excite an electron from valance band of TiO_2 to the conduction band. The excitation creates holes in the valence band

and electrons in the conduction band. These electrons and holes can initiate a redox reaction of a species, which is in close vicinity of TiO_2 nano particles.[18] The photocatalytic ability of TiO_2 can be remarkably enhanced by addition of small amounts of noble metals such as Pt or Rh.[18, 19] This enhancement can be explained by the quick transfer of the photo generated electron from conduction band of TiO_2 to the metal catalyst. This results a decrease in electron-hole recombination that increases the charge separation, resulting in the initiation of redox reactions more efficiently. Time-resolved spectroscopy experimental results have proven that noble metals have an important role as charge carriers in the photolysis.[19,20] These noble metals act as active sites for the formation of hydrogen gas.

However, these TiO_2 cannot be used as an effective catalyst for the photolysis by using visible light. This is due to their large gap between valence and conduction band, which is 3.2 eV[17] corresponding to wavelengths shorter than 388 nm. That means TiO_2 needs large portion of UV radiation for the excitation of an electron from valence band to the conduction band. Therefore, TiO_2 can use only 3 - 4% of solar energy from the total amount of solar energy received by the earth's surface.[17] Consequently, TiO_2 alone cannot be used as a photolysis catalyst to generate hydrogen by solar energy. A new catalyst which is capable of using a considerable amount of the solar energy should be developed to commercially produce hydrogen by this method.

Many investigators have attempted to solve this obstacle by using sacrificial donors. A sacrificial donor is a chemical species which in its reduced form can release an electron more easily than water by oxidation.[21] Released electrons can be used to initiate the redox reactions. Organic compounds such as triethylenediamine, tetraacetic acid, triethanolamine can be used as sacrificial donors.[21] Utilization of sacrificial donors greatly enhances the production of hydrogen by photolysis, but this has a drawback due to the high cost of sacrificial donors. A sacrificial donor is more expensive than the value of produced hydrogen.

Even 35 years after the discovery of photolysis of water to generate hydrogen,[17] the goal to develop a stable and efficient catalytic system to split water by sunlight has not been fully accomplished.

2.2 Artificial Photosynthesis by Sensitizer Relay Assemblies

Photosysnthesis is a multifunctional process which harvests sunlight, first evolved 2-3 billion years ago.[22] Photosynthetic reaction centers are the main units which are responsible for the photosynthesis. They first appeared in primitive life forms such as cyanobacteria and algae. These photosynthetic reaction centers appeared in the plants about 500 million years ago during the time plants first started colonizing dry land.[22] Release of oxygen by photosynthesis changed the chemical components of the earth's atmosphere. This causes the evolution of animals in the dry land. In the photosynthesis, CO_2 and H_2O were used to synthesize carbohydrates and O_2 using solar energy. The highest conversion yield of photosynthesis is about 1 - 3%, however, efficiency of the photosynthesis in an average plant is about 0.5%.[23]

Approximately 1.78 x 10^{21} W of solar energy reach earth's surface every year. This massive amount of energy corresponds to 1.367 kW/ m^2.[23] It has been estimated that 30 minutes of sunlight delivers an equivalent amount of energy consumed all over the world per year.[23] Accordingly, 17 days of sunlight can deliver an energy equivalent to the energy of all the fossil fuel reserves in our planet.[23]

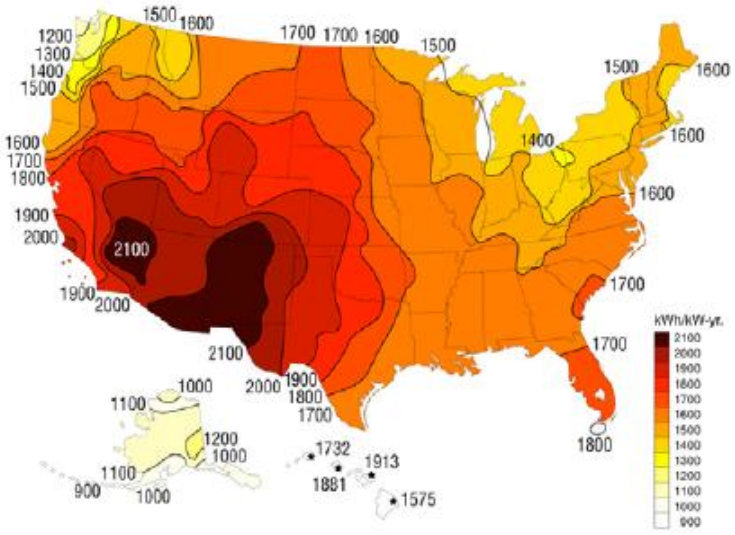

Figure 2.5: Map of solar irradiation in United States of America[24]

Figure 2.5 shows the solar irradiation of US every year; this diagram shows that most of the states receive huge amounts of energy by sunlight. With 10% efficiency, 100 x 100 $miles^2$ area can generate enough energy for US per year.[24] This area can be compared with the surface area of US highways which corresponds to 20,000 $miles^2$. Artificial photosynthesis is an artificial

process which mimics the photosynthesis to harvest sunlight. Therefore, artificial photosynthesis has the potential to satisfy the global energy demand. There is another added advantage of artificial photosynthesis due to its ability to use CO_2 as a row material and generate lower hydrocarbons. Earth's atmosphere can benefit from this process by reducing the already increased CO_2 percentages in the atmosphere.[25]

Artificial photosynthesis can be considered as a supramolecular system which is depicted in Figure 2.6. Artificial photosynthetic systems consists of three major components to produce H_2 and O_2 from water:[21] A sensitizer, an electron carrier which is the relay, and a catalyst, to store and use the electrons in reduction reactions. The process starts with the irradiation of sunlight on the sensitizer, which can release an electron. The released electron is transferred by the electron carrier to the catalyst. The oxidized sensitizer can be reduced back to its original state by oxidizing water to O_2 and H^+ (Figure 2.6). Electrons migrate to the catalyst and protons are reduced to hydrogen gas.

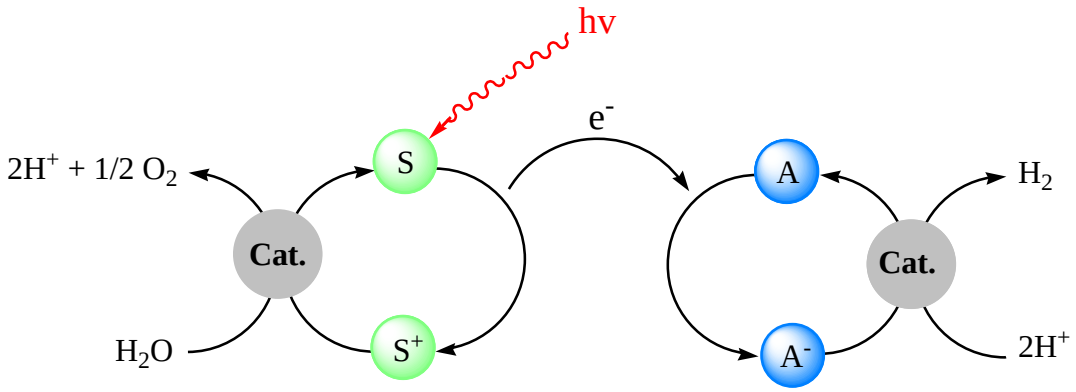

Figure 2.6: Schematic diagram of artificial photosynthesis[21]

Semiconductors, metal pyridine (Figure 2.7) complexes and metal porphyrins are widely used as sensitizers in artificial photosynthesis.[26] Bis-ammonium salt like methylviolegens (Figure 2.8) and more complex molecules such as cobalt sepulchrate are used as relays.[27] Metals[28,26] such as Pt, Rh, Pd, Ru, Os and the metal oxides such as RuO_2[29], ZrO_2[30] are considered as the most commonly employed catalysts.

To achieve higher efficiency in production of hydrogen and oxygen, each component used in artificial photosynthesis should be optimized. A good sensitizer should have to have the following characteristic features;[21] should absorb in the visible region of the electromagnetic spectrum, should have a longer life time for the excited state. Long excited state life times can be

achieved if the sensitizer has an efficient intersystem crossing from photochemically excited singlet state to more stable triplet state. These sensitizers should have to have suitable redox potentials to initiate the redox reaction of water. Sensitizers should be stable in the photochemical reaction conditions. Finally, all bimolecular electron transfer reaction has to be fast.

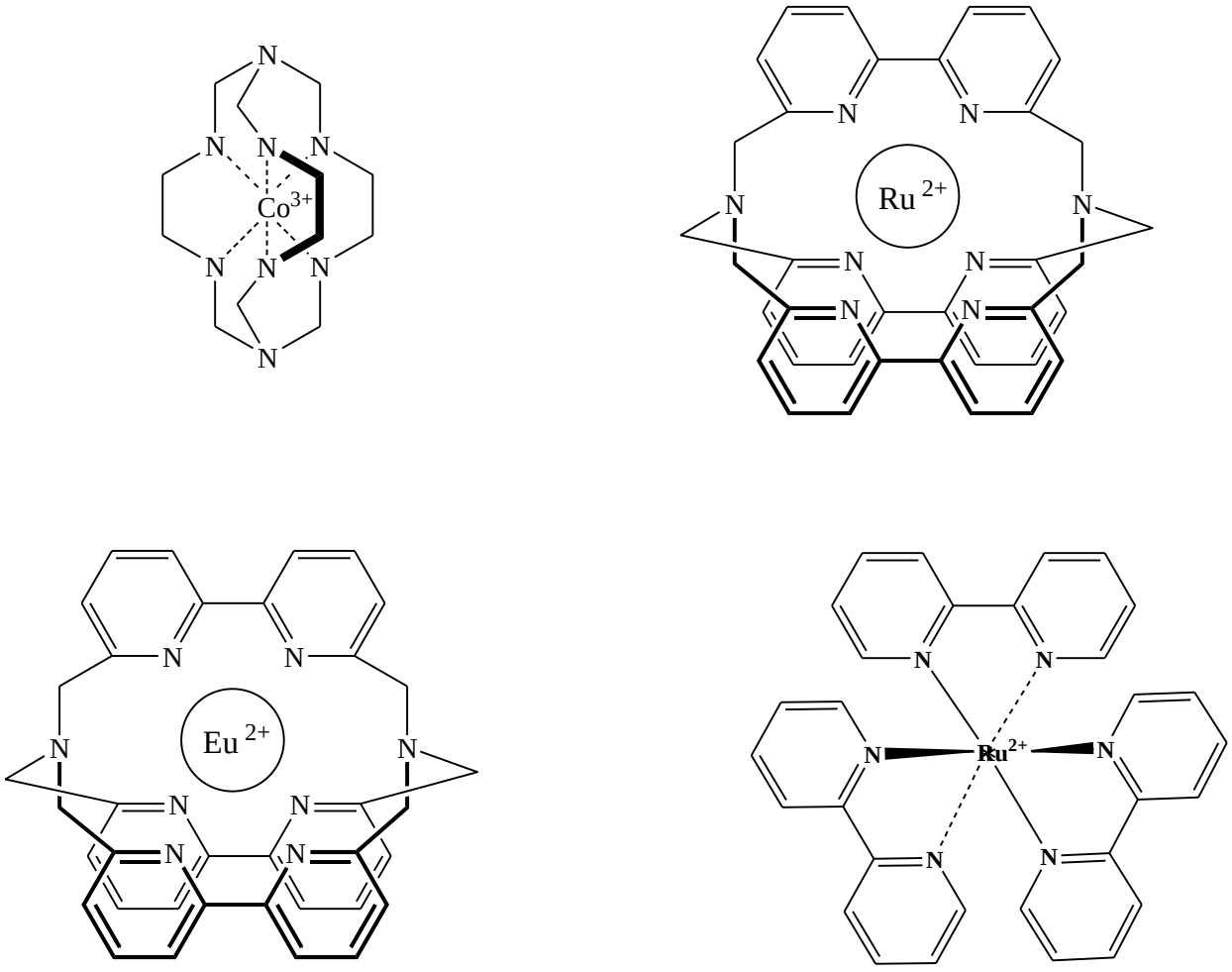

Figure 2.7: Structures of some sensitizers used in artificial photosynthesis[21]

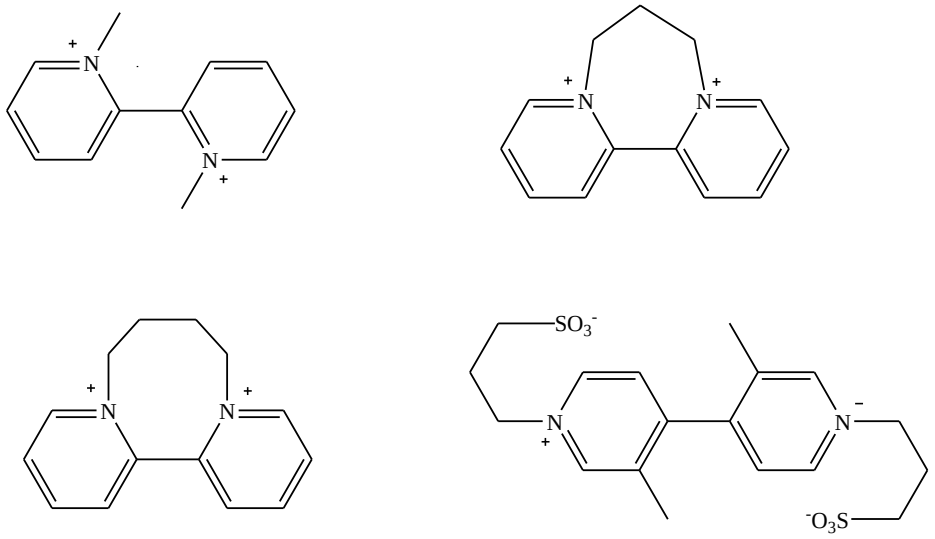

Figure 2.8: Examples for the charged relays used in artificial photosynthesis[31]

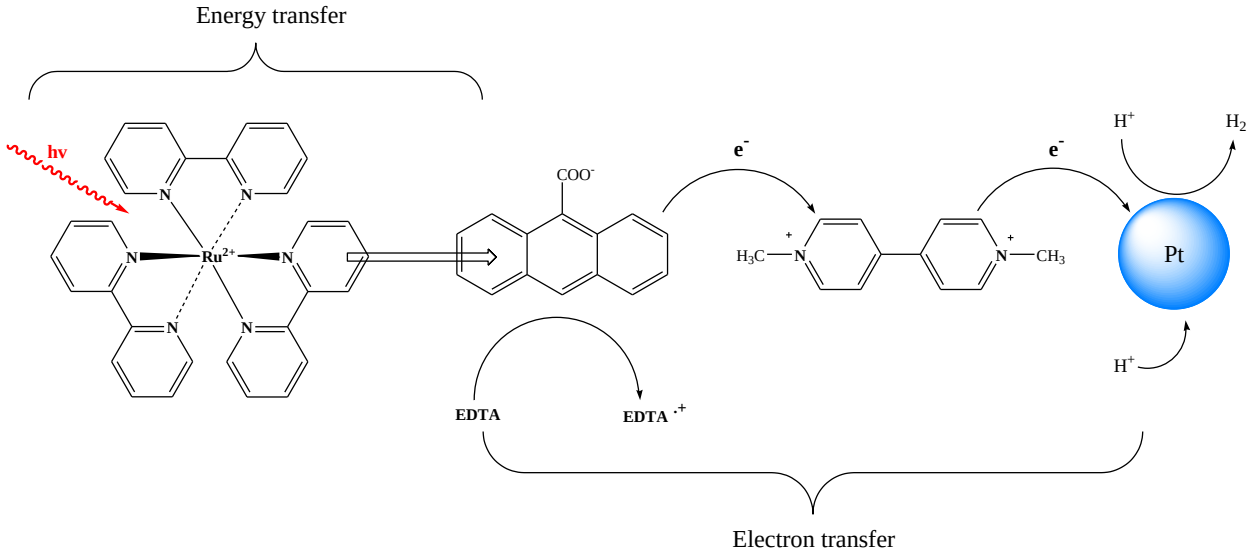

Figure 2.9: Energy transfer/ electron transfer in reduction of water to hydrogen[31]

Figure 2.9 shows the energy and the electron transfer of a system which consists of a sensitizer, electron relay and catalyst to split the water.[32] First, $Ru(bpy)_3^{2+}$ absorbs energy from the visible light. Due to the efficient triplet energy transfer from the ^{3}MLCT to the 9-anthracene-carbixylic acid, 9-anthracene-carbixylate anion forms by abstracting an electron from EDTA. The electron transfers to the Pt catalyst via methyl viologen and reduce H^+ to hydrogen.

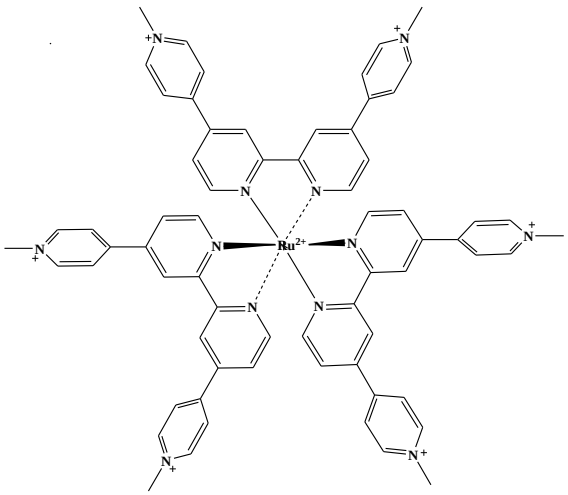

Figure 2.10: Structure of a covalently linked sensitizer-relay assembly[33]

There is another approach in which covalently linked sensitizer relay assemblies are used for the artificial photosynthesis (Figure 2.9). In the sensitizer-relay molecule, sensitizer (2,2'-bipyridine) and relays (modified 4,4'-violagens) are combined covalently.[33] The use of sensitizer-relay assemblies can substitute the electron carrier which is necessary in artificial photosynthesis. Dürr *et. al.*[33] has observed nanosecond range luminescence life times for these sensitizer relay assemblies. This is a considerable increase with comparable to the luminescence life time of the sensitizer molecules such as metal porphyrins and metal polypyridines. Dürr *et. al*[33]. have also observed the evolution of hydrogen of the sacrificial system which uses the compound in Figure 2.10 in the absence of the relay.

2.2.1 Reduction of CO_2 to methane by sensitizer relay sacrificial systems

In the photosynthesis, CO_2 and H_2O used as row materials to synthesize carbohydrates. Consequently, artificial photosynthesis would be able to reduce CO_2 to lower hydrocarbons. However, there is not much research been done on the photochemical reduction of carbon dioxide using artificial photosynthesis. Reduction of carbon dioxide has two major advantages[24] 1. This can remove the CO_2 from the atmosphere, higher CO_2 levels already causes unfavorable environmental effects such as increasing atmospheric temperature, climatic changes and melting of arctic ice. 2. Lower hydrocarbons such as methane can be utilized as an energy source or as row materials to synthesize more useful higher hydrocarbons.

Table 2.1 illustrates the redox potentials of CO_2 to produce various hydrocarbons at pH 7. According to the reduction potential given in Table 2.1, it is almost impossible to do one electron reduction of CO_2. According to the reduction potentials, multi electron reduction reactions of CO_2 look thermodynamically favorable. Reduction potential of CO_2 to CH_4 is even smaller than the reduction potential of H^+ to hydrogen. Although CO_2 to CH_4 is more favorable than the reduction of H^+ to hydrogen (thermodynamically), kinetically CO_2 to CH_4 reduction is difficult due to the requirement of multi-electrons for the reduction. However, to reduce CO_2 successfully to CH_4 and H_2O, the catalyst should be able to undergo efficient multi-electron and multi-proton transfer reactions.[34]

Table 2.1: Standard redox potentials of various reduction reactions at pH 7[34,35]

Reaction	*E^o (V vs. SHE)*
$CO_2 + 1e^- \longrightarrow CO_2^{\cdot-}$	-2
$CO_2 + 2H^+ + 2e \longrightarrow HCOOH$	- 0.61
$CO_2 + 2H^+ + 2e \longrightarrow CO + H_2O$	-0.52
$CO_2 + 4H^+ + 4e \longrightarrow HCHO + H_2O$	-0.48
$2H^+ + 2e \longrightarrow H_2$	-0.41
$CO_2 + 6H^+ + 6e \longrightarrow CH_3OH + H_2O$	-0.38
$CO_2 + 8H^+ + 8e \longrightarrow CH_4 + 2H_2O$	-0.24
$CO_2 + 4H^+ + 4e \longrightarrow C + 2H_2O$	-0.20

Unfortunately reduction potential of CO_2 to elemental carbon is smaller than the reduction potential of CO_2 to CH_4 (Table 2.1). This may cause a problem in photo catalytic generation of methane by depositing elemental carbon on the surface of the catalyst. The deposition of carbon particles on the catalyst can decrease the catalytic performance. Therefore, a method has to be developed to avoid the deposition of carbon on the catalytic surface. This is essential to use this photo catalytic method for the generation of methane by CO_2 for longer time periods.

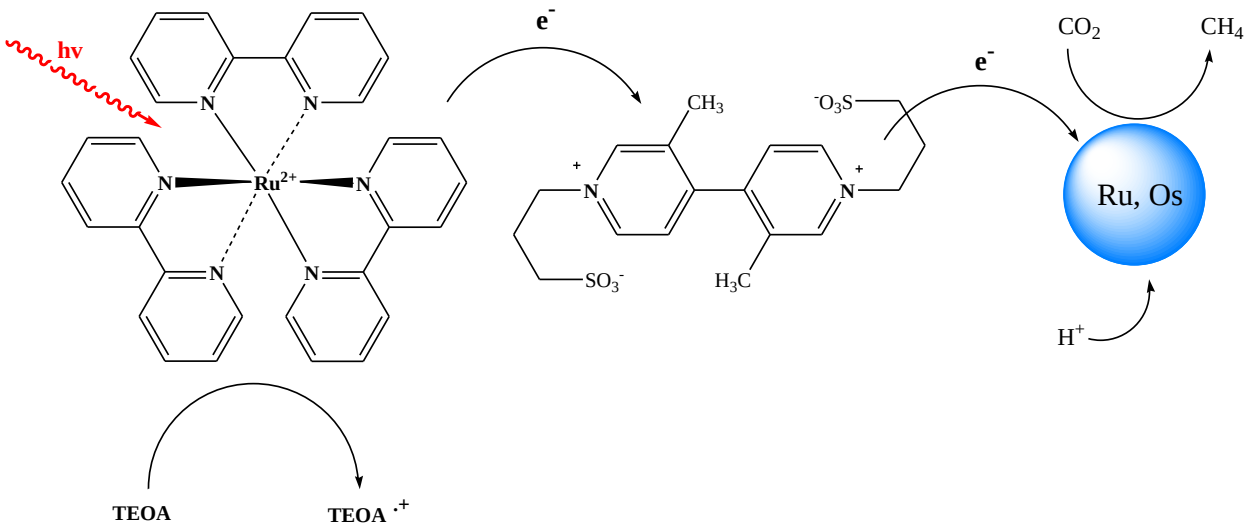

Figure 2.11: Generation of CH_4 from the CO_2 by using a sensitizer relay assembly[31]

Figure 2.11 is the schematic diagram of oxidative cycle which shows the generation of methane from CO_2, which is published by Bossmann *et. al.*[33] In the reaction scheme depicted in Figure 2.11, $Ru(bpy)_3^{2+}$ was utilized as the sensitizer. First, $Ru(bpy)_3^{2+}$ is irradiated with the visible light; $Ru(bpy)_3^{2+}$ is excited and abstracted an electron from the sacrificial donor (triethanolamine). $Ru(bpy)_3^{+}$ releases the abstracted electron to the electron carrier and oxidizes back to its initial state. Electron carrier transports the electrons to the catalyst, where the multi-electron reduction is taking place to reduce CO_2 to methane. Catalyst acts as electron storage units to perform a multi-electron reduction. Nevertheless, the catalytic activity decreased with the time due to the deposition of elementary carbon on the catalyst.

2.3 Photocatalytic Generation of Hydrogen and Methane Using Pd/ TiO_2 Heterogeneous Catalysts and Ruthenium(II)quaterpyridinium Complexes

Highly charged ruthenium(II)quaterpyridinium complexes have been synthesized as described in chapter 1. Figure 2.1 shows a 3D structure of $Ru(QP\text{-}C1)_3^{8+}$ which has been generated by Chem3D MM2 calculations. These +8 charged ruthenium(II)quaterpyridinium complexes act as sensitizers and electron relay upon irradiation of sunlight in the presence of a appropriate donor and go through the reductive pathway, which will be discussed later in this chapter.[36]

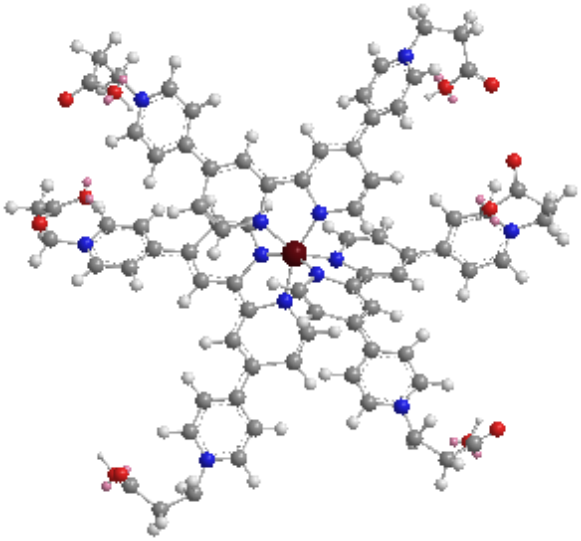

Figure 2.12: 3D structure of +8 charged ruthenium(II)quaterpyridinium complex ($Ru(QP\text{-}C1)_3^{8+}$)

Figure 2.13 shows the solar energy distribution in outer atmosphere and on the surface of the earth.[37] According to the Figure 2.13, it is apparent that the largest portion of energy is reaching the surface of the earth is between 400-800 nm in wavelength. Therefore, the maximum amount of solar energy can be harvested by the chemical compounds which absorb light energy in the 400-800 nm range. In other words, a effective sensitizer should be able to harvest energy in the range of 400-800 nm wavelength.

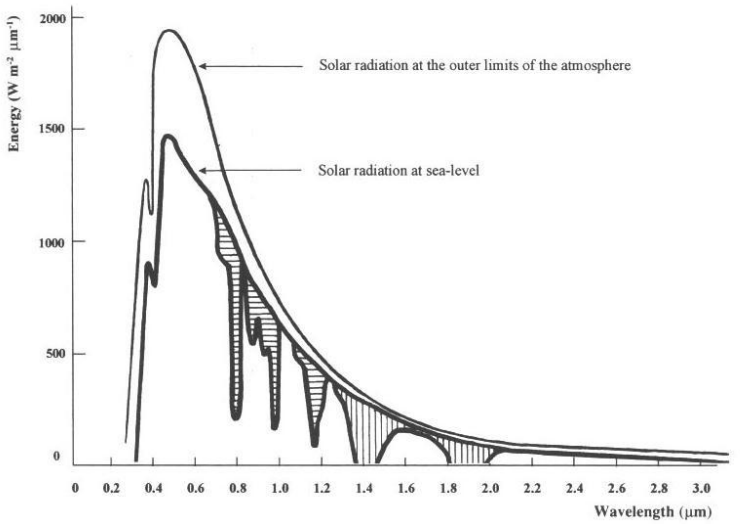

Figure 2.13: Solar irradiation in space and on the surface of the earth[37]

Figure 2.14 shows the absorption and the emission spectra of $Ru(QP\text{-}C1)_3^{8+}$; these spectra clearly show that the ruthenium C2 complex features a ^{3}MLCT absorption band (metal to ligand charge transfer) around 490 nm. These spectra confirm that the ruthenium complex $Ru(QP\text{-}C1)_3^{8+}$ can be used to harvest the energy from the sunlight. Therefore, the charged ruthenium complexes can be employed as good sensitizers in the artificial photosynthesis.

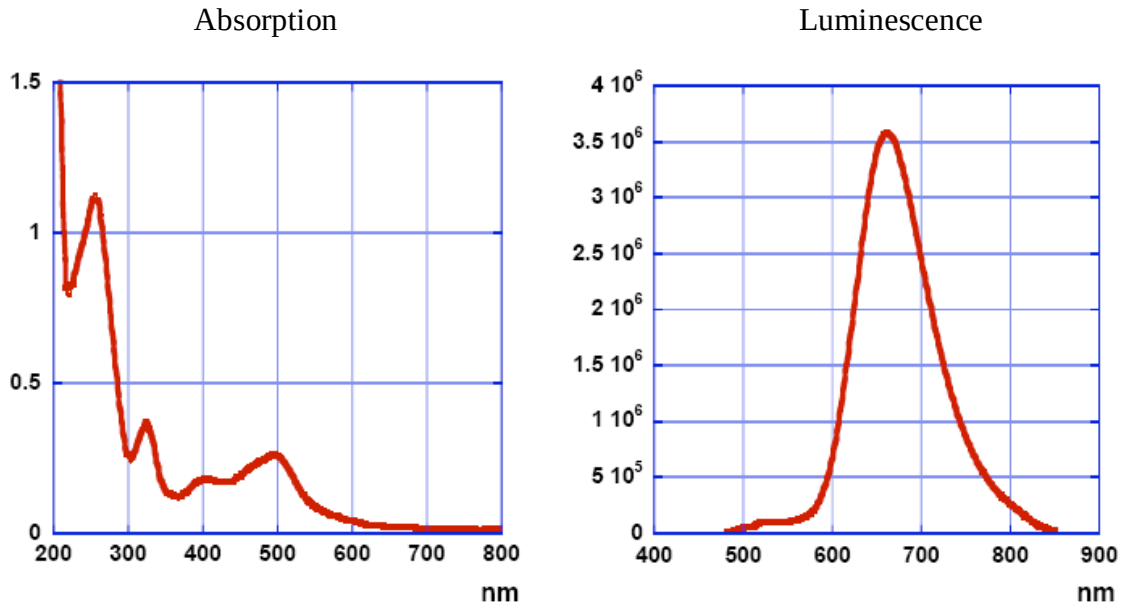

Figure 2.14: Absorption and luminescence spectra of $Ru(QP\text{-}C1)_3^{8+}$ (1 x 10^{-5} M in CH_3OH) $Ru(QP\text{-}C1)_3^{8+}$ was exited at λ = 486 nm

The absorption threshold of the $Ru(QP\text{-}C1)_3^{8+}$ complex is close to 700 nm, which permits the harvest of large amounts of energy from the solar irradiation. According to Table 1.3, which shows the photophysical properties of highly charged ruthenium complexes, all of these complexes with +8 or +14 charge (compounds 11-22) show a strong light absorption due to their metal to ligand charge transfer bands around 470 - 490 nm. Therefore, theoretically, all highly charged complexes that have been synthesized in my thesis can be used as sensitizer relay assemblies to generate hydrogen and methane in a photocatalytic system. Since $Ru(QP\text{-}C2)_3^{8+}$ complex is the most simple complex, it has been mainly used for the electrochemical experiments, which were performed to do the thermodynamic calculations.

First, amperometric current versus time experiments were performed for the $Ru(QP\text{-}C2)_3^{8+}$ complex, using electrochemical analyzer (CHI model 600B series). In the amperometric current versus time experiments, a constant potential is applied to the electrolytic solution and the current as a function of time is measured.

The experimental setup is illustrated in Figure 2.15. As depicted in the figure given below, three electrodes were used in the experiment. The carbon electrode was used as the working electrode, a Pt electrode was used as the counter electrode and an Ag/AgCl electrode was used as the reference electrode. A Hg lamp (Mercury 150 W, with Oriel 68806 basic power supply) was used to simulate sunlight. A constant voltage (60V) was given to the lamp throughout the IT curve experiments.

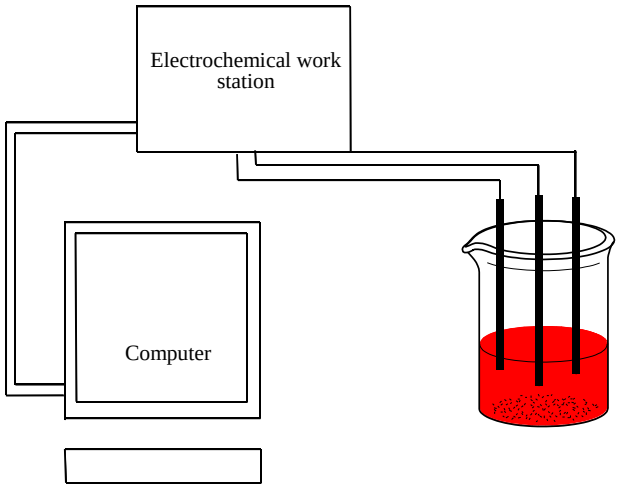

Figure 2.15: Instrument setup for the amperometric current (I) versus time (T) experiments

First, a 1 x 10^{-5} M $Ru(QP\text{-}C2)_3^{8+}$ solution was prepared by using a 0.33 M KCl solution. Another 0.33 M KCl solution was used as the reference solution. Two i-t curve experiments were performed employing the ruthenium complex solution and KCl solution. The i-t curves obtained are given in Figure 2.16.

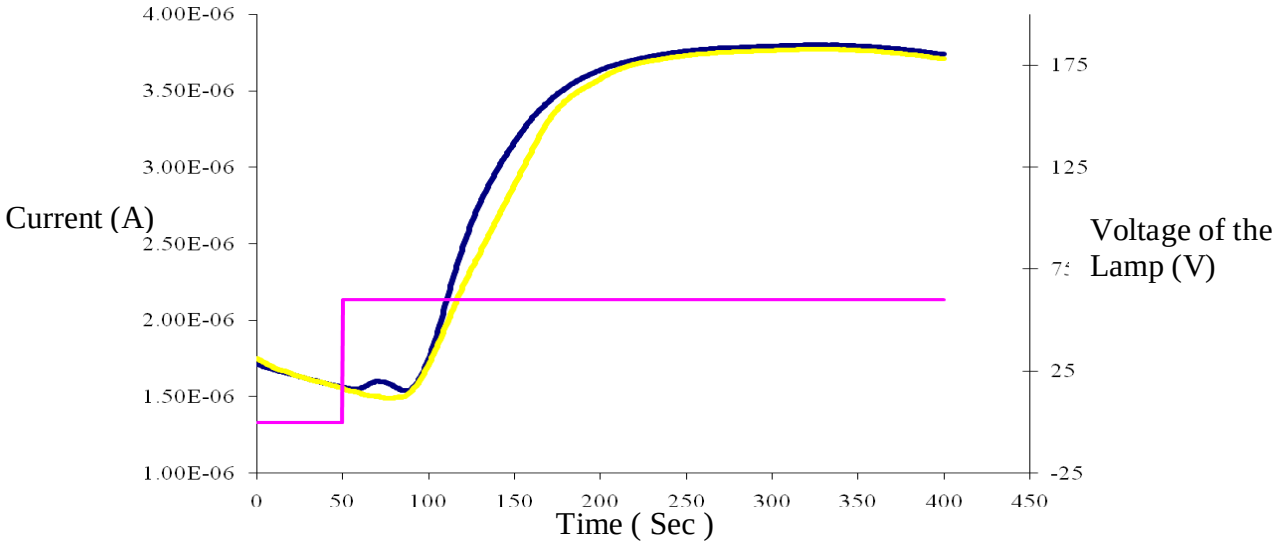

Figure 2.16: Amperometric current versus time (i-t) curves of $Ru(QP\text{-}C2)_3^{8+}$ (1 x 10^{-5}M) in KCl (0.33 M, blue line) and KCl (0.33 M, yellow line)

In Figure 2.16, the light purple line shows the voltage of the UV lamp. The UV lamp was switched on for 50 seconds after the start of the scan. Right after the lamp was switched on, a small peak was observed in the case of $Ru(QP\text{-}C2)_3^{8+}$ solution; after that peak, i-t curves of the complex and reference solution looks almost identical, but it can be observed that the i-t curve of the ruthenium complex is slightly higher than that of KCl. It can be observed well in the subtracted i-t curves which are depicted in Figure 2.17.

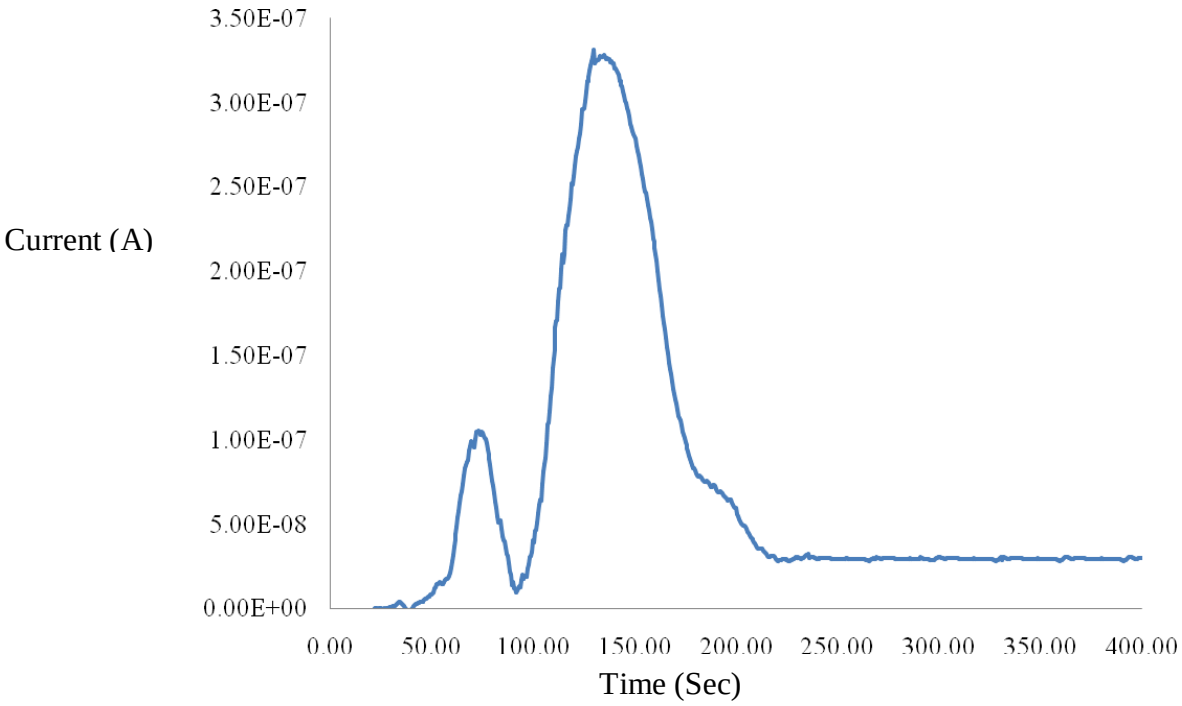

Figure 2.17: Subtracted i-t Curves for the $Ru(QP\text{-}C2)_3^{8+}$ (1 x 10^{-5}M) in KCl (.33 M) vs KCl (0.33M) solution

First peak can be observed around 60 seconds into the experiment, which is due to the reduction of Ru^{II*} to Ru^{I}. The ruthenium complex solution exclusively has Ru^{II} ions before the UV light was switched on, and when the light was switched on, Ru^{II} was excited to Ru^{II}*. Then Ru^{II*} is reduced to Ru^{I} by taking up one electron from the electrode! Since there is only Ru^{II*} and Ru^{II} present right after the light was switched on, there was an imbalance between Ru^{II} and Ru^{I}. After the light was switched on, Ru^{II*} reduced to Ru^{I} which causes the first peak in the subtracted i-t curve. There is another large peak which appeared around 150 minutes of starting the experiment. This peak can be explained by the initial increase of the conductivity due to the heating of the solution. Increase in conductivity results in a higher current in the reduction of Ru^{II} to Ru^{I}. Then a constant current was observed, which is called a steady state current. This steady state current can be explained by the following steady-state "equilibrium" (Figure 2.18), in which the electron uptake by the photoexcited Ru(II)complex (^{3}MLCT) and the electron loss to the anode or in a chemical reaction are balanced.

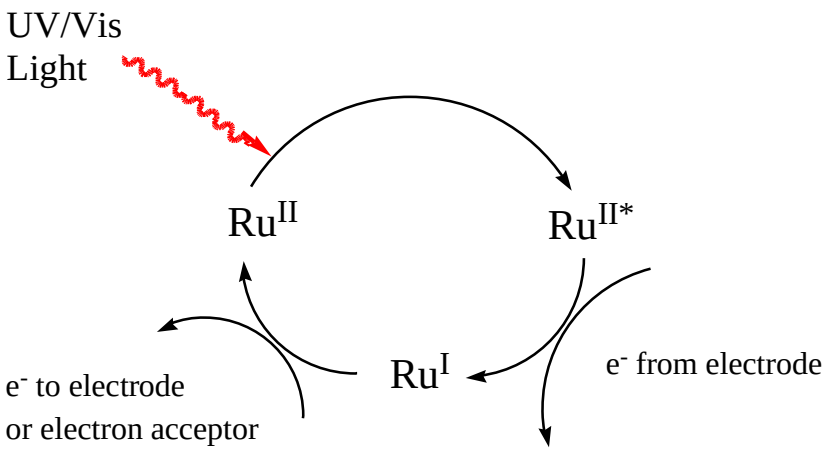

Figure 2.18: Equilibrium between Ru^{I} and Ru^{II}

Before switching on the UV light, the ruthenium complex solution exclusively has Ru^{II} complexes. When the light was switched on, Ru^{II} was excited to Ru^{II*}, and its reduced to Ru^{I}. Ru^{I} is oxidized to Ru^{II} again and completes the cycle as shown in Figure 2.18. Continuation of this cycle results in the generation of a steady state current in the ruthenium complex solution. These data confirms that Ru^{II} can reduce to Ru^{I} and it can oxidize back to Ru^{II}. In order to do so, there must be an electron acceptor for Ru^{I}, which either diffuses to the anode in the electrochemical setup or reacts with oxidative impurities in the buffer. Figure 2.19 shows the proposed schematic diagram (reductive ruthenium-cycle), which depicts $Ru(QP\text{-}C2)_3^{8+}$ as the sensitizer as well as the electron relay upon photo-irradiation. Before irradiation, $Ru(QP\text{-}C2)_3^{8+}$ is exclusively present in the catalytic solution; upon irradiation of light, Ru^{II} is excited to Ru^{II*}. This excited ruthenium complex (Ru^{II*}) can abstract an electron from the sacrificial donor (triethanolamine) or indium tin oxide (ITO) electrode and reduce to Ru^{I}. Reduced Ru^{I} can then release an electron and oxidize back to Ru^{II}. Electrons released from the ruthenium complexes are stored by a catalyst (Pd/ TiO_2). The stored electrons are utilized in the multi-electron reductions, such as reducing CO_2 to methane and water to hydrogen. Regenerated Ru^{II} complex can undergo the same cycle and produce more electrons to be used in reduction reactions.

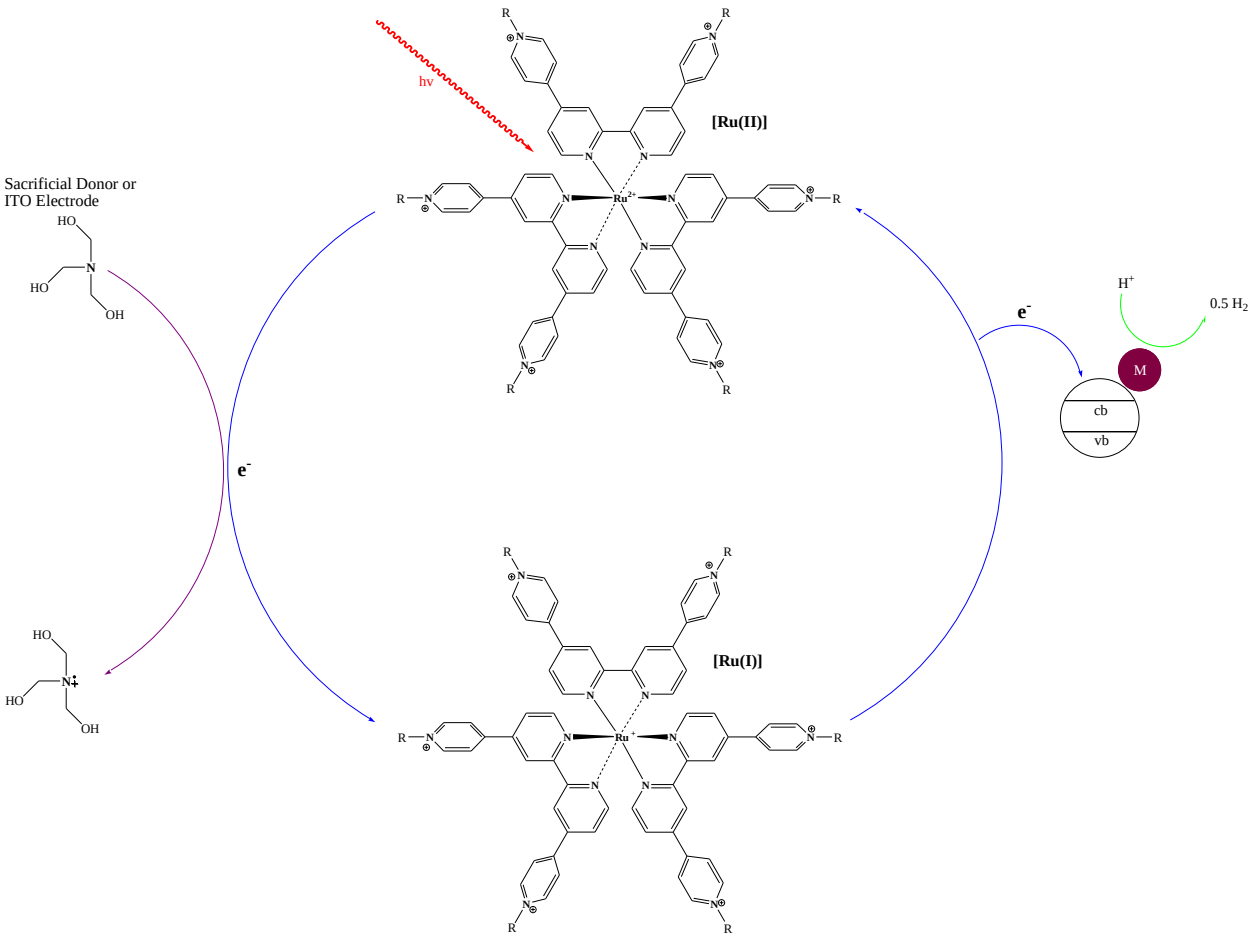

Figure 2.19 : Schematic diagram of sacrificial donor mediated photoelectron transfer to generate hydrogen (reductive cycle).

2.3.1 Measurement of the Redox Potentials of the Ruthenium(II)Quaterpyridinium Complexes

The redox potentials $Ru^{3+/2+}$ and $Ru^{2+/1+}$ of the ruthenium(II)quaterpyridinium complexes have been measured in aqueous solution (0.50M KCl) and 0.050M phosphate buffer (pH=7.0) employing the method of Differential Pulse Voltammetry (DPV, Electrochemical Analyzer, CHI model 600B series).[38] A platinum working electrode was employed, together with an Ag/AgCl counter electrode. The concentration of the ruthenium complexes was 1 x 10^{-5}M. The pH of the solutions was thoroughly checked before and after the experiments

Differential pulse voltammetry (DPV) is the ideal method to measure redox potentials in water. In opposite to cyclic voltammetry, redox potentials of quasi-reversible and non-reversible

electron transfer reactions can be determined without any experimental problem. DPV can be considered as a derivative of linear sweep voltammetry or staircase voltammetry, with a series of regular voltage pulses superimposed on the potential linear sweep or stair steps. The current is measured immediately before each potential change, and the current difference is plotted as a function of potential. By sampling the current just before the potential is changed, the effect of the charging current can be decreased. As a consequence, the baseline can be kept constant, which permits the detection of electron exchange reactions at lower concentrations of the redox active substrates, compared to cyclic voltammetry.[39] The parameters used in Electrochemical Analyzer (CHI model 600B series) for the DVP experiment are given in Table 2.2.

Table 2.2: Parameters used for DPV experiments

Parameter	*Value*
Initial E (V)	**-1.5**
Final E (V)	**1.5**
Increase E (V)	**0.004**
Amplitude (V)	**0.05**
Pulse Width (sec)	**0.025**
Sampling Width (sec)	**0.0167**
Pulse Period (sec)	**0.25**
Quite Time (sec)	**10**

A typical result from the DPV characterization of the tris-homoleptic ruthenium-complex RuC3 is shown in Figure 2.20. The $Ru^{3+/2+}$ and the $Ru^{2+/+}$ redox transitions are clearly resolved. Note that the size of the redox peaks are greatly influenced by kinetic parameters. Therefore, conclusions about the number of electrons exchanged cannot be drawn from these measurements.

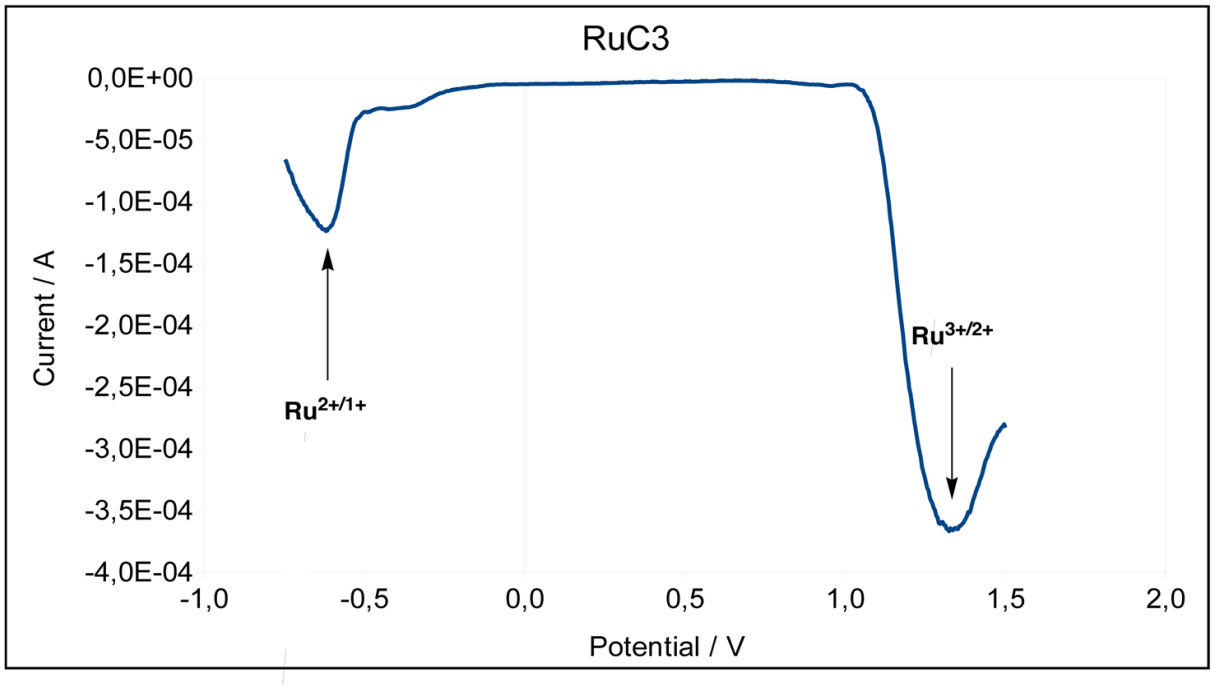

Figure 2.20: DPV of RuC3 ($1.0x10^{-5}$M) in aqueous buffer (0.50M KCl, 0.050M phosphate buffer, pH=7.0)

An Ag/AgCl reference electrode has been employed. Consequently, all redox potentials are shifted by +0.227V vs. SHE (standard hydrogen electrode).

Set of DPV experiments were carried out for all the ruthenium(II)quaterpyridine complexes by using Electrochemical Analyzer (CHI model 600B series). The results are summarized in table 2.4. where,

E_0 $Ru^{3+/2+}$: Standard potential for the Ru^{3+}/ Ru^{2+} redox transition in aqueous KCl (0.50M) at pH=7.0 (0.050M phosphate buffer).

E_0 $Ru^{2+/1+}$: Standard potential for the Ru^{2+}/ Ru^{1+} redox transition in aqueous KCl (0.50M) at pH=7.0 (0.050M phosphate buffer).

$\Delta E_{0\text{-}0}$: Excited State Energy of the ^{3}MLCT-states (eV), determined from the onset of the ^{3}MLCT luminescence bands at room temperature.

E_0* $Ru^{3+/2+}$: standard potential for the Ru^{3+*}/ Ru^{2+} redox transition occurring from the ^{3}MLCT state in aqueous KCl (0.50M) at pH=7.0 (0.050M phosphate buffer).

E_0* $Ru^{2+/1+}$: standard potential for the Ru^{2+*}/ Ru^{1+} redox transition occurring from the ^{3}MLCT state in aqueous KCl (0.50M) at pH=7.0 (0.050M phosphate buffer).

The excited state potentials reported in Table 4.3, have been calculated according to the following equations:

$$E_0{}^*Ru^{3+/2+} = E_0Ru^{3+/2+} - \Delta E_{0-0}$$
$$E_0{}^*Ru^{2+/1+} = E_0Ru^{2+/1+} + \Delta E_{0-0}$$

2.3.1.1 Quantitative Understanding of the Redox-Properties of Ruthenium-Quaterpyridinium Complexes

According to the general paradigm that has been developed by Balzani *et al*.[40] the ligand strength of polypyridyl-ligands that are bound to the central Ru^{2+} cation increases with the charge density on the nitrogen that facilitates the binding (N-1 in Figure 2.21). Therefore, the redox potentials, as measured by DPV, have been plotted vs. the charge density on N-1, which was obtained by PM3 calculations.[41] PM3 was chosen, because it permits the use of constraints that keep the ligands in the position that is mandatory for binding to the central Ru(II)-cation. Furthermore, the calculated charge densities from PM3 have been proven to be reliable as the data from more sophisticated approaches, such as density function calculations.[41]

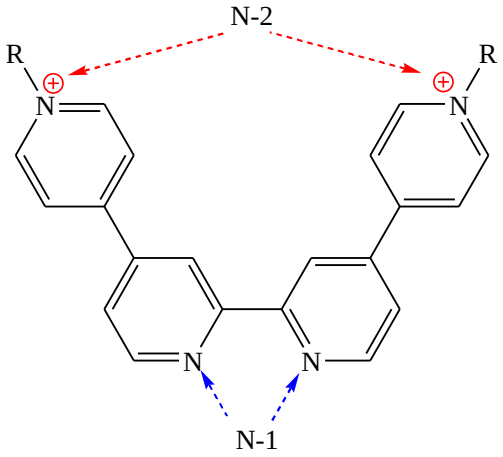

Figure 2.21: Principle geometry chosen for PM3 calculations

Table 2.3: Ground-State and Excited State (^{3}MLCT) Redox Potentials of the Ruthenium Complexes Synthesized in this Thesis

Complex	E_0 $Ru^{3+/2+}$ V (vs. SHE)	E_0 $Ru^{2+/1+}$ V (vs. SHE)	$\Delta E_{0\text{-}0}$ eV	E_0* $Ru^{2+/3+}$ V (vs. SHE)	E_0* $Ru^{2+/1+}$ V (vs. SHE)
$RuC1^{2+}$ (pH=7)	1.507	-0.46900	2.20	-0.693	1.731
$RuC2^{2+}$ (pH=7)	1.571	-0.44500	2.20	-0.629	1.755
$RuC3^{2+}$ (pH=7)	1.551	-0.39300	2.20	-0.649	1.807
$RuC4^{2+}$ (pH=7)	1.537	-0.40100	2.20	-0.663	1.799
$RuC1COO^{2+}$ (pH=7)	1.495	-0.52000	2.22	-0.725	1.670
$RuC2COO^{2+}$ (pH=7)	1.537	-0.47700	2.22	-0.683	1.743
$RuC3COO^{8+}$ (pH=7)	1.580	-0.36500	2.22	-0.640	1.855
$RuC4\ COO^{8+}$ (pH=7)	1.550	-0.44000	2.22	-0.650	1.780
$RuC1py^{8+}$ (pH=7)	1.462	-0.53000	2.14	-0.678	1.462
$RuC2py^{8+}$ (pH=7)	1.509	-0.48550	2.14	-0.631	1.509
$RuC3py^{8+}$ (pH=7)	1.505	-0.49850	2.14	-0.635	1.505
$RuC4py^{8+}$ (pH=7)	1.538	-0.46250	2.14	-0.602	1.538
Ru-C2Phosphonate	1.525	-0.423	2.25	-0.725	1.525

As it can be discerned from Figure 2.22, the redox potential of Ru^{3+}/Ru^{2+} increases with increasing negative charge density on N-1. This finding supports the general paradigm which was published by Balzani *et.al*[40], that stronger ruthenium-polypyridyl complexes feature higher redox potentials. This experimental finding can be explained by the greater stability of the +2 ruthenium oxidation state when the Ru-N bonds are stronger. A higher negative partial charge on N-1 leads to stronger binding.

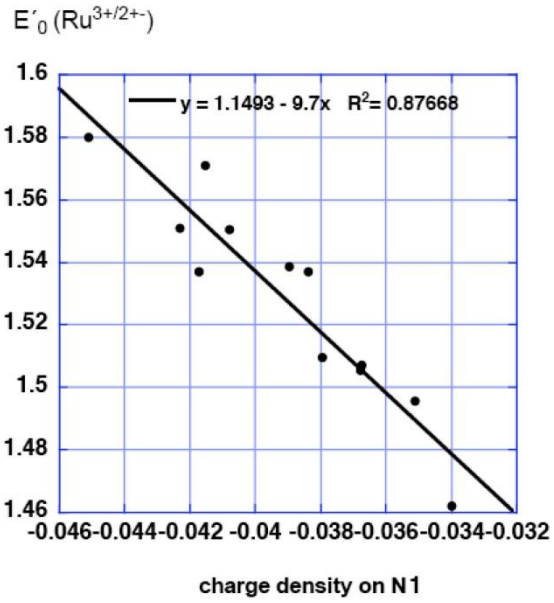

Figure 2.22: Plot of the redox potentials for the transition Ru^{3+}/Ru^{2+} in aqueous buffer (0.50M KCl, 0.05M phosphate buffer, pH=7.0) vs. the charge density on N-1 as calculated using PM3

The same tendency as for Ru^{3+}/Ru^{2+} can be seen for Ru^{2+}/Ru^{1+} in aqueous solution. The redox potential of Ru^{2+}/Ru^{1+} increases with the increase of partial negative charge on N-1 in the same manner as previously described (Figure 2.23). It is typical that both, the Ru^{3+}/Ru^{2+}- and the Ru^{2+}/Ru^{1+}-transitions are shifting in dependence on the same structural features of the ruthenium complexes.[40] This work has clearly identified the charge density on N-1 as an important factor.

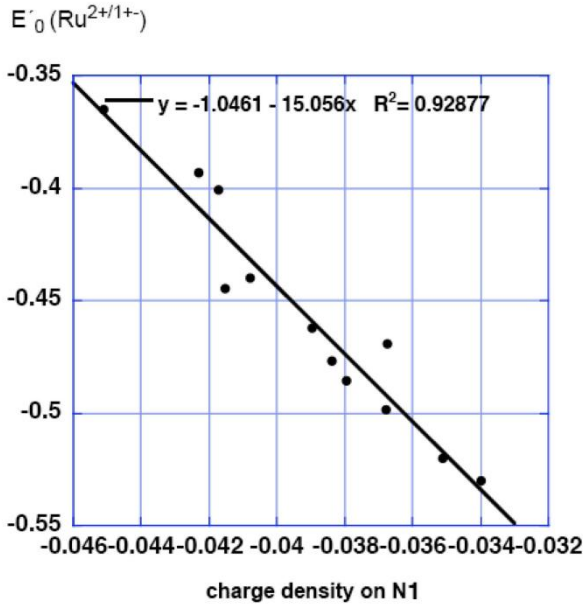

Figure 2.23: Plot of the redox potentials for the transition Ru^{2+}/Ru^{1+} in aqueous buffer (0.50M KCl, 0.05M phosphate buffer, pH=7.0) vs. the charge density on N-1 as calculated using PM3

To further study the effects of structural features of the synthesized ruthenium(II) quaterpyridinium complexes on their redox properties, the redox potentials vs. charge density on N2 were explored. The redox potentials for the Ru^{3+}/Ru^{2+} transition in aqueous buffer (0.50M KCl, 0.050M phosphate buffer, pH=7.0) were plotted vs. the partial negative charge density on N-2 (Figure 2.24) calculated by PM3. N-2 is the quaternized sp^2-nitrogen of the viologen function of the investigated ruthenium complexes. Dependency of Ru^{2+}/Ru^{1+} redox potential (0.50M KCl, 0.050M phosphate buffer, pH=7.0) with the charge density of N-2 is illustrated in Figure 2.25.

According to the Figure 2.24 and Figure 2.25 redox potentials of Ru^{3+}/Ru^{2+} and Ru^{2+}/Ru^{1+} are slightly increased with the increase of charge density on N-2. Therefore, we conclude that the charge density on N-2 is not a major structural factor that determines the redox potentials for the Ru^{3+}/Ru^{2+} and Ru^{2+}/Ru^{1+} redox transitions in ruthenium-quaterpyridinium complexes.

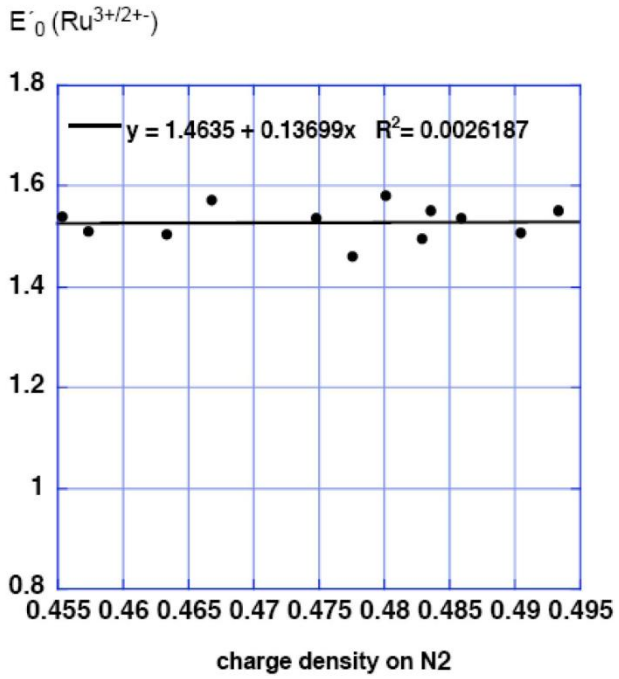

Figure 2.24: Plot of the redox potentials for the transition Ru^{3+}/Ru^{2+} in aqueous buffer vs. the charge density on N-2 calculated by using PM3

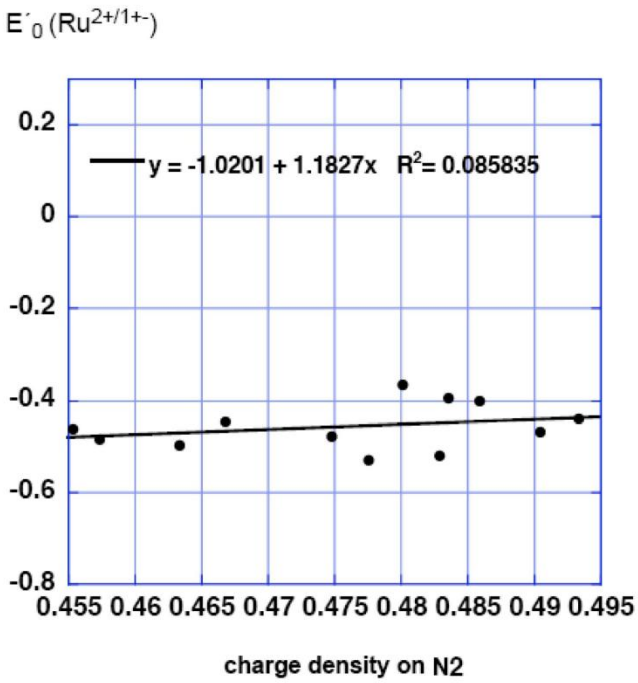

Figure 2.25: Plot of the redox potentials for the transition Ru^{2+}/Ru^{1+} in aqueous buffer vs. the charge density on N-2 calculated by using PM3

2.3.2 Selection of Suitable Catalysts for the Electron Storage

I have experimented with two suitable catalysts for the storage of electrons to be used in the multi-electron reductions. The catalysts used were Ru metal on TiO_2 nanoparticles and Pd on TiO_2 nanoparticles.

These catalysts were synthesized by a method which is published by Bossmann, S. H. *et. al.* [42] In a brief method summary, $RuCl_3$, TiO_2 and citric acid were dissolved in water and the mixture was stirred at 60 ^{0}C for 18 hours. Unreacted citric acid was washed with water and the catalyst was separated by centrifuging. The catalyst was obtained as an ash colored powder.

The same method was used to prepare the Pd on TiO_2 nanoparticles. TiO_2, $RuCl_3$ (wt ratio 10:1) and citric acid were dissolved in water and the mixture was stirred at 60 ^{0}C for 18 hours. Unreacted citric acid was washed with water and the catalyst was separated by centrifuging. The catalyst was obtained as an ash colored powder after drying in the oven for 48 hours.

2.3.3 Experimental section for the generation of hydrogen and methane

Two catalytic mixtures were prepared as given in the Table 2.4. These catalytic mixtures were used to phtotocatalytic reduction of water to hydrogen, by using the apparatus set up shown in Figure 2.26.

Table 2.4: Composition of catalytic mixtures used in photocatalytic generation of H_2

Components	*Ru/TiO_2 Mixture*	*Pd/TiO_2 Mixture*
$Ru(QP\text{-}C2)_3^{8+}$ (3 x 10^{-3} M)	6.00 ml	6.00 ml
Triethanolamine (TEA)	1.5 ml	1.5 ml
Catalyst	75 mg	75 mg
Water	42.5 ml	42.5 ml

The apparatus setup consists of a solar imitator and a specially designed photochemical reactor with a gas collector (Figure 2.26). First 50 ml of catalytic solution was filled inside the photochemical reactor. The reactor was then sealed with a rubber septum. Then the gas collector

was degassed and filled with argon to make sure no other gases were left in the gas collector. Degassing was performed another two times to make sure that virtually only argon gas is present inside the gas collector, because traces of oxygen would react with the hydrogen on the surface of the catalysts and would cause long induction periods.

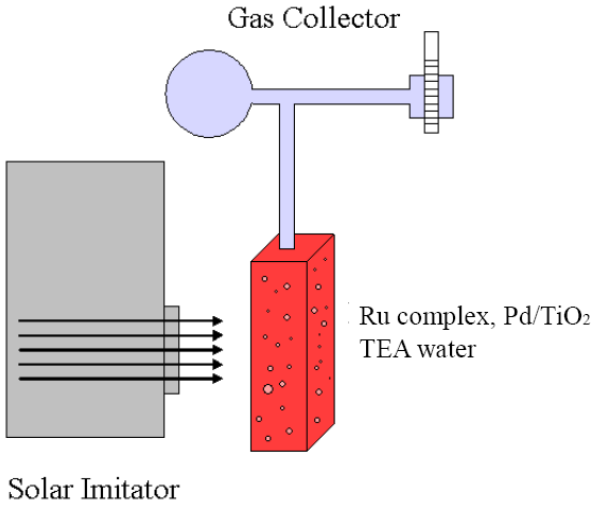

Figure 2.26: Apparatus setup for the generation of hydrogen and methane

UV/Vis light (mercury pressure lamp, 150 W, Philips) was continuously shined on the glass cuvette containing the catalytic mixture, while the mixture was stirred by means of a magnetic stirrer. Very small gas bubbles were observed after 40 minutes in the catalytic solution, which contained the Pd/TiO_2 catalyst. Gas bubbling was not observed in the solution with Ru/TiO_2, even after one hour of irradiation.

Gas samples were taken out by a Hamilton syringe at different time intervals and analyzed by Gas Chramatography (GOW-MAC, Series 580). A typical GC trace obtained for the mixture with Pd/TiO_2 after one hour of continuous irradiation is shown in Figure 2.27. Three peaks appear in the GC spectrum, and the peaks were identified as H_2, O_2 and N_2 by using their retention times. With the increase of the irradiation time the amounts of H_2 and O_2 produced increased.

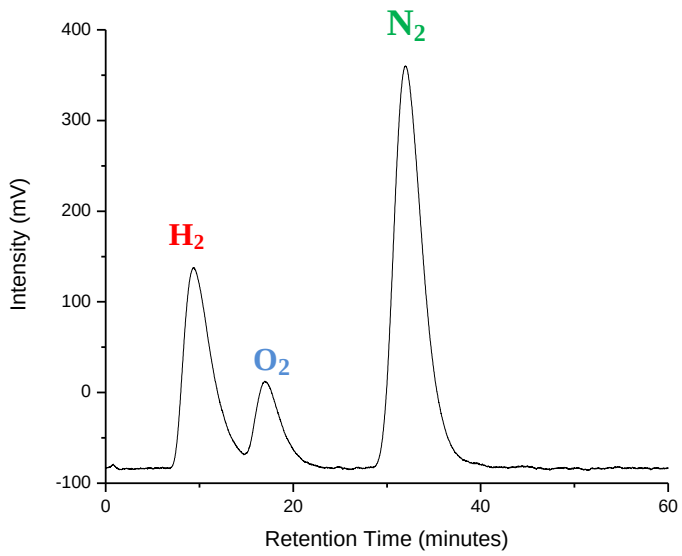

Figure 2.27: Gas Chromatography spectrum of photocatalytic reduction of water

Next, a set of experiments was carried out by using the same catalytic mixtures and measure the hydrogen production at different time intervals. These experiments were performed at the University of Karlsruhe, Germany. The results were plotted in Figure 2.28. Another experiment was carried out by using a catalytic solution which contains ruthenium(II)bipyridine and Pd/TiO_2 . The amount of hydrogen produce with the time is plotted in the same graph (Figure 2.28). Mercury pressure lamp (150W, Philips) and catalytic mixtures prepared in the Table 2.3 were used for all the experiments. The temperature of the reaction vessel was 293K.

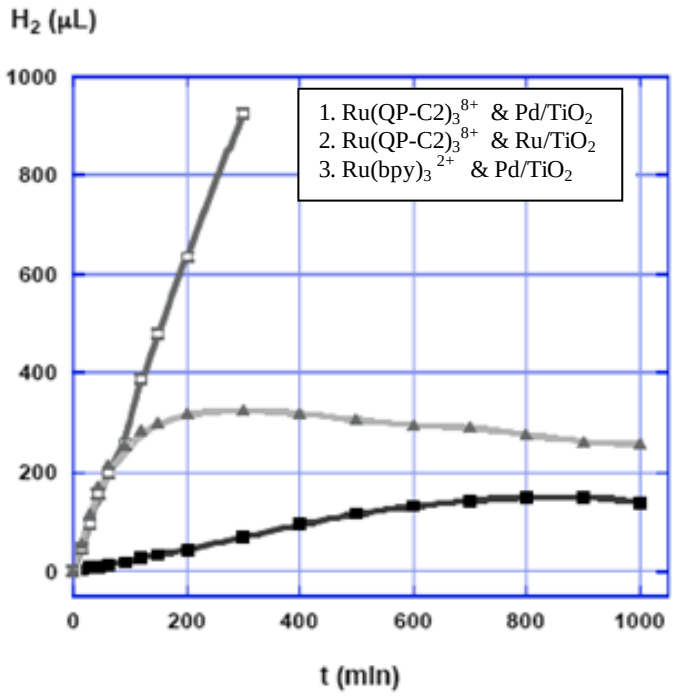

Figure 2.28: Amount of hydrogen produced by different sensitizers and different catalytic systems

Figure 2.28 clearly shows that there is a considerable difference in the production of hydrogen depending on the sensitizer and the catalytic mixture. $Ru(QP\text{-}C2)_3^{8+}$ (sensitizer) and Pd/TiO_2 catalytic mixture produce the hydrogen with highest efficiency. The experiment with the $Ru(QP\text{-}C2)_3^{8+}$ and Ru/TiO_2 starts releasing the hydrogen with the same efficiency as $Ru(QP\text{-}C2)_3^{8+}$ and Pd/TiO_2 catalytic mixture. About 100 minutes after starting the experiment hydrogen production was decreased in the catalytic mixture which consist of $Ru(QP\text{-}C2)_3^{8+}$ and Ru/TiO_2. The reason for this finding is most likely hydrogenation of the viologen units at the noble metal particles' surface of the catalysts. The catalytic mixture with the ruthenium(II)bypyridine and Pd/TiO_2 produced a considerably lower amount of hydrogen compared to the other two catalytic mixtures. That could be due to the lower excited state life time of the ruthenium(II)bypyridine and/or the lack efficient electron carrier (electron relay) in the catalytic system. According to the results (Figure 2.28) the catalytic mixtures, which contain $Ru(QP\text{-}C2)_3^{8+}$ and Pd/TiO_2, can be considered as the best catalytic system investigated to produce hydrogen with the highest efficiency.

Another set of experiments were carried out to produce CH_4 and other lower hydrocarbons by reducing the CO_2 using artificial photosynthesis (These experiments were performed at the University of Karlsruhe, Germany). Same experimental setup (Figure 2.26) was used as the production of hydrogen and oxygen by splitting water. Methane production was measured in four different catalytic systems. The compositions of the catalytic mixtures are given in Table 2.4. First, 50 ml of catalytic solution (Table 2.4) was poured inside the photochemical reactor. Then the reactor was sealed with a rubber septum. Then the gas collector was degassed and filled with CO_2 to make sure there is no oxygen and other gases left in the gas collector. Degassing was performed another two times. Then the reactor was filled with CO_2 to make sure there is no O_2 left in the system and only CO_2 gas was present inside the gas collector.

Table 2.5: Composition of catalytic mixtures used in photocatalytic generation of methane

Components	*1*	*2*	*3*	*4*
$Ru(QP\text{-}C2)_3^{8+}$ (3 x 10^{-3} M)	12 ml	12 ml	-	-
$Ru(bpy)_3^{2+}$ (3 x 10^{-3} M)	-	-	12 ml	-
$Ru(tepy)_3^{2+}$ (3 x 10^{-3} M)	-	-	-	12 ml
Pd/TiO_2	100 mg	-	100 mg	100 mg
Ru/TiO_2	-	100 mg	-	-
Triethanolamine (TEA)	2.5 ml	2.5 ml	2.5 ml	2.5 ml
Water	35.5 ml	35.5 ml	35.5 ml	35.5 ml

UV/Vis light (mercury pressure lamp, 150 W, Philips) was continuously shined on the glass cuvette containing the catalytic mixture, while the mixture was stirred vigorously by means of a magnetic stirrer. Gas was collected from the gas collector at different time intervals and analyzed by gas chromatography. The amounts of methane produced in different catalytic systems at different times are plotted in Figure 2.29. The catalytic system, which consists of $Ru(QP\text{-}C2)_3^{8+}$ and Pd/TiO_2 showed again the highest efficiency in the production of methane. But the production of methane was extremely low compared to the production of hydrogen. The

catalytic system with $Ru(QP\text{-}C2)_3^{8+}$ and Ru/TiO_2 showed a better efficiency than the system with Pd/TiO_2 at the initial 400 minutes. But the efficiency of the catalytic system decreased with the time.

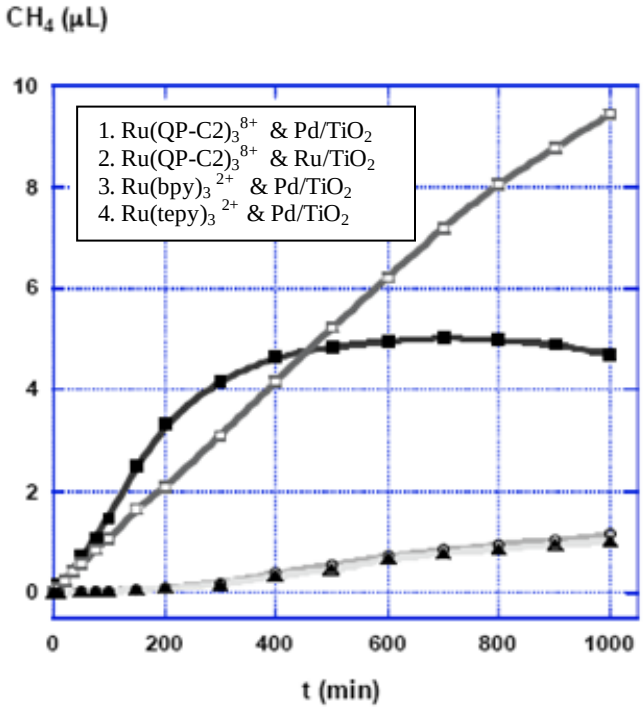

Figure 2.29 : Amount of methane produced by different sensitizers and different catalytic systems

The catalytic mixtures number 3 and 4, which consisted of ruthenium(II)bypyridine and ruthenium(II) tetrapyridine as sensitizers showed very low efficiencies. That could be mainly due to the lack of efficient electron transfer. The catalytic mixtures 3 and 4 have acted almost identical in their methane production. According to the results, the catalytic mixture containing $Ru(QP\text{-}C2)_3^{8+}$ and Pd/TiO_2 can be considered as the best photocatalytic mixture for the reduction of water and carbon dioxide to hydrogen and methane, respectively.

2.4 Stepwise Cathode Assembly

These photocatalytic systems were investigated further to avoid the use of the sacrificial donor (triethanolamine). As the first step in the catalytic cycle, electrons are needed to reduce the sensitizer relay assemblies (+ 8 charged ruthenium complex). These electrons were provided by the triethanolamine, which acts as the sacrificial donor in the generation of hydrogen. The use of indium tin oxide cathodes can provide the electrons necessary for the reduction of sensitizer relay assemblies. This can substitute the use of triethanolamine. Inspired by nature, multilayer architectures of ruthenium complex on ITO electrode were investigated to achieve the production of hydrogen more efficiently without consuming any sacrificial donor.

Ruthenium complex ($Ru(QP\text{-}C2)_3^{8+}$) should be coated on the ITO surface to create an ITO cathode, but these ruthenium complexes are very water soluble, and therefore, the $Ru(QP\text{-}C2)_3^{8+}$ coat is washed away with water. Consequently, two novel +8 charged phosphonate-tethred-ruthenium(II) quaterpyridinium complexes were synthesized. Phosphonate groups in these complexes anchor strongly to the surface of the ITO electrodes. Therefore, these complexes can form a coat on the ITO electrodes, which does not wash out with water. [43,44]

The synthesis of phosphonate-tethered ruthenium(II)quaterpyridinium complexes (Figure 2.30) can be started from tris(4,4':2',2":4",4"'-quaterpyridine-N',N")ruthenium(II) dichloride (2). First, compound 2 was reacted with dibromoalkanes (1,2 and 1,3) by means of the high pressure reaction method. The reactants were reacted at 80 ^{0}C and 800 psi for 17 hours; NMR and MS data provides evidence for the quaternization of sp^2 nitrogen on quaterpyridine. This high pressure reaction pathway provides yields between 70 - 75% for the synthesis of complexes with non polar alkyl substituent with terminal bromine. Next, the Michael-Arbusov reaction[45] was used to attach phosphonate esters to the compound 36 & 37 by substituting the terminal bromine (the high pressure reactor was used again, PARR 5500 series compact reactor). Finally, the phosphonate ester was hydrolyzed by 1M HCl. Purification of phosphonate-tethered ruthenium(II)quaterpyridinium complexes was done by ion exchange chromatography.

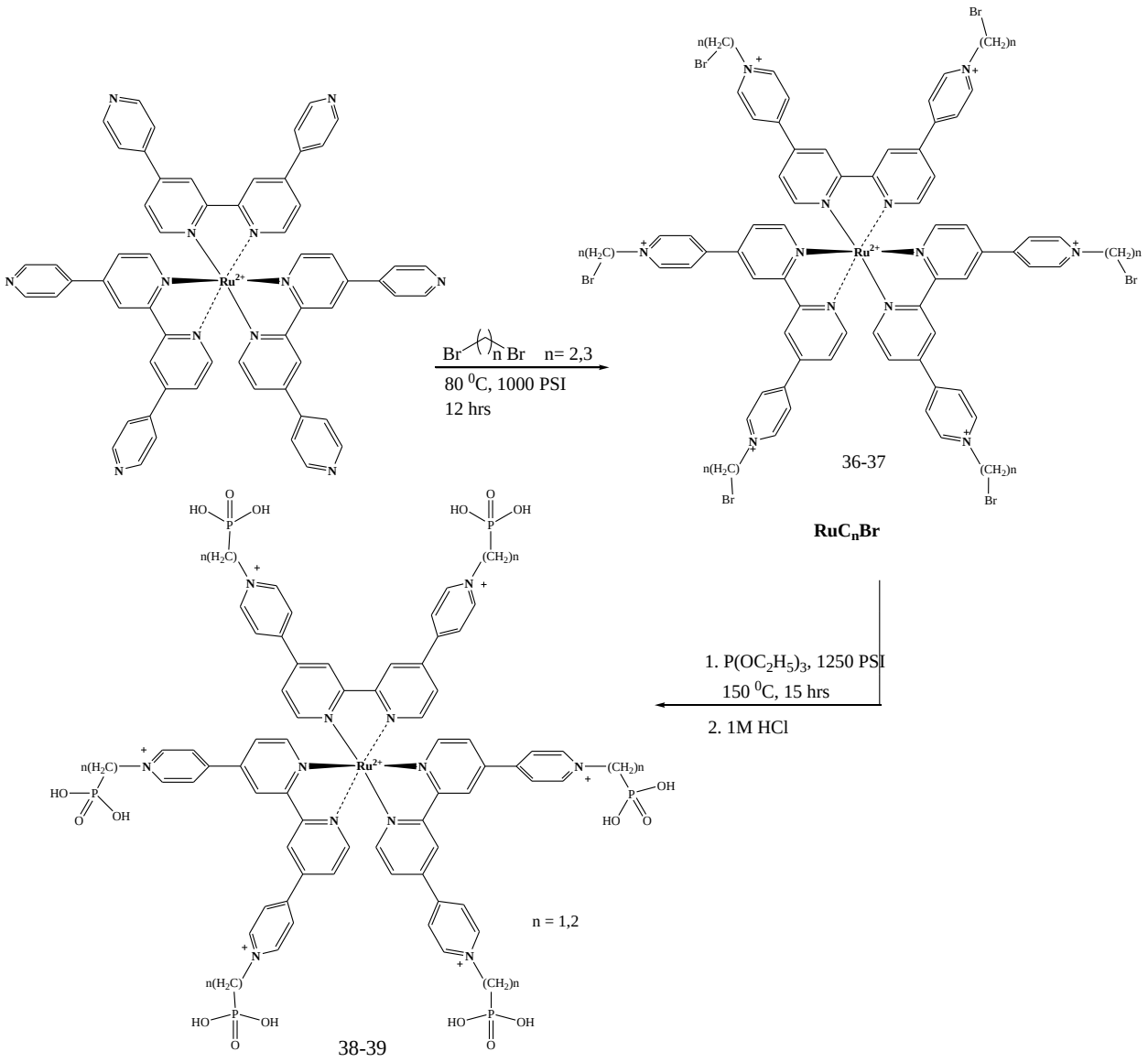

Figure 2.30: Synthesis of phosphonate-tethered ruthenium(II)quaterpyridinium complexes

The 3D structures generated by Chemdraw 3D and the diameter of phosphonate-tethered ruthenium(II)quaterpyridinium complexes, which are calculated using the MM2 calculations, are given in Table 2.6.

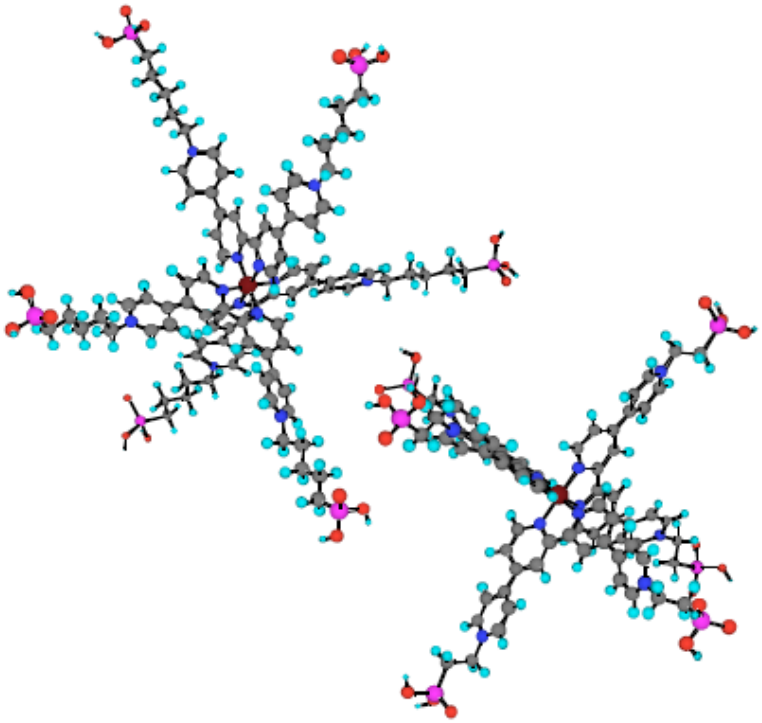

Complexes	*-$(CH_2)_n$-*	*Diameter [nm]*
$Ru(QP\text{-}P_2)_3^{8+}$	2	2.73
$Ru(QP\text{-}P_3)_3^{8+}$	3	3.05

Table 2.6: Diameters of phosphonate-tethered ruthenium(II)quaterpyridinium complexes

A procedure, which has been published by Schwartz *et. al.* [46] was used to create a dense layer of phosphonate-tethered ruthenium(II)quaterpyridinium complexes on ITO electrodes (Figure 2.31). Surface roughness of the ITO electrodes (Colorado concept coating, 10-15 Ωcm^{-1}) is between orders of two to five. First, these electrodes were cut into pieces of the size of 1 cm x 1cm. A series of steps were used to clean the ITO electrodes to make sure that ITO electrode surface does not have any organic material left. Briefly, the ITO electrodes were sonicated with soap water for 10 minutes and washed with water. Next, the ITO electrodes were sonicated in acetone solution for 10 minutes. Finally, ITO electrodes were dried in the oven and stored in a desiccator. In the next step, complexes were bound into ITO surface by using terminal phosphate groups of phosphonate-tethered ruthenium(II) quaterpyridinium complexes.[39,42]

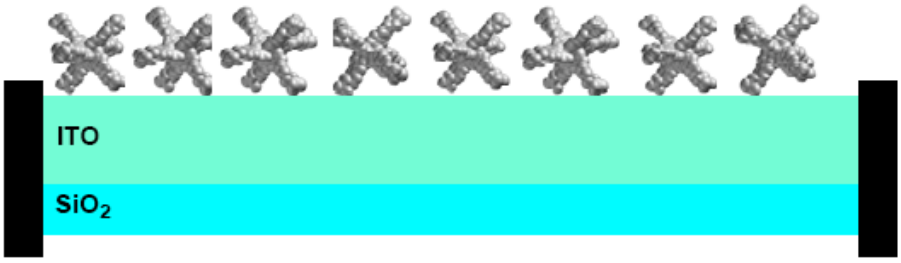

Figure 2.31: Cross section of a phosphonate-tethered ruthenium(II)quaterpyridinium complex coated ITO electrode

First, $1x10^{-6}$M solution of phosphonate-tethered ruthenium(II)quaterpyridinium complexes was spin coated on the cleaned ITO electrode. Then the spin coated electrode was dried in the oven for 48 hours at 120 ^{0}C. The ruthenium complex coated electrode was washed with water to make sure that the complex does not wash away with water. Atomic Force Microscopy (SPM 2000, Agilent) images of the ITO electrodes with (Figure 2.32) and without (Figure 2.33) the ruthenium complex coating were taken and analyzed.

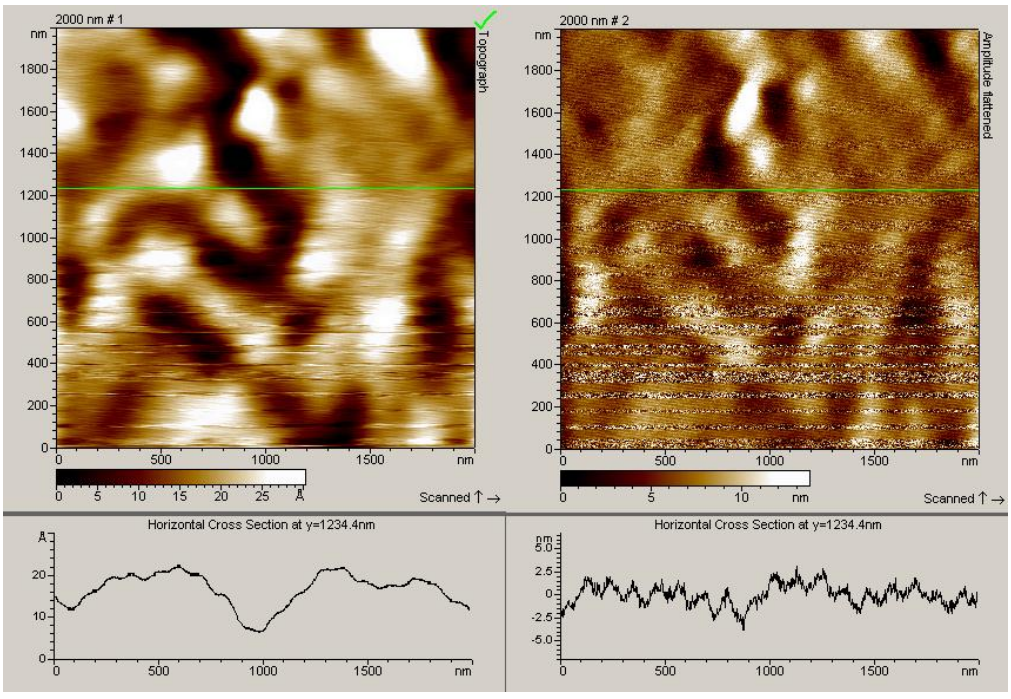

Figure 2.32**:** AFM image of ITO electrode surface

Figure 2.32 shows an AFM (SPM 2000, Agilent, Magnetic AC mode) image of the cleaned ITO electrode surface. The left hand side image shows the actual topology of the surface and the right hand side image shows the phase image. Changes in the phase of oscillations can be used to discriminate between materials, possessing different viscoelastic properties. These AFM images show that the ITO surface is not completely flat. Figure 2.28 shows an AFM (SPM 2000, Agilent, Magnetic AC mode) image of an ITO electrode which is coated with phosphonate-tethered ruthenium(II)quaterpyridinium complexes. Nanoparticles coated on the ITO surface can be clearly observed in the AFM image (2.33). This confirms that the ruthenium(II) complexes with phosphate terminal groups can anchor strongly into the surface of ITO electrodes.

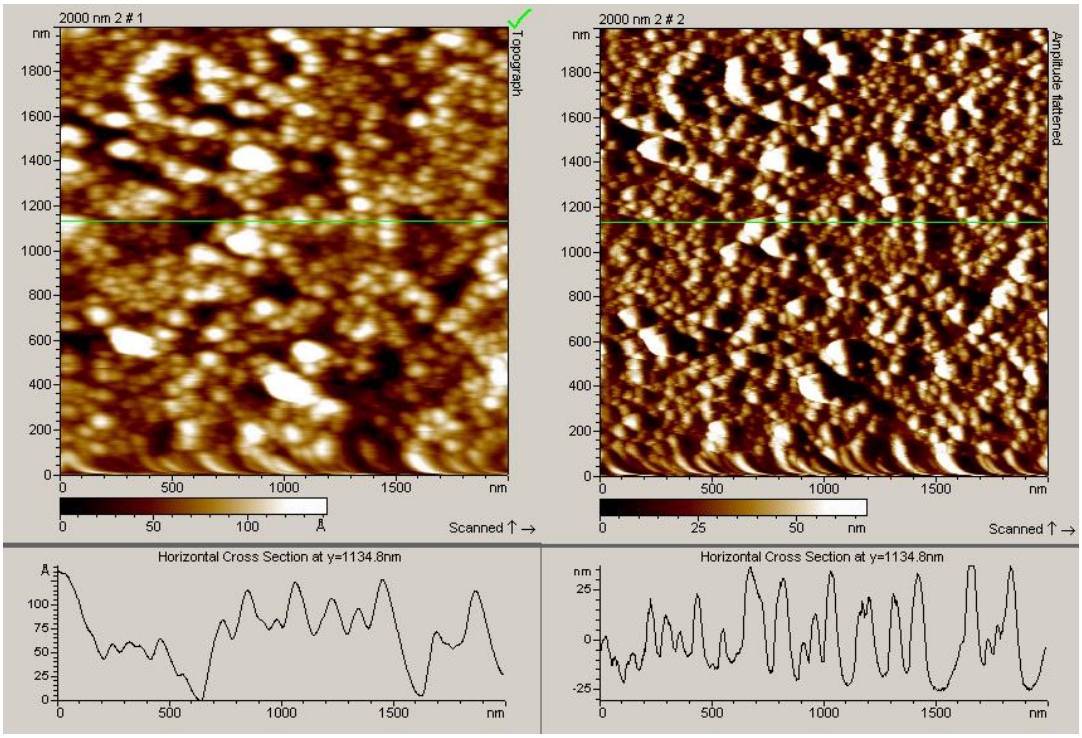

Figure 2.33: AFM image of the phosphonate-tethered ruthenium(II)quaterpyridinium complex-coated ITO electrode

Another set of DPV experiments were carried out to confirm the binding of the phosphonated ruthenium complexes to the ITO electrode surface. Parameters used in the DPV experiment are given in Table 2.7.

Table 2.7: Parameters used for DPV experiments

Parameter	*Value*
Initial E (V)	**0.2**
Final E (V)	**-1.3**
Increase E (V)	**0.005**
Amplitude (V)	**0.05**
Pulse Width (sec)	**0.025**
Sampling Width (sec)	**0.0167**
Pulse Period (sec)	**1**
Quite Time (sec)	**30**
Sensitivity (A/V)	**1×10^{-4}**

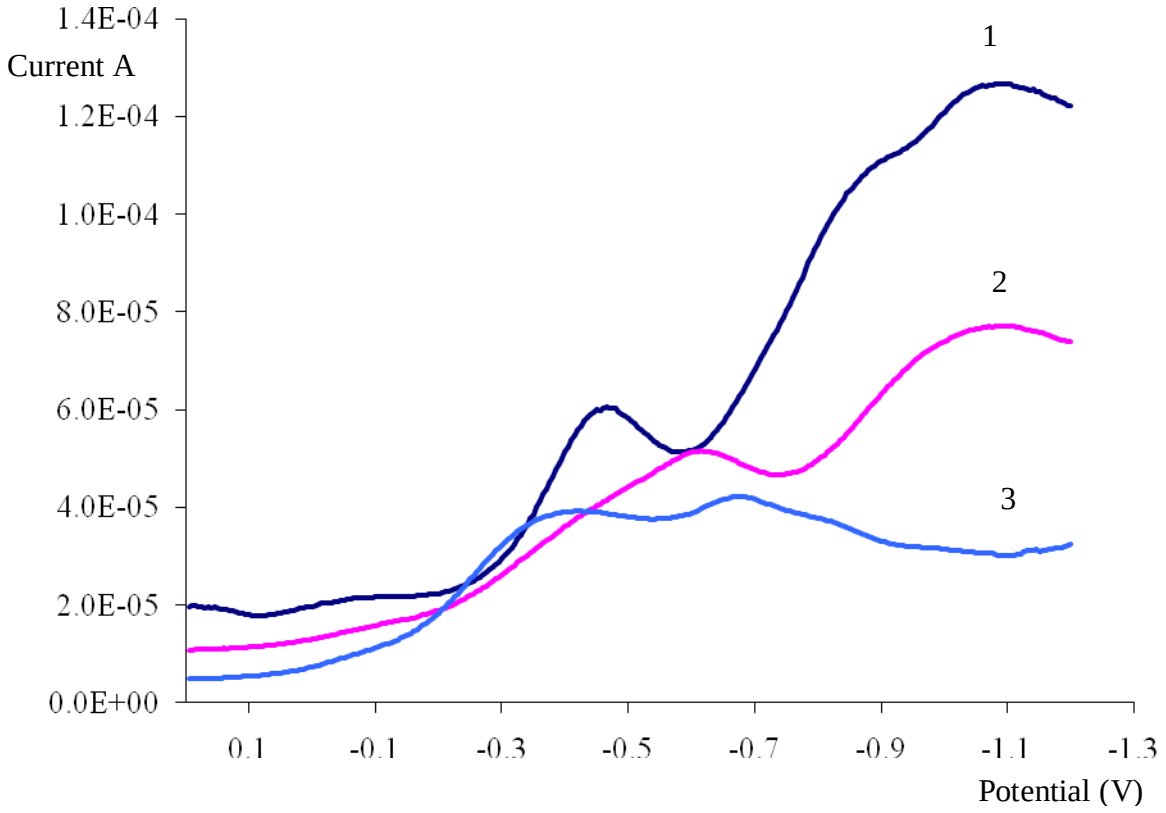

Figure 2.34: DPV curves of three different experiments. (dark blue- $Ru(QP\text{-}C2)_3^{8+}$ in solution, light purple- RuC2PO4 coated ITO, light blue- $Ru(QP\text{-}C2)_3^{8+}$ coated ITO)

Figure 2.34 shows the DPV curves in three different experiments. The dark blue line (1) represents the DPV curve of the 1 x 10^{-5} mol/l $Ru(QP\text{-}C2)_3^{8+}$ solution. This curve shows the Ru^{II} to Ru^{I} reduction peak around -1.10 V. Light blue line (3) represents the ITO electrode which is spin coated (3000 rpm, 30 sec) with 1 x 10^{-3} mol/ l $Ru(QP\text{-}C2)_3^{8+}$. This ITO electrode was dried in the oven for 48 hour (120 ^{0}C), and washed with water. The light blue curve does not have the characteristic Ru^{II} to Ru^{I} reduction peak. This means that the ITO electrode is not coated with ruthenium complexes on its surface. A major fraction of the spin-coated ruthenium complex was washed away with water. The light purple curve (2) represents the ITO electrode which was spin coated (3000 rpm, 30 sec) with 1 x10^{-3}mol/l phosphonate-tethered ruthenium(II) quaterpyridinium complex solution. This electrode was dried in the oven for 48 hours at 120 ^{0}C and washed with water prior to the DPV experiment. This ITO electrode shows the characteristic ruthenium peak around -1.10V. This confirms that phosphonate-tethered ruthenium(II) quaterpyridinium complexes are anchored strongly to the ITO electrode surface, and the coating has not been washed away with water (a major fraction remains on the surface).

In the next step, a layer of Pd/ TiO_2 catalyst was added on top of the ITO with a coat of phosphonate-tethered ruthenium(II)quaterpyridinium complex (Figure 2.35). A slurry was prepared by mixing the Pd/ TiO_2 with water and spin coated (3000 rpm, 30 sec) on the ruthenium complex coated ITO. The ITO electrodes were dried in the oven at 120 ^{0}C for 48 hours. Unbound terminal phosphate groups facilitate the binding of TiO_2 nanoparticles into the ruthenium complex coating.[38,39]

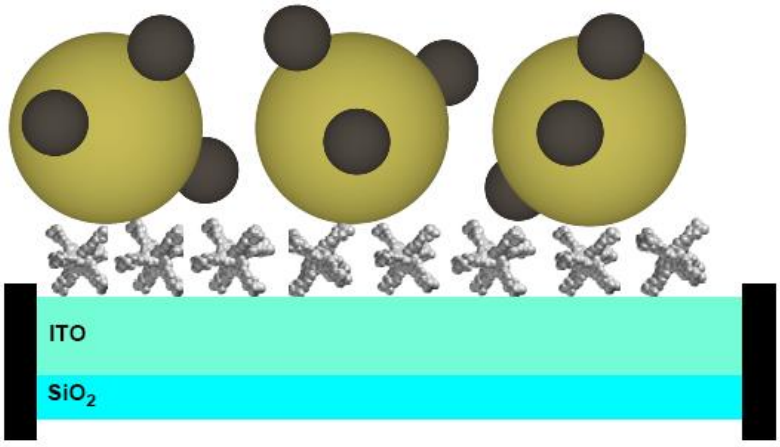

Figure 2.35: Cross section of Pd/ TiO_2 and phosphonate-tethered ruthenium(II)quaterpyridinium complex coated ITO electrode

Figure 3.36 is a schematic diagram which shows an application of another phosphonate-tethered ruthenium(II)quaterpyridinium complex layer on top of the Pd/ TiO_2 nanoparticle layer. A solution of phosphonate-tethered ruthenium(II)quaterpyridinium ($1x10^{-3}$M) was spin-coated (3000 rpm, 30 sec) on ITO, which already has two layers of phosphonate-tethered ruthenium(II)quaterpyridinium complex and Pd/ TiO_2 catalyst. The ITO electrode was dried in the oven for 24 hours (120 ^{0}C) to facilitate the binding of phosphate groups on to the surface of TiO_2 nano particles.[39,42] Afterwards, the ITO surface was washed with water to remove the non bonded ruthenium complex from the ITO surface.

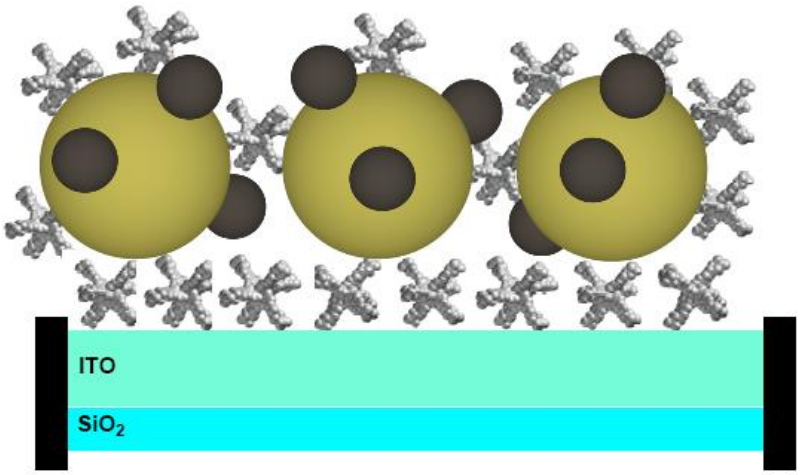

Figure 2.36: Cross section of Pd/ TiO_2 and two layers of phosphonate-tethered ruthenium(II) quaterpyridinium complex coated ITO electrode

Finally, the resulting electrode's surface properties were analyzed by the atomic force microscopy (Digital Instruments 2000, contact mode). Figure 2.37 shows the AFM image of the ITO electrode which is depicted in Figure 2.35. Large nano particles on the surface can be clearly visualized with comparable to the size of ruthenium complex which appeared in the AFM image in Figure 2.33. Figure 2.38 shows the AFM image (Digital Instruments 2000, contact mode) of the surface of ITO electrode which is depicted in Figure 2.36. We observed small particles which surrounds larger TiO_2 nanoparticles.

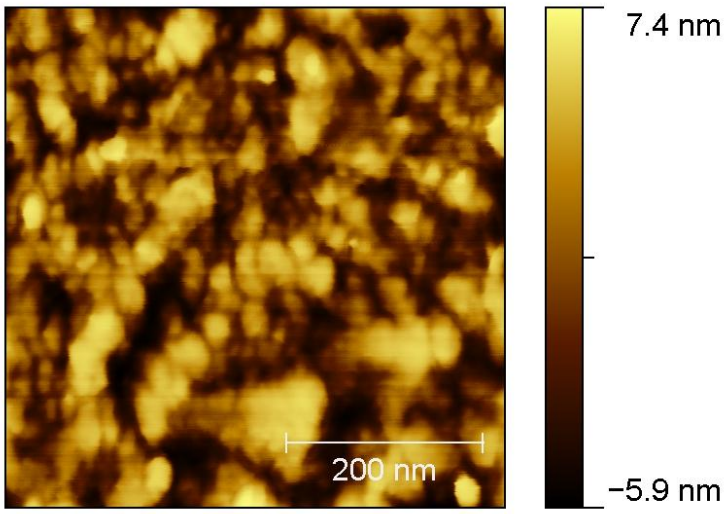

Figure 2.37: AFM image of the Pd/ TiO_2 catalyst on the ruthemium complex coated ITO

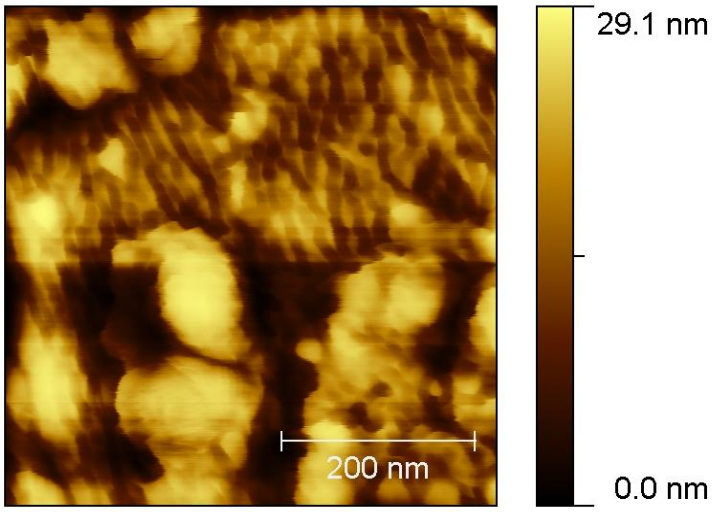

Figure 2.38: AFM image of the surface of ITO after the application of another ruthenium complex on the Pd/ TiO2 catalyst

Figure 2.39 shows a schematic diagram of the proposed photochemical cell for the generation of hydrogen or methane by solar energy. Pt electrode is proposed to use as the anode where the oxidation of water will take place to produce oxygen gas and protons.[47] The produced protons will diffuse to the side of the cathode through Nafion type membrane.[48]

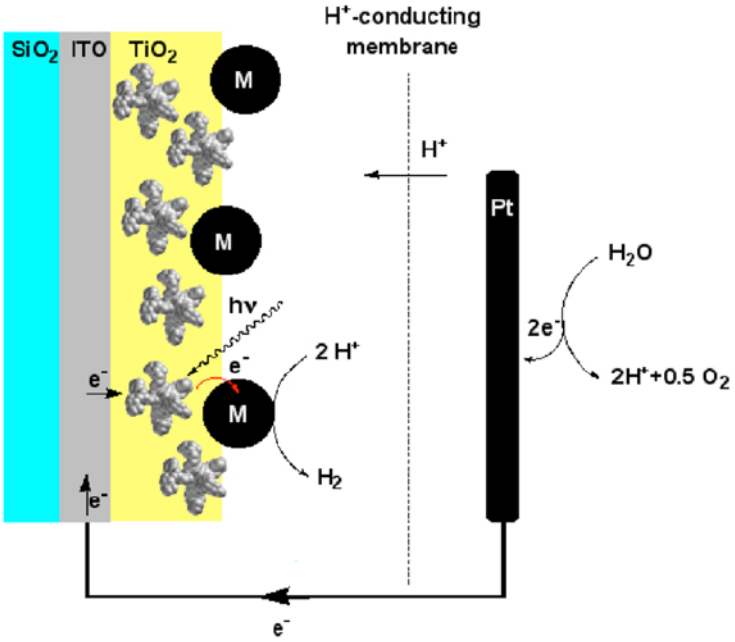

Figure 2.39: Schematic diagram of the proposed photochemical cell

When ruthenium(II)-quaterpyridinium complex is irradiated with the visible light it will excite to $Ru^{(II)*}$. The $Ru^{(II)*}$ will reduce to Ru(I) by taking an electron from the ITO electrode, which has its redox potential around -0.55 +/- 0.05 V. This $Ru^{(I)}$ complex act as an electron relay and transfer one electron to the redox catalyst (Pd or Ru) via the conduction band of TiO_2 and oxidized back to the ruthenium(II) complex. The redox catalysts keep the electrons and use them in two or eight electron reductions to generate hydrogen or methane.

2.6 Experimental Section

Ruthenium(II)C2 phosphonate

A mixture of compound 2 (0.33g) and 1,2-dibromoethane (1.70g, 1:30) was dissolved in MeOH (30ml). The mixture was stirred under N_2 at 800 psi (PARR 5500 series compact reactor) for 17 hours at 80 ^{0}C in high-pressure reactor. The solvent was removed by rotary evaporator. The dark red residue was washed with acetone (15 ml x 3) to remove unreacted organic materials. The product was dried in high vacuum for 24 hours. Dark red crystals were obtained.Yield 350 mg (69 %).

Compound 36 (100 mg) and triethyl phosphonate (1.26 g) were dissolved in 30 ml of MeOH. The mixture was stirred for 15 hours at 150 ^{0}C/ 1250 PSI in a high-pressure reactor (PARR 5500 series compact reactor). The solvent was removed by a rotary evaporator and a viscous liquid was obtained. The viscous liquid was dissolved in 1M HCl (50ml) and stirred for 3 days. The solvent was evaporated and the residue was dried in high vacuum for 48 hours. A dark red viscous liquid was obtained. Tris-homoleptic ruthenium(II) phosphonate complexes were purified by anion exchange chromatography on Dowex-50. Yield 105 mg (93 %)

^{1}H (DMSO-d6, 400 MHz) δ 3.21 (12H), 4.29 (12H), 8.23 (12H), 8.93 (6H), 8.98 (6H), 9.46 (6H), 10.08 (12H). ^{13}C (DMSO-d6, 400 MHz) δ 46.96, 61.96, 122.16, 125.36, 125.84, 142.48, 144.42, 145.68, 147.68, 149.04, 160.08.

Ruthenium(II)C3 phosphonate

A mixture of compound 2 (0.33g) and 1,3-dibromopropane (1.90g, 1:30) was dissolved in MeOH (30ml). The mixture was stirred under N_2 at 800 psi pressure (PARR 5500 series compact reactor) for 17 hours at 80 ^{0}C in a high pressure reactor. The solvent was removed in a rotary evaporator. A dark red residue was washed with acetone (15 ml x 3) to remove unreacted organic materials. The product was dried in high vacuum for 24 hours. Dark red crystals were obtained.
Yield 375 mg (71%).

Compound 37 (200 mg) and triethyl phosphonate (1.8 g) were dissolved in 30 ml of MeOH. Mixture was stirred for 15 hours at 150 ^{0}C/ 1250 PSI in a high pressure reactor(PARR 5500 series compact reactor). The solvent was removed in a rotary evaporator and a viscous liquid was obtained. The viscous liquid was dissolved in 1M HCl (50ml) and stirred for 3 days. The solvent was evaporated and the residue was dried in high vacuum for 48 hours. A dark red

viscous liquid was obtained. Tris-homoleptic ruthenium(II) phosphonate complexes were purified by anion exchange chromatography on Dowex-50. Yield 203 mg (91%).
^{1}H (DMSO-d6, 400 MHz) δ 1.86 (12H), 3.32 (12H), 4.36 (12H), 8.19 (12H), 8.97 (6H), 9.05 (6H), 9.47 (6H), 10.06 (12H). ^{13}C(DMSO-d6, 400 MHz) δ 21.76, 44.16, 61.92, 121,12, 123.36, 124.24, 141.76, 143.92, 148.32, 161.56

Preparation of Pd/ TiO_2 Catalyst

A mixture of TiO_2 (300 mg), $PdCl_2$ (30 mg) and citric acid (1.5 g) was suspended in 40 ml of water. The mixture was stirred at 60 ^{0}C for 18 hours, light yellow turbidity was obtained. Suspension was sonicated for two minutes. The residue was separated by centrifugation (10000 g, 45 minutes, RT, Legend T+/RT+). The residue was washed with water (15 ml x 2) to remove the citric acid, the supernatant was separated by centrifugation (1000 g, 45 min, RT). A pale white powder was obtained after drying the product in an oven.

Preparation of Ru/TiO_2 Catalyst

A mixture of TiO_2 (1 g), $RuCl_3$ (100 mg) and citric acid (4.5 g) was suspended in 80 ml of water. Mixture was stirred at 60 ^{0}C for 18 hours, a light yellow turbidity was obtained. The suspension was sonicated for two minutes. The residue was separated by centrifugation (10000 g, 45 minutes, RT, Legend T+/RT+). The residue was washed with water (15 ml x 2) to remove the citric acid; the supernatant was separated by centrifugation (1000 g, 45 min, RT). An ash colored powder was obtained after drying the residue in oven for 24 hours.

2.7 Conclusions

Ruthenium (II)quaterpyridinium complexes with +8 charge were successfully utilized as effective sensitizer-relay-assemblies for the photocatalytic generation of hydrogen and methane by reducing water and carbon dioxide. Pd coated TiO_2 nanoparticles has been used as very effective catalysts for the electron storage and utilize them in the multi electron reduction reactions. Newly synthesized phosphonate-tethered ruthenium(II)quaterpyridinium complex have anchored strongly on the ITO electrode surface. That has confirmed by our DPV and AFM experiments. These phosphonate-tethered ruthenium(II)quaterpyridinium complexes are more

promising to fabricate multi layer electrodes which has higher potential to generate hydrogen and methane in large scale without sacrificing the sacrificial donor.

2.8 References

[1] United Nations Population Division, The world at six billion report (Available at : www.un.org/esa/population/publications/sixbillion/sixbilpart1.pdf , December 2006)

[2] World Energy and Economic Outlook, Energy Informaiton Administration International Energy Outlook (2006), 1:7.

[3] Thomson, Allison M.; Rosenberg, Norman J.; Izaurralde, R. Cesar; Brown, Robert A., Climate Change Impacts for the Conterminous USA: An Integrated Assessment, *Climatic Change* (2005), 69(1), 89-105.

[4] www.hydrogencarsnow.com

[5] Turner, John; Sverdrup, George; Mann, Margaret K.; Maness, Pin-Ching; Kroposki, Ben; Ghirardi, Maria; Evans, Robert J.; Blake, Dan, Renewable hydrogen production, *International Journal of Energy Research*, (2008), 32(5), 379-407.

[6] US Department of Energy, office of Energy Efficincy and Renewable Energy, Washington DC, (Available at www.eere.energy.gov/hydrogenandfuelcells/mypp/pdfs/production.pdf , February (2007).

[7] Levene J.; Ramsden T., Summary of Electrolytic Hydrogen Production, National Renewable Energy Laboratory: Golden, CO, MP-560-41099, (2007).

[8] Milne T. A; Elam C. C; Evans R. J., Hydrogen from biomass, State of the art and challenges, IEA/H2/TR-02/001, (2002).

[9] Gray, Clarke T.; Gest, Howard, Biological formation of molecular hydrogen, *Science* (Washington, DC, United States), (1965), 148(3667), 186-92.

[10] Saint-Amans, Sylvie; Girbal, Laurence; Andrade, Jose; Ahrens, Kerstin; Soucaille, Philippe, Regulation of carbon and electron flow in Clostridium butyricum VPI 3266 grown on glucose-glycerol mixtures, *Journal of Bacteriology*, (2001), 183(5), 1748-1754.

[11] Demain AL, Newcomb M, Wu JHD. Cellulase, clostridia, and ethanol, Microbiology *and Molecular Biology Reviews*, (2005), 69, 124–154.

[12] Datar, Rohit; Huang, Jie; Maness, Pin-Ching; Mohagheghi, Ali; Czernik, Stefan; Chornet, Esteban, Hydrogen production from the fermentation of corn stover biomass pretreated with a steam-explosion process, *International Journal of Hydrogen Energy*, (2007), 32(8), 932-939.

[13] Kadar, Zsofia; De Vrije, Truus; Budde, Miriam A. W.; Szengyel, Zsolt; Reczey, Kati; Claassen, Pieternel A. M., Hydrogen production from paper sludge hydrolysate, *Applied Biochemistry and Biotechnology*, (2003), 105-108 557-566.

[14] (a)Fletcher E. A., Solarthermal processing: a review, *Journal of Solar Energy Engineering*, (2001), 123, 63–74.

[15] J. E., Thermochemical production of hydrogen via multistage water splitting processes, *International Journal of Hydrogen Energy*, (1976), 1, 33–43.

[16] www.curvebank.calstatela.edu/arearev/arearev.htm

[17] Fujishima A.; Honda K., Electrochemical photolysis of water at a semiconductor electrode, *Nature*, (1972), 238(5358), 37-8.

[18] Anpo, Masakazu; Takeuchi, Masato, The design and development of highly reactive titanium oxide photocatalysts operating under visible light irradiation, *Journal of Catalysis*, (2003), 216(1-2), 505-516.

[19] Furube, Akihiro; Asahi, Tsuyoshi; Masuhara, Hiroshi; Yamashita, Hiromi; Anpo, Masakazu, Direct observation of interfacial hole transfer from a photoexcited TiO_2 particle to an adsorbed molecule SCN- by femtosecond diffuse reflectance spectroscopy, *Research on Chemical Intermediates*, (2001), 27(1-2), 177-187.

[20] Furube, Akihiro; Asahi, Tsuyoshi; Masuhara, Hiroshi; Yamashita, Hiromi; Anpo, Masakazu, Charge Carrier Dynamics of Standard TiO_2 Catalysts Revealed by Femtosecond Diffuse Reflectance Spectroscopy, *Journal of Physical Chemistry B* (1999), 103(16), 3120-3127.

[21] Duerr, H.; Bossmann, S.; Kilburg, H.; Trierweiler, H. P.; Schwarz, R., Supramolecular sensitizers and sensitizer / relay assemblies, A novel approach to electron transfer reactions. *Front. Supramol. Org. Chem. Photochem.*, (1991), 453-76.

[22] Voet, D.; Voet, J.G., Biochemistry, John Wiley & Sons: New York, (1995), 1361.

[23] Barber, J.; Anderson, B., Revealing the blueprint of photosynthesis, *Nature* (London, United Kingdom), (1994), 370(6484), 31-4.

[24] Schaller, Richard D.; Sykora, Milan; Pietryga, Jeffrey M.; Klimov, Victor I., Seven Excitons at a Cost of One: Redefining the Limits for Conversion Efficiency of Photons into Charge Carriers, *Nano Letters*, (2006), 6(3), 424-429.

[25] Ganopolski, Andrey, Anthropogenic global warming: evidence, predictions and consequences, *Advances in Solar Energy*, (2005), 16, 1-33.

[26] (a)Rau, Sven; Walther, Dirk; Vos, Johannes G., Inspired by nature: light driven organometallic catalysis by heterooligonuclear Ru(II) complexes, *Dalton Transactions*, (2007), (9), 915-919.
(b) Kobuke, Yoshiaki, Artificial light-harvesting systems by use of metal coordination, *European Journal of Inorganic Chemistry*, (2006), (12), 2333-2351.

[27] Houlding, Virginia; Geiger, Thomas; Koelle, Ulrich; Graetzel, Michael, Electrochemical and photochemical investigations of two novel electron relays for hydrogen generation from water, *Journal of the Chemical Society, Chemical Communications*, (1982), (12), 681-3.

[28] Kalyanasundaram, Kuppuswamy; Kiwi, John; Graetzel, Michael, Hydrogen evolution from water by visible light, a homogeneous three component test system for redox catalysis, *Helvetica Chimica Acta*, (1978), 61(7), 2720-30.

[29] Harriman, Anthony; Pickering, Ingrid J.; Thomas, John M.; Christensen, Paul A., Metal oxides as heterogeneous catalysts for oxygen evolution under photochemical conditions, *Journal of the Chemical Society, Faraday Transactions 1: Physical Chemistry in Condensed Phases* (1988), 84(8), 2795-806.

[30] Sayama, K.; Arakawa, H., Photocatalytic decomposition of water and photocatalytic reduction of carbon dioxide over zirconia catalyst, *Journal of Physical Chemistry*, (1993), 97(3), 531-3.

[31] Willner, Itamar; Maidan, Ruben; Mandler, Daphna; Duerr, Heinz; Doerr, Gisela; Zengerle, Klaus, Photosensitized reduction of carbon dioxide to methane and hydrogen evolution in the presence of ruthenium and osmium colloids: strategies to design selectivity of products distribution, *Journal of the American Chemical Society*, (1987), 109(20), 6080-6.

[32] Bossmann, S. H.; Dürr, H., *Artificial Photosynthesis*; Atwood, J.; Dekker Encyclopedias (Taylor & Francis Books): London, Atlanta, (2005), 1-11.

[33] Duerr, Heinz; Thiery, Urs; Infelta, P. P.; Braun, A. M., A sensitizer - relay assembly with improved properties in electron transfer processes, *New Journal of Chemistry*, (1989), 13(8-9), 575-7.

[34] Willner, Itamar; Maidan, Ruben; Mandler, Daphna; Duerr, Heinz; Doerr, Gisela; Zengerle, Klaus, Photosensitized reduction of carbon dioxide to methane and hydrogen evolution in the presence of ruthenium and osmium colloids: strategies to design selectivity of products distribution, *Journal of the American Chemical Society*, (1987), 109(20), 6080-6.

[35] Engman, Lars.; Lind, Johan.; Merenyi, Gabor. Redox Properties of Diaryl Chalcogenides and Their Oxides. *Journal of Physical Chemistry* (1994), 98(12), 3174-82.

[36]Duerr, H.; Bossmann, S.; Kilburg, H.; Trierweiler, H. P.; Schwarz, R., Supramolecular sensitizers and sensitizer / relay assemblies - A novel approach to electron transfer reactions, *Front. Supramol. Org. Chem. Photochem.*, (1991), 453-76.

[37] http://sel18.hut.fi/304/Valomylly/Image3.jpg

[38] Legeai, Sophie; Chatelut, Michelle; Vittori, Olivier, Differential pulse voltammetry at microdisk electrodes, *Electrochimica Acta*, (2005), 50(20), 4089-4096.

[39] Lever, A. B. P.; Ramaswamy, B. S.; Licoccia, S., Sensitized photoreduction of methyl viologen by metalloporphyrins, *Journal of Photochemistry*, (1982), 19(2), 173-82.

[40] Juris, A.; Balzani, V.; Barigelletti, F.; Campagna, S.; Belser, P.; Von Zelewsky, A., Ruthenium (II) polypyridine complexes : photophysics, photochemistry, electrochemistry, and chemiluminescence, *Coordination Chemistry Reviews* (1988), 84, 85-277.

[41] Repasky, M. P.; Chandrasekhar, J.; Lorgensen, W. L. PDDG/PM3 and PDDG/MNDO: Improved semiempirical methods., *Journal of Computational Chemistry* (2002), 23, 1601-1622

[42] Bossmann, Stefan; Duerr, Heinz; Mayer, Eduard., Novel biomimetic systems for visible light induced water reduction, Zeitschrift fuer Naturforschung, B: *Chemical Sciences*, (1993), 48(3), 369-86.

[43] Guo, J.; Koch, N.; Bernasek, S. L.; Schwartz, J., Enhanced hole injection in a polymer light emitting diode using a small molecule monolayer bound to the anode, *Chem. Phys. Lett*, (2006), 426, 370-373.

[44] McDowell, M.; Hill, I. G.; McDermott, J. E.; Bernasek, S. L.; Schwartz, J., Improved organic thin-film transistor performance using novel self-assembled monolayers, *Appl. Phys. Lett*, (2006), 88, 073505/1-073505/3.

[45] Saady, M.; Lebeau, L.; Mioskowski, C., Synthesis of di- and triphosphate ester analogs via a modified Michaelis-Arbuzov reaction, *Tetrahedron Letters*, (1995), 36, 5183-6.

[46] Hanson, Eric L.; Schwartz, Jeffrey; Nickel, Bert; Koch, Norbert; Danisman, Mehmet Fatih, Bonding Self - Assembled , Compact Organophosphonate Monolayers to the Native Oxide Surface of Silicon, *Journal of the American Chemical Society*, (2003), 125(51), 16074-16080.

[47] Rossmeisl, J.; Logadottir, A.; Norskov, J. K., Electrolysis of water on (oxidized) metal surfaces, *Chemical Physics*, (2005), 319(1-3), 178-184.

[48] Hickner, M. A.; Pivovar, B. S., The chemical and structural nature of proton exchange membrane fuel cell properties, *Fuel Cells (Weinheim, Germany)*, (2005), 5(2), 213-229.

CHAPTER 3 - DEVELOPING NEW STRATEGIES FOR THE TREATMENT OF TUBERCULOSIS EMPLOYING RUTHENIUM(II)QUATERPYRIDYL COMPLEXES

3.1 Introduction

Tuberculosis is, according to the World Health Organization[1], the most dangerous infectious disease, causing more deaths than any other single infection. This is a bacterial disease caused by *Mycobacterium tuberculosis*.[1] Approximately one third of the world's population is already infected. More than 4,000,000 new cases and more than 2,000,000 deaths have to be accounted for each year.[1] During the last two decades, multi-resistant strains have appeared due to the discontinuing treatment of tuberculosis in many countries, threatening all countries which experience immigration. Therefore, entirely new strategies are required to obtain the basic knowledge, which will then enable the successful development of new anti-TB-therapies. *Mycobacterium tuberculosis* possess an especially thick outer membrane (called "cell envelope"), which acts as a hydrophobic shield against antibiotics.[2] Channel proteins ("porins") form the main hydrophilic pathways through the cell envelope. The porin from *M. smegmatis* (MspA)[3] was employed as a model channel from a bacterium, which is closely related to *M. tuberculosis*, but non-pathogenic. MspA[3] can serve as an ideal host system for highly-charged ruthenium(II)-quaterpyridyl complexes, because it possesses 16 aspartates in its constriction-zone of the diameter of approximately 1 nm. This chapter reports luminescence and HPLC-studies comprising MspA[3] and four recently synthesized ruthenium(II)polypyridyl complexes.[4] The geometric dimensions of the ruthenium(II)quaterpyridinium complexes have been optimized to permit optimal binding within the inner pore of MspA. The biggest driving force for the observed binding is the charge attraction between the negatively charged inner pore of MspA and the positively charged Ru(II) complexes.

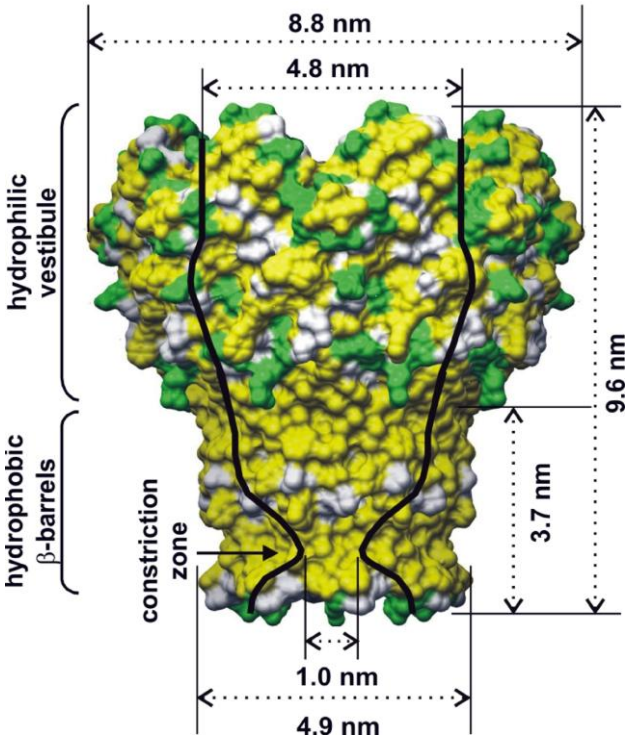

Figure 3.1: The structure of *MspA* (PDB-code 1UUN): yellow: hydrophobic amino acids; green: hydrophilic amino acids[3]

Proteins are macromolecules with dimensions in the nanometer range and can be tailored to specific needs by site-directed mutagenesis. However, their use in nanotechnology has been severely hampered by the problem that most proteins lose their structural integrity in a nonnative environment, impeding their use in technical processes.[5] The MspA is a porin protein which extracted from *M.smegmatis*.[3] MspA is an extremely stable protein, retaining its channel structure even after boiling in 3% SDS, heating to 100 ^{o}C or extraction with organic solvents.[2,6] A distinct advantage of MspA is its amphiphilic nature. Not only is the interior channel surface much more hydrophilic than its exterior, the exterior is subdivided in two distinct zones. MspA features a very hydrophobic "docking region" at the stem of its "goblet", whereas its "rim" section is formed by alternating hydrophilic and hydrophobic residues so that it is much more hydrophilic. The geometric dimensions of the "docking region" are 3.7 nm in length, and 4.9 nm in diameter.[2]

3.2 Experimental Methods

MspA was isolated in our laboratories using established procedures.[7,8] The ruthenium(II)-tris-(4,4',2',2'',4'',4'''quaterpyridinium) complexes are synthesized as described in the chapter one. Four different complexes with +8 charge were used in the experiments reported in this chapter. Those complexes and their abbreviations are depicted in Figure 3.2.

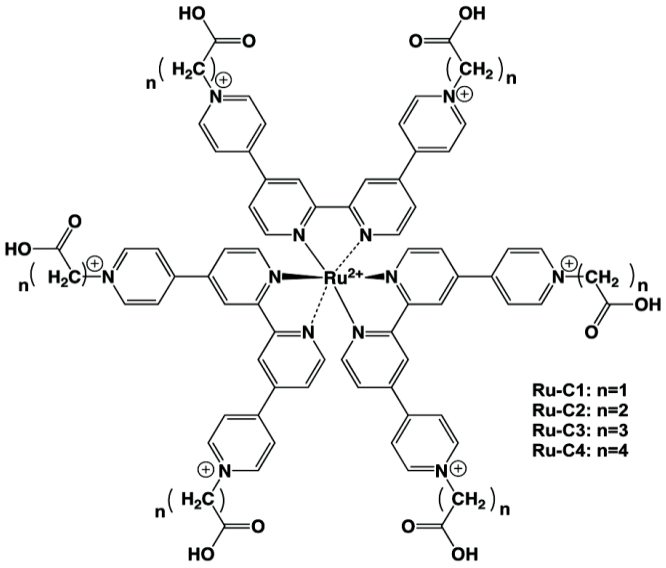

Figure 3.2: Ruthenium(II)-tris-(4,4',2',2'',4'',4'''quaterpyridinium) complexes Ru(II)-C1 to Ru(II)-C4.

3.2.1 UV/Vis-Absorbance and Luminescence Experiments

Both experiments were carried out in 4.0 mL quartz-cuvettes (Helma) using a spectrofluoro-meter (Fluoromax2) with dual monochromators and a diode array UV-vis absorption spectrometer (HP 8453). 0.05M Phosphate buffer (pH=6.8) was used as the solvent.

3.2.2 Laser Flash Photolysis

The times-resolved (ns) measurements of the luminescence and Vis-absorption lifetimes were performed in the research laboratories of Dr. Claudia Turró, Department of Chemistry, Ohio State University, Columbus Ohio.

The transient absorption spectra and lifetimes were measured by using a previously published procedure.[9,10] Briefly, instrument was pumped by a tripled (355nm) Spectra Physics GCR-150 Nd:YAG laser. The lamp (150 W Xe arc lamp) was focused onto sample at 90^0 angel with respect to the laser beam. The transmitted white light from the sample was focused to entrance slit of a Ppex HR-20 single monochromator (1200 gr/mm). Hamamatsu R928 photomultiplier tube was used as the detector and the data was processed by Tektronics 400 MHz oscilloscope (TDS 380)

The excitation wavelength used was 532nm (second harmonic of the exciting YAG laser). Luminescence was recorded at 680nm, excited state absorbance at 480nm. In addition, excited state absorption spectra of RuC1COOH to RuC4COOH have been recorded.

3.2.3 HPLC experiments

The binding constants of Ru(II)quaterpyridyl complexes to MspA are measured by HPLC (Shimadzu Prominence) employing a POROS HQ/20 anion exchange column and a flux of 0.50 ml min^{-1}. Two buffers are used: AOP05 (25mM HEPES, pH 7.5, 10 mM NaCl, 0.5% OPOE) and BOP05 (25 mM HEPES, pH 7.5, 2 M NaCl, 0.5% OPOE). A typical gradient is 100% AOP05 (0-5min.), followed by a linear gradient to 100% BOP05 (5-35min.). The eluent is kept at 100% BOP05 (35-50min.). Finally, the salt concentration is returned linearly to 10mM (100% AOP05) (50-60min). The stop time is set at 65min. Peak detection is achieved using UV/Vis (diode-array). The binding constants were calculated according to equation (1):

$$K_B = \frac{[Ru(II)cpx@MspA]}{([Ru(II)cpx]^0 - [Ru(II)cpx@MspA])([MspA]^0 - [Ru(II)cpx@MspA])} \quad (1)$$

Where, K_B: binding constant, [Ru(II)cpx@MspA]: concentration (mol/L) of the supramolecular assembly of the ruthenium(II)quaterpyridyl complexes Ru-C1 to Ru-C4 and MspA; $[MspA]^0$: concentration of MspA (mol/L) in the absence of nanoparticles; $[Ru(II)cpx]^0$: starting concentration of the ruthenium(II)quaterpyridyl complexes (mol/L).

3.3 Results and Discussion

3.3.1 Ruthenium(II)polypyridyl Complexes

Ruthenium(II)-polypyridyl complexes possess extraordinary thermal and photochemical stabilities. They are also kinetically stable, which means that they usually do not show ligand-exchange reactions in the dark.[11] Since they possess D^3-geometries when three equal ligands are employed (tris-homoleptic complexes), their geometric extensions can be estimated employing molecular modeling methods.[12] Furthermore, it should be noted that ruthenium(II)-quaterpyridine complexes absorb light in the UV- and Vis-region from λ=-650nm, depending on their ligand structures. Finally, it should be noted that the redox potentials of Ru(III)-, Ru(II)- and Ru(I)-complexes are easily accessible.[17]

3.3.2 Ruthenium(II)-quaterpyridinium Complexes and their Binding Within MspA

Due to their positive charges and geometric dimensions, Ru(II)-quaterpyridyl complexes are the ideal guests for the MspA-pore. However, it must be noted that these complexes can undergo partial deprotonation at neutral pH. This process is able to diminish their net positive charges (maximally eight) to a certain extent. Quantitative data on the acid/base-properties of Ru-C1 to RuC4 are not yet available. The presence of the aspartate residues D90 and D91 provides up to 16 negative counter anions for the Ru(II)-complexes. Our results indicate a strong charge attraction and consequent binding of the Ru(II)-complex within the pore of MspA.

3.3.3 UV/Vis-Absorption Characteristics

The first step of the photophysical characterization of the ruthenium(II)complexes consisted in the determination and the assignment of the major absorption peaks.[17] Our results are summarized in Table 3.1.

Table 3.1: Absorption Coefficients of the Ru(II)quaterpyridyl complexes in phosphate buffer at pH=6.8

Complexes	λ_{max} nm	$\varepsilon(M^{-1}cm^{-1})$	Assignment
	257	70452	$\pi \rightarrow \pi^*$
Ru(II)-C1	323	26202	$d \rightarrow \pi^*$
	491	17352	^{3}MLCT
	258	111358	$\pi \rightarrow \pi^*$
Ru(II)-C2	316	30610	$d \rightarrow \pi^*$
	490	18708	^{3}MLCT
	248	71808	$\pi \rightarrow \pi^*$
Ru(II)-C3	309	39478	$d \rightarrow \pi^*$
	479	16454	^{3}MLCT
	257	107416	$\pi \rightarrow \pi^*$
Ru(II)-C4	306	36231	$d \rightarrow \pi^*$
	481	15523	^{3}MLCT

Figure 3.3, shows the comparisons of UV absorption spectra of different Ru(II)quarter-pyridinium complexes C1 (upper left), C2 (upper right), C3 (lower left), and C4 (lower right) in water (pH=6.8, blue) and in the presence of MspA (red).

As it can be discerned from the four comparisons (Figure 3.3) between the Ru(II)-quaterpyridinium complexes C1, C2, C3, and C4, only minor changes occur in the UV/Vis-spectra if MspA is present. We attribute these changes to the formation of supramolecular adducts between the ruthenium complexes and MspA. However, it is impossible to determine the strength of this interaction from the UV/Vis-spectra. Therefore, we have performed steady-state luminescence spectroscopy and HPLC-determinations of the binding constants.

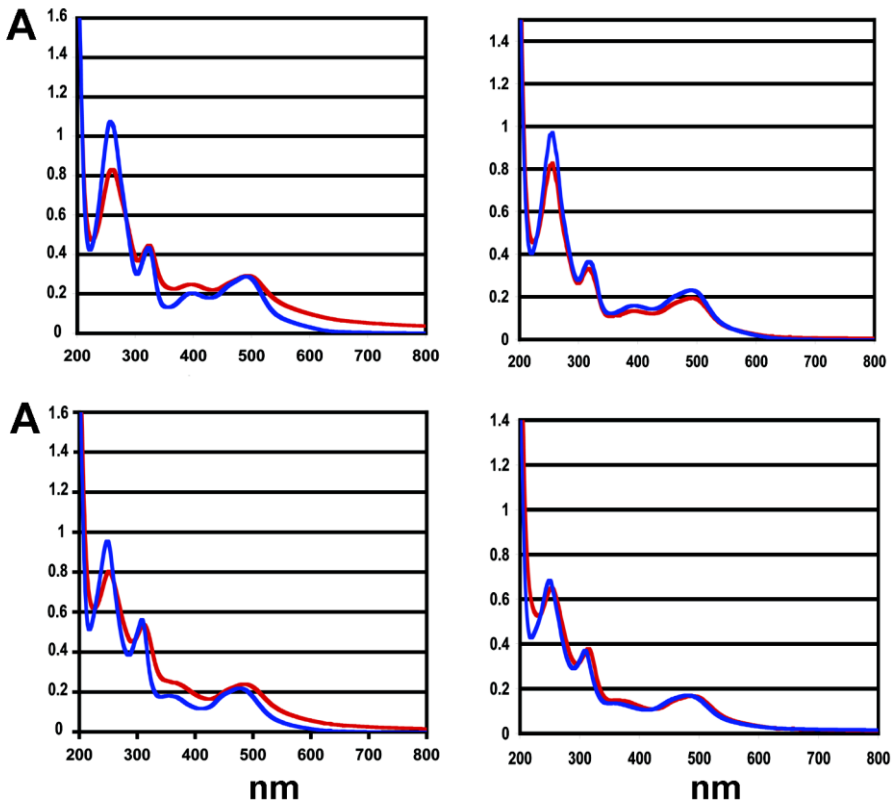

Figure 3.3: UV/Vis-Absorption Spectra of the Ruthenium(II)-tris-(4,4',2',2'',4'',4'''-quarter-pyridinium) complexes

(Ru(II)-C1 to Ru(II)-C4 (approx. 1.15x10^{-5} M in the presence (red) and absence (blue) of MspA (10 μg mL^{-1})).

3.3.4 Steady-state Luminescence Spectroscopy

The luminescence data summarized in Figure 3.4 shows the typical behavior for ruthenium(II)-polypyridyl complexes which are bound by proteins.[13] The luminescence arising from the ^{3}MLCT (triplet metal to ligand charge transfer) of the Ru(II)-complexes is partially quenched by H_2O.[14] When binding occurs, the complex stripped off a part of its hydrate shell. Therefore, the quantum yield of luminescence often increases. This behavior is especially pronounced for Ru(II)-C2. However, proton quenching can decrease the luminescence intensity and, therefore, a significant increase cannot be observed. Apparently, this is the case for the binding of Ru(II)-C1.

A second mechanistic criterion is the occurrence of a red shift of the luminescence-maximum upon complex binding. In tris-homoleptic complexes, which we exclusively used in these studies as luminescence probes, this shift is caused by the extension of the "ligand-field" surrounding the metal center due to supramolecular interaction with the biological structure.[15] As it becomes apparent from Figure 3.4 and 3.5, the magnitude of the red shift of luminescence increases with increasing size of the complex.[16,17]

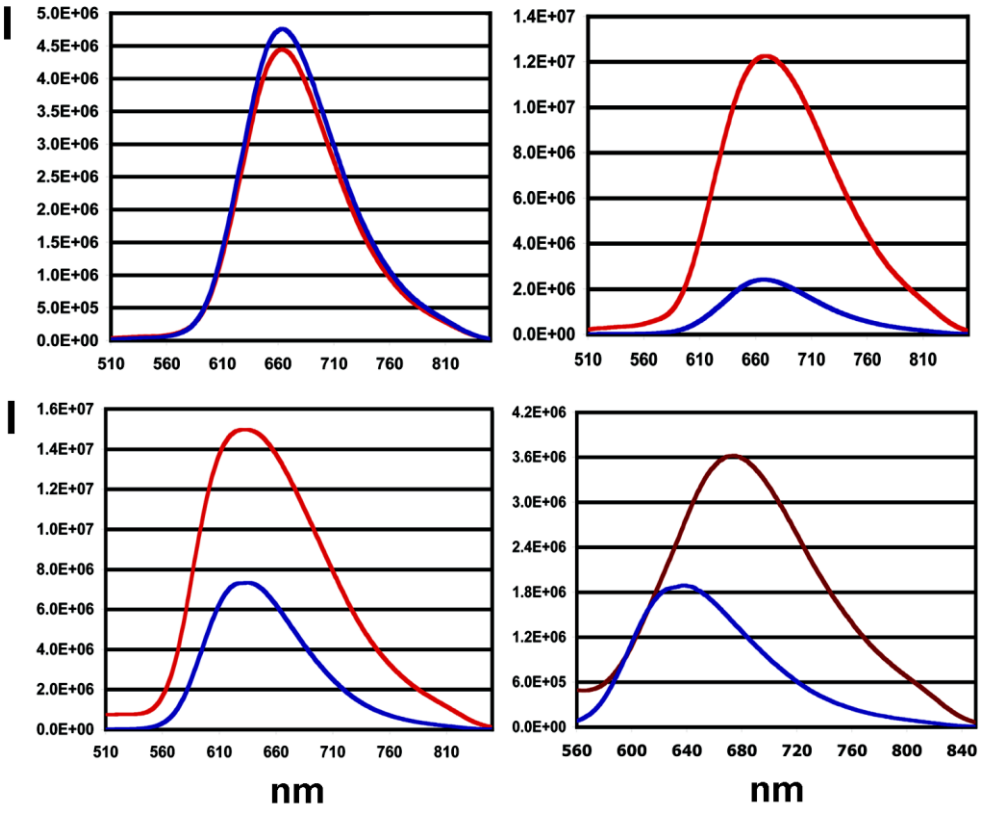

Figure 3.4: Luminescence Spectra of the Ruthenium(II)-tris-(4,4',2',2'',4'',4'''quarter-pyridinium) complexes

(Ru(II)-C1 to Ru(II)-C4 (1.15x10^{-5} M in the presence (red) and absence (blue) of MspA (10 μg mL^{-1}))

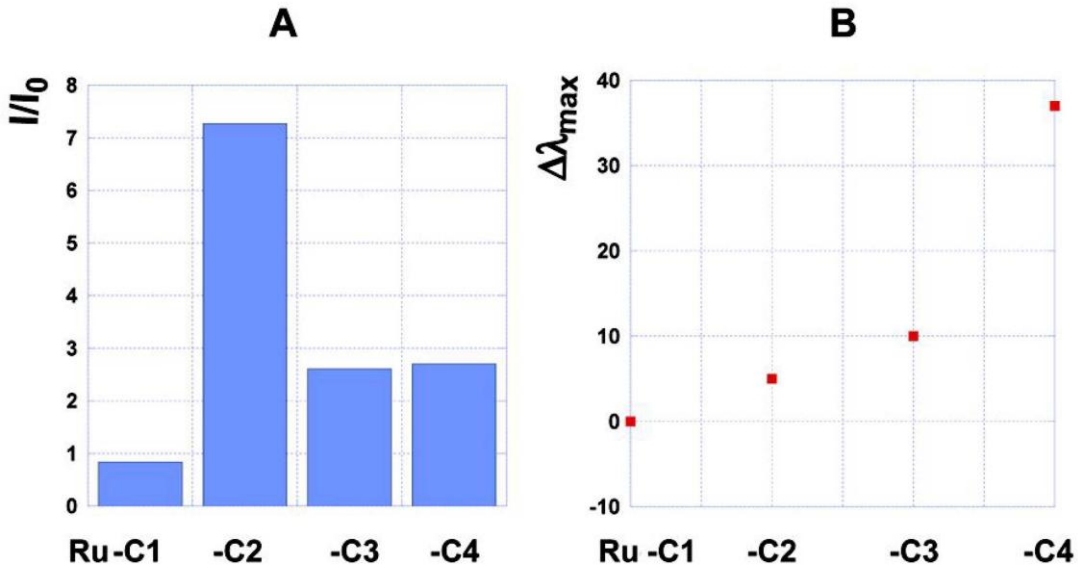

Figure 3.5: Indications for Binding of Ru(II)-C1 to C4 - complexes within MspA

Figure 3.5A shows the luminescence enhancement of the ruthenium(II)quaterpyridine complexes in the presence of MspA. Luminescence enhancement is a strong indication for the binding of Ru(II)-polypyridyl complexes.[15]

Figure 3.5B shows a consecutively progressing shift in the wave-length of the emission maximum is indicative of different binding sites of various Ru(II)-quaterpyridinium complexes of increasing diameters (C1 -> C4) within MspA.

3.3.5Time-Resolved Absorption Spectroscopy

In collaboration with the research group of Dr. Claudia Turro at Ohio State University, Columbus, OH, the time resolved absorption spectra of the ruthenium complexes (RuC1COOH to RuC4COOH) in the presence of MspA have been measured. Exactly the same systems (comprised of 1.15×10^{-5} M of ruthenium quaterpyridyl complex and 10 μg mL^{-1} of MspA) as for the steady-state luminescence experiments have been studied.

Table 3.2: Steady-state and time-resolved ^{3}MLCT-luminescence data and time-resolved absorption data of RuC1COOH to RuC4COOH in aqueous solution

Complex pH=7	^{3}MLCT- Emission λ_{max} (nm)	^{3}MLCT-Emission τ (ns)	^{3}MLCT-Absorption τ (ns)	^{3}MLCT-Absorption τ (ns), with MspA
RuC1COO^{2+}	662	601	516	8.2
RuC2COO^{2+}	666	263	166	18.2
RuC3COO^{2+}	638	133	49	13.3
RuC4COO^{2+}	640	140	107	11.0

It is remarkable that the binding of RuC1COOH to RuC4COOH in/at MspA leads to a significant decrease in the observed luminescence lifetime. Furthermore, these luminescence decays are still mono-exponential indicating that the binding/dissociation processes occur at a faster time-scale that the luminescence from the ^{3}MLCT states. The presence of the carboxylic acid and carboxylate groups of MspA appears to be quenching the ^{3}MLCT states via a proton-quenching mechanism.[18]

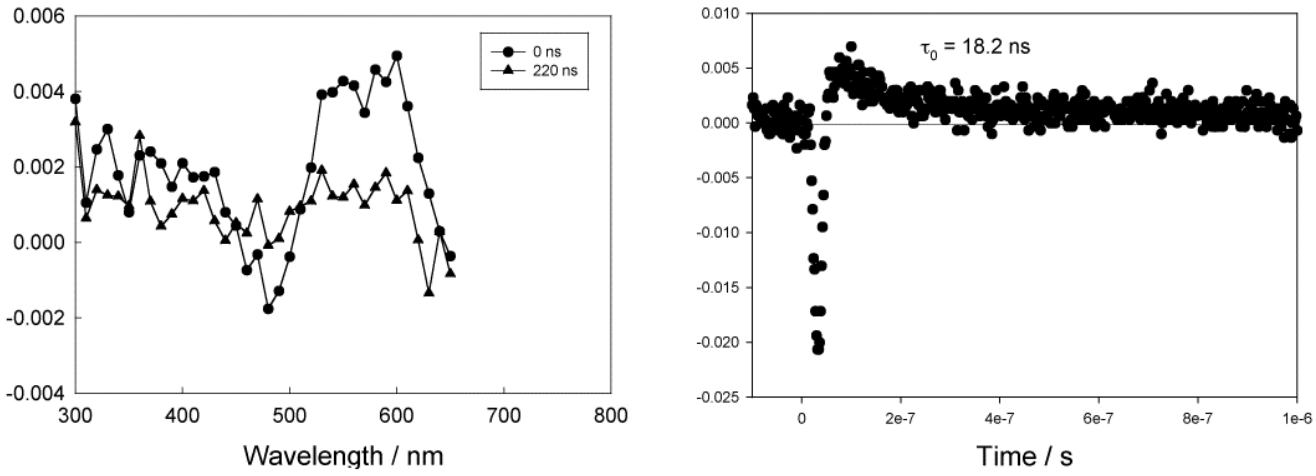

Figure 3.6: Nanosecond absorption spectrum of RuC2COOH in aqueous solution ($1.15x10^{-5}$M in 0.050M phosphate buffer) in the presence of 10 μg mL^{-1} of MspA (excitation wavelength: 532nm).

However, the exclusion from water, which is known to quench the ^{3}MLCT states of ruthenium-polypyridyl complexes via a vibrational relaxation mechanism[19] leads to a significant increase of luminescence from RuC2COOH to RuC4COOH when bound to MspA.

Table 3.3 shows the calculated binding constants by HPLC experiments. A decrease in binding constants were observed with the increase of the diameter of the ruthenium(II)-quaterpyridine complexes.

Table 3.3: Highly Charged Ruthenium(II)-quaterpyridinium Complexes with Diameters in nanometer Range and Binding Constants within MspA, as Determined by HPLC

Ru(II)-complex	-$(CH_2)_n$-	d [nm]	K_B [M^{-1}]
Ru-C1	1	2.43	7.5 x10^9
Ru-C2	2	2.92	5.8 x10^9
Ru-C3	3	2.99	3.4 x10^9
Ru-C4	4	3.18	1.1 x10^9

3.4 Conclusions

The experimental data obtained from steady-state luminescence and HPLC are indicative of binding of the ruthenium(II)quaterpyridyl complexes at/within MspA. HPLC indicated very high binding constants. This behaviour could be expected because of the presence of a double ring of aspartates in the constriction zone of MspA (D90 and D91) and the positively charged ruthenium(II)complexes. Interestingly, neither the observed luminescence enhancement nor the red shift of the luminescence correlate with the measured binding constants. Ru(II)-C1 binds most strongly because it is the smallest complex, as modelling indicates, be closest to the constriction zone (Figure 3.7). Therefore, it is certainly stripped off a part of its hydrate shell. As a result, its quantum yield of luminescence should increase, but a slight decrease is observed instead. This unexpected behavior can be attributed to the presence of the 16 aspartic acid units (D90 and D91) in the homo-octameric MspA.

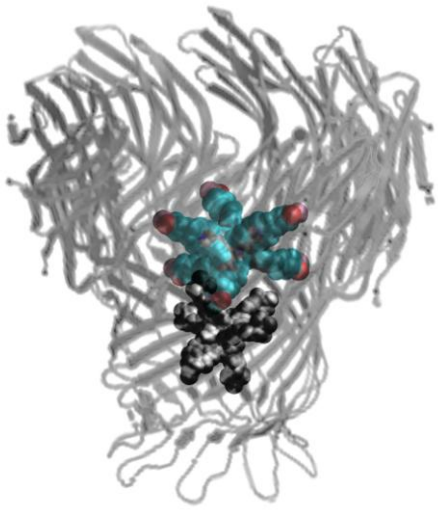

Figure 3.7: Modelling of the Binding of two Ru(II)-complexes to MspA Ru(II)-C1: black; Ru(II)-C4: coloured

At an (outer) pH of 6.8, we can expect that not all aspartic acids are deprotonated. Therefore, proton quenching may occur. Ru(II)-C2 shows the strongest luminescence enhancement, whereas Ru(II)-C3 and Ru(II)-C4 exhibit luminescence enhancement to a lesser extent when bound to MspA. However, they show the largest red shifts in luminescence due to an enhanced ^{3}MLCT-delocalization. The observed differences in luminescence enhancement and red shift clearly prove that each ruthenium(II)complex is bound at a different location inside the vestibule of MspA due to increasing diameter and the funnel-shape of the inner MspA pore. Our results indicate that channel blockers featuring high binding constants to mycobacterial porins can be designed. Ru(II)-complexes are especially suited for photophysical experiments, however Zn(II)-polypyridyl complexes may be better suited for in-vivo applications due to their lower toxicity.

3.5 References

[1] www.who.int

[2] Niederweis, M.; Bossmann, S. H., Nanostructuring at surfaces using proteins. *Encyclopedia of Nanoscience and Nanotechnology*, (2004), 7, 851-867.

[3] Faller, M.; Niederweis, M.; Schulz, G. E., The Structure of a Mycobacterial Outer-Membrane Channel., *Science*, (2004), 303, 1189-1192.

[4] Shi, A.; Pokhrel, M. R.; Bossmann, S. H., Synthesis of highly charged ruthenium(II)-quaterpyridinium complexes: a bottom-up approach to monodisperse nanostructures., *Synthesis*, (2007), 4, 505-514.

[5] Engelhardt, H.; Gerbl-Rieger, S.; Krezmar, D.; Schneider-Voss, S.; Engel, A.; Baumeister, W., Structural properties of the outer membrane and the regular surface protein of Comamonas acidovorans, *J Struct Biol*, (1990), 105, 92-102.

[6]Siroy, Axel; Mailaender, Claudia.; Harder, Daniel.; Koerber, Stephanie.; Wolschendorf, Frank.; Danilchanka., Olga.; Wang, Ying.; Heinz, Christian.; Niederweis, Michael. Rv1698 of Mycobacterium tuberculosis represents a new class of channel -forming outer membrane proteins. *Journal of Biological Chemistry* (2008), 283(26), 17827-17837.

[7] Heinz, C.; Roth, E.; Niederweis, M., Purification of porins from Mycobacterium smegmatis., *Meth. Mol. Biol.*, (2003), 228*(Membrane Protein Protocols)*, 139-150.

[8] Heinz, Christian; Niederweis, Michael, Selective Extraction and Purification of a Mycobacterial Outer Membrane Protein, *Analytical Biochemistry*, (2000), 285(1), 113-120.

[9] Bradley, Patricia M.; Bursten, Bruce E.; Turro, Claudia, Excited-State Properties of $Rh_2(O_2CCH_3)_4(L)_2$ (L = CH_3OH, THF, PPh_3, py), *Inorganic Chemistry*, (2001), 40(6), 1376-1379.

[10] Warren, Jeremy T.; Chen, Wei; Johnston, Dean H.; Turro, Claudia, Ground-State Properties and Excited-State Reactivity of 8-Quinolate Complexes of Ruthenium(II), *Inorganic Chemistry*, (1999), 38(26), 6187-6192.

[11] Duerr, H.; Bossmann, S., Ruthenium Polypyridine Complexes. On the Route to Biomimetic Assemblies as Models for the Photosynthetic Reaction Center., *Acc. Chem. Res.*, (2001), 34, 905-917.

[12] Lutterman, D. A.; Chouai, A.; Liu, Y.; Sun, Y.; Stewart, C. D.; Dunbar, K. R.; Turro, C., Intercalation Is Not Required for DNA Light-Switch Behavior., *J. Am. Chem. Soc.*, (2008), 130, 1163-1170.

[13] Pyle, A. M.; Rehmann, J. P.; Meshoyrer, R.; Kumar, C. V.; Turro, N. J.; Barton, J. K., Mixed-Ligand Complexes of Ruthenium(II): Factors Governing Binding to DNA, *J. Am. Chem. Soc*., (1989), 111, 3051-3058.

[14] Turro, C.; Bossmann, S. H.; Leroi, G. E.; Barton, J. K.; Turro, N. J., Ligand-Specific Charge Localization in the MLCT Excited State of $Ru(bpy)_2(dpphen)^{2+}$ Monitored by Time-Resolved Resonance Raman Spectroscopy., *Inorg. Chem*., (1994), 33, 1344-1347.

[15] Pyle, A. M.; Rehmann, J. P.; Meshoyrer, R.; Kumar, C. V.; Turro, N. J.; Barton, J. K. Mixed-Ligand Complexes of Ruthenium(II): Factors Governing Binding to DNA, *J. Am. Chem. Soc*., (1989), 111, 3051-3058.

[16] Turro, N. J.; Barton, J. K.; Tomalia, D. A., Molecular recognition and chemistry in restricted reaction spaces. Photophysics and photoinduced electron transfer on the surfaces of micelles, dendrimers, and DNA., *Acc. Chem. Res*., (1991), 24, 332-340.

[17] Turro, Nicholas J.; Barton, Jacqueline K., Paradigms , supermolecules , electron transfer and chemistry at a distance. What's the problem? The science or the paradigm? JBIC, *Journal of Biological Inorganic Chemistry*, (1998), 3(2), 201-209.

[18] Turro, Claudia; Bossmann, Stefan H.; Jenkins, Yonchu; Barton, Jacqueline K.; Turro, Nicholas J., Proton Transfer Quenching of the MLCT Excited State of $Ru(phen)_2dppz^{2+}$ in Homogeneous Solution and Bound to DNA, *Journal of the American Chemical Society*, (1995), 117(35), 9026-32.

[19] Juris, A.; Balzani, V.; Barigelletti, F.; Campagna, S.; Belser, P.; Von Zelewsky, A., Ruthenium (II) polypyridine complexes : photophysics, photochemistry, electrochemistry, and chemiluminescence, *Coordination Chemistry Reviews*, (1988), 84, 85-277.

CHAPTER 4 - POLY-N-ISOPROPYLACRYLAMIDE/ACRYLIC ACID COPOLYMERS FOR THE GENERATION OF NANOSTRUCTURES AT MICA SURFACES AND AS HYDROPHOBIC HOST SYSTEMS FOR THE PORIN MspA FROM *Mycobacterium smegmatis*

4.1 Introduction

Novel efficient methods for the design of bioelectronic devices[1], such as biosensors[2], bio fuels cells[3] and memory storage devices[4], have to be developed to permit their broad application in the near future. This pertains to the generation of 2-D nanostructures at surfaces[5,6,7] (e.g. nanoscopic cavities of a low polydispersity) as well as ultraflat organic surfaces that can be used as host layers for proteins.[8] Since many proteins have to associate with natural or artificial membranes to retain their biological functions, the development of adaptable and cost-efficient artificial hosting systems for proteins is of great importance for the technical implementation of biolelectronic devices.[9] The use of self-assembled monolayers (SAM's) for protein adsorption and protection is prevalent.[10,11] Recently, several procedures for the preparation of nanolayers of oligopeptides that were able to stabilize proteins[12] and protein complexes[13] have been reported. Polymer-layers, such as Poly-N-isopropyl-acrylamide on HOPG (highly ordered pyrolytic graphite) surfaces were used to provide protein-stabilization.[7]

The work presented in this chapter aims at utilizing poly-N-isopropyl-acrylamide copolymers to create a nanostructure on mica surfaces by a simple spin-casting procedure. The resulting surfaces were characterized by using Atomic Force Microscopy (magnetic AC-mode).[14] We have synthesized a series of pH and temperature responsive P(NIPAM-co-AA) (NIPAM: N-isopropyl-acrylamide, AA: acrylic acid) copolymers by free radical[15] and living free radical copolymerization[16] of N-isopropylacrylamide and acrylic acid.

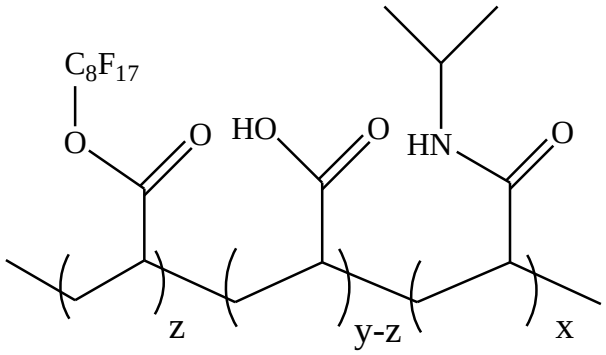

Figure 4.1: P(NIPAM$_x$-co-AA$_y$-coAAC$_8$F$_{19\ z}$)-copolymers for the spincasting of nanothin layers on Mica

Post polymerization modification was achieved by reacting the free carboxylates with perfluoro-8-iodooctane (Figure 4.1).[17] The polymers were spin-cast[18] onto freshly cleaved Mica surfaces, followed by incubation in an environmental chamber under defined temperature and humidity. Crosslinking of individual polymer chains permitted the deposition of ultraflat nanolayers, which were able to host the mycobacterial channel protein MspA,[19] retaining its channel function!

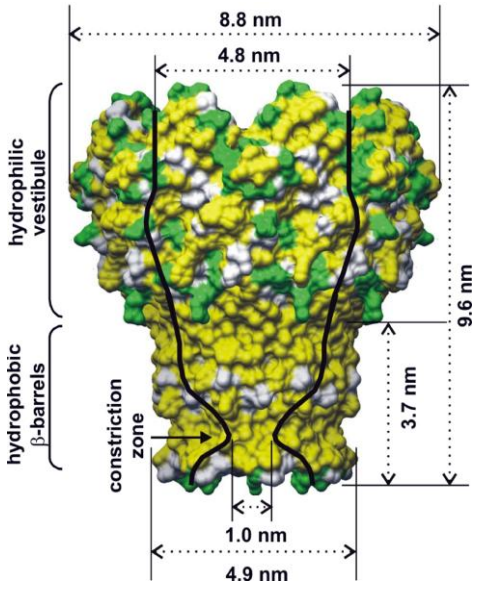

Figure 4.2: Structure of *M. smegmatis* (side view)
(The arrow depicts the constriction zone; green: hydrophilic amino acids; yellow: hydrophobic amino acids; dimensions given in nm. The coordinates were taken from the crystal structure of MspA (PDB code: 1UUN).[21])

The MspA porin from *M. smegmatis* is an extremely stable protein (Figure 4.2), retaining its channel structure even after boiling in 3% SDS, heating to 100^{o}C or extraction with organic solvents.[1] MspA is the only mycobacterial porin that can be purified in mg quantities.[20] Another distinct advantage of MspA is its amphiphilic nature.[21] Not only is the interior channel surface much more hydrophilic than its exterior, the exterior is subdivided in two distinct zones. MspA features a very hydrophobic "docking region" at the stem of its "goblet", whereas its "rim" section is formed by alternating hydrophilic and hydrophobic residues so that it is much more hydrophilic.[21] The geometric dimensions of the "docking region" are 3.7 nm in length, and 4.9 nm in diameter. It is our goal to prepare hosting nanolayers for MspA in a simple and straightforward experimental procedure. It is noteworthy that MspA does not require a stabilizing layer,[22] however the presence of an insulating layer between a channel protein and an electrode is mandatory for many bioelectronic and sensing applications. Bossmann group have demonstrated in earlier work that MspA is an ideal host for photonic and magnetic nanoparticles, which can be bound within its hydrophilic vestibule.[22,23]

4.2 Results and Discussion

Polymers responsive to external stimuli such as pH, temperature, ionic strength and electric field have been the focus of many studies in view of the potential applications in diverse fields, such as medicine or bioelectronics.[8] PNIPAM exhibits thermo-reversible phase separation behavior in aqueous solution, which makes the polymer useful as a thermoresponsive material and is characterized by a lower critical solution temperature (LCST).[24] On the molecular level PNIPAM has been used in many forms including single chains, macroscopic gels, microgels, latexes, thin films, membranes, coatings, and fibers.[25]

The phase transition behavior of PNIPAM in aqueous solution has been widely investigated by calorimetric, turbiditimetric and spectroscopic techniques.[26,27,28,29] An interesting feature common to other thermosensitive polymers lies in the possibility of tuning the LCST by adding cosolvents [29,] salts[30], surfactants[31] or polyelectrolytes[31] to the PNIPAM solutions or by incorporating comonomers with variable degree of hydrophilicity[32,33] Increasing or decreasing the hydrophilic content of a copolymer will usually result in an increase or decrease of PNIPAM's LCST, respectively. Furthermore, polymerizing N-isopropylacrylamide (NIPAM)

with weakly ionizable commoners allows to obtain intelligent polymers capable of responding to both temperature and pH variations; interestingly, owing to the variation of their degree of ionization with pH, systems with pH dependent LCST[34,35] are obtained. Polymers bearing carboxylic acid functional group such as polyacrylic acid, are pH sensitive, as they adopt a coiled conformation in solutions at low pH, where the carboxylic acid groups are protonated, and an extended conformation in solutions of high pH where the negatively charged carboxylates under go strong electrostatic repulsion. Consequently, pH and temperature of aqueous solutions for spin-casting of P(NIPAM-co-AA) polymers are very important parameters that had to be closely observed to achieve reproducibility of the spin-casting experiments reported in this chapter. In the work reported here a series of copolymers of N-isopropylacrylamide with the co-monomer acrylic acid was synthesized and investigated the influence of both temperature and pH on their solution behavior.

4.2.1Synthesis of Poly(N-isopropylacrylamide-co-Acrylic acid) Copolymers

Four P(NIPAM /AA) copolymers with molar ratios 99, 98, 95 and 90 of NIPAM and 1, 2, 5 and 10 mol. % of AA were synthesized. All syntheses were carried out at 70°C in t-BuOH by free radical polymerization initiated by AIBN (Figure 4.3).[36]

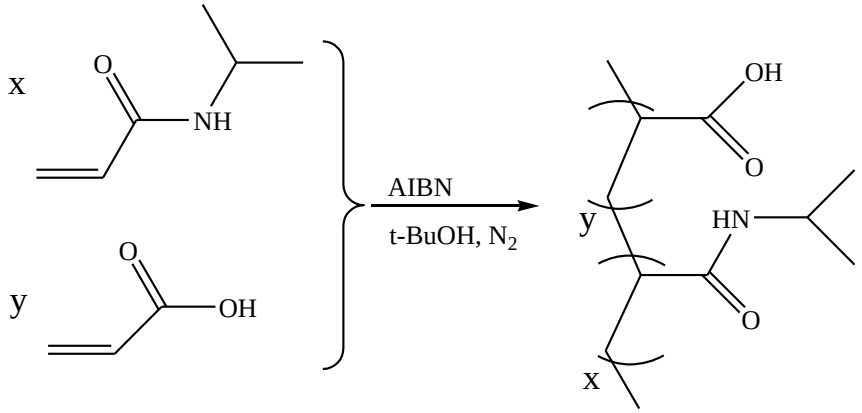

Figure 4.3: Radical statistical polymerization of P(NIPAM-co-AA) copolymers

The initiator AIBN undergoes thermal homolytic dissociation at about 40-60°C under nitrogen. The formed free radical namely dimethylcyanomethyl radical, reacts with monomer and form a chain initiator which then undergoes a series of chain growing reaction (chain

propagation) with monomer and finally leads to the formation of a copolymer. The termination of the polymerization reaction takes place by both recombination and disproportionation reactions.

The purification of the copolymer is very important and the most difficult task as it contains residual monomer, initiator and solvent as impurities. The copolymers were purified by repeated precipitations of tetrahydrofuran solutions into n-hexane, a non-solvent for copolymers, but a good solvent of all the monomers. The purity of the copolymers was ascertained by GPC (gel permeation chromatography) analysis, which shows the absence of low molecular weight species (i.e. monomers) in the purified copolymers. The GPC and CHN analysis described in this chapter were performed at research laboratories of Dr. André M. Braun at the Institute of Environmental Analysis Technology (Lehrstuhl für Umweltmesstechnik) at the Engler-Bunte-Institute, University of Karlsruhe, Germany.

Classic CHN analysis[37] was used to determine the composition of the copolymers: NIPAM is the only monomer that contains nitrogen. Therefore, the ratio of carbon and nitrogen is indicative of the polymer composition. The results from these measurements are reported in Table 1. Polymer composition and polydispersity of polymers were determined by CHN analysis and gel permeation chromatography. They indicate that NIPAM and acrylic acid possess very similar propagation constants and, therefore, the ratios of the monomers in the polymer are very similar to the feed ratios. These results are in good agreement with a previous publication.[38] Furthermore we assume that some of the more polar, acrylic acid rich fractions of the copolymer were lost during the precipitation and washing procedures.

We have applied the method of *living radical chain polymerization*[16] to decrease the polydispersity of the P(NIPAM-co-AA) copolymers (Table 1). In this reaction, the initial 2-cyanoprop-2-yl radicals react with 2-mercaptoacetic acid to form the corresponding thiyl radical, which then slowly initiates polymerization (Figure 4.4). This approach leads to a defined number of growing radical chains, which compete for the available monomers. The resulting polydispersities (P_D=1.18 to 1.25) are significantly lower in the absence of 2-mercaptoacetic acid.

Table 4.1: Composition and polydispersity of N-isopropyl-acrylamide/acrylic acid copolymers (M_n, number average macromolecular mass, M_w: weight average macromolecular mass, N_i: mol fraction, M_i: weight fraction)

Radical statistical copolymerization	Composition according to CHN analysis	$M_n = \frac{\sum M_i N_i}{\sum N_i}$	$M_w = \frac{\sum M_i^2 N_i}{\sum M_i N_i}$	$PDI = \frac{M_w}{M_n}$
P[(NIPAM)$_{99}$-co-AA)$_1$]	P[(NIPAM)$_{99.2}$-co-(AA)$_{0.8}$]	52,400	73,900	1.41
P[(NIPAM)$_{98}$-co-AA)$_2$]	P[(NIPAM)$_{98.4}$-co-(AA)$_{1.6}$]	48,200	69,900	1.45
P[(NIPAM)$_{95}$-co-AA)$_5$]	P[(NIPAM)$_{95.5}$-co-(AA)$_{4.5}$]	46,500	72,100	1.55
P[(NIPAM)$_{90}$-co-(AA)$_{10}$]	P[(NIPAM)$_{90.4}$-co-(AA)$_{9.6}$]	47,300	71,900	1.52
Living statistical copolymerization				
P[(NIPAM)$_{99}$-co-(AA)$_1$]	P[(NIPAM)$_{99.3}$-co-(AA)$_{0.7}$]	72,500	87,700	1.21
P[(NIPAM)$_{98}$-co-(AA)$_2$]	P[(NIPAM)$_{98.6}$-co-(AA)$_{1.4}$]	75,500	89,100	1.18
P[(NIPAM)$_{95}$-co-(AA)$_5$]	P[(NIPAM)$_{95.3}$-co-(AA)$_{4.7}$]	74,100	92,600	1.25
P[(NIPAM)$_{90}$-co-(AA)$_{10}$]	P[(NIPAM)$_{90.5}$-co-(AA)$_{9.5}$]	69,800	85,200	1.22

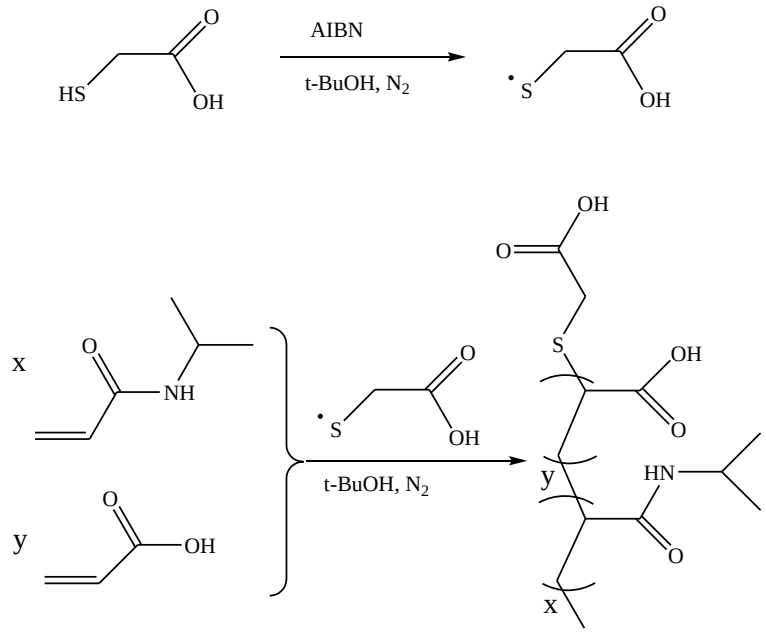

Figure 4.4: Thiyl-initiated living radical chain polymerization of N-isopropyl-acrylamide (NIPAM) and acrylic acid (AA) in tert. Butanol.

Our experimental approach of comparing copolymers of the same composition and similar macromolecular masses, but different polydispersities is guided by the paradigm that the physical properties of all polymers are influenced by their macromolecular mass distribution, although this influence is negligible in some cases. The copolymers from AIBN-initiated radical polymerization feature polydispersities typical for polyacrylates[39], whereas it is apparent that the method of *living radical chain polymerization* leads to distinctly narrower molecular weight distributions (Table 1).

A postpolymerization modification reaction was performed to introduce strongly hydrophobic labels (Figure 4.5). Perfluoroalkyl-bearing copolymers were obtained from both types of P(NIPAM-co-AA) copolymers by reacting their carboxylate groups with perfluoro-iodo-octane in DMF using sodium carbonate as a strong base. Their composition is summarized in Table 2.

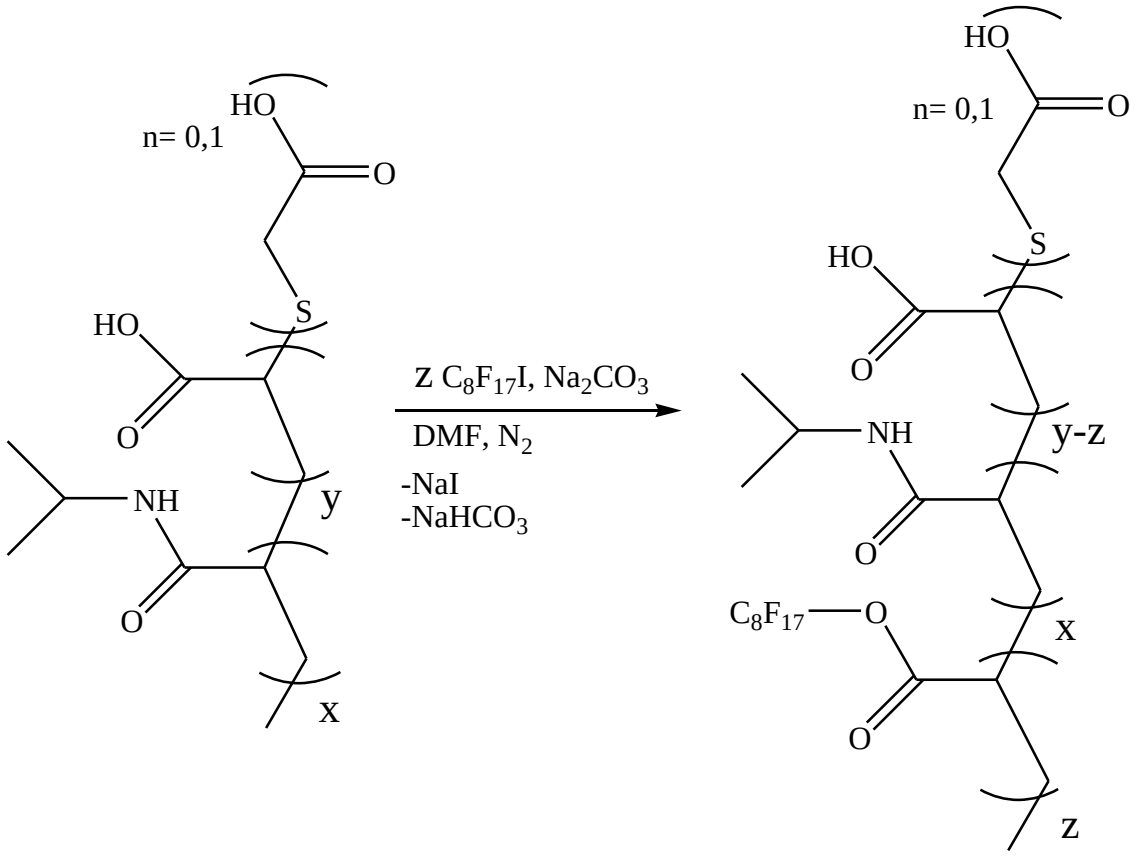

Figure 4.5: Postpolymerization modification of P(NIPAM-co-AA) with perfluoro-iodo-octane in DMF in the presence of sodium carbonate as base.

Table 4.2: Composition and polydispersity of N-isopropyl-acrylamide/acrylic acid copolymers after postpolymerization

(M_n, number average macromolecular mass, M_w: weight average macromolecular mass, N_i: mol fraction, M_i: weight fraction)

Copolymer by Radical statistical copolymerization	Composition according to CHN analysis	$M_n = \frac{\sum M_i N_i}{\sum N_i}$	$M_w = \frac{\sum M_i^2 N_i}{\sum M_i N_i}$	$PDI = \frac{M_w}{M_n}$
P[(NIPAM)$_{99}$-co-(AA)$_{0.5}$-AAC$_8$F$_{17\ 0.5}$]	P[(NIPAM)$_{99}$-co-(AA)$_{0.5}$-AAC$_8$F$_{17\ 0.3}$]	59,100	83,300	1.41
P[(NIPAM)$_{98}$-co-(AA)$_{1.0}$-AAC$_8$F$_{17\ 1.0}$]	P[(NIPAM)$_{98}$-co-(AA)$_{1.0}$-AAC$_8$F$_{17\ 0.6}$]	50,000	73,500	1.47
P[(NIPAM)$_{95}$-co-(AA)$_{2.5}$-AAC$_8$F$_{17\ 2.5}$]	P[(NIPAM)$_{95}$-co-(AA)$_{2.7}$-AAC$_8$F$_{17\ 1.8}$]	49,500	77,800	1.57
P[(NIPAM)$_{90}$-co-(AA)$_{5.0}$-AAC$_8$F$_{17\ 5.0}$]	P[(NIPAM)$_{90}$-co-(AA)$_{5.0}$-AAC$_8$F$_{17\ 4.6}$]	55,700	86,300	1.55
Copolymer by living statistical copolymerization				
P[(NIPAM)$_{99}$-co-(AA)$_{0.5}$-AAC$_8$F$_{17\ 0.5}$]	P[(NIPAM)$_{99}$-co-(AA)$_{0.4}$-AAC$_8$F$_{17\ 0.3}$]	73,200	88,600	1.21
P[(NIPAM)$_{98}$-co-(AA)$_{1.0}$-AAC$_8$F$_{17\ 1.0}$]	P[(NIPAM)$_{98}$-co-(AA)$_{0.8}$-AAC$_8$F$_{17\ 0.9}$]	77,900	91,900	1.18
P[(NIPAM)$_{95}$-co-(AA)$_{2.5}$-AAC$_8$F$_{17\ 2.5}$]	P[(NIPAM)$_{95}$-co-(AA)$_{2.5}$-AAC$_8$F$_{17\ 2.2}$]	80,100	103,300	1.29
P[(NIPAM)$_{90}$-co-(AA)$_{5.0}$-AAC$_8$F$_{17\ 5.0}$]	P[(NIPAM)$_{90}$-co-(AA)$_{5.4}$-AAC$_8$F$_{17\ 4.1}$]	80,500	99,900	1.24

4.2.2 Spin Casting Experiments

4.2.2.1 Copolymer Superstructures on Mica

The P[(NIPAM)-co-(AA)] and P[(NIPAM)-co-(AA)-co-AAC$_8$F$_{17}$] copolymers were dissolved in water (1.0 gL^{-1}) and stored at 295K. Before the spincasting procedure, 1.0 mL of the stock solution and 1.0mL of freshly distilled MeOH were mixed. The presence of the cononsolvent (MeOH) remarkably decreases the LCST.[29] A cononsolvent is a water-miscible solvent that leads to the precipitation of the PNIPAM-(co)polymer. Consequently, all copolymers formed precipitates under these conditions. These mixtures of cononsolvent and

precipitate were allowed to ripen for 10min. and then spincast onto freshly cleaved Mica at 3000 rpm. After drying in air for 1 h, the polymer-coated Mica plates were incubated in an environmental chamber (Agilent) at 295 K and 50% relative humidity for 24 h. It is noteworthy that the pH of the aqueous copolymer solution had a remarkable influence on the morphology of the spincast polymer nanofilms. We have determined the pK_a of P(NIPAM-co-AA) copolymers to be 4.60, which is very close to the pK_a of polyacrylic acid (pKa=4.55).[40] The pH has been adjusted by adding aliquots of HCl or NaOH and measuring the pH with a pH-electrode (Methrohm). Above pH 5 non-structured polymer precipitates on mica from the aqueus polymer solution. However at pH=4 and pH=3 that the nanolayers were found on mica after deposition and subsequent incubation. We attribute this reproducible behavior to the presence of carboxylic acid functions in the polymer, which can form hydrogen-bonding networks.[41] We have carried out the spincasting experiments reported here at pH=4.0. The best results, which are shown here, were obtained by employing copolymers with 95 percent of NIPAM content and 5 percent of either acrylic acid or acrylic acid and its perfluoro-octylester combined. The perfluoro-alkyl-postpolymerization modified copolymers did only show reproducible results when the products resulting from living radical polymerization were employed. In all other cases, the polydispersity of the investigated copolymers did not have a significant influence in the observed surface features.

4.2.2.2 Ultraflat Polymer Surfaces on Mica

P[$(NIPAM)_{95}$-co-$(AA)_5$] was precipitated from aqueous solution (pH=4.0, see above) by raising the temperature to 310^{o}K, which is above its LCST. The precipitate was filtered off, dried in high vacuum and re-dissolved in freshly distilled THF (c=1.0 g L^{-1}). This solution was mixed 1:1 (v/v) with a freshly prepared solution of dicyclohexyl-carbodiimide (DCC) (0.10g L^{-1}) and N-hydroxy-succinimide (NHS) (0.020 gL^{-1}) and 1,3-diaminopropane (0.0180 g L^{-1}) in THF and spincast at 3000 rpm. One application of the polymer solution gave the best results. The drying and incubation procedure previously described was not changed. A mechanistic hypothesis explaining why the cross-linking procedure employing 1,3-diamino-propane leads to ultraflat polymer surface on Mica, is shown in Figure 4.6: The free carboxylate groups react with 1,3-diamino-propane to form amides.[42] Crosslinking of individual chains during the spin-casting process apparently leads to extended polymer networks that adhere flatly to the Si-OH groups of the Mica surface.

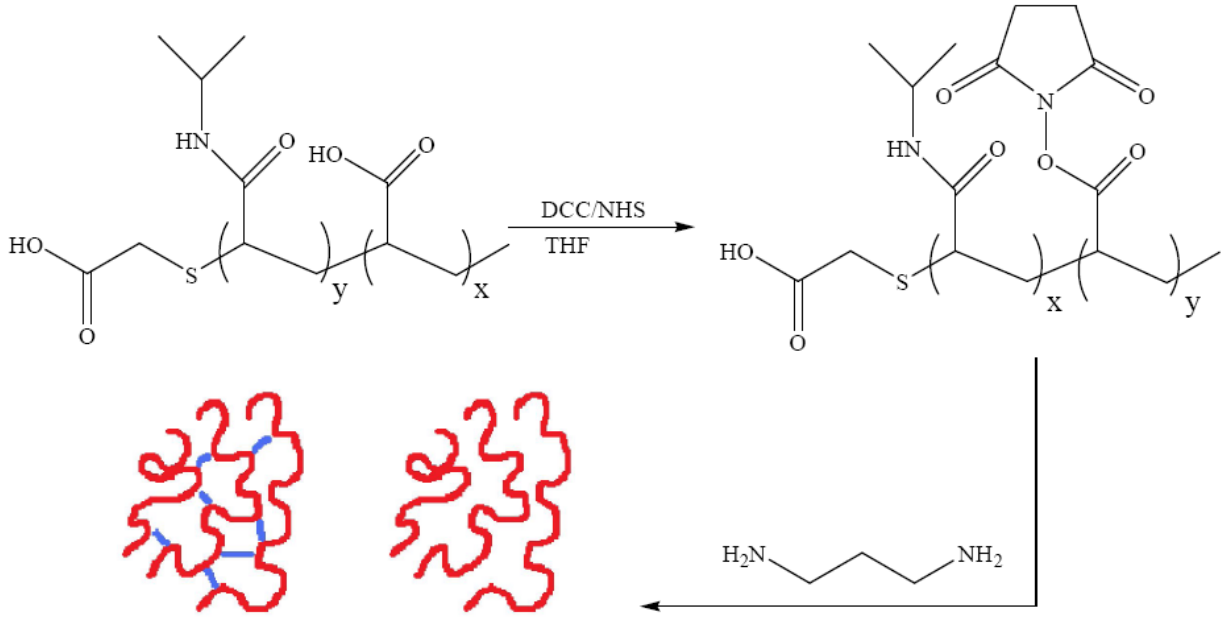

Figure 4.6: Linking of individual polymer chains by introducing amide-crosslinking

4.2.3 Atomic Force Microscopy (AFM) Measurements

AFM images were recorded using the PicoScan 2000 AFM (Agilent Technologies) in the Magnetic A/C-mode (MACmode).[14] The measurements were performed at the polymer/air interface. AFM can determine the topology of the sample. Furthermore, there exists a discernible sensitivity of the phase of the cantilever oscillations to the tip-sample interaction forces. Changes in the phase of oscillations can be used to discriminate between materials, possessing different viscoelastic properties. The thermally induced transitions of poly-N-isopropyl-acrylamide[43] and its copolymers with acrylic acid[44], styrene[45] and ethylene oxide[46] on surfaces, as well as poly-N-isopropyl-acrylamide-hydrogels[47] and Langmuir-Blotgett-films[48] have been investigated by AFM. Our AFM-study aims at a greater spatial resolution and investigates the pattern on copolymer surfaces, which can be formed by supramolecular interaction of spincast poly-N-isopropyl-acrylamide copolymers above their LCST. We have estimated from the size of the Mica plates (1 x 1cm) and the weight of the deposited copolymers that the thickness of the deposited polymer layer is of the order of 25 to 50nm.

4.2.3.1 Poly-NIPAM-acrylic acid Copolymers

After spincasting P[(NIPAM)$_{95.5}$-co-(AA)$_{4.5}$] in water/MeOH (pH=4.0) onto Mica, followed by drying in air and incubation at 50 percent relative humidity at 295K for 24h, the resulting polymer layer shows nanoscopic pores.

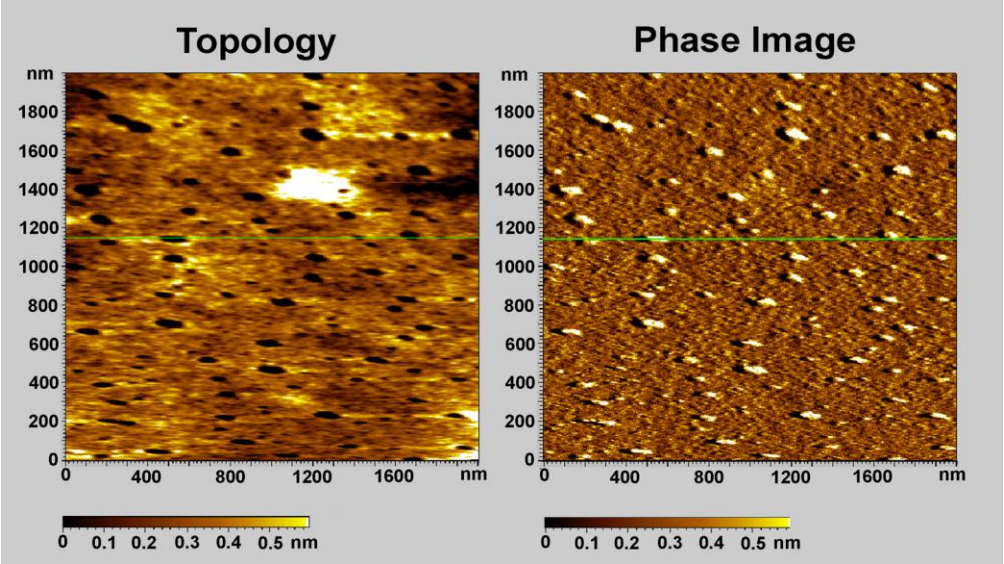

Figure 4.7: Nanostructured layer of P[(NIPAM)$_{95.5}$-co-(AA)$_{4.5}$] (PDI=1.55) on Mica.

We have investigated the statistical distribution of the pore-diameters employing the program image, which is available from NIH. [49] The mean pore diameters, calculated from the data summarized in Figure 4.8, are 23.8±2.4nm for the higher polydispersity material (PDI=1.55) and 21.8±4.2nm for the lower polydispersity material (PDI=1.25). This means that within our experimental margin of error, we cannot discern a significant influence of the polydispersity of the employed copolymers on their ability to form nanopores.

We have recorded AFM-images of the same surfaces with higher resolution to determine the depth and the profile of the nanopores. Figure 4.9 shows a typical result. The maximal depth of the investigated pore is approx. 4nm. The observed pore curvature is gentle (approx. 0.2nm per nm).

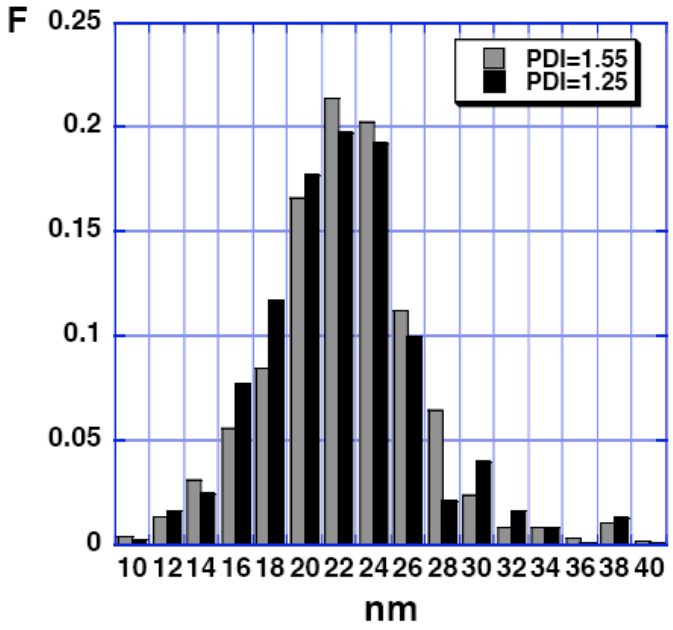

Figure 4.8: Statistical distribution of the apparent pore diameters from five independently prepared samples of P[(NIPAM)$_{95.5}$-co-(AA)$_{4.5}$] (PDI=1.55) and P[(NIPAM)$_{95.3}$-co-(AA)$_{4.7}$] (PDI=1.25) on Mica (F: fraction of pores)

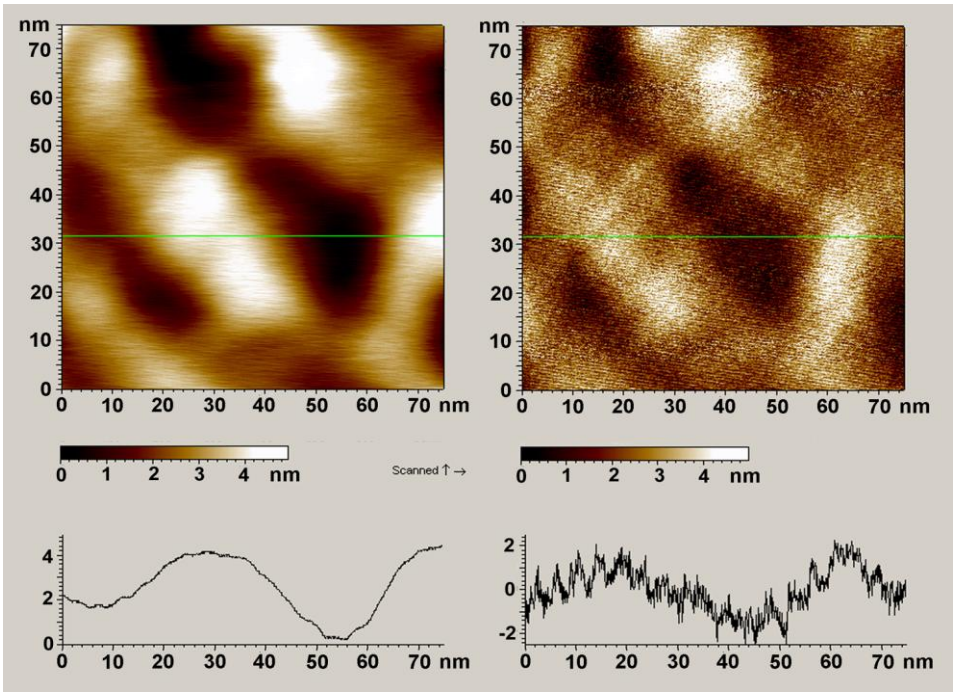

Figure 4.9: Nanostructured layer of P[(NIPAM)$_{95.5}$-co-(AA)$_{4.5}$] (PDI=1.55) on Mica (Right: topology image; left: phase image)

4.2.3.2 Perfluoro-octyl-ester Modified Poly-NIPAM-acrylic acid Copolymer Layers

We have repeated the spincasting, drying and incubation cycle with the copolymer P[(NIPAM)$_{95}$-co-(AA)$_{2.5}$-AAC$_8$F$_{17\ 2.2}$] (PDI=1.29), featuring the very hydrophobic perfluoro-octyl group in 2.2 percent of its side chains. As already noted earlier, only the low polydispersity material led to meaningful and reproducible results. The resulting pores on the surface of the copolymer layer were larger (mean diameter: 35.8±7.1nm, see Figure 4.11) when employing the more hydrophobic material. They were also more shallow (see Figure 4.12). It should be noted that the discernible phase contrasts are only very minor indicating that the hydrophilic and hydrophobic groups of the copolymer are almost evenly distributed. There are no indications for demixing effects, as one would expect for a statistic copolymer. The presence of hydrophobic groups enhances the hydrophobic forces in the copolymer, which causes the decrease in LCST. Therefore, the supramolecular interactions of the hydrophobic groups (N-isopropyl acrylamide, above the LCST and perfluorooctyl acrylate) is improved and the ability to form hydrogen-bonding networks due to the presence of acrylic acid is decreased when compared to P[(NIPAM)$_{95.3}$-co-(AA)$_{4.7}$] (PDI=1.25).

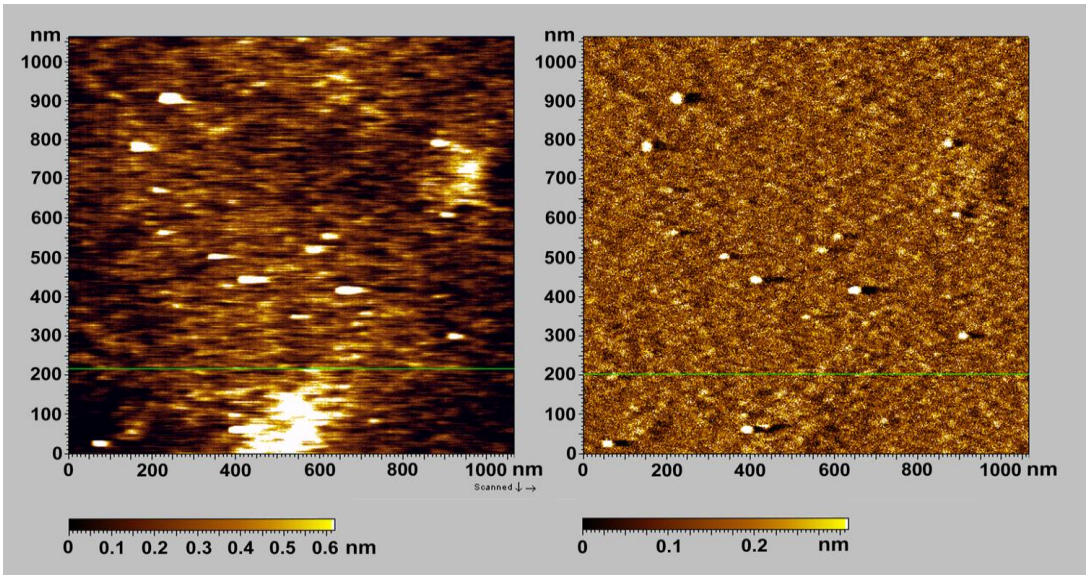

Figure 4.10: Nanostructured layer of P[(NIPAM)$_{95}$-co-(AA)$_{2.5}$-AAC$_8$F$_{17\ 2.2}$] (PDI=1.29) on Mica. Right: topology image; left: phase image

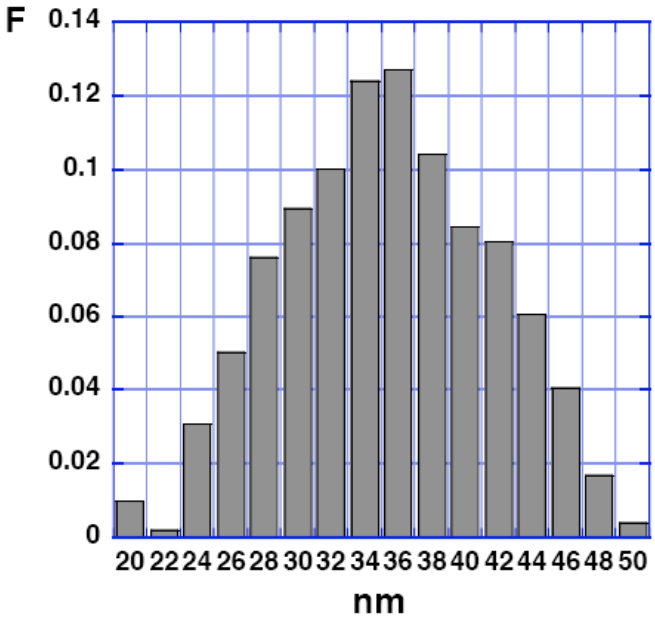

Figure 4.11: Statistical distribution of the apparent pore diameters from three independently prepared samples of P[(NIPAM)$_{95}$-co-(AA)$_{2.5}$-AAC$_8$F$_{17\ 2.2}$] (PDI=1.29) on Mica
(F: fraction of pores)

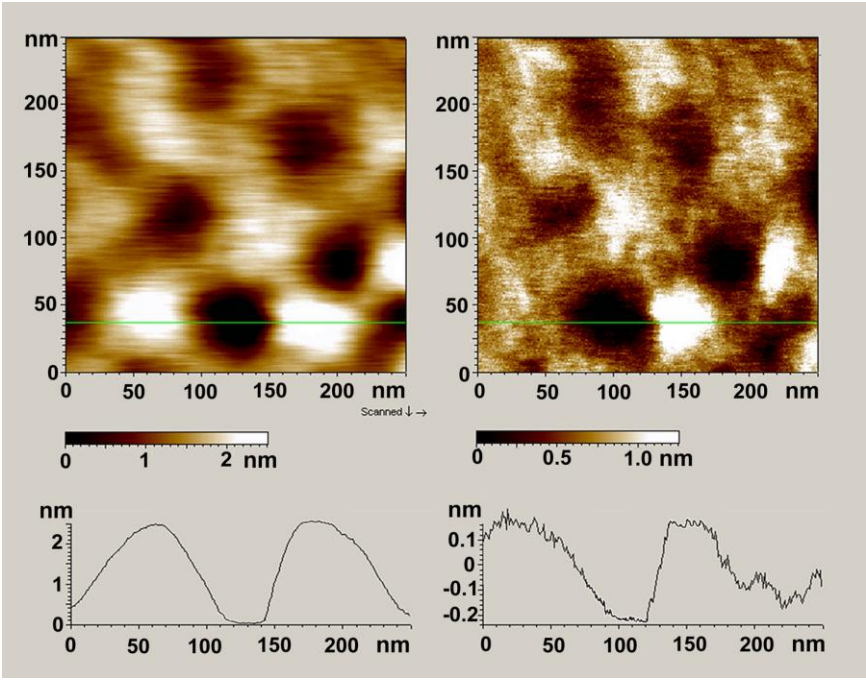

Figure 4.12: Nanostructured layer of P[(NIPAM)$_{95}$-co-(AA)$_{2.5}$-AAC$_8$F$_{17\ 2.2}$] (PDI=1.29) on Mica.
Right: topology image; left: phase image

As Figure 4.12 indicates, the depth of the pores formed by P[$(NIPAM)_{95}$-co-$(AA)_{2.5}$-$AAC_8F_{17\ 2.2}$] is approximately 2 nm, about half than observed when depositing P[$(NIPAM)_{95.3}$-co-$(AA)_{4.7}$]. The curvature decreases to 0.05nm per nm. Consequently, they are more like nano-vales than nano-pores.

4.2.3.3 Deposition of Ultra-Flat Copolymer Layers on Mica

The next logical step, considering that we already have created nano-pores and nano-vales, is the generation of ultra-flat copolymer layers on Mica. We have adapted the spin-casting procedure by adding 1,3-diamino-propane as crosslinker and DCC/NHS as versatile reagents for the formation of stable amide bonds between the copolymer's carboxylate groups. Spincasting of the copolymer without adding the linker did not lead to the formation of ultra-flat surfaces. As it can be seen from Figure 4.13, the overall structure of the crosslinked copolymer layer is similar to the non crosslinked copolymer layer. As the phase image indicates, there are no demixing effects (e.g. zones of different nanoelastic properties) However the differences in height greatly decreased. The observed changes in height are below 0.05nm. AFM techniques are very precise in their height measurements, whereas their spatial resolution is a function of the measurement mode and the employed AFM-tip. Crosslinking of individual copolymer chains (see Figure 4.6) seems to force the deposition of the copolymer chains to assemble in one plane or in a plane-by-plane fashion so that relative maxima and minima in height are avoided. This method of simultaneous copolymer deposition and crosslinking offers an easy and inexpensive alternative to self-assembled monolayers of surfactants or oligopeptides for the reconstitution and stabilization of functional proteins.

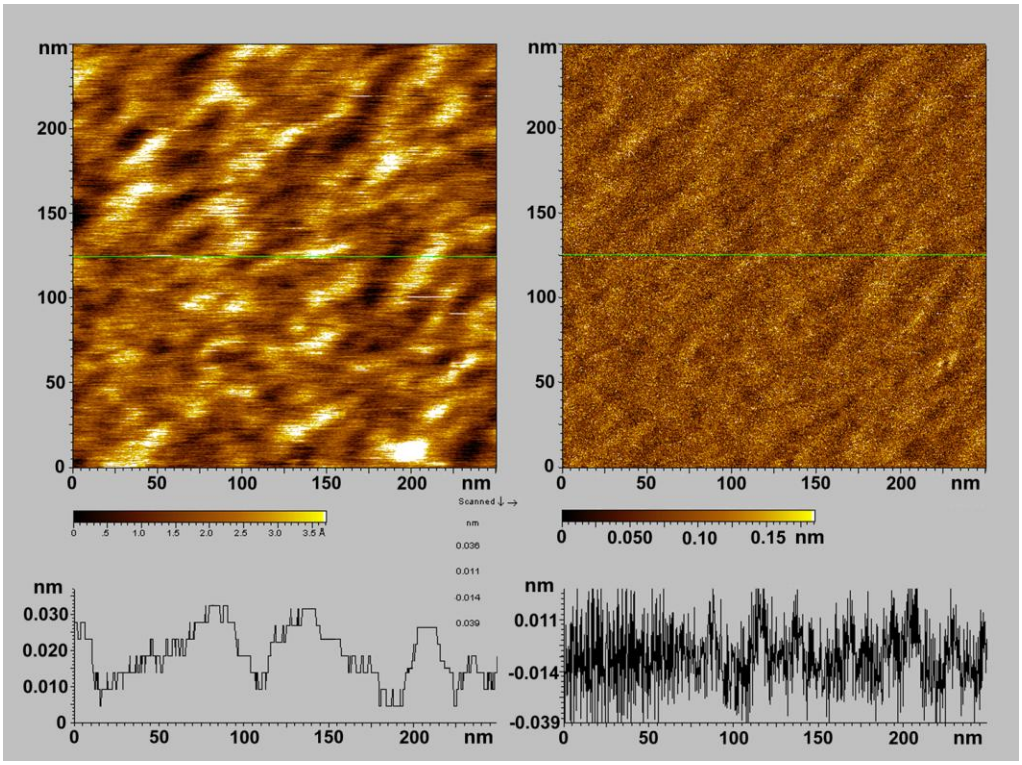

Figure 4.13: Ultraflat layer of P[(NIPAM)$_{95.3}$-co-(AA)$_{4.7}$] (PDI=1.25) on Mica.
(Right: topology image; left: phase image)

4.2.4 Reconstitution of the Mycobacterial Channel Porin MspA from Mycobacterium smegmatis within the Ultraflat Copolymer Layers on Mica.

We were able to reconstitute the mycobacterial porin MspA by immersing the ultraflat (crosslinked) copolymer layer in a phosphate-buffered saline MspA solution for 1h, followed by 10 immersions in ultrapure water. As Figure 4.14 indicates, a fraction of the mycobacterial porin was deposited on top of the copolymer layer (see lower halves of the images), whereas another fraction was able to reconstitute within the copolymer layer (see upper halves). Apparently, the crosslinking procedure does not generate a tightly linked polymer material, because MspA is still able to reconstitute. As numerous studies have indicated[7,12,21-23], the strongly hydrophobic *docking zone*, which is located at the stem of the MspA homo-octamer, facilitates its reconstitution into hydrophobic SAM´s and polymers.

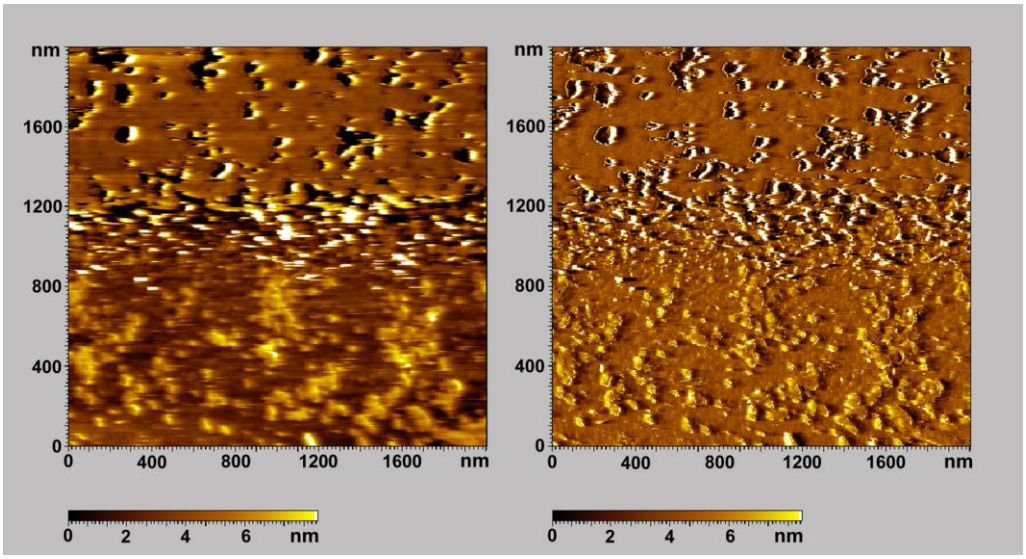

Figure 4.14: MspA on (lower halves of the images) and reconstituted in (upper halves) a 1,3-diamino-propane crosslinked ultraflat layer of P[(NIPAM)$_{95.3}$-co-(AA)$_{4.7}$] (PDI=1.25) on Mica (Right: topology image; left: phase image)

AFM-imaging of the MspA pore in P[(NIPAM)$_{95.3}$-co-(AA)$_{4.7}$] on Mica (see Figure 4.15) revealed that the channel protein is almost completely immersed into the crosslinked copolymer layer. This is a remarkable difference to MspA reconstitution in SAM's [12] where normally the docking zone is in (hydrophobic) contact with the aliphatic chains. Consequently, MspA, which has a lengths of approx. 10 nm, is towering over the SAM and can be easily detected by AFM.[12] Here, MspA extends slightly (< 2nm) beyond the copolymer layer. This means that 8nm of MspA are covered, and electrically insulated. This finding is important, because gold nanoparticles are known to bind strongly to MspA.[23] Embedding of MspA-nanoparticle composites by copolymers will allow the construction of electrically well-insulated noble metal (or magnetic) nanodevices, which could be reversibly charged and de-charged, leading to observable Coulomb-barriers at room temperature.[12] Furthermore, the immersion of MspA in this copolymer layer is much more similar to its natural reconstitution process in the outer cell membrane of *Mycobacterium smegmatis* than within a SAM. This may lead to the construction of models for mycobacterial surfaces.

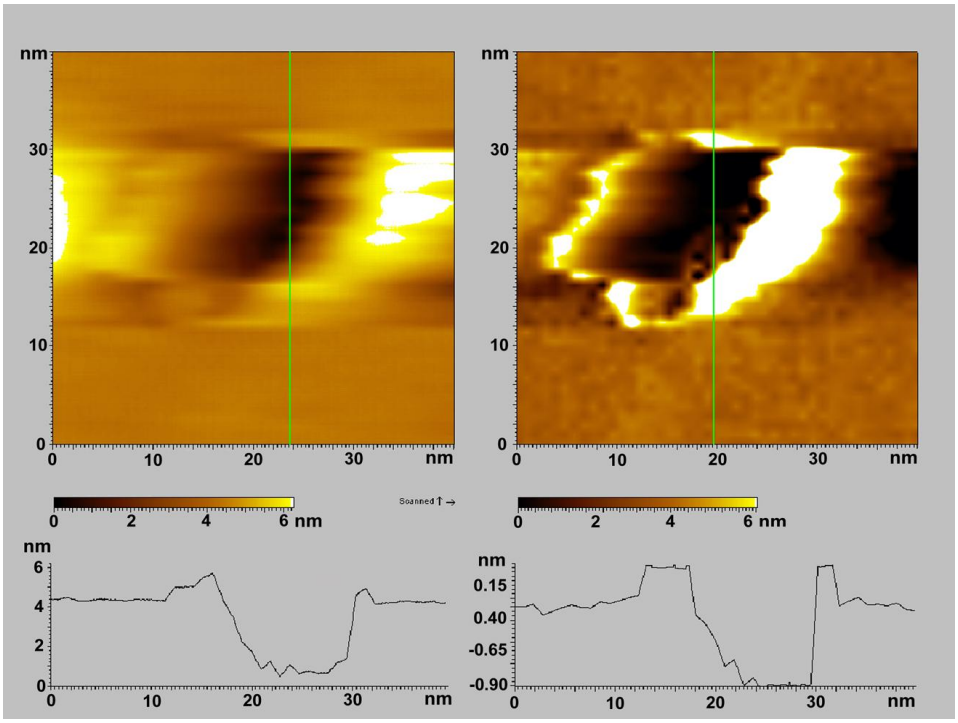

Figure 4.15: MspA in a 1,3-diamino-propane crosslinked ultraflat layer of P[(NIPAM)$_{95.3}$-co-(AA)$_{4.7}$] (PDI=1.25) on Mica

Since the AFM tip diameter exceeded the width of the nanopore, the inner pore of MspA is not completely detectable by AFM, even in the magnetic AC mode. Note that the phase image shows only minor changes in depths. This behavior is most likely caused by the experimentally well-known fact that MspA pores are water filled[7], which leads to the coupling of MspA's wall and pore mobility.

4.3 Experimental Section

All commercial chemicals were purchased from Aldrich Chemical Co. unless otherwise noted. N-isopropylacrylamide, acrylic acid, 2,2'-azoisobutyronitrile, perfluoro-octyl-iodide, 2-mercaptoacetic acid, 1,3-diamino-propane, methanol, tert-butyl alcohol, tetrahydrofuran, n-hexane and diethyl ether were used without purification unless noted otherwise. Mica was freshly cleaved prior to the spin-casting of P(NIPAM-co-AA) and P(NIPAM-co-AA-AC$_8$F$_{17}$) solutions.

CHN-analysis has been performed on a C, H, N, and S- Analyzer (LECO Instruments) in collaboration with the Department of Organic Chemistry of the University of Saarbrücken/Germany.

Gel permeation chromatography (GPC) experiments were carried out with an HP-79911 GP-103 column (PL Gel 10 mm, 100 A, 7.5 x 300 mm) eluted with THF at a flow rate of 0.50 mL min^{-1}. The concentration of the samples injected ($V_{inj.}$ = 1.0 µL) in THF was 1.0 x 10^{-3} g L^{-1}. Calibration was performed using 9 monodisperse PMMA samples. (M_w = 2,000; 8,000; 30,000; 50,000; 75,000; 100,000; 150,000; 200,000; 460,000). The detection of the polymer was achieved using a detection wavelength of λ= 220 nm as well as refractive index detection.

AFM images were recorded using the PicoScan 2000 AFM (Agilent Technologies) in the Magnetic A/C-mode (MACmode).[14] MacMode type II tips from Agilent Technologies were used (tip radii < 7nm, nominal k value = 2.8 N/m, resonance frequency = 50-75 kHz in air). The size of the images was corrected according to the results from a calibration procedure using tris-homoleptic ruthenium(II)-quaterpyridinium-complexes[50] as model compounds.[12]

4.3.1 Synthesis of P(NIPAM-co-AA) Copolymers

4.3.1.1 AIBN-Initiated Radical Polymerizaton

Poly-N-isopropyl-acrylamide-acrylic acid copolymers were synthesized via radical chain polymerization in *t*-butanol using AIBN as radical initiator, as described previously[36]: A solution of NIPAM (10.0g, 0.088 mol) and a given amount of AA (Table 4.1) in tert.-butyl alcohol (50 mL) was stirred at room temperature under N_2 for 2 hours. The solution was heated to 70°C and then a solution of AIBN (60.0 mg) in tert.-butyl alcohol (2 mL), which underwent the same purging procedure, was added at once. The mixture was stirred for 15 h at 70°C. The solvent was evaporated and the copolymer was isolated by successive precipitations from THF solution into n-hexane. The product was dried at 40°C for 24 hours. Copolymers of NIPAM and AA possessing 99, 98, 95 and 90 mol % of NIPAM and 1, 2, 5 and 10 mol % of AA were synthesized following this procedure, The amounts isolated after precipitation ranged from 9.0 to 9.5 g.

4.3.1.2 Living Radical Polymerizaton

The same procedure was performed as described above, except that 0.050g of mercapto-acetic acid (5.4×10^{-4} mol) was added together with the AIBN to the monomer solution.

4.3.1.3 Postpolymerization Modification with Perfluoro-iodo-octane

P(NIPAM-co-AA) (3.0 g) was dissolved in anhydrous DMF (50 mL) and purged with nitrogen for 1h. 1-iodo-perfluoro-n-octane (1.09 g, 0.002 mol) and Na_2CO_3 (2.0 g) were added and the reaction was allowed to proceed for 24 hr at 80°C. The solution was filtered at 60°C in order to remove inorganic salts. After cooling to 10°C, diethyl ether (80 mL) was slowly added to induce polymer precipitation. The polymer was allowed to precipitate at 0°C for 1h. The copolymer was then taken up in 1.0M aqueous HCl at 10°C and precipitated by heating to 50°C. This precipitation procedure was repeated twice. All the P(NIPAM-co-AA/AC_8F_{17})-copolymers (Table 4.2) were synthesized by using this procedure. The yields after precipitation ranged from 2.0 to 2.5 g.

4.3.2 Spincasting Procedure

The P[(NIPAM)-co-(AA)] and P[(NIPAM)-co-(AA)-co-AAC_8F_{17}] copolymers were dissolved in water at pH=4.0 (1.0 gL^{-1}) and stored at 295K. Before spincasting, 1.0 mL of the stock solution and 1.0mL of freshly distilled MeOH were mixed, allowed to ripen for 10min. and then spincast onto freshly cleaved Mica at 3000 rpm. After drying in air for 1 h, the polymer-coated Mica plates were incubated in an environmental chamber (Agilent) at 293°K and 50% relative humidity for 24 h.

4.3.3 In-Situ Crosslinking Procedure

P[$(NIPAM)_{95}$-co-$(AA)_5$] was precipitated from aqueous solution (pH=4.0), dried in high vacuum for 12h and re-dissolved in freshly distilled THF (c=1.0 g L^{-1}). This solution was mixed 1:1 (v/v) with a freshly prepared solution of dicyclohexyl-carbodiimide (DCC) (0.10g L^{-1}) and N-hydroxy-succinimide (NHS) (0.020 gL^{-1}) and 1,3-diaminopropane (0.0180 g L^{-1}) in THF and stirred the mixture for 2h and spincast at 3000 rpm on mica.

4.3.4 Reconstitution of MspA Within the Ultraflat Copolymer Layers on Mica

The Mica plates coated with the crosslinked ultraflat copolymer layer were immersed in a phosphate-buffered aqueous solution (5 mM phosphate-buffer, pH=7.02, 100 mM, NaCl, 2% SDS) of the mycobacterial channel porin MspA (5 micrograms mL^{-1}) for 1h and then immersed 10 times in ultrapure water, dried in air for 10min. and then incubated in an environmental chamber at 295 K and 50% relative humidity for 24 h.

4.4 Conclusions

We have developed a reliable procedure for the deposition of copolymer nanolayers onto Mica surfaces comprising the following steps: A) spincasting of MeOH/H_2O dispersions of poly-N-isopropyl-acrylamide-co-acrylic acid (-co perfluoro-octyl acrylate) copolymers, which are above their respective lower critical solution temperatures (LCST's) onto Mica. B) Drying of the spincast copolymer layers in air. C) Incubation at a defined temperature (295K) in 50% relative humidity. The resulting copolymer layers have been investigated by AFM (magnetic AC mode). Our study has confirmed that the pH of the aqueous copolymer solution prior to deposition is a very important parameter. Copolymer depositions from pH=4.0 gave well-reproducible results. Furthermore, we have investigated the influence of the polydispersity of the synthesized copolymers on their ability to form surface structures. When using N-isopropyl-acrylamide/acrylic acid copolymers, the polydispersity did not have a significant influence: The mean pore diameters were 23.8±4.4nm for P[$(NIPAM)_{95.5}$-co-$(AA)_{4.5}$] (PDI=1.55) and 21.8±4.2nm for P[$(NIPAM)_{95.3}$-co-$(AA)_{4.7}$] (PDI=1.25). Both nanopores were approx. 4nm deep. Modifying the copolymer composition proved to be the key for the reproducible formation of nanopores. When depositing P[$(NIPAM)_{95}$-co-$(AA)_{2.5}$-$AAC_8F_{17\ 2.2}$] (PDI=1.29) on Mica, the resulting mean pore diameter was 35.8±7.1nm. These nano-pores were only 2nm in depth, therefore we'll refer to them rather as nano-vales than as nanopores. Note that only the low-polydispersity copolymer material allowed the reproducible generation of nanostructures polymer layers on Mica.

We have interpreted this behavior as follows: the increased hydrophobic interaction due to the presence of the perfluoro-octyl-ester labels has increased the interaction between the individual copolymer strands. Therefore, the copolymer has developed a greater tendency to deposit onto Mica according to a layer-by-layer mechanism, which results in larger and

shallower pores. The next logical step of this endeavor consisted of the crosslinking of individual polymer chains by employing 1,3-diamino-propane as diamide-linker. As predicted, ultraflat P[$(NIPAM)_{95.3}$-co-$(AA)_{4.7}$] (PDI=1.25) copolymer layers on Mica were formed. These layers have been used as host system for the reconstitution of the mycobacterial porin MspA. MspA did almost completely immerse in the ultraflat and weakly crosslinked copolymer layer proving that these polymer layers could be of future use as components in biolelectronic devices.

4.5 References

[1] Willner, I.; Katz, E. *Bioelectronics: From Theory to Applications*; Wiley/VCH: New York, Weinheim, (2005), pp 475.

[2] Baldrich, Eva; Laczka, Olivier; Javier del Campo, F.; Munoz, Francesc Xavier, Self-assembled monolayers as a base for immunofunctionalization: unequal performance for protein and bacteria detection, *Analytical and Bioanalytical Chemistry*, (2008), 390(6), 1557-1562.

[3] Calvo, Ernesto J.; Rothacher, M. Silvina; Bonazzola, Cecilia; Wheeldon, Ian R.; Salvarezza, Roberto C.; Vela, Maria Elena; Benitez, Guillermo, Biomimetics with a Self-Assembled Monolayer of Catalytically Active Tethered Isoalloxazine on Au, *Langmuir*, (2005), 21(17), 7907-7911.

[4] Roth, Kristian M.; Dontha, Narasaiah; Dabke, Rajeev B.; Gryko, Daniel T.; Clausen, Christian; Lindsey, Jonathan S.; Bocian, David F.; Kuhr, Werner G., Molecular approach toward information storage based on the redox properties of porphyrins in self-assembled monolayers, *Journal of Vacuum Science & Technology*, B: Microelectronics and Nanometer Structures (2000), 18(5), 2359-2364.

[5] Niederweis, Michael; Heinz, Christian; Janik, Katharine; Bossmann, Stefan H., Nanostructuring of Carbon Surfaces by Deposition of a Channel-Forming Protein and Subsequent Polymerization of Methyl Methacrylate Prepolymers, *Nano Letters*, (2001), 1(4), 169-174.

[6] Niederweis, Michael; Heinz, Christian; Janik, Katharine; Bossmann, Stefan H., Nanostructuring by Deposition of Protein Channels Formed on Carbon Surfaces, *Nano Letters*, (2002), 2(11), 1263-1268.

[7] Bossmann, Stefan H.; Janik, Katharine; Pokhrel, Megh Raj; Heinz, Christian; Niederweis, Michael, Reconstitution of a porin from Mycobacterium smegmatis at HOPG covered with hydrophobic host layers, *Surface and Interface Analysis*, (2004), 36(2), 127-134.

[8] Mendes, Paula M., Stimuli-responsive surfaces for bio-applications, *Chemical Society Reviews*, (2008), 37(11), 2512-2529.

[9] Tsukruk, Vladimir V., Adaptive surface nanoassemblies, Tuning macroscopic properties through reversible nanoscale reorganization, *PMSE Preprints*, (2003), 89, 260.

[10] Jonkheijm, Pascal; Weinrich, Dirk; Schroeder, Hendrik; Niemeyer, Christof M.; Waldmann, Herbert, Chemical strategies for generating protein biochips, *Angewandte Chemie*, International Edition, (2008), 47(50), 9618-9647.

[11] Estrela, Pedro; Paul, Debjani; Li, Peng; Keighley, Simon D.; Migliorato, Piero; Laurenson, Sophie; Ferrigno, Paul Ko, Label-Free Detection of Protein interactions with peptide aptamers by open circuit potential measurement, *Electrochimica Acta*, (2008), 53(22), 6489-6496.

[12] Woerner, Michael; Lioubashevski, Oleg; Basel, Matthew T.; Niebler, Sandra; Gogritchiani, Eliso; Egner, Nicole; Heinz, Christian; Hoferer, Juergen; Cipolloni, Michela; Janik, Katharine; Katz, Evgeny; Braun, Andre M.; Willner, Itamar; Niederweis, Michael; Bossmann, Stefan H., Characterization of nanostructured surfaces generated by reconstitution of the porin MspA from Mycobacterium smegmatis, *Small*, (2007), 3(6), 1084-1097.

[13] Das, Rupa; Kiley, Patrick J.; Segal, Michael; Norville, Julie; Yu, A. Amy; Wang, Leyu; Trammell, Scott A.; Reddick, L. Evan; Kumar, Rajay; Stellacci, Francesco; Lebedev, Nikolai; Schnur, Joel; Bruce, Barry D.; Zhang, Shuguang; Baldo, Marc, Integration of Photosynthetic Protein Molecular Complexes in Solid-State Electronic Devices, *Nano Letters*, (2004), 4(6), 1079-1083.

[14] Han, Wenhai; Lindsay, S. M.; Jing, Tianwei., A magnetically driven oscillating probe microscope for operation in liquids, *Applied Physics Letters*, (1996), 69(26), 4111-4113.

[15] Rapoport, Natalya, Physical stimuli-responsive polymeric micelles for anti-cancer drug delivery, *Progress in Polymer Science*, (2007), 32(8-9), 962-990.

[16] Chen, J.-P.; Cheng, T.-H., *Colloids and Surfaces A: Physicochemical and Engineering Aspects*, (2007), 313-314, 254-259.

[17] Pokhrel, Megh Raj; Bossmann, Stefan H., Synthesis, Characterization, and First Application of High Molecular Weight Polyacrylic Acid Derivatives Possessing Perfluorinated Side Chains and Chemically Linked Pyrene Labels, *Journal of Physical Chemistry, B* (2000), 104(10), 2215-2223.

[18] Overney, R. M.; Buenviaje, C.; Luginbuhl, R.; Dinelli, F., Glass and structural transitions measured at polymer surfaces on the nanoscale, *Journal of Thermal Analysis and Calorimetry*, (2000), 59(1-2), 205-225.

[19] Niederweis, Michael., Mycobacterial porins - new channel proteins in unique outer membranes, *Molecular Microbiology*, (2003), 49(5), 1167-1177.

[20] Heinz Christian; Roth Eva; Niederweis Michael, Purification of porins from Mycobacterium smegmatis, *Methods in molecular biology*, (Clifton, N.J.) (2003), 228 139-50.

[21] Faller Michael; Niederweis Michael; Schulz Georg E., The structure of a mycobacterial outer-membrane channel, *Science* (New York, N.Y.), (2004), 303(5661), 1189-92.

[22] Basel, Matthew T.; Dani, Raj Kumar; Kang, Myungshim; Pavlenok, Mikhail; Chikan, Viktor; Smith, Paul E.; Niederweis, Michael; Bossmann, Stefan H., Direct Observation of Gold Nanoparticle Assemblies with the Porin MspA on Mica, *ACS Nano*, (2009), 3(2), 462-466.

[23] Dani, Raj Kumar; Kang, Myungshim; Kalita, Mausam; Smith, Paul E.; Bossmann, Stefan H.; Chikan, Viktor, MspA Porin-Gold Nanoparticle Assemblies: Enhanced Binding through a Controlled Cysteine Mutation, *Nano Letters*, (2008), 8(4), 1229-1236.

[24] Liu, Roger C. W.; Cantin, Sophie; Perrot, Francoise; Winnik, Francoise M., Effects of polymer architecture and composition on the interfacial properties of temperature-responsive hydrophobically-modified poly(N-isopropylacrylamide), *Polymers for Advanced Technologies*, (2006), 17(9-10), 798-803.

[25] Bunker, Bruce C.; Huber, Dale L.; Manginell, Ronald P.; Kim, Byung-Il; Boal, Andrew K.; Bachand, George D.; Rivera, Susan B.; Bauer, Joseph M.; Matzke, Carolyn M., Incorporation of bioactive materials into integrated systems, *Proceedings of SPIE-The International Society for Optical Engineering*, (2003), 5220(Nanofabrication Technologies), 28-36.

[26] Schild, Howard G.; Muthukumar, M.; Tirrell, David A., Cononsolvency in mixed aqueous solutions of poly(N-isopropylacrylamide), *Macromolecules*, (1991), 24(4), 948-52.

[27] Winnik, Francoise M.; Ringsdorf, H.; Venzmer, J., Methanol-water as a co-nonsolvent system for poly(N-isopropylacrylamide), *Macromolecules*, (1990), 23(8), 2415-16.

[28] Winnik, Francoise M.; Ottaviani, M. Francesca; Bossmann, Stefan H.; Pan, Wenseng; Garcia-Garibay, Miguel; Turro, Nicholas J., Cononsolvency of poly(N-isopropylacrylamide): a look at spin-labeled polymers in mixtures of water and tetrahydrofuran, *Macromolecules*. (1993), 26(17), 4577-85.

[29] Winnik, Francoise M.; Ottaviani, M. Francesca; Bossmann, Stefan H.; Garcia-Garibay, M.; Turro, Nicholas J., Consolvency of poly(N-isopropylacrylamide) in mixed water-methanol solutions: a look at spin-labeled polymers, *Macromolecules*, (1992), 25(22), 6007-17.

[30] Cho, C.; Jung, J.; Sung, Y.; Lee, Y., *Macromol Chem Rapid Commun*,1(994), 15, 727-732.

[31] Yoo, Mi Hyong; Sung, Yong Kiel; Cho, Chong Su; Lee, Young Moo, Effect of polymer complex formation on the cloud-point of poly(N-isopropylacrylamide) (PNIPAAm) in the poly(NIPAAm-co-acrylic acid): polyelectrolyte complex between poly(acrylic acid) and poly(allylamine), *Polymer*, (1997), 38(11), 2759-2765.

[32] Taylor, Lloyd D.; Cerankowski, Leon D., Preparation of films exhibiting a balanced temperature dependence to permeation by aqueous solution, Lower consolute behavior, *Journal of Polymer Science, Polymer Chemistry Edition*, (1975), 13(11), 2551-70.

[33] Priest, John H.; Murray, Sheryl L.; Nelson, R. John; Hoffman, Allan S., Lower critical solution temperatures of aqueous copolymers of N-isopropylacrylamide and other N-substituted acrylamides, ACS Symposium Series, (1987), 350(Reversible Polym. Gels Relat. Syst.), 255-64.

[34] Hahn, Mathias; Goernitz, Eckhard; Dautzenberg, Herbert, Synthesis and Properties of Ionically Modified Polymers with LCST Behavior, *Macromolecules*, (1998), 31(17), 5616-5623.

[35] Chen, Guohua; Hoffman, Allan S., A new temperature- and pH-responsive copolymer for possible use in protein conjugation, *Macromolecular Chemistry and Physics*, (1995), 196(4), 1251-9.

[36] Ottaviani, M. Francesca; Winnik, Francoise M.; Bossmann, Stefan H.; Turro, Nicholas J., Phase separation of poly(N-isopropylacrylamide) in mixtures of water and methanol: a spectroscopic study of the phase-transition process with a polymer tagged with a fluorescent dye and a spin label, *Helvetica Chimica Acta*, (2001), 84(9), 2476-2492.

[37] Benrebouh, A.; Avoce, D.; Zhu, X. X., Thermo- and pH-sensitive polymers containing cholic acid derivatives, *Polymer*, (2001), 42(9), 4031-4038.

[38] Bignotti, F.; Penco, M.; Sartore, L.; Peroni, I.; Mendichi, R.; Casolaro, M.; D'Amore, A., Synthesis, characterisation and solution behaviour of thermo- and pH-responsive polymers bearing L-leucine residues in the side chains, *Polymer*, (2000), 41(23), 8247-8256.

[39]Matyjaszewski, K.; Davis, T. P., *Handbook of Radical Polymerization*; Wiley-IEEE: New York, (2003), 920.

[40] Das, K. K.; Somasundaran, P., Ultra-low dosage flocculation of alumina using polyacrylic acid, Colloids and Surfaces, A: *Physicochemical and Engineering Aspects* (2001), 182(1-3), 25-33.

[41] Nair, A. Sreekumaran; Kimura, Keisaku, Charge Transport Behavior of N-(2-Mercaptopropionyl glycine)-Protected Gold Clusters with Temperature, *Langmuir*, (2009), 25(3), 1750-1756.

[42] Murphy C. J.; Arkin M. R.; Jenkins Y.; Ghatlia N. D.; Bossmann S. H.; Turro N. J.; Barton J. K., Long-range photoinduced electron transfer through a DNA helix, *Science* (New York, N.Y.) (1993), 262(5136), 1025-9.

[43] Montagne, Franck; Polesel-Maris, Jerome; Pugin, Raphael; Heinzelmann, Harry, Poly(N-isopropylacrylamide) Thin Films Densely Grafted onto Gold Surface: Preparation, Characterization, and Dynamic AFM Study of Temperature-Induced Chain Conformational Changes, *Langmuir*, (2009), 25(2), 983-991.

[44] Schmidt, Stephan; Motschmann, Hubert; Hellweg, Thomas; von Klitzing, Regine, Thermoresponsive surfaces by spin-coating of PNIPAM-co-PAA microgels: A combined AFM and ellipsometry study, *Polymer*, (2008), 49(3), 749-756.

[45] Song, M.; Guo, D.; Pan, C.; Jiang, H.; Chen, C.; Zhang, R.; Gu, Z.; Wang, X., (2008), 19, 165102/1-165102/7.

[46] Heinz, P.; Bretagnol, F.; Mannelli, I.; Sirghi, L.; Valsesia, A.; Ceccone, G.; Gilliland, D.; Landfester, K.; Rauscher, H.; Rossi, F., Poly(N-isopropylacrylamide) Grafted on Plasma-Activated Poly(ethylene oxide): Thermal Response and Interaction With Proteins, *Langmuir* , (2008), 24(12), 6166-6175.

[47] Lapeyre, Veronique; Renaudie, Natacha; Dechezelles, Jean-Francois; Saadaoui, Hassan; Ravaine, Serge; Ravaine, Valerie, Multiresponsive Hybrid Microgels and Hollow Capsules with a Layered Structure, *Langmuir*, (2009), 25(8), 4659-4667.

[48] Liu, Roger C. W.; Segui, Florence; Viitala, Tapani; Winnik, Francoise M., Temperature responsive LB films formed at the air/water interface by poly(N-isopropylacrylamide)s bearing fluorocarbon and/or hydrocarbon chains, *PMSE Preprints*, (2004), 90 105-106.

[49] http://rsb.info.nih.gov/nih-image/

[50] Shi, Aibin; Pokhrel, Megh Raj; Bossmann, Stefan H., Synthesis of highly charged ruthenium(II)-quaterpyridinium complexes: a bottom-up approach to monodisperse nanostructures, *Synthesis*, (2007), (4), 505-514.

Appendix A - ^{1}H and ^{13}C NMR Spectra

Figure A.1: - (a) ^{1}H NMR of Compound 1 (b) ^{13}C NMR of Compound 1

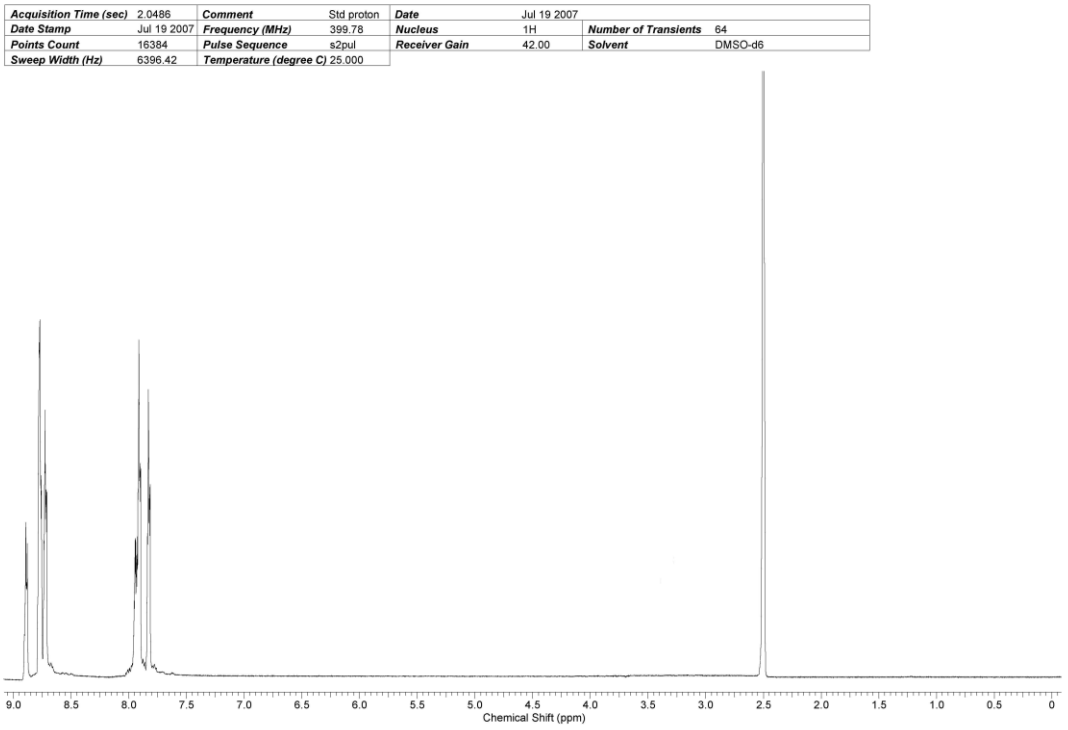

(a)

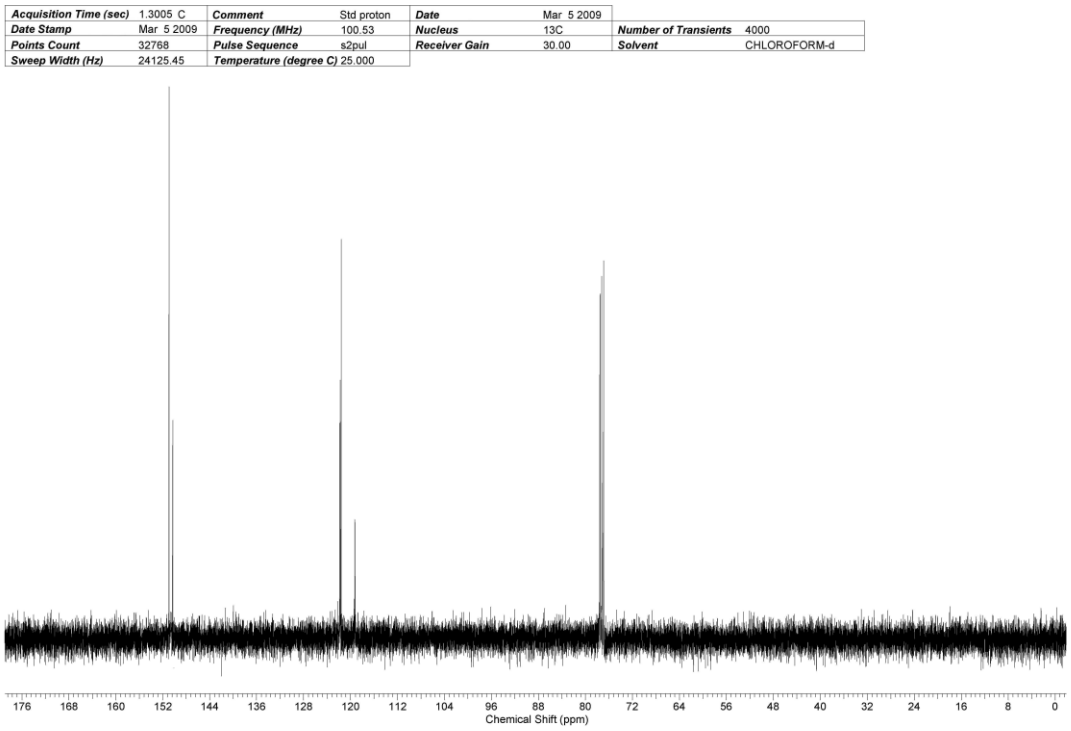

(b)

Figure A.2: - (a) ^{1}H NMR of Compound 2 (b) ^{13}C NMR of Compound 2

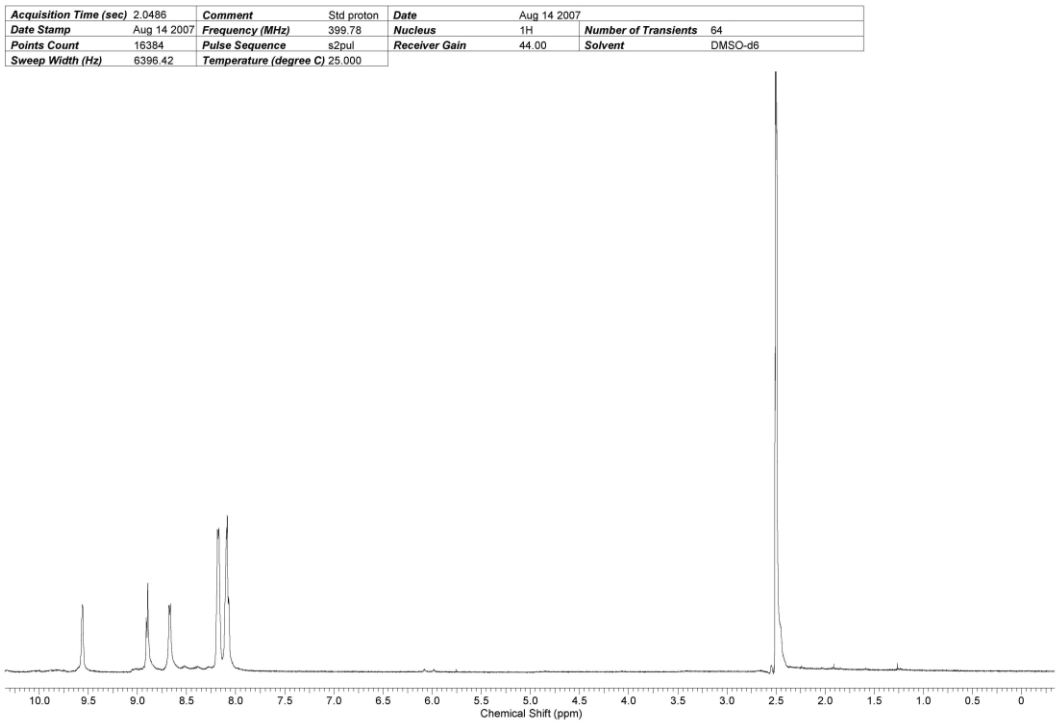

(a)

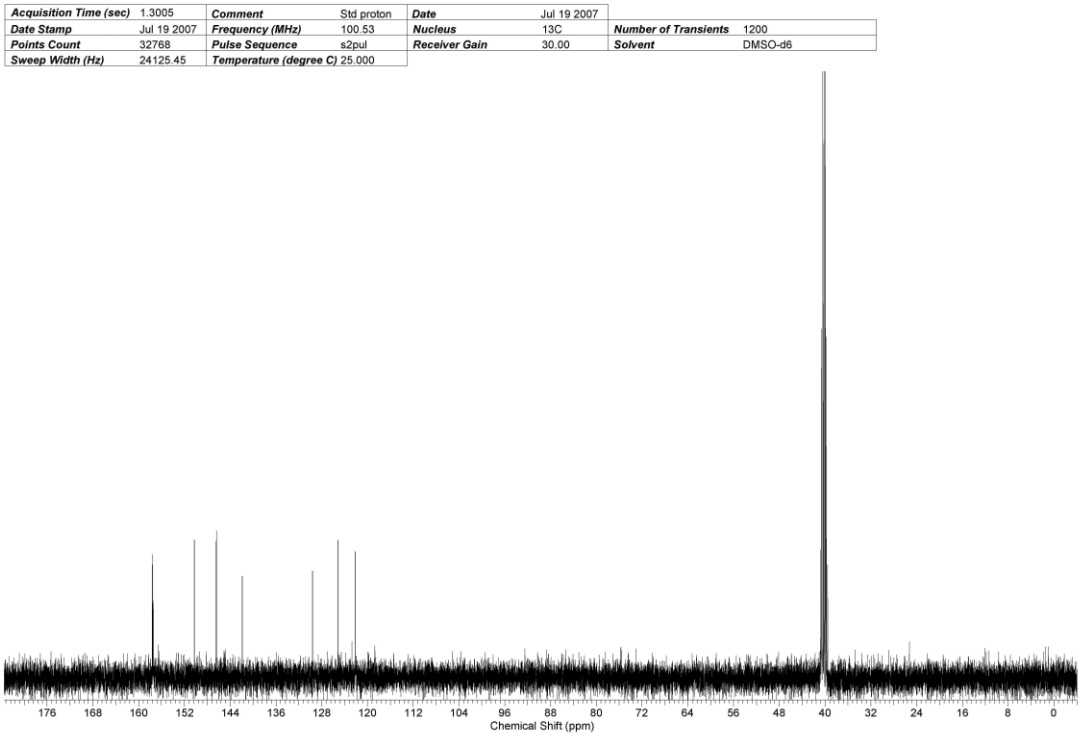

(b)

Figure A.3: - (a) ^{1}H NMR of Compound 3 (b) ^{1}H NMR of Compound 4

Acquisition Time (sec)	1.9945	***Comment***	STANDARD 1H OBSERVE			***Date***	Apr 14 2008
Date Stamp	Apr 14 2008			***Frequency (MHz)***	199.98	***Nucleus***	1H
Number of Transients	64	***Original Points Count***	5984	***Points Count***	8192	***Pulse Sequence***	s2pul
Solvent	DMSO-d6	***Spectrum Offset (Hz)***	1002.3162	***Sweep Width (Hz)***	3000.30	***Temperature (degree C)***	29.000

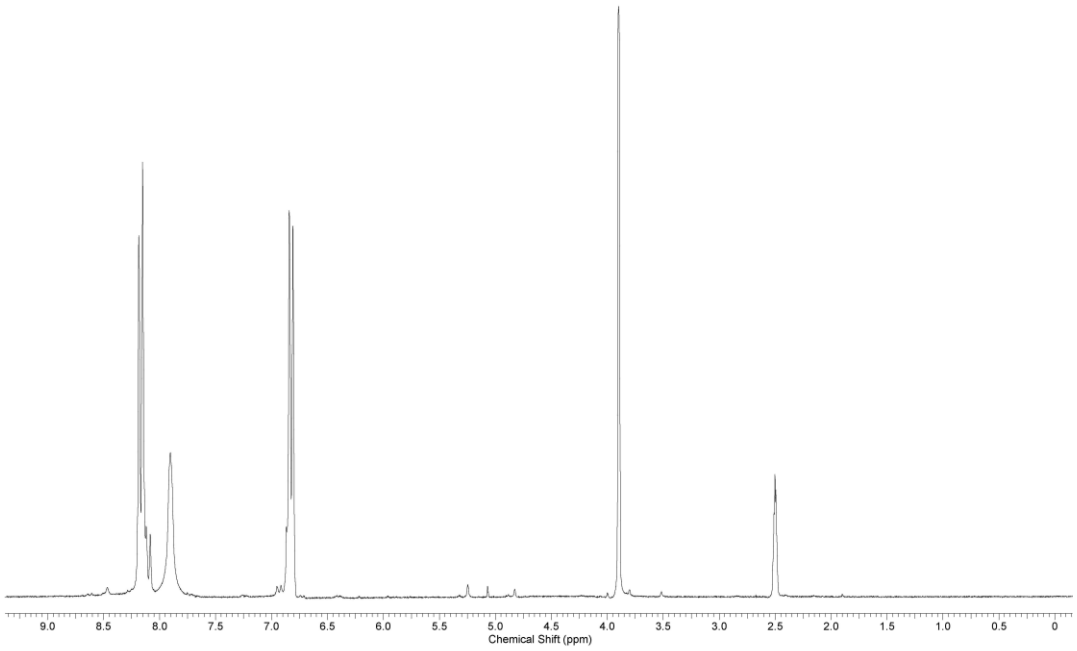

(a)

Acquisition Time (sec)	1.9945	***Comment***	STANDARD 1H OBSERVE			***Date***	Jul 17 2008
Date Stamp	Jul 17 2008	***Frequency (MHz)***	199.98	***Nucleus***	1H	***Number of Transients***	100
Points Count	8192	***Pulse Sequence***	s2pul	***Receiver Gain***	30.00	***Solvent***	DMSO-d6
Sweep Width (Hz)	3000.30	***Temperature (degree C)***	29.000				

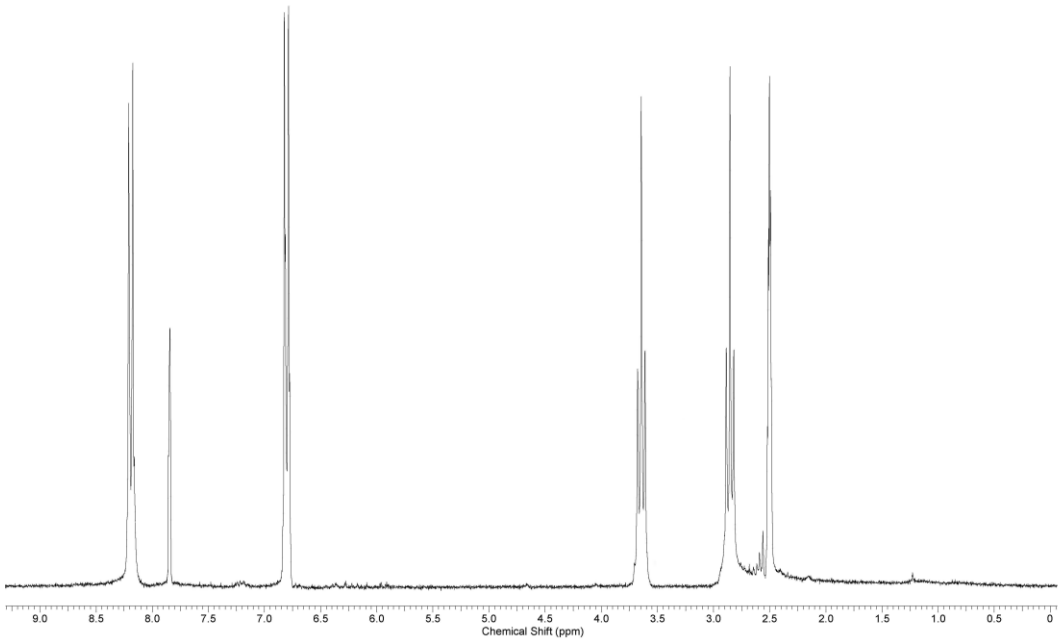

(b)

Figure A.4: - (a) ^{1}H NMR of Compound 5 (b) ^{1}H NMR of Compound 6

Acquisition Time (sec)	1.9945	***Comment***	STANDARD 1H OBSERVE			***Date***	Mar 11 2009
Date Stamp	Mar 11 2009			***Frequency (MHz)***	199.98	***Nucleus***	1H
Number of Transients	64	***Original Points Count***	5984	***Points Count***	8192	***Pulse Sequence***	s2pul
Solvent	DMSO-d6	***Spectrum Offset (Hz)***	962.1274	***Sweep Width (Hz)***	3000.30	***Temperature (degree C)***	29.000

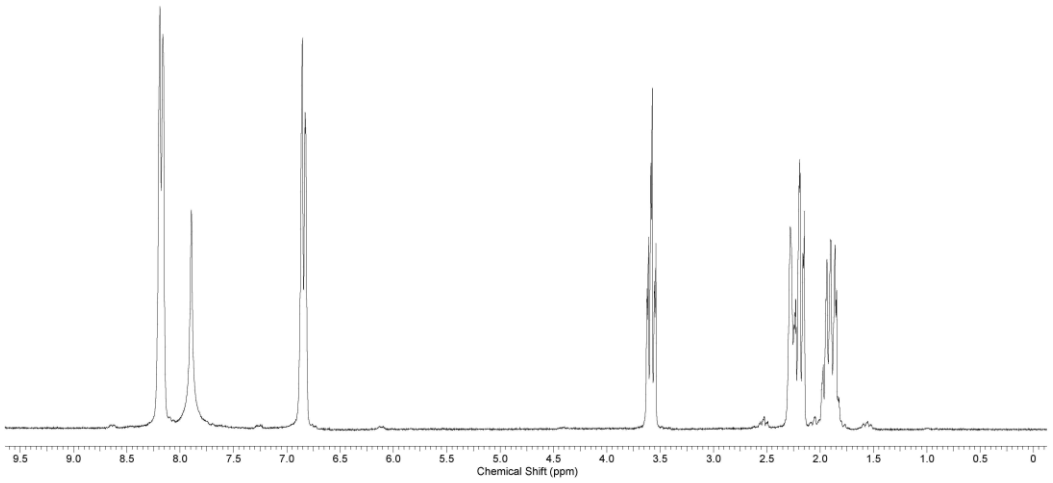

(a)

Acquisition Time (sec)	1.9945	***Comment***	STANDARD 1H OBSERVE			***Date***	Mar 9 2009
Date Stamp	Mar 9 2009	***Frequency (MHz)***	199.98	***Nucleus***	1H	***Number of Transients***	64
Points Count	8192	***Pulse Sequence***	s2pul	***Receiver Gain***	28.00	***Solvent***	DMSO-d6
Sweep Width (Hz)	3000.30	***Temperature (degree C)***	29.000				

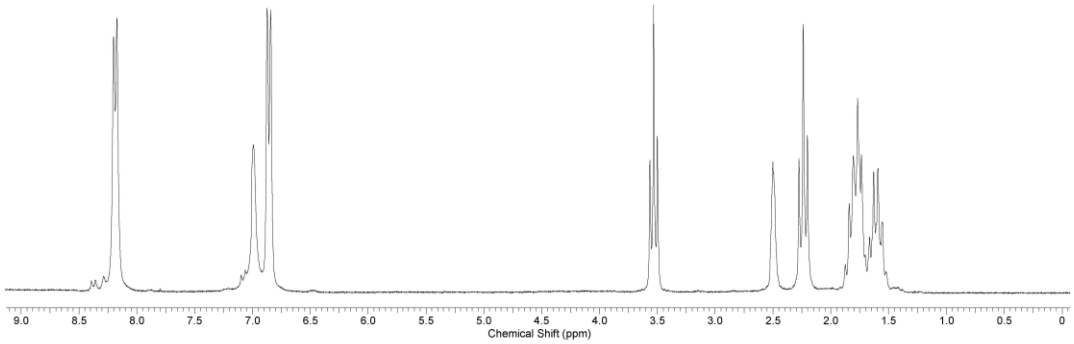

(b)

Figure A.5: - (a) ^{1}H NMR of Compound 7 (b) ^{13}C NMR of Compound 7

Acquisition Time (sec)	1.9945	***Comment***	STANDARD 1H OBSERVE			***Date***	Apr 13 2009
Date Stamp	Apr 13 2009			***Frequency (MHz)***	199.98	***Nucleus***	1H
Number of Transients	64	***Original Points Count***	5984	***Points Count***	8192	***Pulse Sequence***	s2pul
Solvent	DMSO-d6	***Spectrum Offset (Hz)***	1002.3162	***Sweep Width (Hz)***	3000.30	***Temperature (degree C)***	29.000

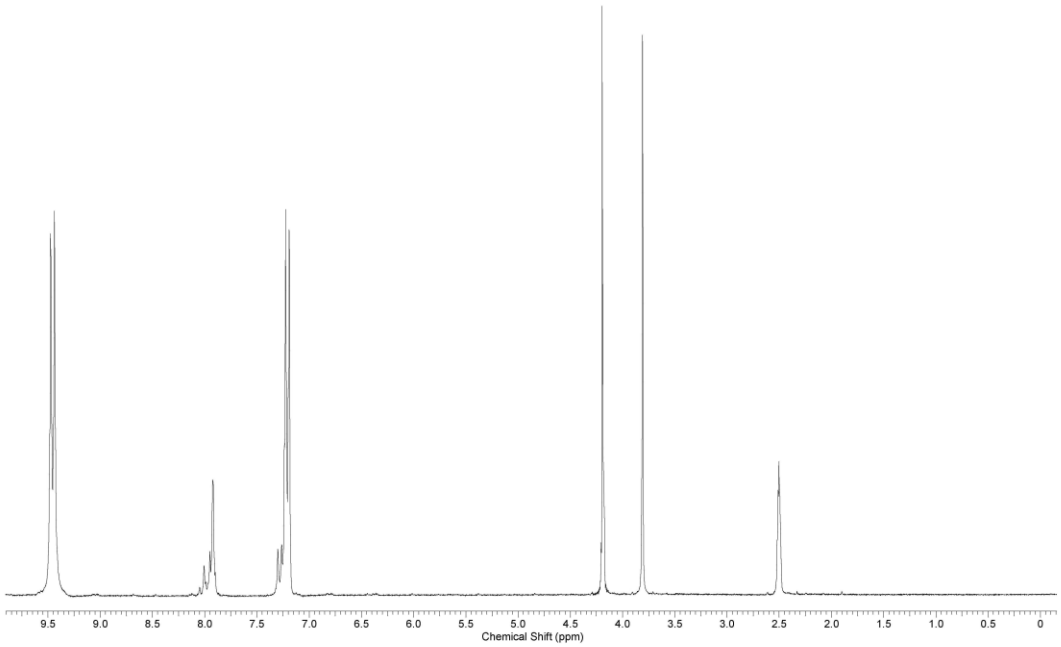

(a)

Acquisition Time (sec)	1.4976	***Comment***	13C OBSERVE			***Date***	Apr 13 2009
Date Stamp	Apr 13 2009			***Frequency (MHz)***	50.29	***Nucleus***	13C
Number of Transients	16000	***Original Points Count***	18720	***Points Count***	32768	***Pulse Sequence***	s2pul
Solvent	DMSO-d6	***Spectrum Offset (Hz)***	4879.4790	***Sweep Width (Hz)***	12500.00	***Temperature (degree C)***	29.000

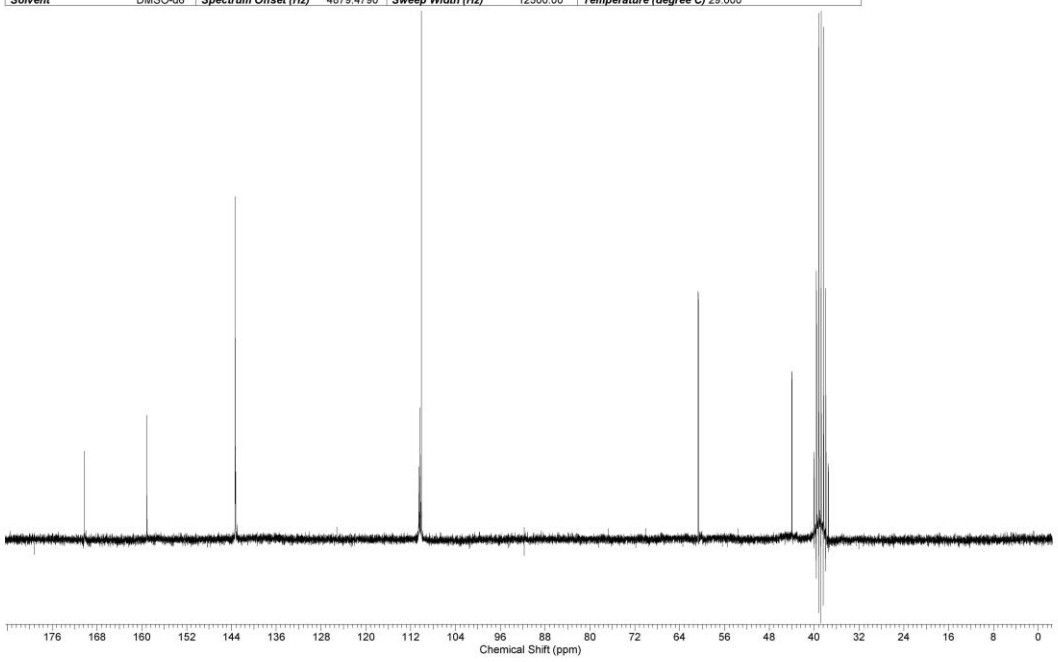

(b)

Figure A.6: - (a) ^{1}H NMR of Compound 8 (b) ^{13}C NMR of Compound 8

Acquisition Time (sec)	2.0487	***Comment***	Std proton	***Date***	Oct 29 2008		
Date Stamp	Oct 29 2008	***Frequency (MHz)***	399.76	***Nucleus***	1H	***Number of Transients***	100
Points Count	16384	***Pulse Sequence***	s2pul	***Receiver Gain***	48.00	***Solvent***	DMSO-d6
Sweep Width (Hz)	6395.91	***Temperature (degree C)***	25.000				

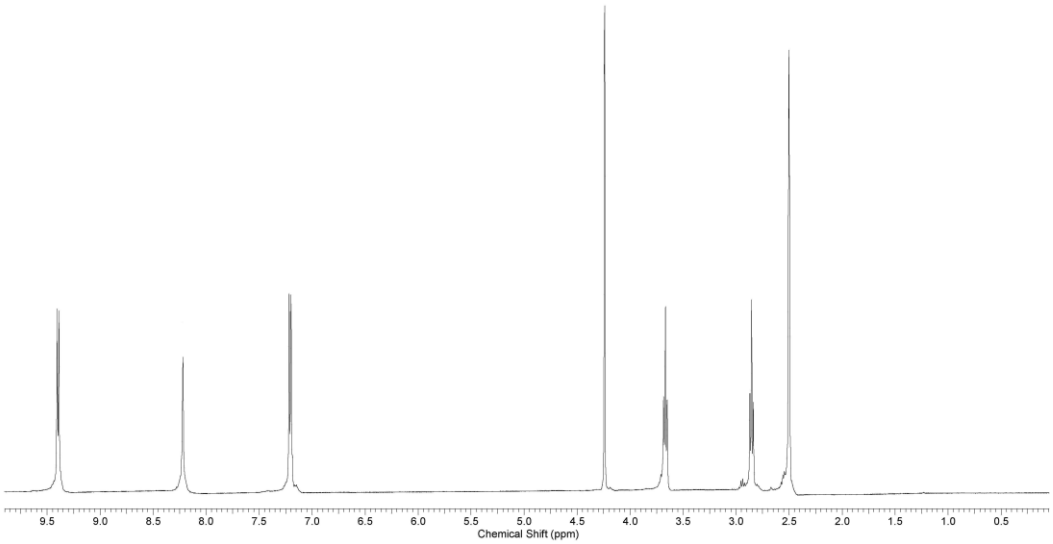

(a)

Acquisition Time (sec)	1.3005	***Comment***	Std proton	***Date***	Apr 13 2009		
Date Stamp	Apr13 2009	***Frequency (MHz)***	100.53	***Nucleus***	13C	***Number of Transients***	12000
Points Count	32768	***Pulse Sequence***	s2pul	***Receiver Gain***	30.00	***Solvent***	DMSO-d6
Spectrum Offset (Hz)	10554.2480	***Sweep Width (Hz)***	24125.45	***Temperature (degree C)***	25.000		

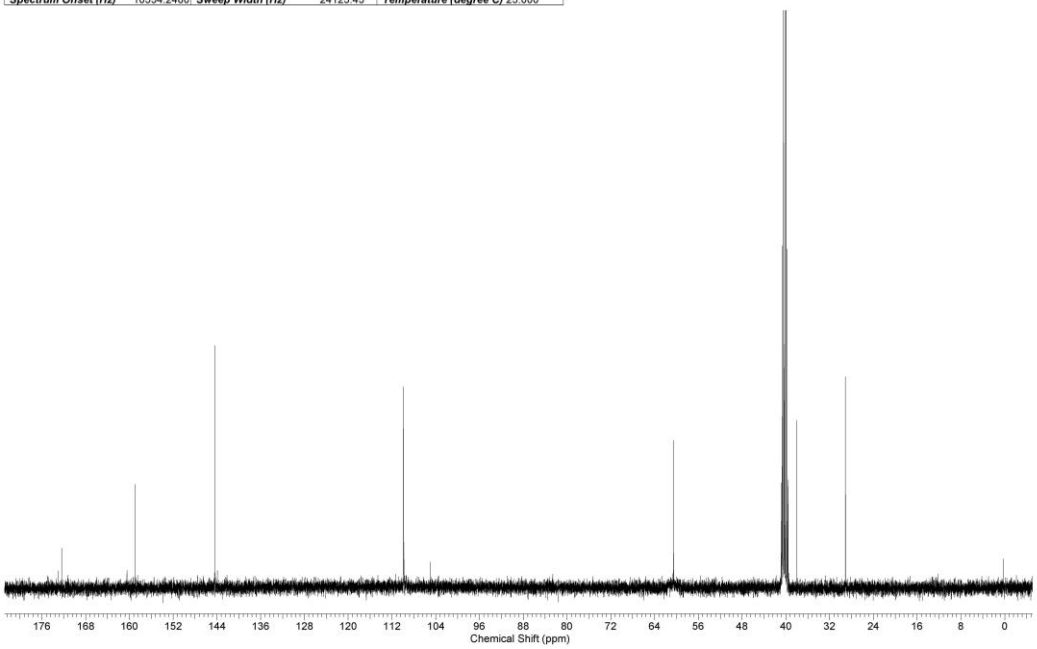

(b)

Figure A.7: - (a) ^{1}H NMR of Compound 9 (b) ^{13}C NMR of Compound 9

Acquisition Time (sec)	2.0487	***Comment***	Std proton	***Date***	Mar 11 2009		
Date Stamp	Mar 11 2009	***Frequency (MHz)***	399.75	***Nucleus***	1H	***Number of Transients***	10
Points Count	16384	***Pulse Sequence***	s2pul	***Receiver Gain***	38.00	***Solvent***	DMSO-d6
Sweep Width (Hz)	6395.91	***Temperature (degree C)***	25.000				

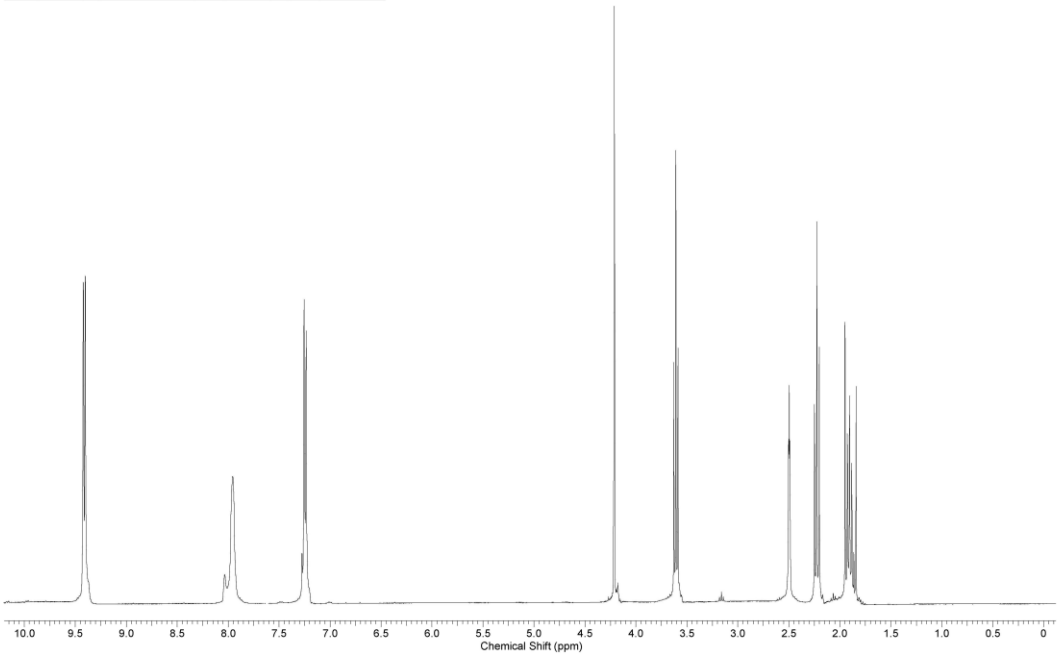

(a)

Acquisition Time (sec)	1.3005	***Comment***	Std proton	***Date***	Mar 11 2009		
Date Stamp	Mar 11 2009	***Frequency (MHz)***	100.53	***Nucleus***	13C	***Number of Transients***	2500
Points Count	32768	***Pulse Sequence***	s2pul	***Receiver Gain***	30.00	***Solvent***	DMSO-d6
Spectrum Offset (Hz)	10554.2480	***Sweep Width (Hz)***	24125.45	***Temperature (degree C)***	25.000		

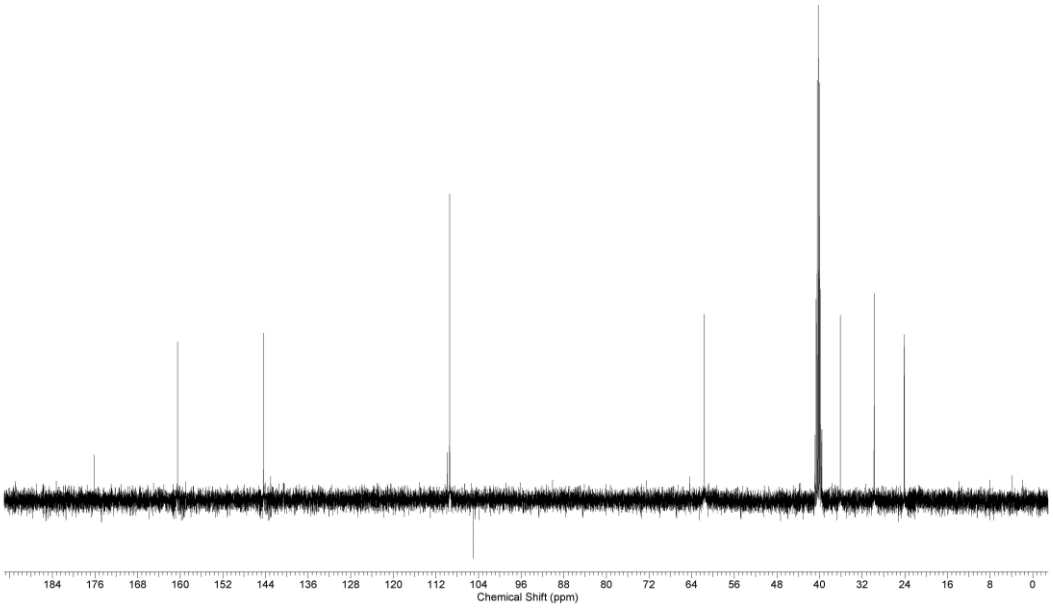

(b)

Figure A.8: (a) ^{1}H NMR of Compound 10 (b) ^{13}C NMR of Compound 10

Acquisition Time (sec)	2.0487	***Comment***	Std proton	***Date***	Mar 9 2009		
Date Stamp	Mar 9 2009	***Frequency (MHz)***	399.75	***Nucleus***	1H	***Number of Transients***	64
Points Count	16384	***Pulse Sequence***	s2pul	***Receiver Gain***	36.00	***Solvent***	DMSO-d6
Sweep Width (Hz)	6395.91	***Temperature (degree C)***	25.000				

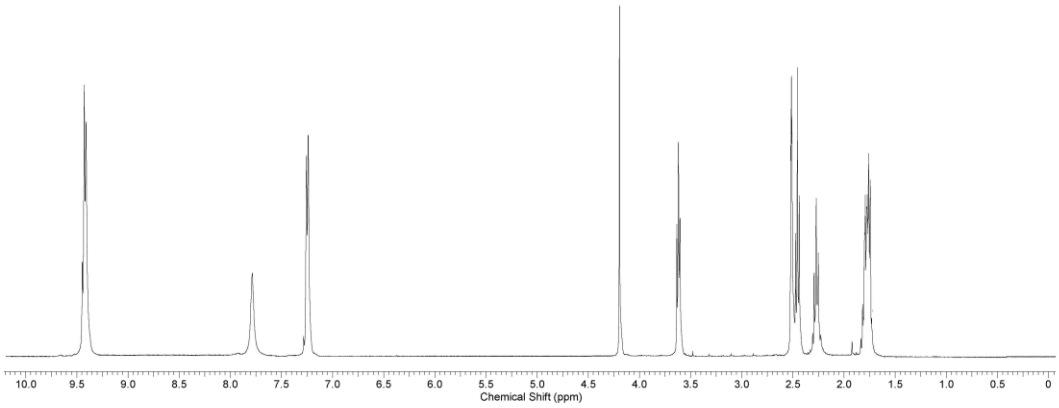

(a)

Acquisition Time (sec)	1.4976	***Comment***	13C OBSERVE			***Date***	Mar 9 2009
Date Stamp	Mar 9 2009			***Frequency (MHz)***	50.29	***Nucleus***	13C
Number of Transients	15000	***Original Points Count***	18720	***Points Count***	32768	***Pulse Sequence***	s2pul
Solvent	DMSO-d6	***Spectrum Offset (Hz)***	4879.4790	***Sweep Width (Hz)***	12500.00	***Temperature (degree C)***	29.000

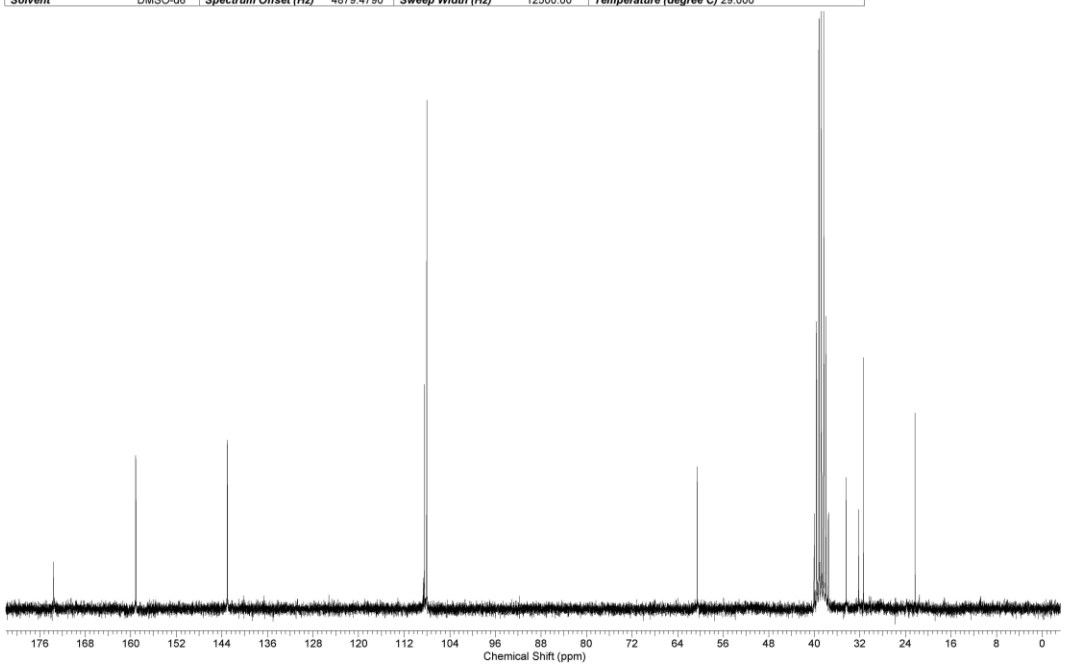

(b)

Figure A.9: - (a) ^{1}H NMR of Compound 11 (b) ^{13}C NMR of Compound 11

Acquisition Time (sec)	2.0487	***Comment***	Std proton	***Date***	Sep 10 2007		
Date Stamp	Sep 10 2007	***Frequency (MHz)***	399.75	***Nucleus***	1H	***Number of Transients***	64
Points Count	16384	***Pulse Sequence***	s2pul	***Receiver Gain***	46.00	***Solvent***	DMSO-d6
Sweep Width (Hz)	6395.91	***Temperature (degree C)***	25.000				

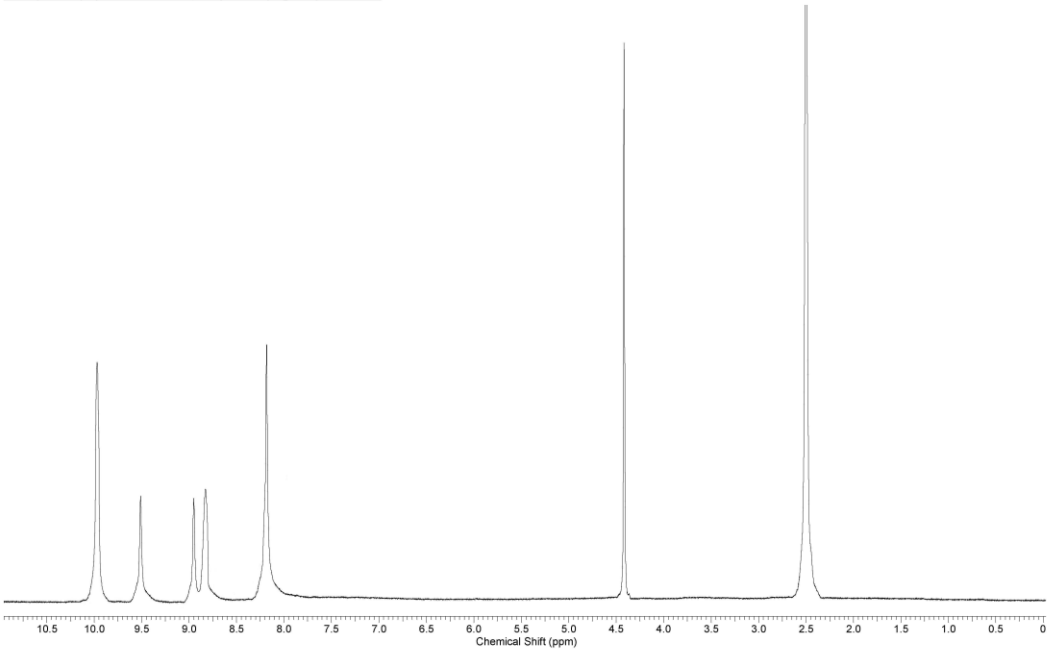

(a)

Acquisition Time (sec)	1.4976	***Comment***	13C OBSERVE			***Date***	Mar 12 2009
Date Stamp	Mar 12 2009			***Frequency (MHz)***	50.29	***Nucleus***	13C
Number of Transients	12000	***Original Points Count***	18720	***Points Count***	32768	***Pulse Sequence***	s2pul
Solvent	DMSO-d6	***Spectrum Offset (Hz)***	4879.4790	***Sweep Width (Hz)***	12500.00	***Temperature (degree C)***	29.000

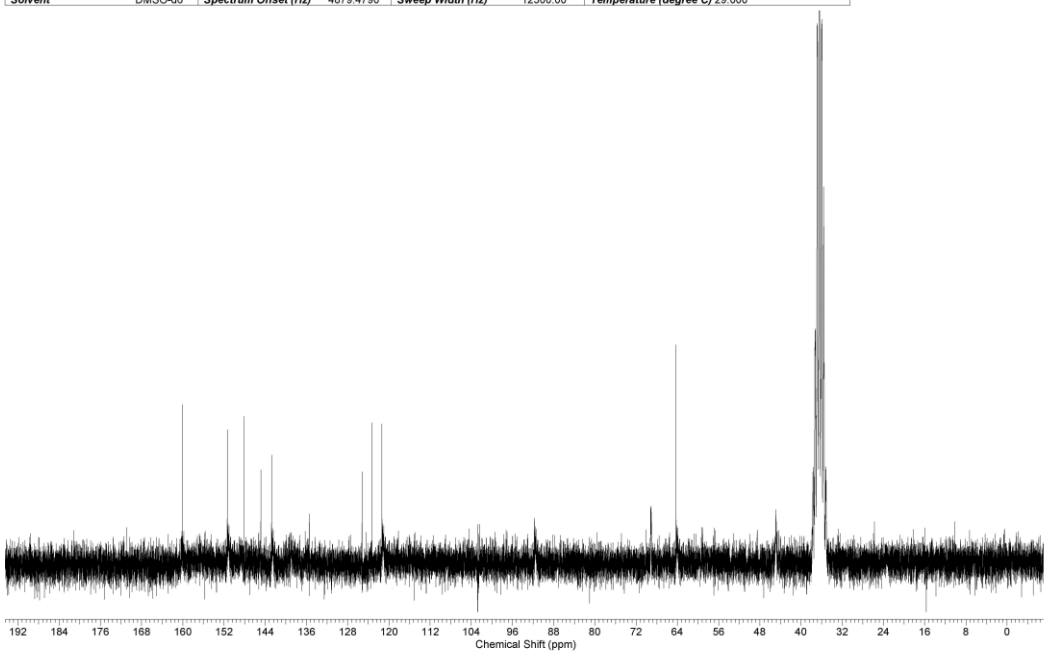

(b)

Figure A.10: - (a) ^{1}H NMR of Compound 12 (b) ^{13}C NMR of Compound 12

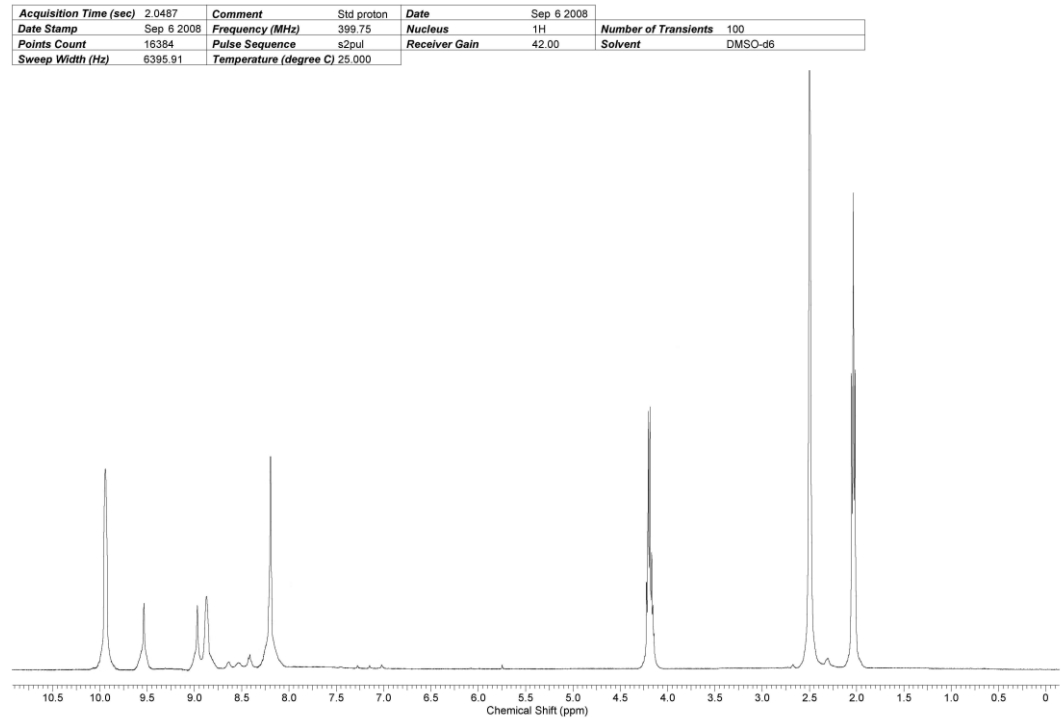

(a)

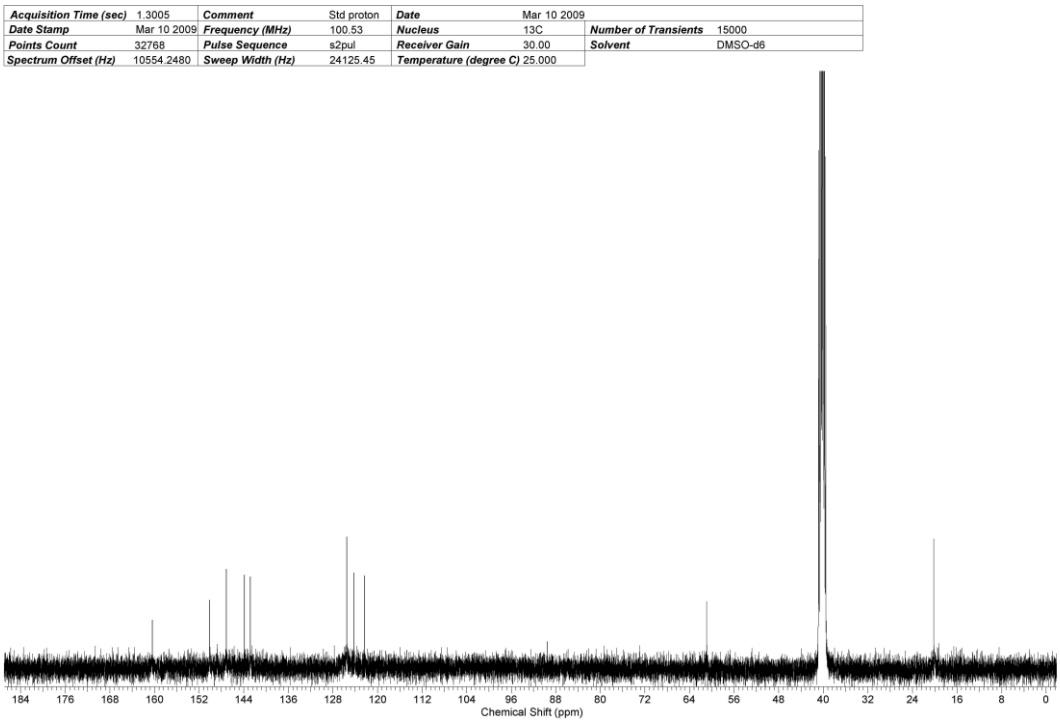

(b)

Figure A.11: - (a) ^{1}H NMR of Compound 13 (b) ^{13}C NMR of Compound 13

Acquisition Time (sec)	2.0487	***Comment***	Std proton	***Date***	Aug 6 2008		
Date Stamp	Aug 6 2008	***Frequency (MHz)***	399.75	***Nucleus***	1H	***Number of Transients***	64
Points Count	16384	***Pulse Sequence***	s2pul	***Receiver Gain***	42.00	***Solvent***	DMSO-d6
Sweep Width (Hz)	6395.91	***Temperature (degree C)***	25.000				

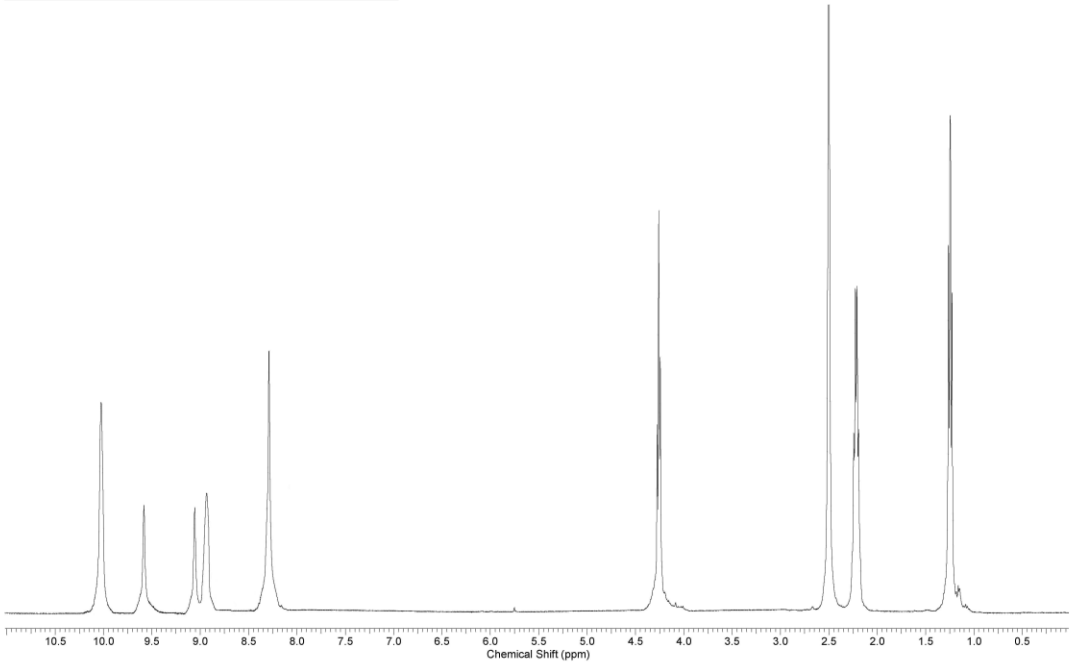

(a)

Acquisition Time (sec)	1.3005	***Comment***	Std proton	***Date***	Mar 9 2009		
Date Stamp	Mar 9 2009	***Frequency (MHz)***	100.53	***Nucleus***	13C	***Number of Transients***	12000
Points Count	32768	***Pulse Sequence***	s2pul	***Receiver Gain***	30.00	***Solvent***	DMSO-d6
Spectrum Offset (Hz)	10554.2480	***Sweep Width (Hz)***	24125.45	***Temperature (degree C)***	25.000		

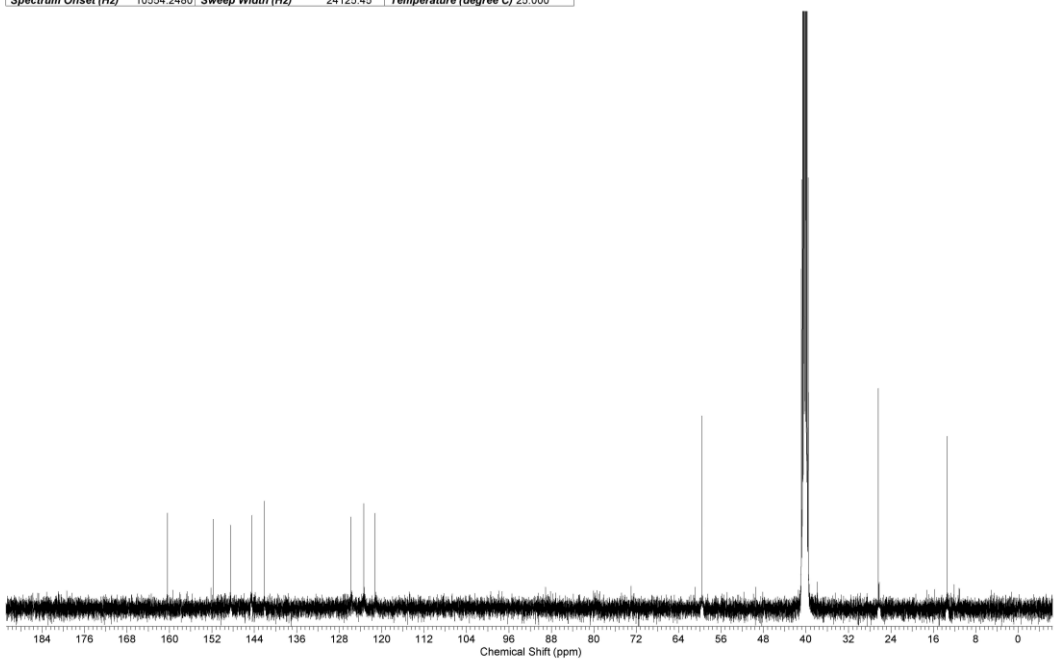

(b)

Figure A.12: - (a) ^{1}H NMR of Compound 14 (b) ^{13}C NMR of Compound 14

Acquisition Time (sec)	2.0487	***Comment***	Std proton	***Date***	Aug 4 2008		
Date Stamp	Aug 4 2008	***Frequency (MHz)***	399.75	***Nucleus***	1H	***Number of Transients***	64
Points Count	16384	***Pulse Sequence***	s2pul	***Receiver Gain***	36.00	***Solvent***	DMSO-d6
Sweep Width (Hz)	6395.91	***Temperature (degree C)***	25.000				

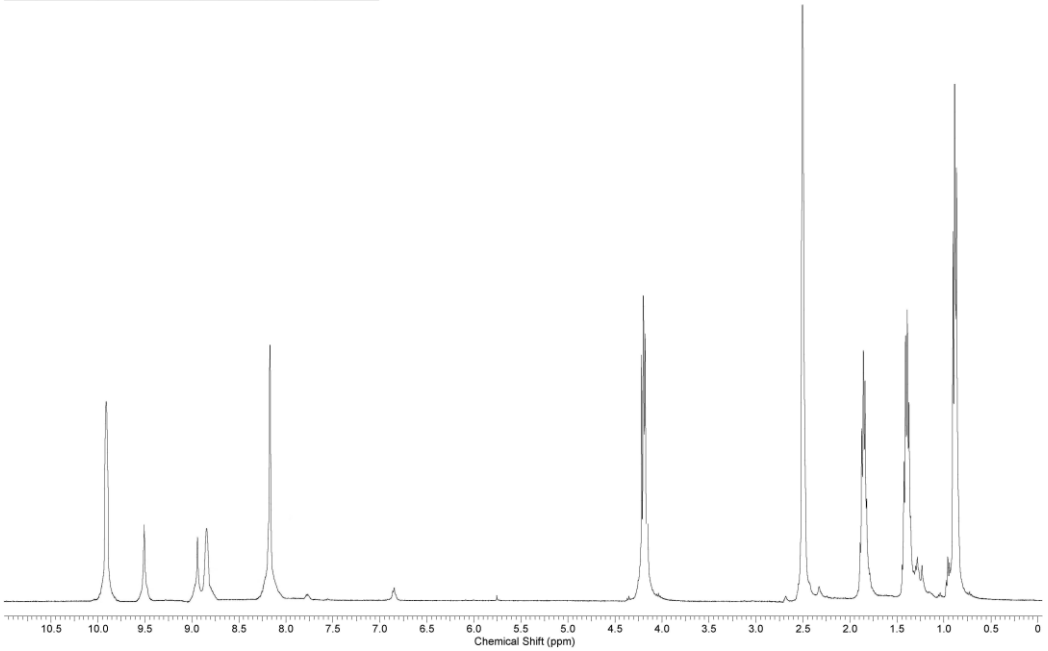

(a)

Acquisition Time (sec)	1.4976	***Comment***	13C OBSERVE			***Date***	Mar 6 2009
Date Stamp	Mar 6 2009			***Frequency (MHz)***	50.29	***Nucleus***	13C
Number of Transients	12000	***Original Points Count***	18720	***Points Count***	32768	***Pulse Sequence***	s2pul
Solvent	DMSO-d6	***Spectrum Offset (Hz)***	4879.4790	***Sweep Width (Hz)***	12500.00	***Temperature (degree C)***	29.000

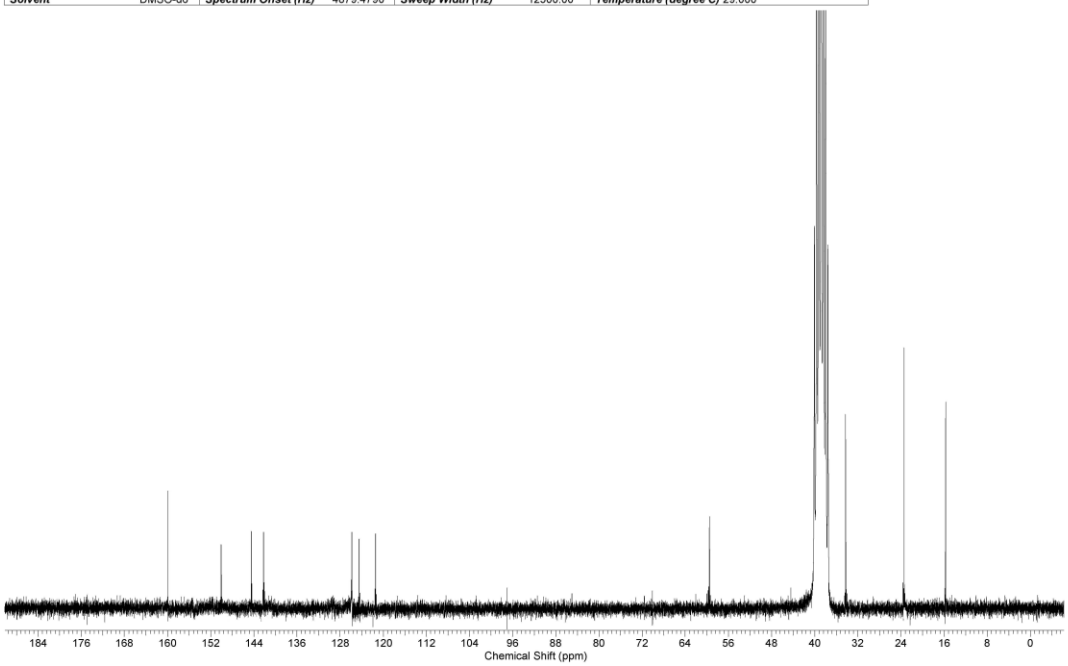

(b)

Figure A.13: - (a) ^{1}H NMR of Compound 15 (b) ^{13}C NMR of Compound 15

Acquisition Time (sec)	2.0487	***Comment***	Std proton	***Date***	Aug 1 2008		
Date Stamp	Aug 1 2008	***Frequency (MHz)***	399.75	***Nucleus***	1H	***Number of Transients***	100
Points Count	16384	***Pulse Sequence***	s2pul	***Receiver Gain***	42.00	***Solvent***	DMSO-d6
Sweep Width (Hz)	6395.91	***Temperature (degree C)***	25.000				

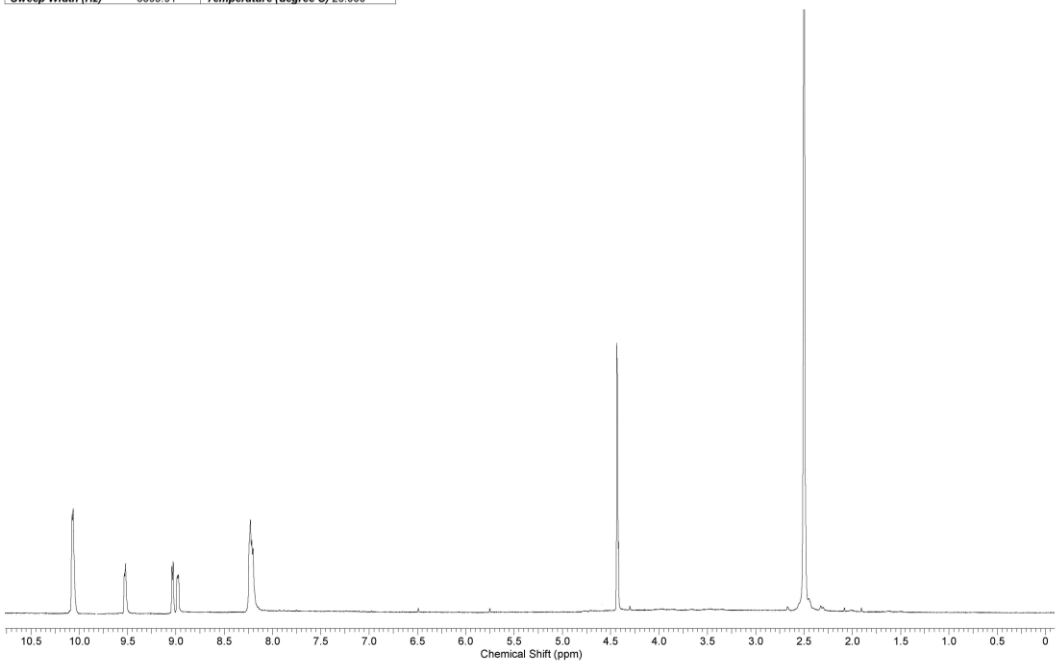

(a)

Acquisition Time (sec)	1.4976	***Comment***	13C OBSERVE			***Date***	Mar 11 2009
Date Stamp	Mar 11 2009			***Frequency (MHz)***	50.29	***Nucleus***	13C
Number of Transients	15000	***Original Points Count***	18720	***Points Count***	32768	***Pulse Sequence***	s2pul
Solvent	DMSO-d6	***Spectrum Offset (Hz)***	4879.4790	***Sweep Width (Hz)***	12500.00	***Temperature (degree C)***	29.000

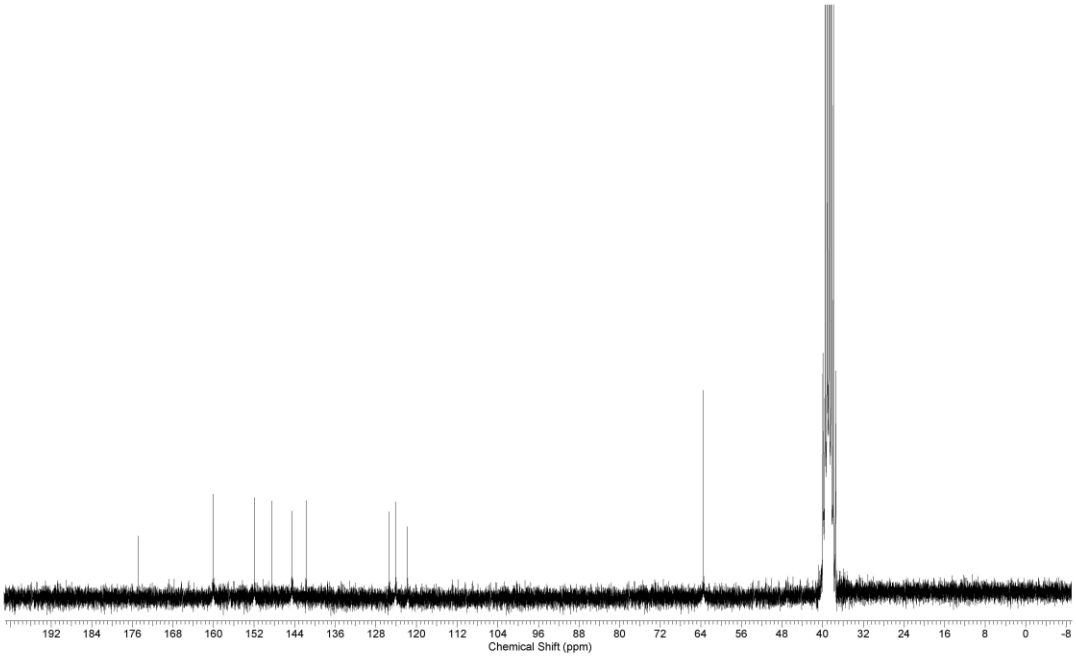

(b)

Figure A.14: (a) ^{1}H NMR of Compound 16 (b) ^{13}C NMR of Compound 16

Acquisition Time (sec)	2.0487	***Comment***	Std proton	***Date***	Nov 6 2008		
Date Stamp	Nov 6 2008	***Frequency (MHz)***	399.76	***Nucleus***	1H	***Number of Transients***	100
Points Count	16384	***Pulse Sequence***	s2pul	***Receiver Gain***	38.00	***Solvent***	DMSO-d6
Sweep Width (Hz)	6395.91	***Temperature (degree C)***	25.000				

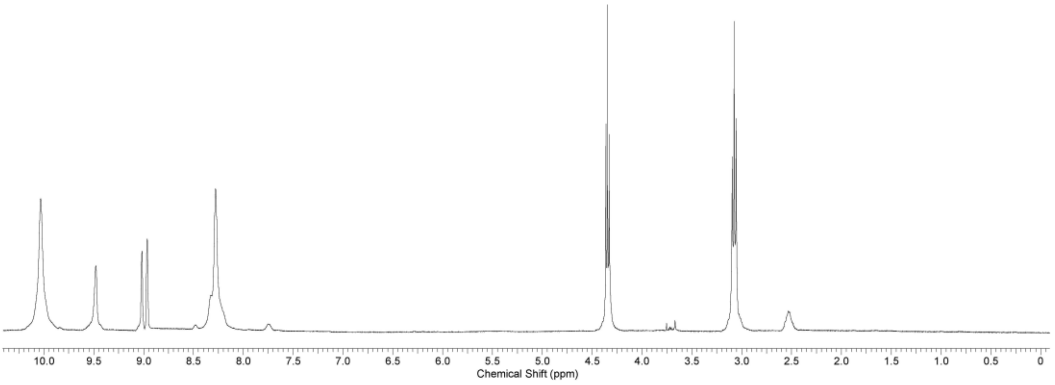

(a)

Acquisition Time (sec)	1.4976	***Comment***	13C OBSERVE			***Date***	Apr 1 2009
Date Stamp	Apr 1 2009	***File Name***		***Frequency (MHz)***	50.29	***Nucleus***	13C
Number of Transients	15000	***Original Points Count***	18720	***Points Count***	32768	***Pulse Sequence***	s2pul
Solvent	DMSO-d6	***Spectrum Offset (Hz)***	4879.4790	***Sweep Width (Hz)***	12500.00	***Temperature (degree C)***	29.000

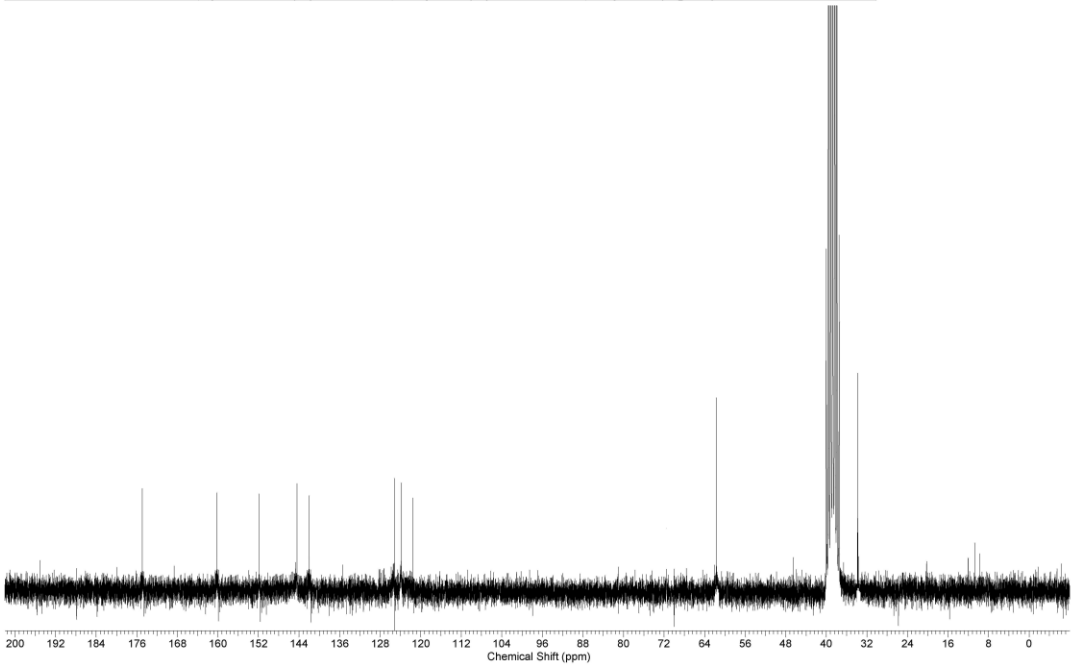

(b)

Figure A.15: - (a) ^{1}H NMR of Compound 17 (b) ^{13}C NMR of Compound 17

Acquisition Time (sec)	2.0487	***Comment***	Std proton	***Date***	Nov 11 2008		
Date Stamp	Nov 11 2008	***Frequency (MHz)***	399.76	***Nucleus***	1H	***Number of Transients***	100
Points Count	16384	***Pulse Sequence***	s2pul	***Receiver Gain***	38.00	***Solvent***	DMSO-d6
Sweep Width (Hz)	6395.91	***Temperature (degree C)***	25.000				

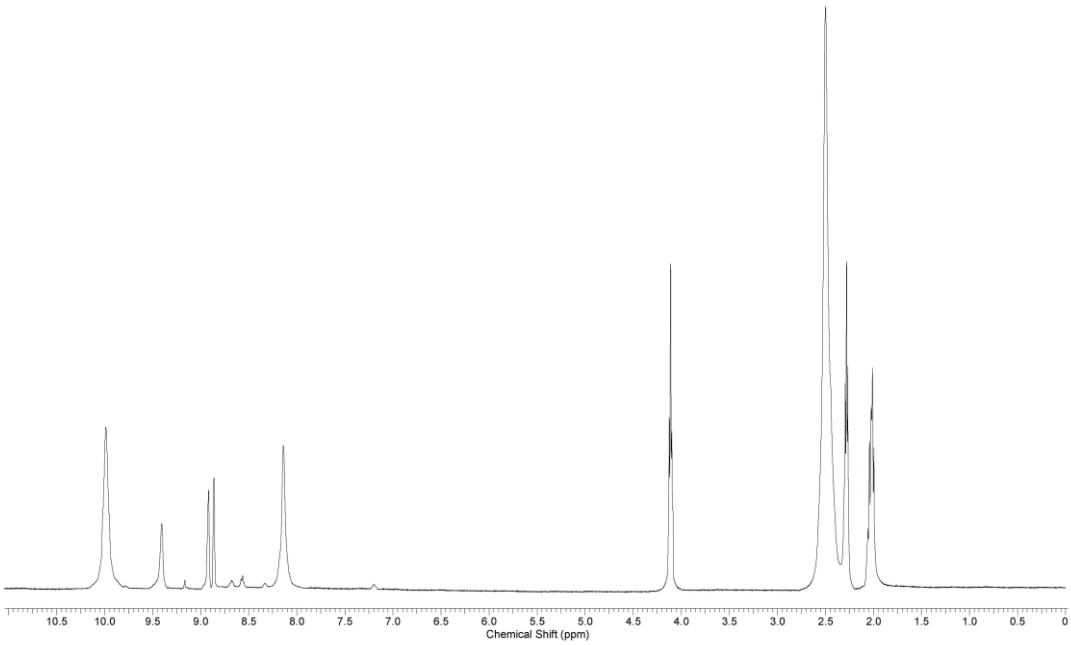

(a)

Acquisition Time (sec)	1.4976	***Comment***	13C OBSERVE			***Date***	Apr 9 2009
Date Stamp	Apr 9 2009			***Frequency (MHz)***	50.29	***Nucleus***	13C
Number of Transients	15000	***Original Points Count***	18720	***Points Count***	32768	***Pulse Sequence***	s2pul
Solvent	DMSO-d6	***Spectrum Offset (Hz)***	4879.4790	***Sweep Width (Hz)***	12500.00	***Temperature (degree C)***	29.000

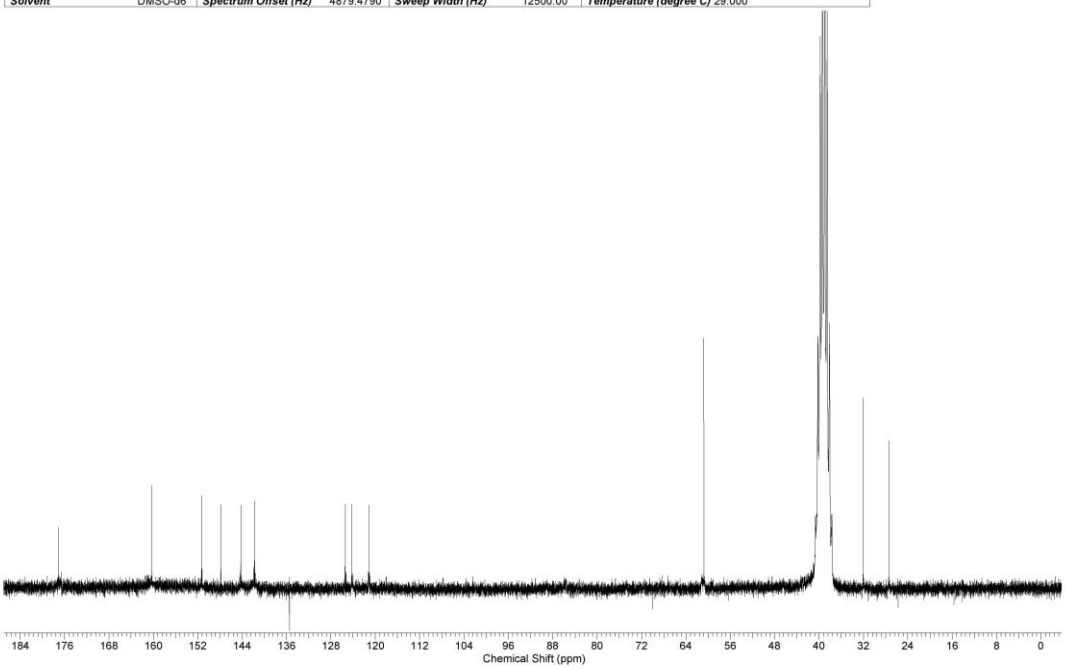

(b)

Figure A.16: - (a) ^{1}H NMR of Compound 18 (b) ^{13}C NMR of Compound 18

Acquisition Time (sec)	2.0487	***Comment***	Std proton	***Date***	Nov 11 2008		
Date Stamp	Nov 11 2008	***Frequency (MHz)***	399.76	***Nucleus***	1H	***Number of Transients***	100
Points Count	16384	***Pulse Sequence***	s2pul	***Receiver Gain***	38.00	***Solvent***	DMSO-d6
Sweep Width (Hz)	6395.91	***Temperature (degree C)***	25.000				

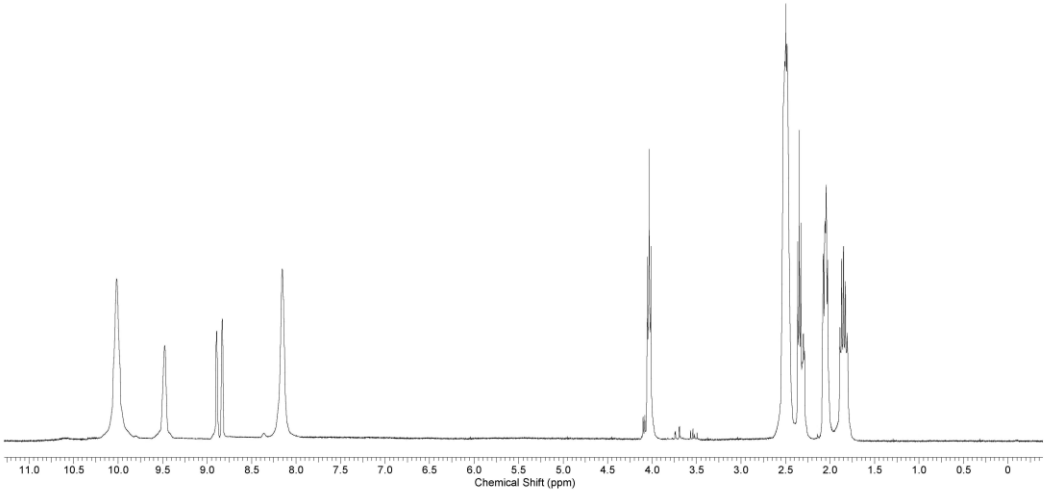

(a)

Acquisition Time (sec)	1.4976	***Comment***	13C OBSERVE			***Date***	Mar 12 2009
Date Stamp	Mar 12 2009			***Frequency (MHz)***	50.29	***Nucleus***	13C
Number of Transients	10000	***Original Points Count***	18720	***Points Count***	32768	***Pulse Sequence***	s2pul
Solvent	DMSO-d6	***Spectrum Offset (Hz)***	4879.4790	***Sweep Width (Hz)***	12500.00	***Temperature (degree C)***	29.000

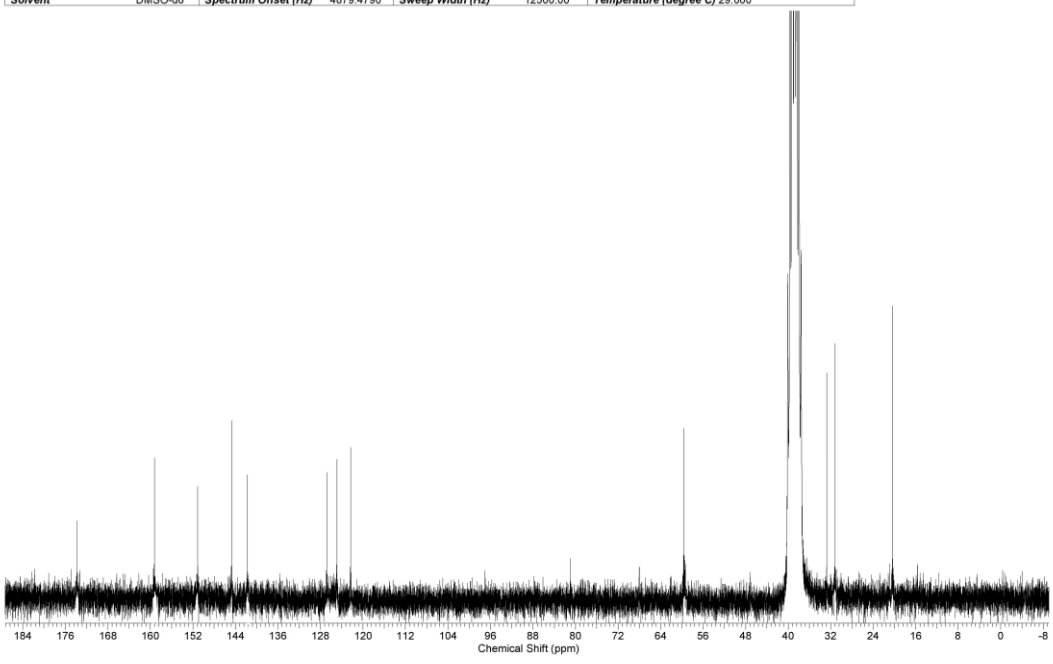

(b)

Figure A.17: - (a) ^{1}H NMR of Compound 19 (b) ^{13}C NMR of Compound 19

Acquisition Time (sec)	2.0487	***Comment***	Std proton	***Date***	Apr 15 2009		
Date Stamp	Apr 15 2009	***Frequency (MHz)***	399.75	***Nucleus***	1H	***Number of Transients***	64
Points Count	16384	***Pulse Sequence***	s2pul	***Receiver Gain***	36.00	***Solvent***	DMSO-d6
Spectrum Offset (Hz)	2398.4700	***Sweep Width (Hz)***	6395.91	***Temperature (degree C)***	25.000		

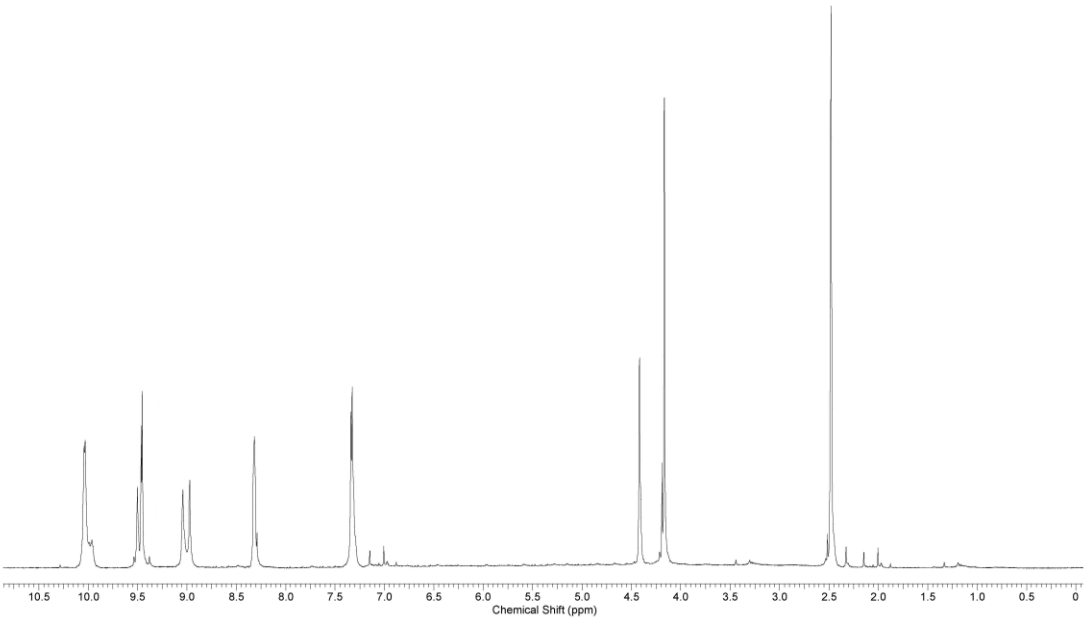

(a)

Acquisition Time (sec)	1.4976	***Comment***	13C OBSERVE			***Date***	Apr 15 2009
Date Stamp	Apr 15 2009			***Frequency (MHz)***	50.29	***Nucleus***	13C
Number of Transients	12000	***Original Points Count***	18720	***Points Count***	32768	***Pulse Sequence***	s2pul
Solvent	DMSO-d6	***Spectrum Offset (Hz)***	4879.4790	***Sweep Width (Hz)***	12500.00	***Temperature (degree C)***	29.000

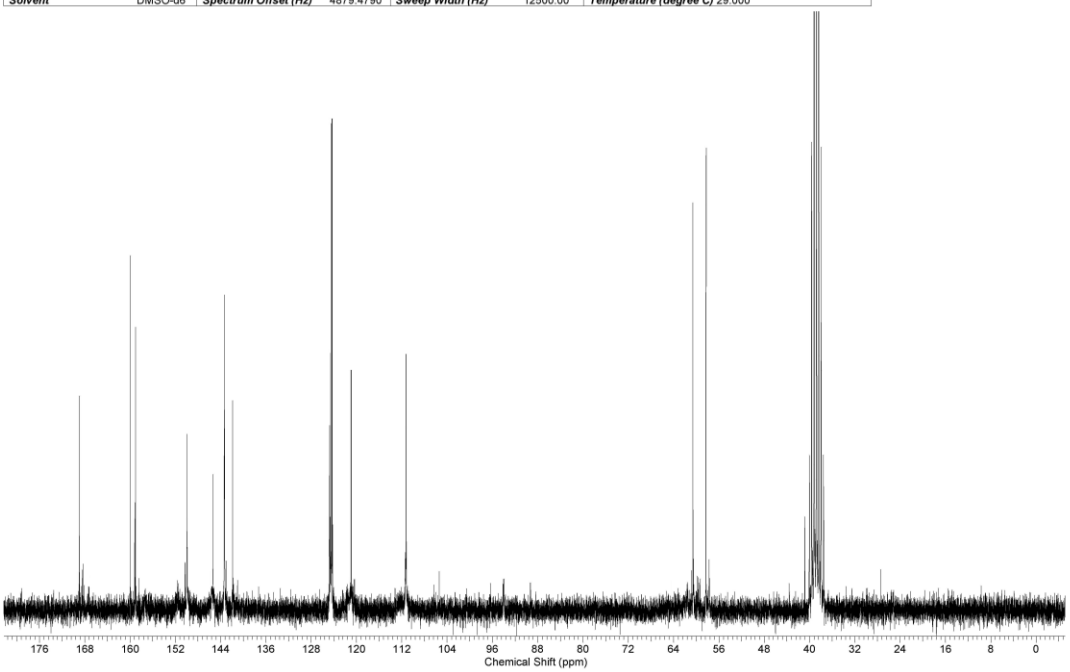

(b)

Figure A.18: - (a) ^{1}H NMR of Compound 20 (b) ^{13}C NMR of Compound 20

Acquisition Time (sec)	2.0487	***Comment***	Std proton	***Date***	Apr 15 2009		
Date Stamp	Apr 15 2009	***Frequency (MHz)***	399.75	***Nucleus***	1H	***Number of Transients***	64
Points Count	16384	***Pulse Sequence***	s2pul	***Receiver Gain***	36.00	***Solvent***	DMSO-d6
Spectrum Offset (Hz)	2398.4700	***Sweep Width (Hz)***	6395.91	***Temperature (degree C)***	25.000		

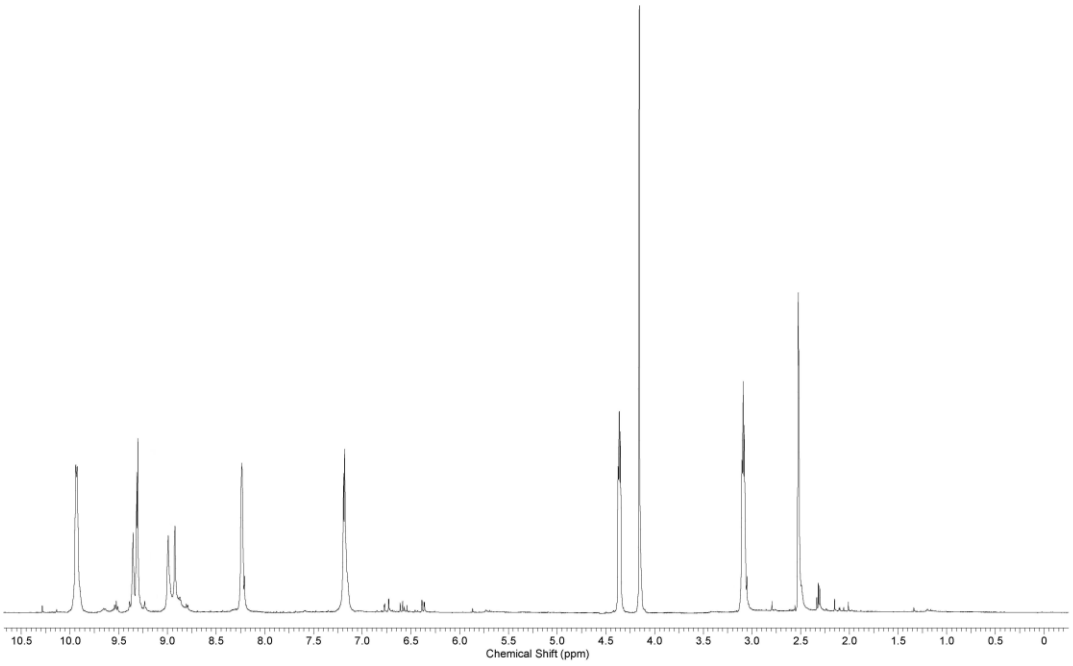

(a)

Acquisition Time (sec)	1.4976	***Comment***	13C OBSERVE			***Date***	Apr 17 2009
Date Stamp	Apr 17 2009			***Frequency (MHz)***	50.29	***Nucleus***	13C
Number of Transients	20000	***Original Points Count***	18720	***Points Count***	32768	***Pulse Sequence***	s2pul
Solvent	DMSO-d6	***Spectrum Offset (Hz)***	4879.4790	***Sweep Width (Hz)***	12500.00	***Temperature (degree C)***	29.000

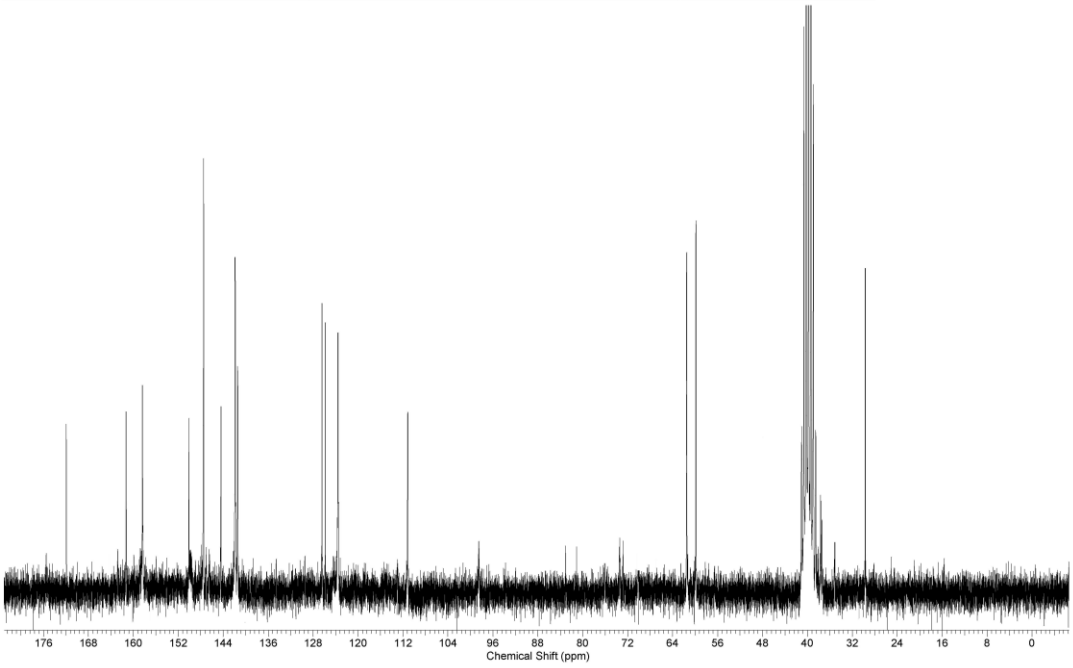

(b)

Figure A.19: - (a) ^{1}H NMR of Compound 21 (b) ^{13}C NMR of Compound 21

Acquisition Time (sec)	2.0487	***Comment***	Std proton	***Date***	Apr 20 2009		
Date Stamp	Apr 20 2009	***Frequency (MHz)***	399.75	***Nucleus***	1H	***Number of Transients***	100
Points Count	16384	***Pulse Sequence***	s2pul	***Receiver Gain***	30.00	***Solvent***	DMSO-d6
Sweep Width (Hz)	6395.91	***Temperature (degree C)***	25.000				

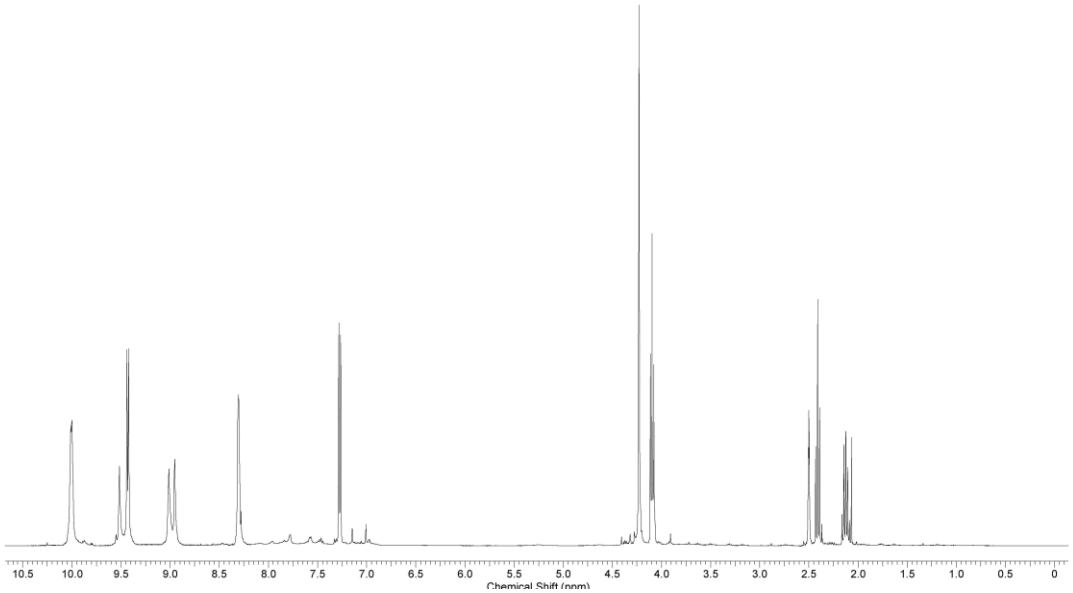

(a)

Acquisition Time (sec)	1.3005	***Comment***	Std proton	***Date***	Apr 17 2009		
Date Stamp	Apr 17 2009	***Frequency (MHz)***	100.53	***Nucleus***	13C	***Number of Transients***	15000
Points Count	32768	***Pulse Sequence***	s2pul	***Receiver Gain***	30.00	***Solvent***	CHLOROFORM-d
Spectrum Offset (Hz)	10554.2480	***Sweep Width (Hz)***	24125.45	***Temperature (degree C)***	25.000		

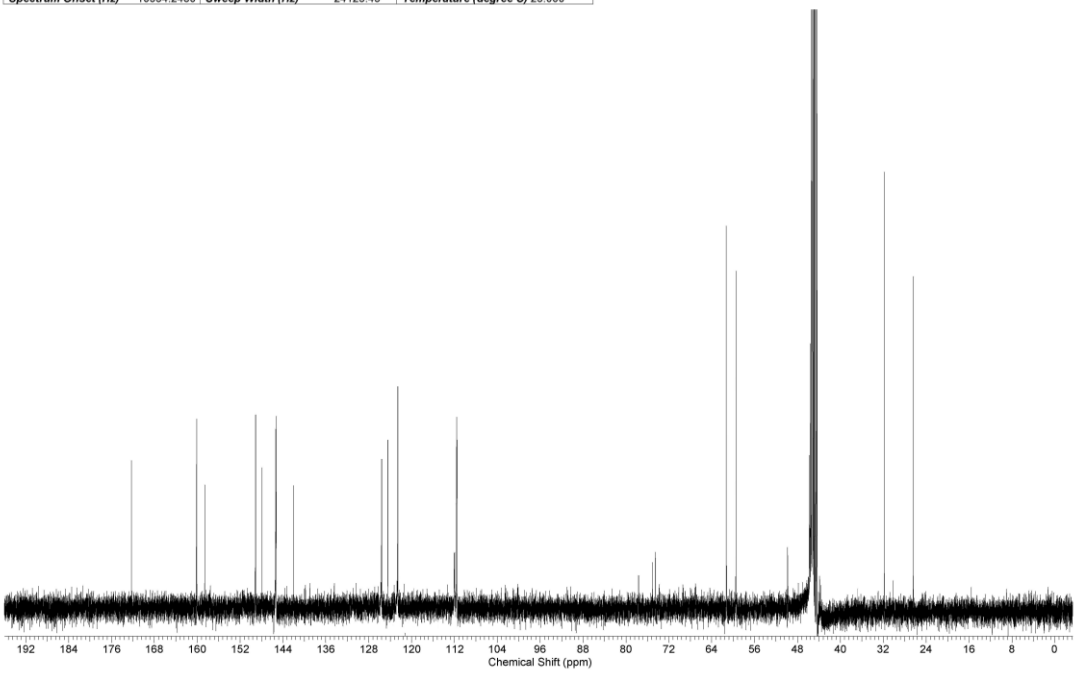

(b)

Figure A.20: - (a) ^{1}H NMR of Compound 22 (b) ^{13}C NMR of Compound 22

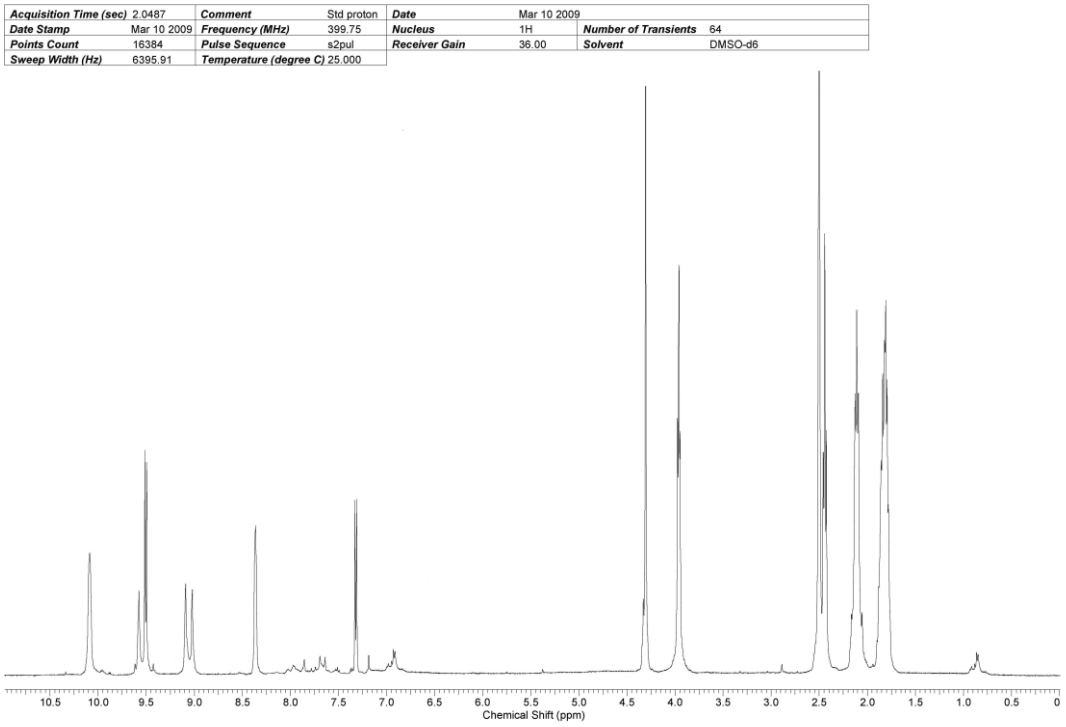

(a)

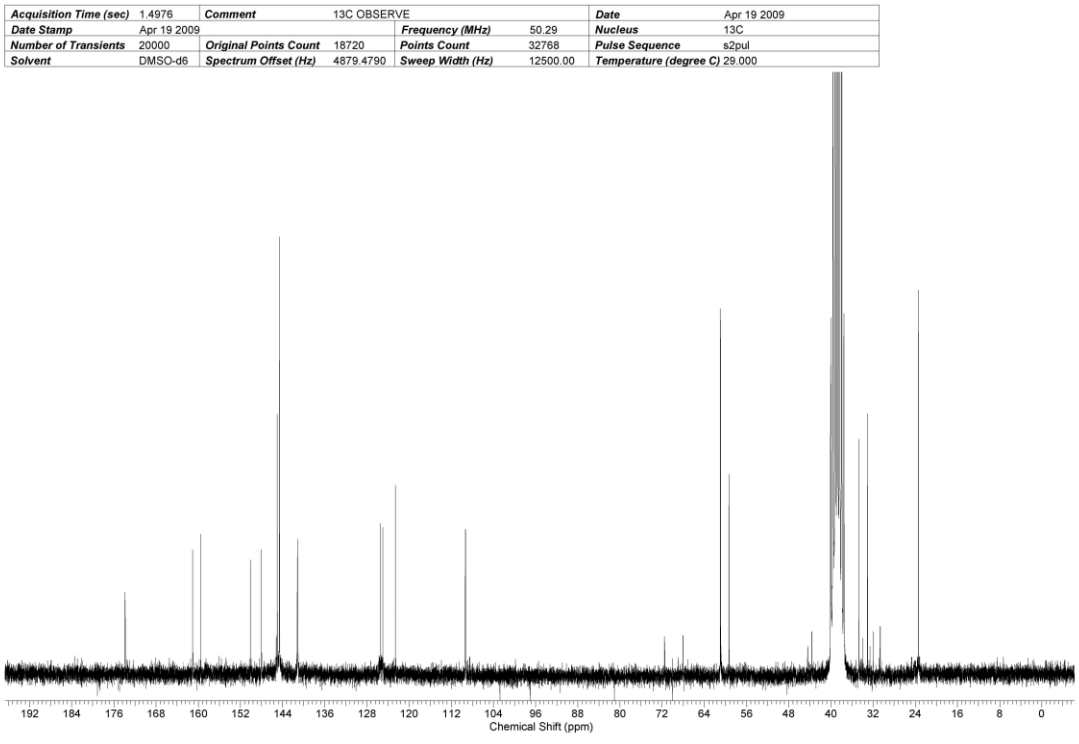

(b)

Figure A.21: - (a) ^{1}H NMR of Compound 24 (b) ^{13}C NMR of Compound 24

Acquisition Time (sec)	1.9945	***Comment***	STANDARD 1H OBSERVE			***Date***	Aug 22 2007
Date Stamp	Aug 22 2007	***Frequency (MHz)***	199.98	***Nucleus***	1H	***Number of Transients***	64
Points Count	8192	***Pulse Sequence***	s2pul	***Receiver Gain***	34.00	***Solvent***	DMSO-d6
Sweep Width (Hz)	3000.30	***Temperature (degree C)***	29.000				

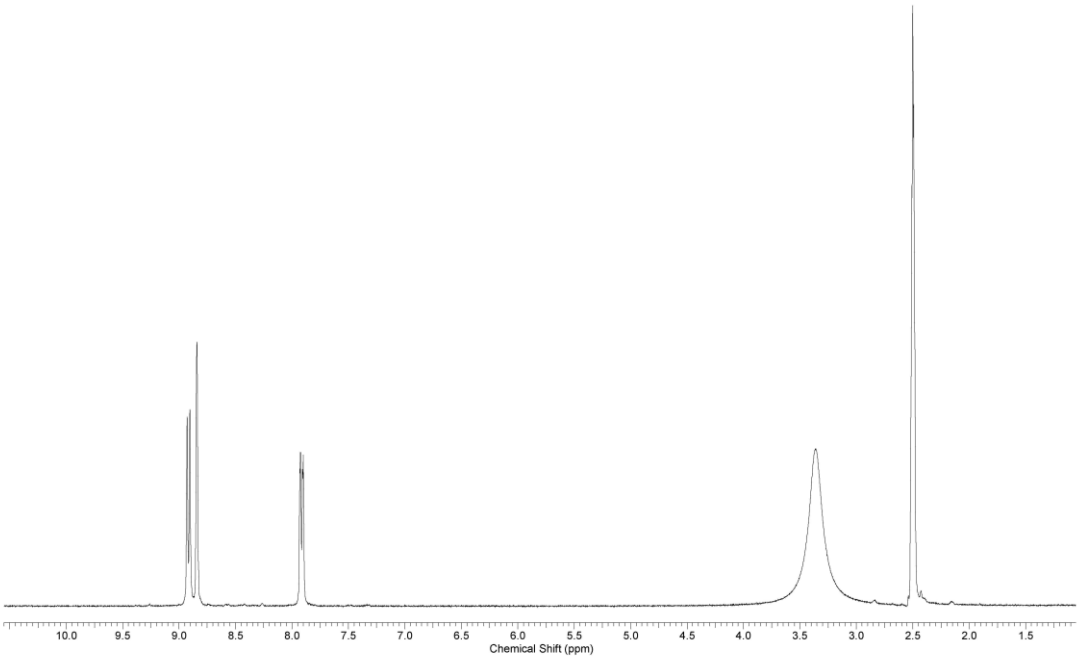

(a)

Acquisition Time (sec)	1.4976	***Comment***	13C OBSERVE			***Date***	Mar 5 2009
Date Stamp	Mar 5 2009	***Frequency (MHz)***	50.29	***Nucleus***	13C	***Number of Transients***	15000
Points Count	32768	***Pulse Sequence***	s2pul	***Receiver Gain***	40.00	***Solvent***	DMSO-d6
Sweep Width (Hz)	12500.00	***Temperature (degree C)***	29.000				

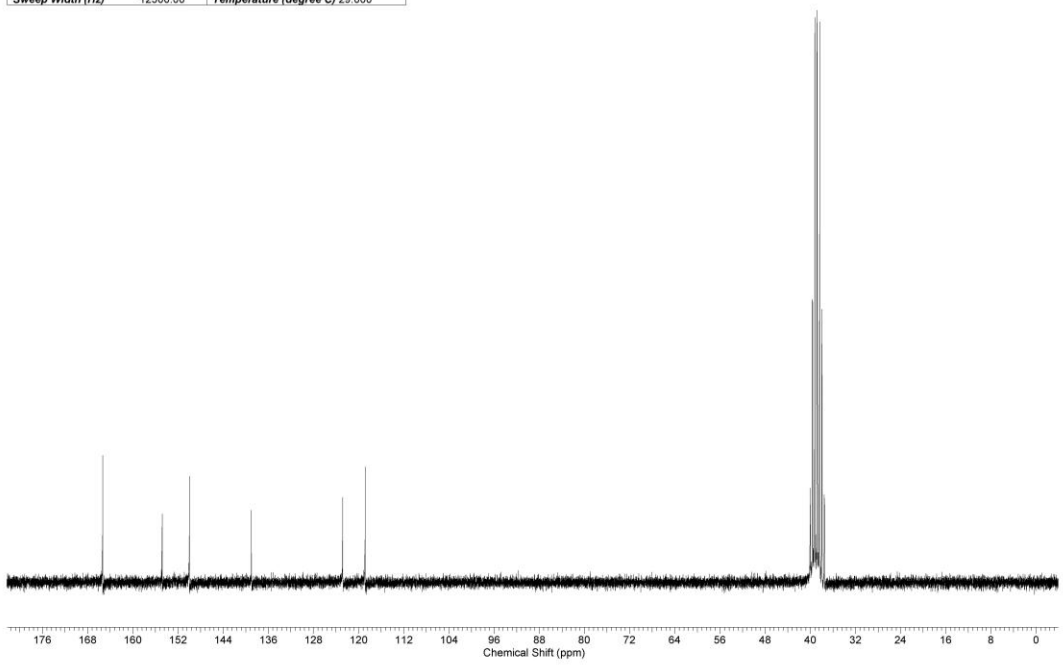

(b)

Figure A.22: - (a) ^{1}H NMR of Compound 25 (b) ^{13}C NMR of Compound 25

Acquisition Time (sec)	2.0486	***Comment***	Std proton	***Date***	Aug 27 2007		
Date Stamp	Aug 27 2007	***Frequency (MHz)***	399.78	***Nucleus***	1H	***Number of Transients***	64
Points Count	16384	***Pulse Sequence***	s2pul	***Receiver Gain***	54.00	***Solvent***	CHLOROFORM-d
Sweep Width (Hz)	7196.19	***Temperature (degree C)***	25.000				

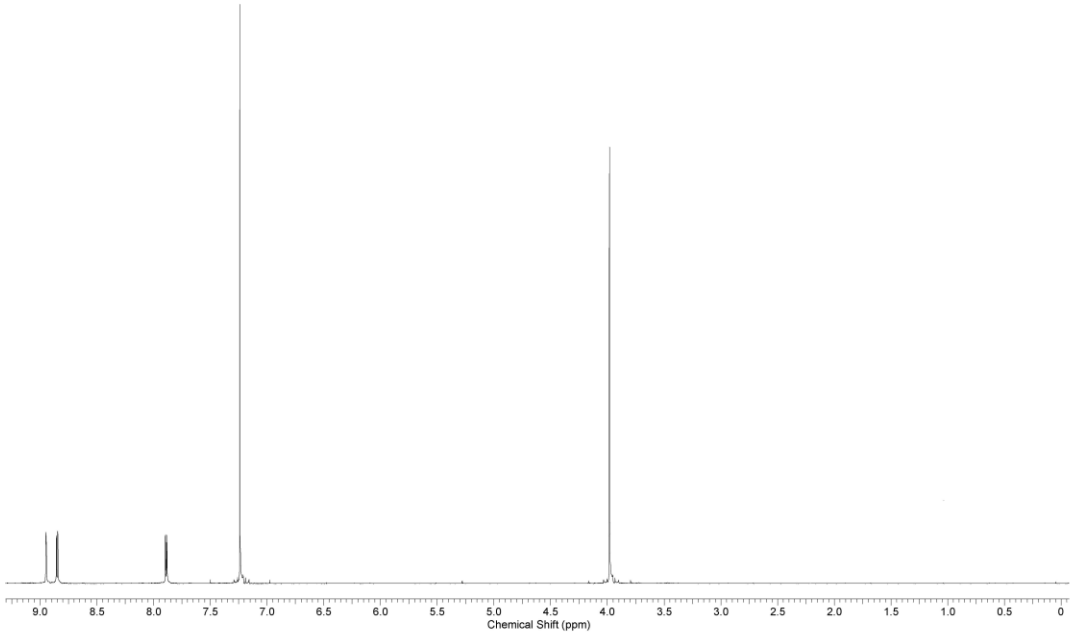

(a)

Acquisition Time (sec)	1.4976	***Comment***	13C OBSERVE			***Date***	Mar 1 2009
Date Stamp	Mar 1 2009	***Frequency (MHz)***	50.29	***Nucleus***	13C	***Number of Transients***	20000
Points Count	32768	***Pulse Sequence***	s2pul	***Receiver Gain***	40.00	***Solvent***	CHLOROFORM-d
Sweep Width (Hz)	12500.00	***Temperature (degree C)***	29.000				

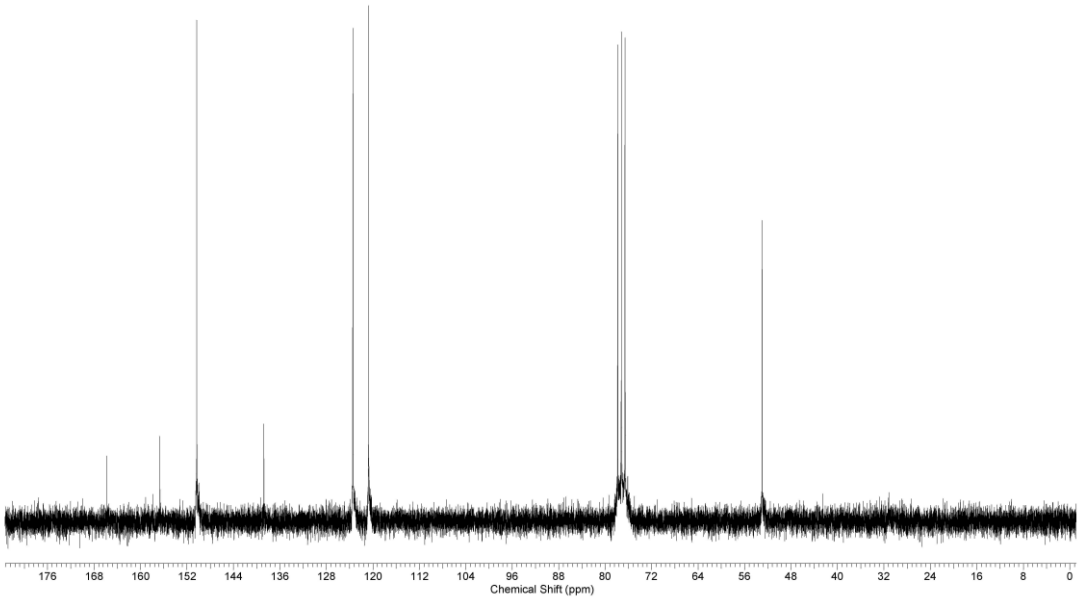

(b)

Figure A.23: - (a) ^{1}H NMR of Compound 26 (b) ^{13}C NMR of Compound 26

Acquisition Time (sec)	2.0486	***Comment***	Std proton	***Date***	Sep 5 2007		
Date Stamp	Sep 5 2007	***Frequency (MHz)***	399.77	***Nucleus***	1H	***Number of Transients***	32
Points Count	16384	***Pulse Sequence***	s2pul	***Receiver Gain***	48.00	***Solvent***	DMSO-d6
Sweep Width (Hz)	6396.42	***Temperature (degree C)***	25.000				

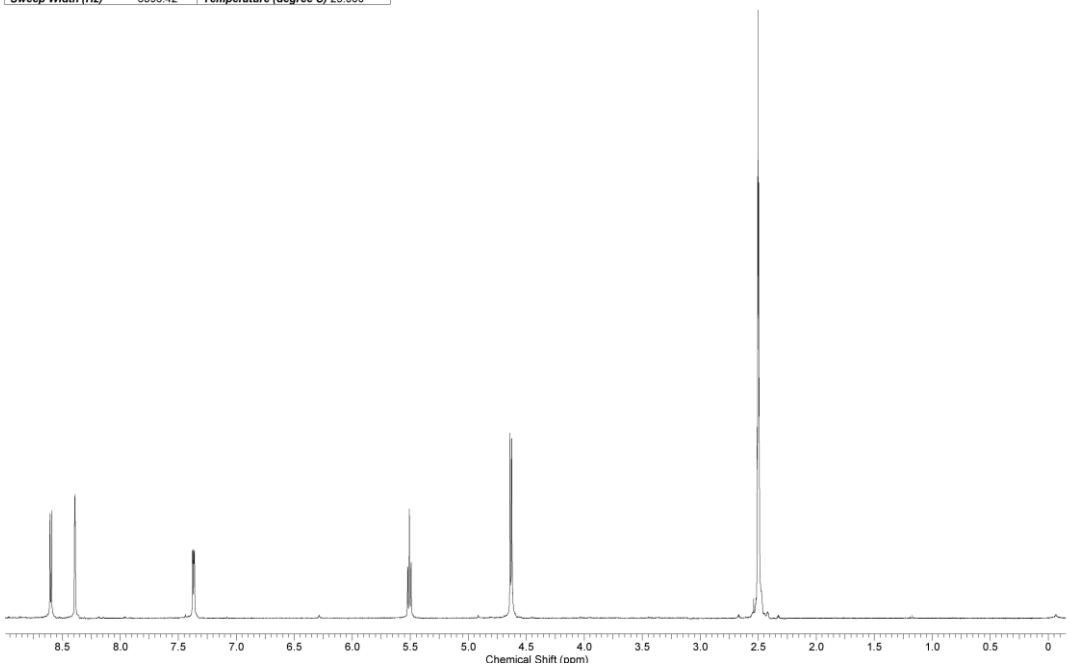

(a)

Acquisition Time (sec)	1.4976	***Comment***	13C OBSERVE			***Date***	Feb 12 2009
Date Stamp	Feb 12 2009	***Frequency (MHz)***	50.29	***Nucleus***	13C	***Number of Transients***	10000
Points Count	32768	***Pulse Sequence***	s2pul	***Receiver Gain***	40.00	***Solvent***	DMSO-d6
Sweep Width (Hz)	12500.00	***Temperature (degree C)***	29.000				

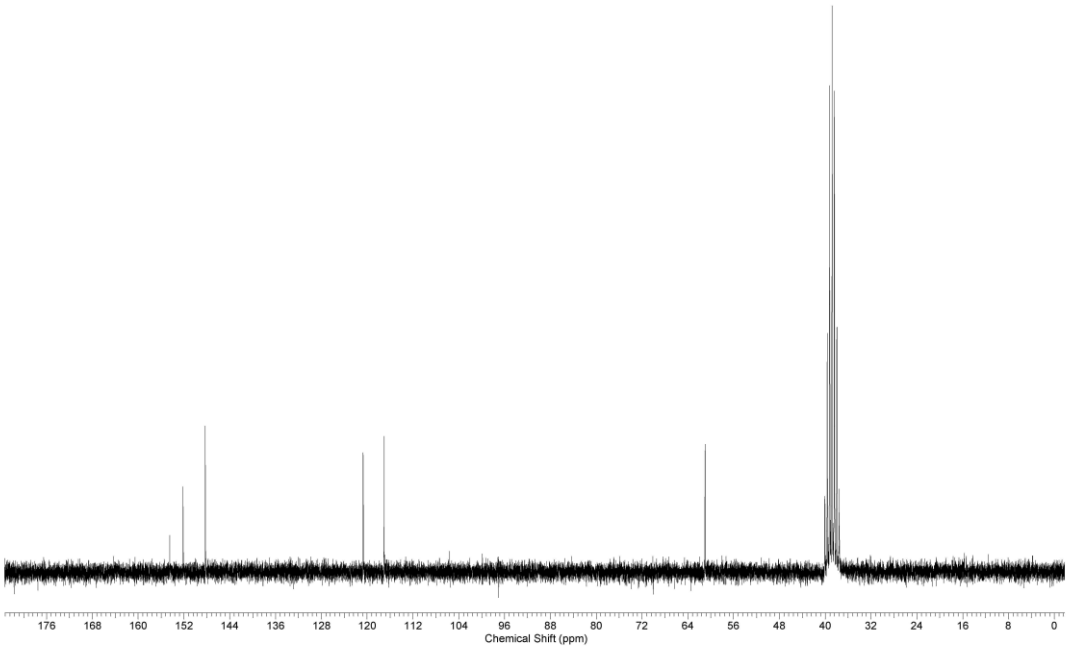

(b)

Figure A.24: - (a) ^{1}H NMR of Compound 28 (b) ^{13}C NMR of Compound 28

Acquisition Time (sec)	2.0486	***Comment***	Std proton	***Date***	Nov 27 2007		
Date Stamp	Nov 27 2007	***Frequency (MHz)***	399.77	***Nucleus***	1H	***Number of Transients***	64
Points Count	16384	***Pulse Sequence***	s2pul	***Receiver Gain***	28.00	***Solvent***	DMSO-d6
Sweep Width (Hz)	6396.42	***Temperature (degree C)***	25.000				

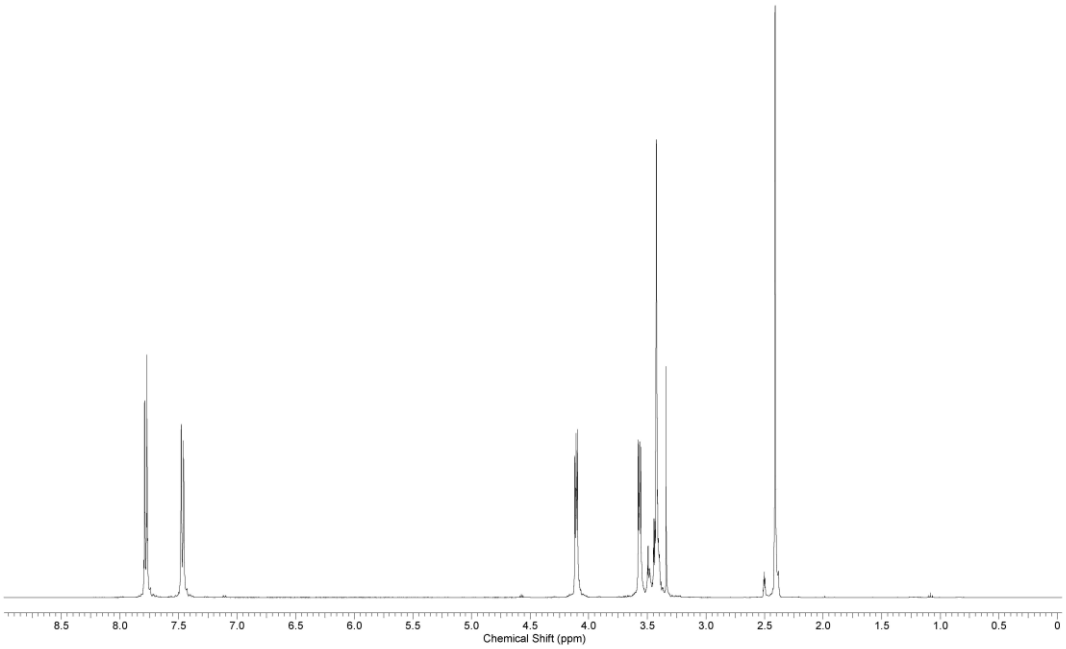

(a)

Acquisition Time (sec)	1.4976	***Comment***	13C OBSERVE			***Date***	Oct 22 2007
Date Stamp	Oct 22 2007			***Frequency (MHz)***	50.29	***Nucleus***	13C
Number of Transients	200	***Original Points Count***	18720	***Points Count***	32768	***Pulse Sequence***	s2pul
Solvent	DMSO-d6	***Spectrum Offset (Hz)***	4879.4790	***Sweep Width (Hz)***	12500.00	***Temperature (degree C)***	29.000

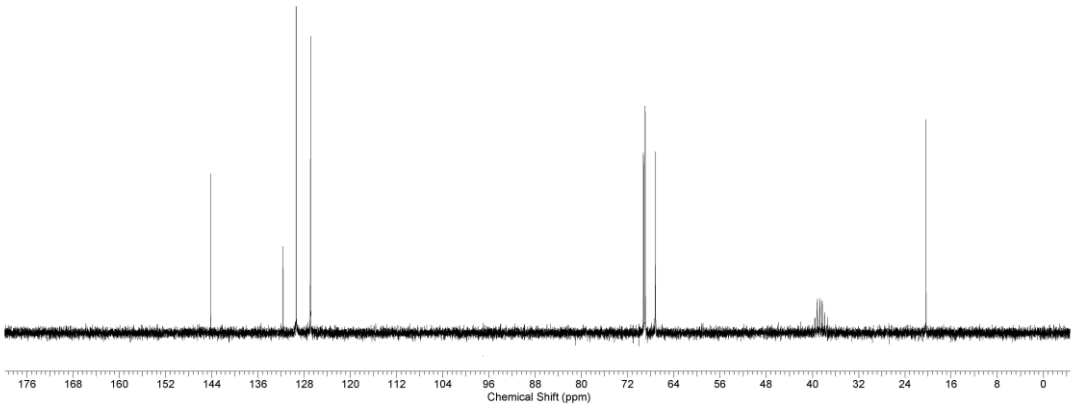

(b)

Figure A.25: - (a) ^{1}H NMR of Compound 30 (b) ^{13}C NMR of Compound 30

Acquisition Time (sec)	1.9945	***Comment***	STANDARD 1H OBSERVE			***Date***	Jan 19 2007
Date Stamp	Jan 19 2007	***Frequency (MHz)***	199.98	***Nucleus***	1H	***Number of Transients***	32
Points Count	8192	***Pulse Sequence***	s2pul	***Receiver Gain***	22.00	***Solvent***	CHLOROFORM-d
Sweep Width (Hz)	3000.30	***Temperature (degree C)***	29.000				

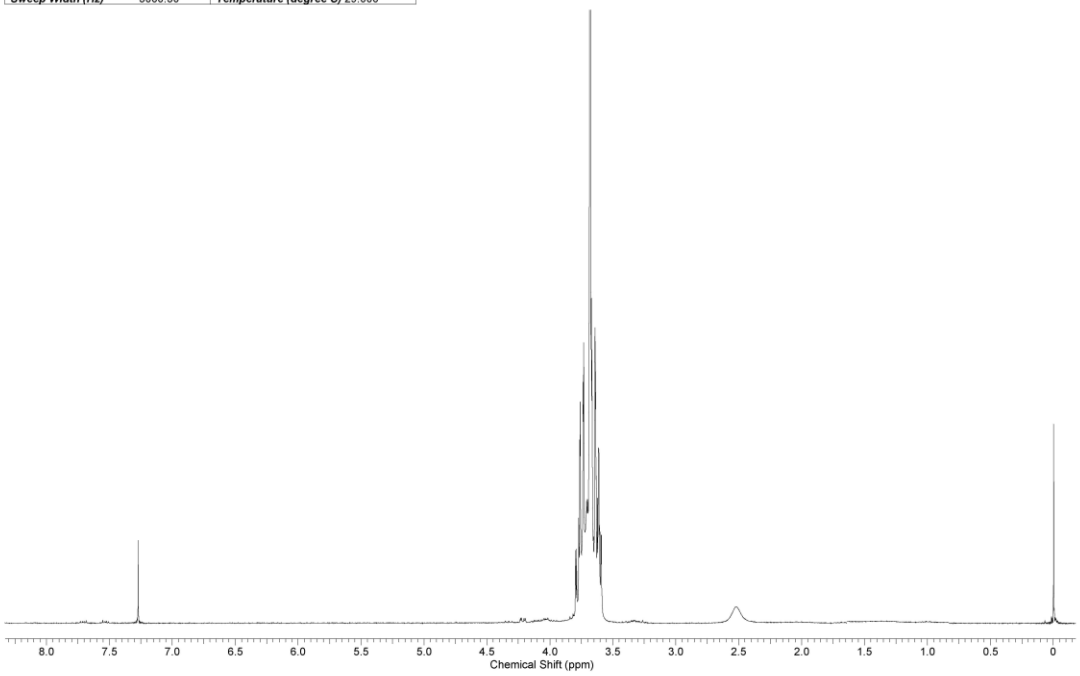

(a)

Acquisition Time (sec)	1.3005	***Comment***	Std proton	***Date***	Jan 15 2008		
Date Stamp	Jan 15 2008	***Frequency (MHz)***	100.53	***Nucleus***	13C	***Number of Transients***	2000
Points Count	32768	***Pulse Sequence***	s2pul	***Receiver Gain***	30.00	***Solvent***	CHLOROFORM-d
Sweep Width (Hz)	24125.45	***Temperature (degree C)***	25.000				

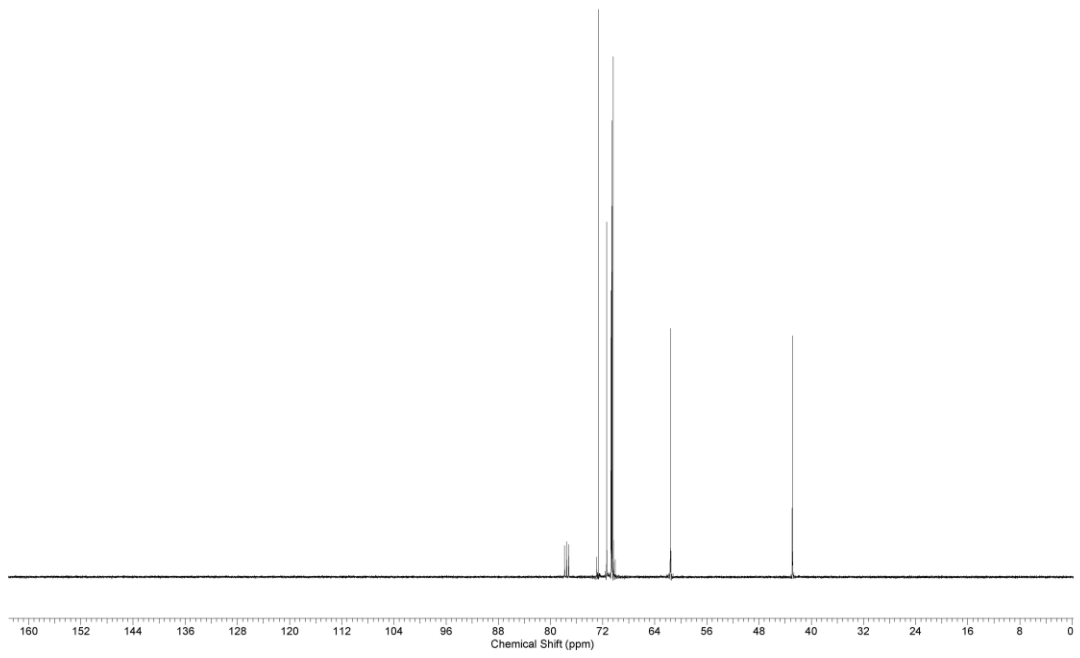

(b)

Figure A.26: - (a) ^{1}H NMR of Compound 31-a (b) ^{13}C NMR of Compound 31-a

Acquisition Time (sec)	2.0486	***Comment***	Std proton	***Date***	Jan 22 2008		
Date Stamp	Jan 22 2008	***Frequency (MHz)***	399.77	***Nucleus***	1H	***Number of Transients***	64
Points Count	16384	***Pulse Sequence***	s2pul	***Receiver Gain***	28.00	***Solvent***	CHLOROFORM-d
Sweep Width (Hz)	6396.42	***Temperature (degree C)***	25.000				

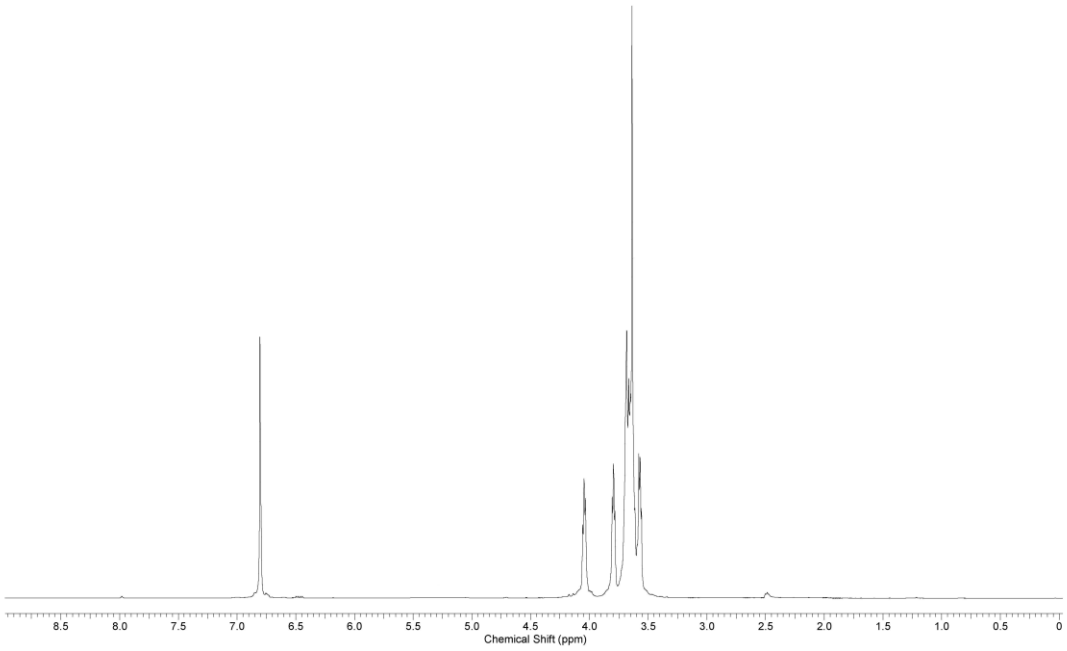

(a)

Acquisition Time (sec)	1.4976	***Comment***	13C OBSERVE			***Date***	Apr 26 2009
Date Stamp	Apr 26 2009			***Frequency (MHz)***	50.29	***Nucleus***	13C
Number of Transients	20000	***Original Points Count***	18720	***Points Count***	32768	***Pulse Sequence***	s2pul
Solvent	CHLOROFORM-d			***Spectrum Offset (Hz)***	4879.4639	***Temperature (degree C)***	29.000

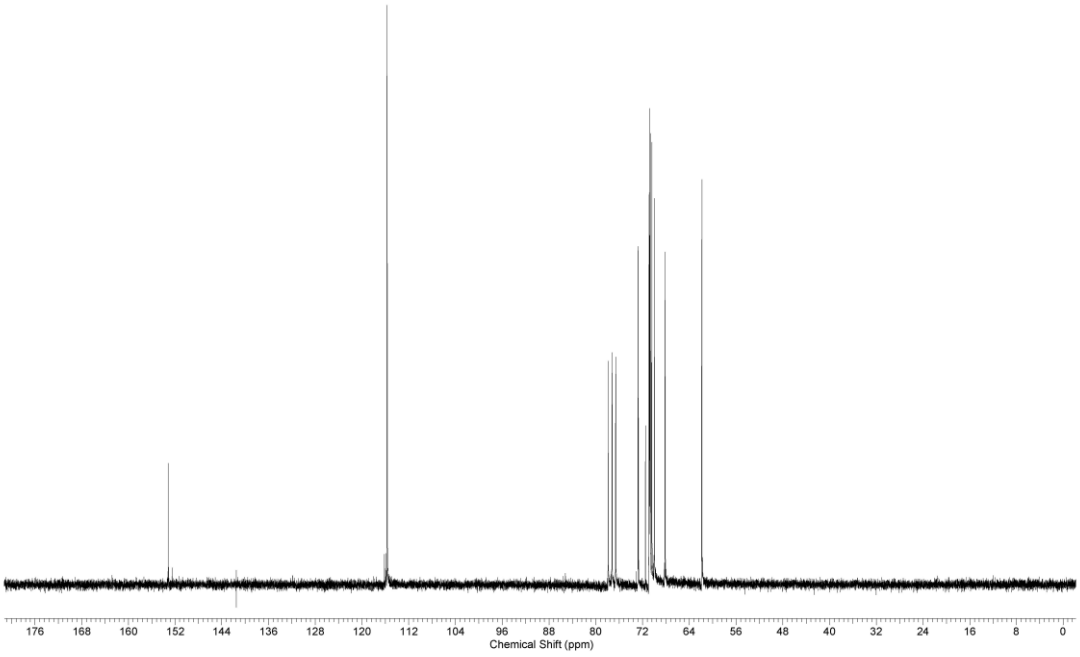

(b)

Figure A.27: - (a) ^{1}H NMR of Compound 31-b (b) ^{13}C NMR of Compound 31-b

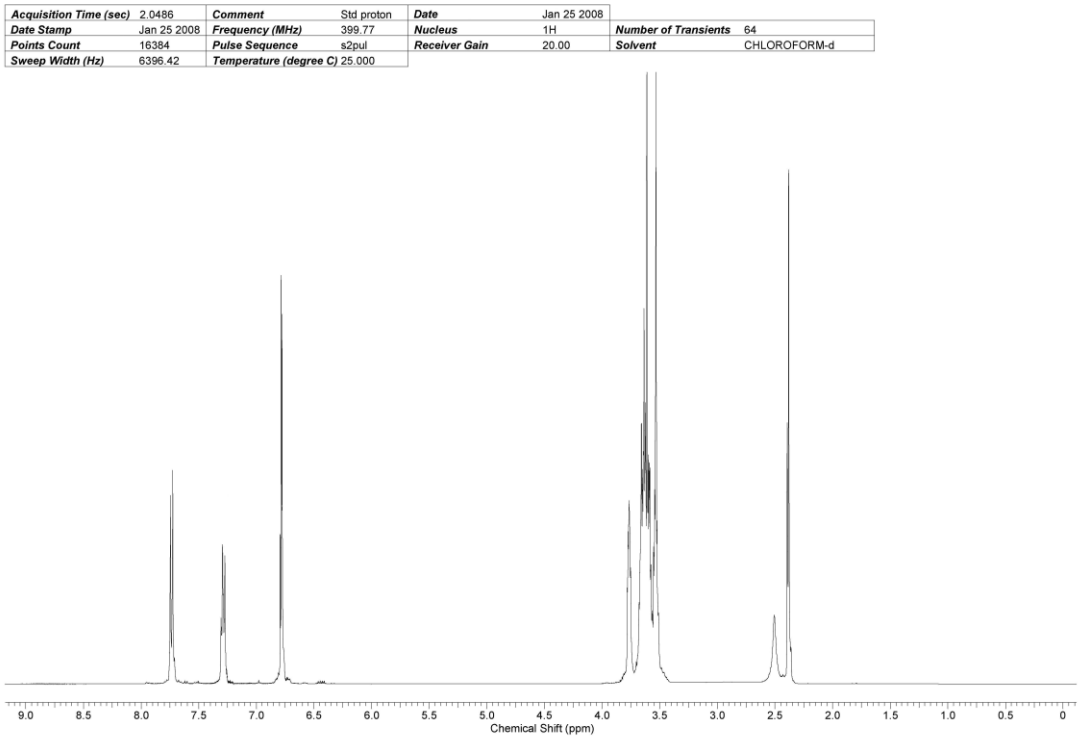

(a)

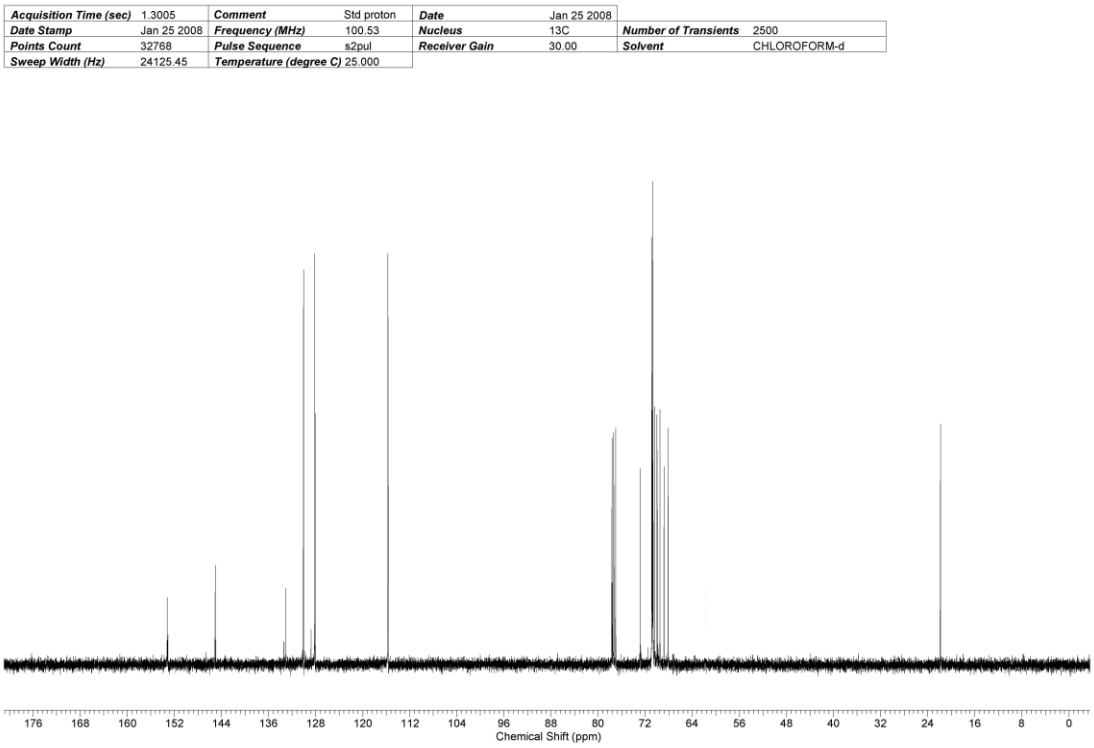

(b)

Figure A.28: - (a) ^{1}H NMR of Compound 32 (b) ^{13}C NMR of Compound 32

Acquisition Time (sec)	2.0486	***Comment***	Std proton	***Date***	Feb 6 2008		
Date Stamp	Feb 6 2008	***Frequency (MHz)***	399.77	***Nucleus***	1H	***Number of Transients***	64
Points Count	16384	***Pulse Sequence***	s2pul	***Receiver Gain***	30.00	***Solvent***	acetone
Sweep Width (Hz)	6396.42	***Temperature (degree C)***	25.000				

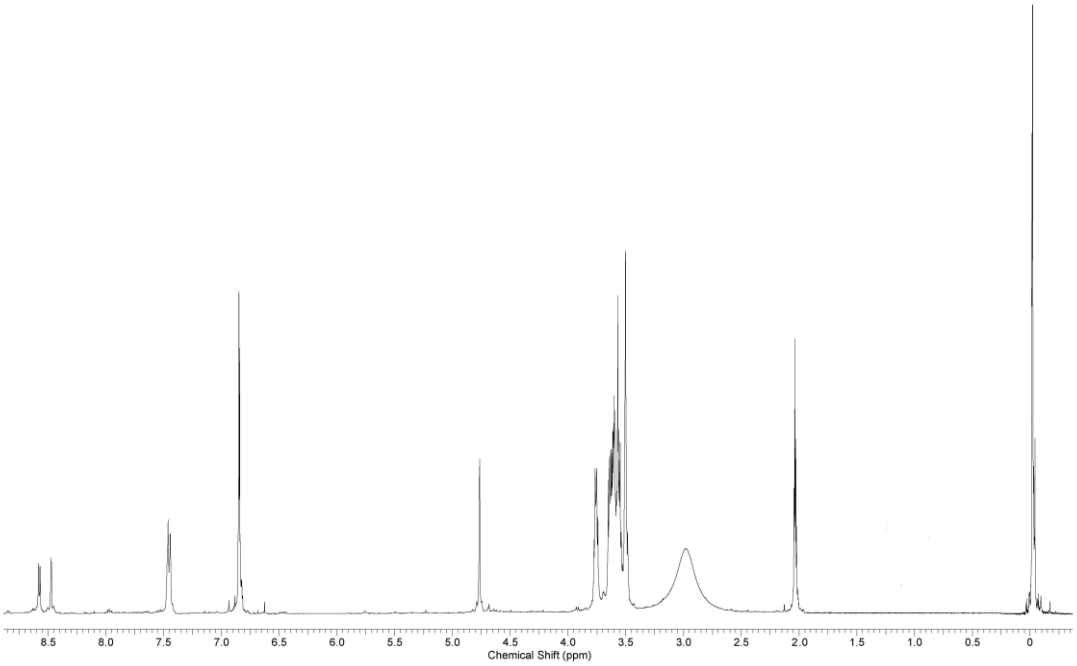

(a)

Acquisition Time (sec)	1.4976	***Comment***	13C OBSERVE			***Date***	Feb 15 2009
Date Stamp	Feb 15 2009	***Frequency (MHz)***	50.29	***Nucleus***	13C	***Number of Transients***	16000
Points Count	32768	***Pulse Sequence***	s2pul	***Receiver Gain***	40.00	***Solvent***	CHLOROFORM-d
Sweep Width (Hz)	12500.00	***Temperature (degree C)***	29.000				

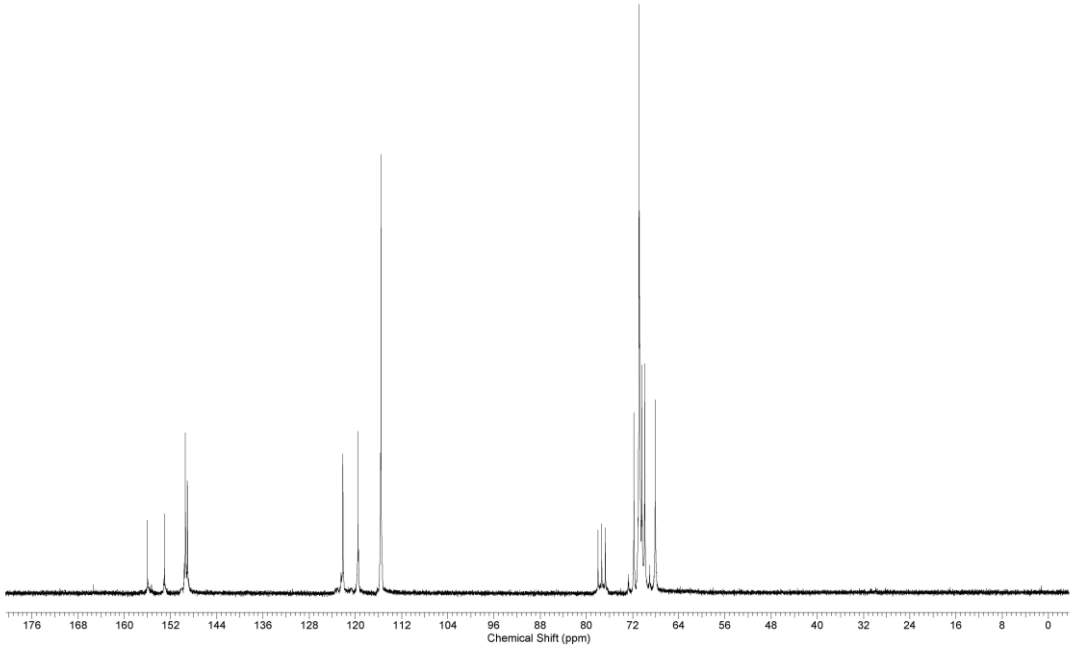

(b)

Figure A.29: - (a) ^{1}H NMR of Compound 38 (b) ^{13}C NMR of Compound 38

Acquisition Time (sec)	2.0486	***Comment***	Std proton	***Date***	Jun 22 2007		
Date Stamp	Jun 22 2007	***Frequency (MHz)***	399.78	***Nucleus***	1H	***Number of Transients***	16
Points Count	16384	***Pulse Sequence***	s2pul	***Receiver Gain***	48.00	***Solvent***	DMSO-d6
Spectrum Offset (Hz)	2398.6436	***Sweep Width (Hz)***	6396.42	***Temperature (degree C)***	25.000		

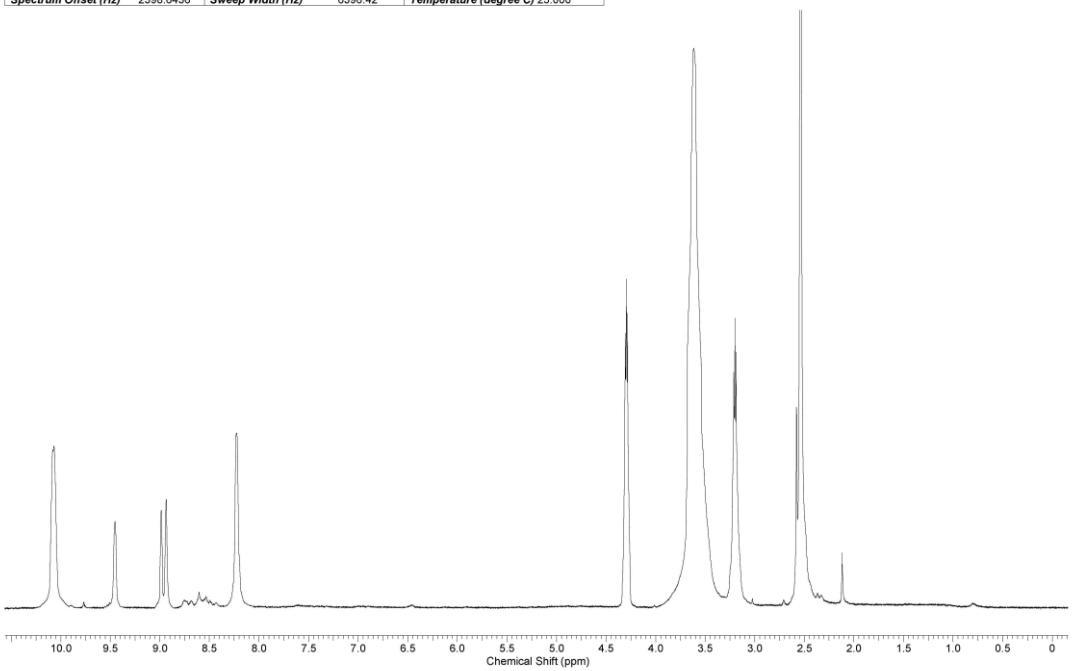

(a)

Acquisition Time (sec)	1.3005	***Comment***	Std proton	***Date***	Apr 19 2009		
Date Stamp	Apr 19 2009	***Frequency (MHz)***	100.53	***Nucleus***	13C	***Number of Transients***	15000
Points Count	32768	***Pulse Sequence***	s2pul	***Receiver Gain***	30.00	***Solvent***	DMSO-d6
Spectrum Offset (Hz)	10463.9238	***Sweep Width (Hz)***	24125.45	***Temperature (degree C)***	25.000		

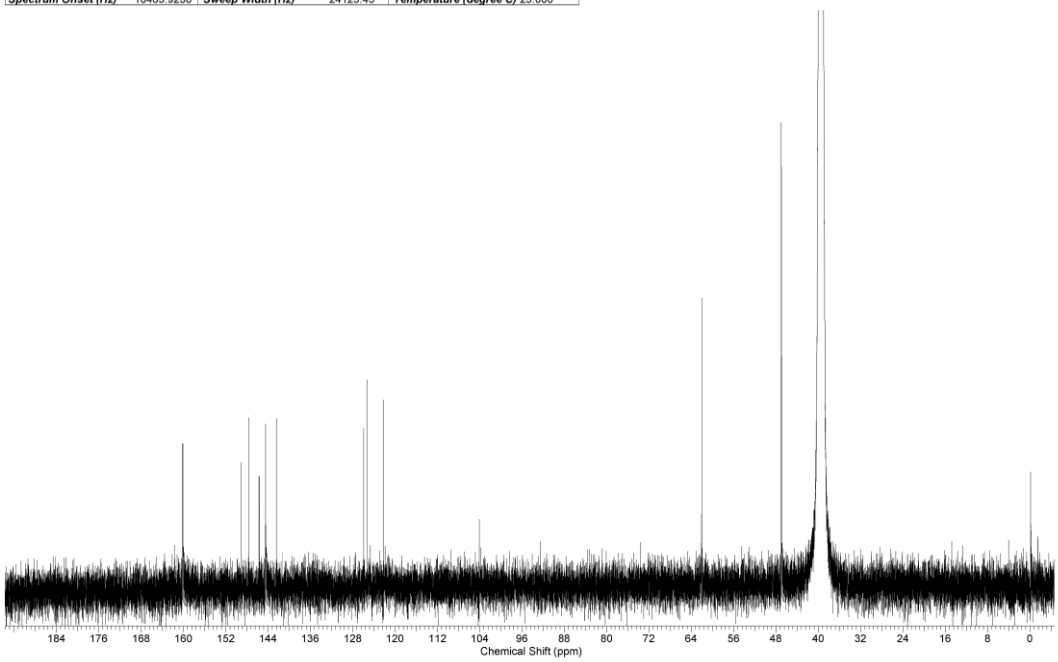

(b)

Figure A.30: - (a) ^{1}H NMR of Compound 39 (b) ^{13}C NMR of Compound 39

Acquisition Time (sec)	2.0486	***Comment***	Std proton	***Date***	Jul 2 2007		
Date Stamp	Jul 2 2007	***Frequency (MHz)***	399.78	***Nucleus***	1H	***Number of Transients***	64
Points Count	16384	***Pulse Sequence***	s2pul	***Receiver Gain***	38.00	***Solvent***	DMSO-d6
Spectrum Offset (Hz)	2398.6597	***Sweep Width (Hz)***	6396.42	***Temperature (degree C)***	25.000		

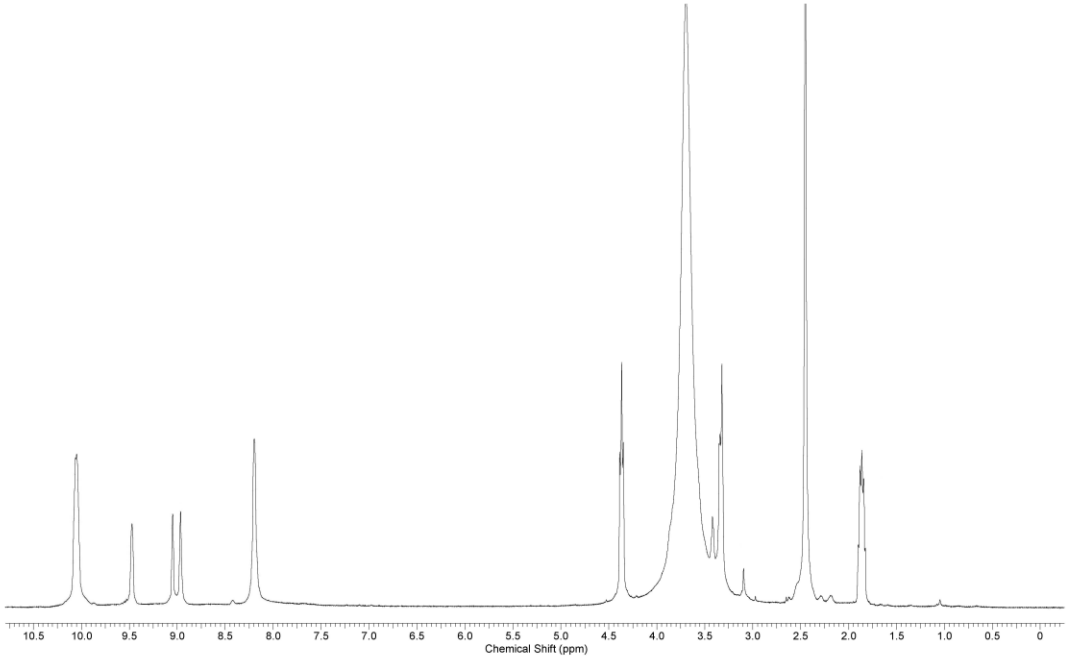

(a)

Acquisition Time (sec)	1.3005	***Comment***	Std proton	***Date***	Aug 12 2007		
Date Stamp	Aug 12 2007	***Frequency (MHz)***	100.53	***Nucleus***	13C	***Number of Transients***	10000
Points Count	32768	***Pulse Sequence***	s2pul	***Receiver Gain***	30.00	***Solvent***	DEUTERIUM OXIDE
Sweep Width (Hz)	24125.45	***Temperature (degree C)***	25.000				

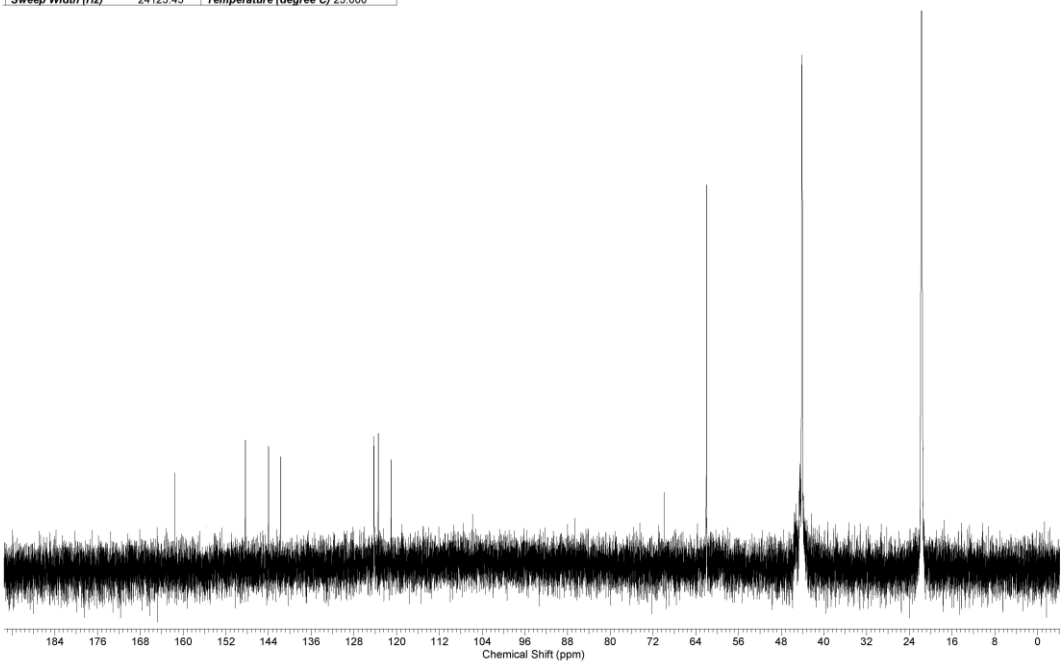

(b)